

Copyright

by

Rahul Pal

2017

**The Dissertation Committee for Rahul Pal Certifies that this is the approved version of  
the following dissertation:**

**Identification of Image-based Markers for Oral Pre-cancers and Cancers  
using *in-vivo* Multimodal Imaging**

**Committee:**

---

Massoud Motamedi, Ph.D., Chair

---

Gracie Vargas, Ph.D., Mentor

---

Andres Oberhauser, Ph.D.

---

Susan McCammon, M.D.

---

Marc Morais, Ph.D.

---

Javier Jo, Ph.D.

---

---

Dean, Graduate School

**Identification of Image-based Markers for Oral Pre-cancers and Cancers  
using *in-vivo* Multimodal Imaging**

**by**

**Rahul Pal, B.Sc., M.Sc.**

**Dissertation**

Presented to the Faculty of the Graduate School of  
The University of Texas Medical Branch  
in Partial Fulfillment of the Requirements  
for the Degree of

**Doctor of Philosophy**

**The University of Texas Medical Branch  
March, 2017**

## DEDICATION

*To my parents. I thank you both for not telling me what I should do but for believing in me and showing me what I am capable of.*

## **Acknowledgements**

The journey of a graduate student is a long journey that could not have been possible without the love and support of my family, both the personal and the professional ones. Over the last 6 years, through ups and downs, I managed to stay on track because the people in my corner always had my back.

My advisor, Dr. Gracie Vargas, has my heartfelt gratitude. Without her support, guidance and invaluable motivation, I would not have thrived as well as I did. She allowed me to attend numerous conferences, write independent grant proposals, mentor students and participate in many more academic activities apart from just carrying out experiments that helped my overall growth as a scientist. She had faith in my efforts and allowed me a freedom in my work that is sincerely appreciated. She not only trained me to become a curious researcher she also taught me that research is a way of thinking. I am grateful to have had an advisor who discussed science with me like an equal. Above all she provided a nurturing environment for me which was my home away from home for almost five years and I thank Dr. Vargas for being a motivating teacher as well as a caring friend.

I would like to also acknowledge my dissertation committee members, Dr. Massoud Motamedi, Dr. Andres Oberhauser, Dr. Susan McCammon, Dr. Marc Morais and Dr. Javier Jo, who have always supported my endeavors with constructive criticism and appreciated my accomplishments. I am grateful to Dr. Motamedi for agreeing to be the chair of my committee and for his invaluable inputs into my research. Dr. Oberhauser, Dr. McCammon, Dr. Morais and Dr. Jo helped me in every aspect of my work from identifying important research problems to designing experiments. I thank them all for guiding me throughout my career as a graduate student.

This journey would not have come to fruition without acknowledging the people in the Department of Biochemistry and Molecular Biology. I thank all three program directors Dr. Sarita Sastry, Dr. Tracy Toliver-Kinsky and Dr. James Lee for helping me to stay on track over the years. Student coordinator Mrs. JoAlice Whitehurst always made sure I was on top of graduate school requirements. My journey would not have been so cheerful without my graduate school friends Dr. Abhijnan Chattopadhyay, Dr. Arijit Dutta and Dr. Levani Zandarashvili. I thank them from the bottom of my heart for being a part of those late-night movies as well as long scientific discussions.

My lab members, Lorenzo Ochoa, Paula Villarreal, Tyra Brown, Jon Luisi and Jinping Yang have been great colleagues and integral part of my journey in the graduate school. They have always helped me out whenever I needed them. Lorenzo and Paula deserve special mention because they were my support both in and out of the lab. I could not have done this without them. They have been my family away from family.

My family and friends in India has been my unwavering strength. I could live in peace thousands of miles away from home because I knew my cousins Mr. Arindam Pal and Mrs. Kasturi Pal and my childhood friend Mr. Rahul Mukherjee are there to look after and support my family. They made me realize professional achievements means nothing without a caring family.

Finally, I owe every bit of myself, everything I am and I will ever become to my mother. Even in her last days, she never gave up on me. Her faith in me has been my beacon of strength. Although my mom and dad are not here to see me graduate, I know they are watching over me. The last two years has been difficult for me and I would not have been able to bear it without my brother's love and support. We went through a lot together and I am grateful for all he has done for me.

# **Identification of Image-based Markers for Oral Pre-cancers and Cancers using *in-vivo* Multimodal Imaging**

Publication No. \_\_\_\_\_

Rahul Pal, Ph.D.

The University of Texas Medical Branch, 2017

Supervisor: Gracie Vargas

## **Abstract:**

The five-year survival rate for oral cancer is 57% and highly correlated to the stage at diagnosis. Early diagnosis is challenging with current clinical approach of detection based on visual conventional oral examination of oral tissue surface with palpation to guide biopsy as subtle alterations often occur in early neoplasia, despite subsurface cellular and molecular alterations that are known to occur. Robust noninvasive methods are needed with improved performance to detect neoplasia and delineate benign tissue from treatable high-risk precancers and cancers for biopsy guidance.

Nonlinear optical microscopy (NLOM) has shown potential to identify optical signatures associated with microstructural and biochemical alterations in cancer, providing *in-vivo* three-dimensional imaging with contrast from endogenous fluorophores, including tissue metabolites,

NADH and FAD. Features revealed by NLOM have shown to parallel histopathology, however, studies are few and have focused on epithelial cells or stromal collagen but rarely together. While NLOM demonstrates potential in detection of neoplasia, image areas are spatially small. Practical implementation will require strategies for assessing larger areas of mucosal surface.

NLOM encompassing epithelial and stromal-based metrics was investigated to delineate neoplasia from normal and benign tissue. To address limited image views, a strategy for multimodal multiscale imaging, combining large area fluorescence imaging with subsurface microscopic evaluation of neoplastic features by NLOM, was devised. *In-vivo* NLOM revealed high sensitivity/specificity for neoplasia. Novel quantitative features from multiple layers were defined, including alterations in epithelial-connective tissue interface (ECTI) and associated with neoplastic cell clusters in 3D. Two approaches for wide-field fluorescence imaging (endogenous and using contrast for glucose metabolism), resulted in high sensitivity, an attribute desired in large area imaging to guide NLOM to suspicious sites. A study was conducted combining WF imaging with NLOM- results indicating feasibility for multiscale imaging with high sensitivity/specificity.

This research has resulted in new knowledge regarding the use of label-free NLOM in epithelial neoplasia and established a proof-of-concept multiscale approach for detection of oral neoplasms. Concepts developed in this dissertation are expected to be beneficial in further development of multimodal image based cancer detection method as well as future research on understanding how neoplastic changes occur in epithelium.



## TABLE OF CONTENTS

Abstract .....	vii
List of Tables .....	xvii
List of Figures.....	xviii
List of Abbreviations.....	xxviii
<b>Chapter 1: Introduction to oral epithelial neoplasms: current detection methods,</b>	
limitations and opportunities for improvements .....	1
1.1 Background: Oral Squamous Cell Carcinoma .....	1
1.2 Current clinical approach for detection of oral epithelial dysplasia	
(OED) and OSCC .....	2
1.2.1 Clinical diagnosis .....	3
1.2.2 Oral epithelium and stages of neoplasia .....	4
1.2.3 Histopathologic grading .....	6
1.3 Opportunities for improvements .....	7
1.4 New methods being explored for noninvasive detection of	
precancer/cancer .....	10
1.4.1 Detection of epithelial neoplasia with OCT and CRM .....	11
1.4.2 Confocal fluorescence microscopy in detection of	
epithelial neoplasms .....	12
1.4.3 Nonlinear optical microscopy (NLOM) .....	12
1.4.4 Advantages of NLOM for in vivo imaging .....	15
1.4.5 Use of NLOM in cancer detection and hallmarks of cancer .....	15
1.4.6 Limitations of NLOM .....	17
1.4.7 Wide-field (WF) fluorescence imaging for quick large	
area screening .....	17
1.4.8 WF autofluorescence (WF-AF) imaging .....	18

1.4.9 WF fluorescence imaging using a molecular contrast .....	19
1.4.10 Limitations of WF fluorescence imaging .....	19
1.5 Critical gaps in the field .....	21
1.6 Proposed approach to address these gaps .....	22
1.7 Thesis Outline .....	22
<b>Chapter 2: Nonlinear Optical Microscopy for layer resolved qualitative .....</b>	<b>26</b>
2.1 Introduction .....	26
2.1.1 Brief history of NLOM in oral cancer detection .....	27
2.1.2 Goal of the current study .....	29
2.2 Materials/Methods .....	31
2.2.1 Animal Model .....	31
2.2.2 MPAM-SHGM System .....	33
2.2.3 Visual grading of NLOM image stacks and validation .....	34
2.2.4 Image processing and data analysis .....	35
2.2.4.1 Thickness of epithelium .....	35
2.2.4.2 MPAM-based cytology .....	35
2.2.4.3 Collagen density .....	36
2.2.4.4 Statistical analysis .....	37
2.3 Results .....	38
2.3.1 In vivo NLOM for layer-resolved three-dimensional imaging in hamster buccal mucosa .....	38
2.3.2 Comparison of cytologic and extracellular atypia observed in NLOM and conventional histopathology .....	40
2.3.3 Cytologic abnormalities observed by qualitative and quantitative assessment of MPAM micrographs in dysplasia .....	42
2.3.4 Detection of extracellular collagen remodeling in dysplasia using SHGM .....	46
2.3.5 Combination of cytologic and extracellular features for	

multivariate analysis showing effects of inflammation .....	48
2.4 Discussion .....	49

### **Chapter 3: Three-dimensional visualization of epithelial-connective tissue interface**

(ECTI) in oral epithelial dysplasia using nonlinear optical microscopy .....	55
3.1 Introduction .....	55
3.1.1 Goal of the current study .....	57
3.2 Materials/Methods .....	58
3.2.1 Animal model .....	58
3.2.2 MPAM-SHGM System .....	59
3.2.3 Image processing and data analysis .....	59
3.2.3.1 Two-dimensional quantitative parameter for rapid evaluation of ECTI remodeling ( $\Delta$ Linearity) .....	59
3.2.3.2 ECTI Contour for three-dimensional quantitative evaluation of ECTI remodeling .....	60
3.2.3.3 Histopathology .....	62
3.2.3.4 Statistical analysis .....	63
3.3 Results .....	64
3.3.1 Visualization of neoplastic abnormalities with ECTI remodeling .....	64
3.3.2 2D evaluation of ECTI geometry and quantification of $\Delta$ Linearity from cross-sectional MPAM-SHGM .....	68
3.3.3 Three-dimensional visualization of ECTI surface in relation to cytologic atypia .....	71
3.3.4 Noninvasive delineation of ECTI contour for quantitative	

assessment of ECTI remodeling during neoplasia .....	74
3.3.5 ECTI remodeling showed spatial correlation with cytologic abnormalities in neoplasia .....	76
3.3.6 Multivariate statistical model for delineation of neoplasia from normal and benign conditions .....	77
3.4 Discussion .....	78
3.4.1 ECTI remodeling quantified as $\Delta$ Linearity in neoplasia .....	79
3.4.2 Volumetric assessment of ECTI remodeling .....	79
3.4.3 Advantages and challenges of volumetric assessment of ECTI remodeling .....	80
3.4.4 Association of ECTI remodeling and cytologic atypia .....	81
3.4.5 Conventional methods to study ECTI remodeling and their limitations .....	82
3.4.6 Advantages of NLOM based study of ECTI remodeling .....	82

#### **Chapter 4: Spectroscopic characterization of Oral Epithelial Dysplasia and Squamous**

Cell Carcinoma using Multiphoton Autofluorescence Micro-spectroscopy .....	84
4.1 Introduction .....	84
4.1.1 Goal of the current study .....	87
4.2 Materials/Methods .....	88
4.2.1 Animal Model .....	88
4.2.2 Microscopy/ Spectroscopy .....	89
4.2.3 Histopathology .....	89
4.2.4 Data Analysis .....	90
4.3 Results .....	90
4.4 Discussion .....	95

4.4.1 Reduced NADH-FAD autofluorescence in oral epithelial neoplasia .....	95
4.4.2 Spectral peak shifts in NADH-FAD autofluorescence .....	96
4.4.3 Potential application to detection efforts .....	96
4.4.4 Autofluorescence spectra and potential relationship to study of metabolism .....	97
4.4.5 Cytoplasmic autofluorescence spectra showed presence of PpIX .....	97
4.4.6 Intracellular dynamics of NADH, FAD and PpIX in a heterogeneous tumor microenvironment .....	98

## **Chapter 5: Large Area (Wide-field) Autofluorescence (WF-AF) Imaging in the Hamster**

Model for Oral Epithelial Neoplasia .....	101
5.1 Introduction .....	101
5.1.1 Goal of the current study .....	104
5.2 Materials/Methods .....	105
5.2.1 Animal Model .....	105
5.2.2 WF-AF Imaging System .....	105
5.2.3 <i>In vivo</i> WF-AF imaging .....	106
5.2.4 Image Analysis .....	107
5.2.5 Statistical Analysis .....	108
5.3 Results .....	109
5.4 Discussion .....	115
5.4.1 Complications of white light clinical diagnosis with benign conditions .....	116
5.4.2 Autofluorescence induced by blue light excitation .....	116

5.4.3 Elevated red autofluorescence in neoplasia .....	117
5.4.4 Performance of red to green intensity ratio .....	117
5.4.5 Performance of red to green intensity ratio in presence of inflammation .....	118

**Chapter 6:** Wide-field fluorescence imaging using a topical fluorescent probe for  
intracellular glucose uptake in the Hamster Model for

Oral Epithelial Neoplasia .....	120
6.1 Introduction .....	120
6.1.1 Goal of the current study .....	126
6.2 Material/Methods .....	127
6.2.1 Sample preparation and background imaging .....	127
6.2.2 2-NBDG topical application .....	127
6.2.3 2-NBDG decay .....	128
6.2.4 2-NBDG uptake by epithelial cells .....	128
6.2.5 Differential 2-NBDG uptake across pathological groups .....	129
6.2.6 Image Analysis .....	130
6.3 Results .....	131
6.4 Discussion .....	139
6.4.1 In vivo topical application of 2-NBDG in identification of oral epithelial neoplasia .....	139
6.4.2 Decay of 2-NBDG fluorescence over time after in vivo uptake in oral mucosa .....	140
6.4.3 Uptake of 2-NBDG by epithelial cells and penetration into basal cell layer .....	141
6.4.4 2-NBDG uptake across all groups .....	142

6.4.5 Performance of 2-NBDG based wide-field imaging in absence and presence of benign conditions .....	143
<b>Chapter 7: Multimodal noninvasive imaging for multiscale detection of oral epithelial neoplasia using wide-field fluorescence imaging and nonlinear optical microscopy .....</b>	<b>146</b>
7.1 Introduction .....	146
7.1.1 Goal of the current study .....	148
7.2 Materials/Methods .....	150
7.2.1 Animal Model .....	150
7.2.2 In vivo multiscale wide-field and NLOM imaging .....	150
7.2.3 Statistical analysis with generalized linear model .....	150
7.3 Results .....	152
7.3.1 Potential for multivariate statistical assessment of WF-AF and NLOM based features of neoplasia .....	153
7.3.2 Three parameter multivariate model .....	157
7.3.3 Potential for combining a glucose analog (2-NBDG) based WF fluorescence imaging with NLOM based features of neoplasia (Pilot study) .....	159
7.4 Discussion .....	162
<b>Chapter 8: Summary, Future directions and Conclusions .....</b>	<b>166</b>
8.1 Summary .....	166
8.2 Future directions .....	172
8.2.1 In vivo assessment of intracellular biochemical and metabolic events in neoplastic tissue .....	172
8.2.2 Continuous efforts in wide-field fluorescence imaging	

with external contrast agent for improved molecular specificity .....	173
8.2.3 Assessment of noninvasive NLOM in human oral mucosa .....	174
8.2.4 Development of compact multimodal imaging device	
for screening of oral mucosa .....	175
8.3 Conclusions .....	176
 <b>Appendix: Potential translation of NLOM in <i>ex vivo</i> human oral</b>	
squamous cell carcinoma .....	177
<b>References</b> .....	183
<b>Vita</b> .....	200



## List of Tables

Table 1. 1	Anneroth's histological grading criteria .....	7
Table 2.1	Sample classification based on NLOM and histopathological grading .....	41
Table 2.2	Summary of the ROC curve analysis of cytologic features and collagen density quantified from in vivo MPAM-SHGM .....	48
Table 3.1	Summary of the statistical analyses performed from $\Delta$ Linearity measurements carried out on cross-section images from MPAM-SHGM or histopathology. SHGM: Second Harmonic generation Microscopy, SD: Standard Deviation, AUC: Area Under the Curve, TP: True Positive, FP: False Positive, TN: True Negative, FN: False Negative .....	70
Table 3.2	AUC, sensitivity and specificity of ECTI contour in absence and presence of inflammation in study population as measured from ROC analysis .....	75
Table 3.3	Visual assessment and distribution of cytological features associated with OED .....	76
Table 5.1	AUC, sensitivity and specificity for normalized R/G values with or without the presence of inflammation in the study group .....	114
Table 6.1	Summary of ROC statistical analysis of normalized 2-NBDG fluorescence quantified from wide-field imaging .....	139
Table 7.1	Statistical models for multivariate linear regression of normalized R/G intensity ratio in combination with NLOM based cytologic parameters. Corresponding intercept, estimate and p-values shown .....	158
Table A1	Cytologic features identified by NLOM in ex vivo human OSCC from floor of Mouth .....	180

## List of Figures

Figure 1.1	Diagram of the basic features of dysplasia seen in a typical histologic examination. Cross-sectional views of a normal mucosa (a), mild dysplasia (b) and severe dysplasia (c) are shown. ....	5
Figure 1.2	Jablonski diagram of common nonlinear processes. Absorption of two photons can lead to fluorescence (left) or second harmonic generation (right). In second harmonic generation (SHG) electronic excitation does not occur .....	14
Figure 2.1	Schematic describing the experimental setup for in-vivo multiphoton autofluorescence microscopy (MPAM) and second harmonic generation microscopy (SHGM). HWP: half wave plate; GT: Glans Thompson prism; BE: beam expander; DF: dichroic filter. The hamster is placed on the stage of the inverted microscope with the buccal pouch exposed and facing the objective .....	34
Figure 2.2	In vivo NLOM of hamster buccal mucosa. Volume reconstructions of a normal (a) and a severe dysplasia (b) showing all three tissue layers (keratin, epithelium and stroma); single optical sections of a normal keratinizing layer (c), epithelial cells (d), and stroma (e) are compared with keratin (f), epithelial cells (g) and stroma (h) of a severe dysplasia. Images shows neoplastic features such as dyskeratosis, enlarged nuclei and ECM degradation in severe dysplasia; In vivo cross-section of the same severe dysplasia site is shown (i) with corresponding H&E (j) .....	39
Figure 2.3	Epithelial Thickness measurements from MPAM-SHGM (a) and histology (b) show statistically significant increase in thickness of mild, moderate and severe dysplasia from normal mucosa. Box plot analyses	

	show the median, 25th and 75th percentiles, and outliers for both MPAM-SHGM and histology. “*” and “***” represent statistical difference between groups at $p < 0.05$ and $0.01$ significance respectively .....	42
Figure 2.4	x-y micrographs from in-vivo MPAM are shown from normal (a), and dysplastic (b,c) epithelium of hamster oral mucosa. White boxes in “a” and “b” shows comparison of nuclear density between a normal and OED. “*” shows presence of keratin pearls (b) and arrows point towards enlarged nuclei (c) in dysplastic epithelium .....	43
Figure 2.5	a-g) x-y micrographs from MPAM showing cytologic atypia in OED. Multiple cytologic features such as increased mitotic figures (a), nuclear and cytoplasmic pleomorphisms (b-c), increase nuclear area (e), irregular polarity (f) and atypical accumulation of autofluorescence around nuclei (g) were observed. Arrows and dotted outlines point towards specific features identified in in-vivo MPAM. Scale bar, $40\mu\text{m}$ .....	44
Figure 2.6	Cytologic features of neoplasia measured from MPAM images. Average basal nuclear density (a), basal nuclear area (b) and coefficient of variation (CoVa) of basal nuclear area (c) in control, inflammation and OED are shown. ROC curves for these parameters are shown in d, e and f respectively. Blue and green ROC curves are for data sets in presence and absence of inflammation as a confounding factor. “*” and “***” represent $p < 0.05$ and $p < 0.01$ respectively .....	45
Figure 2.7	Reduction of collagen density in OED. x-y SHGM micrographs of normal (a) and OED (b) are shown in single planes. “*” in (b) indicates area of degraded collagen. Overall reduction of SHG signal density in OED compared with control and inflammation is shown in c). “***” represent $p < 0.01$ .....	47

Figure 2.8	Multivariate linear models created by using basal nuclear CoVa and collagen density. a) Scatter plot for control and dysplasia; b) scatter plot for control, inflammation and dysplasia. The dotted straight line represents optimal separation of groups as calculated from the linear model ..... 49
Figure 3.1	Cross-sectional x-z SHGM micrograph is shown in (a). Figure (b) shows an ECTI (solid white line) extracted from (a) after the FeatureJ: Edges plugin in ImageJ was applied. The dashed line represents the reference linear distance between the two ends of the image. The equations on the right were used to calculate $\Delta\text{Linearity}$ ( $\Delta L_{\text{norm}}$ ). Scale bar: 50 $\mu\text{m}$ .....60
Figure 3.2	Layer resolved volumetric MPAM-SHGM of hamster oral mucosa showed cytologic and microstructural features associated with neoplasia. Single optical sections and three-dimensional volumes of representative control (a), and dysplastic (b) hamster oral epithelium. x-y micrographs from MPAM (magenta) at different depth shows autofluorescence from keratinizing and epithelial layers. SHG (green) from collagen fibers in the lamina propria is shown in green. Histologic sections of control and dysplasia of corresponding ROIs are shown in respective insets.  K: Keratinizing layer, SE: Superficial epithelium, BE: Basal epithelium, LP: Lamina propria. Scale bar, 50 $\mu\text{m}$ . ..... 65
Figure 3.3	Early events during neoplastic transformation. MPAM-SHGM micrographs (a, c, e) and histological sections (b, d, f) of hamster oral mucosa for normal (a, b), mild dysplasia (c, d) and severe dysplasia (e, f) are shown. In-vivo autofluorescence from MPAM (Red) co-registered with SHG (Green) are overlaid to produce cross-sectional MPAM-SHGM micrographs (a, c, e) comparable to histology (b, d, f). K: Keratinizing layer; E: Epithelial layer, M: Lamina propria or ECM. White and black arrows point

	towards ECTI and “*” shows enlarged nuclei in dysplastic epithelium.	
	Scale bar: 50µm .....	67
Figure 3.4	<p><math>\Delta L_{norm}</math> measurements from MPAM-SHGM (a) and histology (b) show statistically significant increase in <math>\Delta</math>Linearity of mild, moderate and severe dysplasia from normal mucosa. Box plot analyses show the median, 25th and 75th percentiles, and outliers for both MPAM-SHGM and histology.</p> <p>“*” and “***” represent statistical difference between groups at <math>p &lt; 0.05</math> and 0.01 significance respectively .....</p>	69
Figure 3.5	<p>ROC curve at 95% confidence for <math>\Delta</math>Linearity calculated from MPAM-SHGM (Blue) and histological (Green) images. ....</p>	71
Figure 3.6	<p>Label-free volumetric imaging revealed remodeling of ECM in OED and confirmed presence of neoplastic cells in areas of SHG voids. a) SHGM of a single image plane from a control lamina propria; b) 3D surface map showing the flat topography of a control lamina propria comprising of 130 image planes from SHGM; c) SHGM of a single image plane from an OED lamina propria; d) 3D surface map showing downward bulging of the OED lamina propria comprising of 160 image planes from SHGM; “*” in (c) and (d) indicates areas of remodeled lamina propria; e) ROI of co-registered MPAM (magenta) and SHGM (green) from an OED showing presence of epithelial cells having neoplastic cytology (“*” and “→”) near remodeled lamina propria; f) en face view of the ROI shown in (e). Scale bar, 50µm .....</p>	73
Figure 3.7	<p>Remodeling of ECTI surface maps results in increased ECTI contour in OED. ECTI surface maps generated from SHGM z-stacks for control (a), inflammation (b) and dysplasia (c) show changes in surface topography. Color scale in (a) indicate changes in depth of the ECTI surface map. Red</p>	

	indicates a point towards the top and blue indicates a point towards the bottom of the surface map. (d) ECTI contour calculated from ECTI surface maps for all three groups. (e) ROC curves of ECTI contour when inflammation is present (blue) or absent (green) in the control group with AUCs 0.91 and 0.95 respectively .....	74
Figure 3.8	Association of cytologic features with ECTI deformation .....	77
Figure 3.9	Multivariate linear models created by using ECTI Contour and basal nuclear CoVa. a) Scatter plot for control and dysplasia; b) scatter plot for control, inflammation and dysplasia. Dotted straight lines represent optimal separation of groups as calculated from the linear model. The arrow in b) indicate the only miss-classified OED in presence of inflammation .....	78
Figure 4.1	Two-photon autofluorescence images of control (a), moderate dysplasia (b), and SCC (c) epithelium at 780 nm excitation. “*” and “→” in (a) indicates cytoplasm and nucleus respectively, and “*” in (b) indicates pleomorphic nuclei. “→” in (c) indicates premature keratinization. Scale bar: 50 $\mu$ m .....	91
Figure 4.2	In vivo two-photon autofluorescence spectra obtained from control, dysplasia and SCC from epithelium of hamster cheek pouch mucosa using 780 nm excitation; (a) raw intensity profile showing comparison between control (blue), two representative dysplasia (red and yellow) and SCC (green) epithelium; (b) same spectra as in (a) normalized to their peak intensities .....	92
Figure 4.3	Distribution of autofluorescence peaks in the 456 nm to 545 nm ranges is shown for all three pathological groups. Histograms indicate most samples in the control (blue) group showed a blue-green peak in lower wavelengths while in dysplasia (red) and SCC (green) showed a wider distribution of the	

	blue-green peak, which was often in the longer wavelengths than control .....	93
Figure 4.4	(a) Difference in peak fluorescence intensity at 635 nm emission between control, dysplasia and SCC; (b) Difference in blue/red intensity ratio between control, dysplasia and SCC. * $p < 0.05$ and ** $p < 0.01$ .....	94
Figure 5.1	Diagram of the WF-AF imaging system for live hamster cheek pouch imaging .....	106
Figure 5.2	USAF resolution target (left) with zoomed in image on the right shows line spacing at group 4 and element 3 (dotted outline) was easily discriminated .....	109
Figure 5.3	Representative white light and WF-AF images of a DMBA treated hamster cheek pouch are shown. a) White light image; b) composite of red and green autofluorescence; c) red autofluorescence and d) green autofluorescence. Examples of a large tumor (white box), dysplasia ('*'), a necrotic tumor ('yellow dashed □'), several other exophylic tumors ('solid arrows') and a normal area (dashed box) are outlined .....	110
Figure 5.4	(a) and (b) are representative white light and WF-AF images respectively of a control cheek pouch mucosa. (c) and (d) shows white light and WF-AF images respectively of an inflamed cheek pouch mucosa .....	112
Figure 5.5	Normalized R/G intensity ratio is shown for control, inflammation, dysplasia and SCC tissue. ** $P < 0.01$ .....	113
Figure 5.6	ROC curves showing the performance of the WF-AF imaging with (blue curve) or without (green curve) the inclusion of inflammation in the study .....	114
Figure 6.1	a) Glucose metabolism in normal cells. End product of glycolysis (Pyruvate) is utilized by mitochondria for oxidative phosphorylation as	

	indicated by a bold green arrow. b) Neoplastic tumor cells have a higher rate of glucose uptake, glycolysis and lactate production indicated by bold back and red arrows .....	122
Figure 6.2	a) Chemical structure of 2-NBDG. b) Excitation and emission spectra of 2-NBDG. c) 2-NBDG is internalized by glucose transporter 1 (GluT1) and subsequently phosphorylated by glycolytic enzyme hexokinase .....	124
Figure 6.3	Wide-field fluorescence imaging setup for 2-NBDG imaging .....	128
Figure 6.4	In vivo uptake of 2-NBDG. a) Time course of 2-NBDG fluorescence with wide-field fluorescence imaging of a DMBA treated hamster oral mucosa. b) Average 2-NBDG fluorescence intensities measured at each imaged time point from multiple ROIs showed the decay kinetics of intracellular 2-NBDG. Blue: tumors; Red: normal .....	132
Figure 6.5	Confocal images of hamster oral mucosa before (a) and after (b) 2-NBDG topical application. c) Analysis of Lambda stacks showed a small autofluorescence peak in native tissue (red) while a large fluorescence peak for 2-NBDG centered around 550 nm was found in the epithelium topically treated with 2-NBDG .....	133
Figure 6.6	Micrographs from two-photon microscopy before and after topical application of 2-NBDG. Both superficial and basal epithelial layers showed increased fluorescence after 2-NBDG staining indicating penetration of 2-NBDG into the basal epithelium .....	134
Figure 6.7	White light (a) pre-stained (b) and post-stained (c) images of a normal hamster cheek pouch are shown. (d) H&E stained cross-section of the ROI (c: red box) normal histopathologic features .....	135
Figure 6.8	White light (a) pre-stained (b) and post-stained (c) images of a tumor are shown. MPAM-SHGM cross-section is shown in (c) and H&E stained	



	cross-section in (d) confirms the pathology .....	135
Figure 6.9	White light (a) pre-stained (b) and post-stained (c) images of a tumor associated epithelium is shown. The region of suspicion is outlined at the top left corner of the tissue in (c). H&E stained cross-section in (d) confirms the pathology to be moderate dysplasia .....	136
Figure 6.10	White light (a) pre-stained (b) and post-stained (c) images of a moderate dysplasia are shown. The region of high 2-NBDG uptake in (c) is outlined. d) H&E stained section of the ROI .....	137
Figure 6.11	a) Normalized 2-NBDG fluorescence intensity as measured from wide-field imaging for normal, inflammation, dysplasia and SCC tissue. b) Normalized 2-NBDG fluorescence for mild, moderate and severe dysplasia. c) Distribution of 2-NBDG uptake for each sample across pathological groups. d) ROC curves using normalized 2-NBDG fluorescence with or without inflammation in the normal group. * $p < 0.05$ , ** $p < 0.01$ , n.s. $p > 0.05$ .....	138
Figure 7.1	Multimodal imaging approach with sequential WF-AF imaging and in vivo NLOM is shown; a) white light image of a DMBA treated hamster oral mucosa; b) WF-AF image of the same mucosa; c) NLOM of the region of interest shown by red colored box in b). Single x-y micrographs from the keratinizing layer, epithelium and stroma is shown in three panels. d) H&E stained section of the imaged site. “*” in a) shows an advanced tumor and “*” in c) and d) indicates a cluster of neoplastic cells. It should be noted that similar cytologic features were observed in NLOM and histopathology .....	153
Figure 7.2	Generalize linear model by combining normalized R/G intensity ratio with basal nuclear CoVa in absence (a) and presence of inflammation (b).	

	The dotted line in each panel shows a representation of the GLM .....	154
Figure 7.3	ROC curves for the generalized linear models of combined R/G intensity ratio and basal nuclear CoVa are shown in absence and presence of inflammation .....	155
Figure 7.4	a) and b) shows generalized linear models when normalized R/G intensity ratios were combined with ECTI contour in absence and presence of inflammation respectively. The dotted line in each panel shows a representation of the GLM .....	156
Figure 7.5	ROC curves for the generalized linear models of combined R/G intensity ratio and ECTI contour are shown in absence and presence of inflammation .....	157
Figure 7.6	ROC curves for the multivariate model of combined R/G intensity ratio, basal nuclear CoVa and ECTI contour are shown in absence and presence of inflammation .....	159
Figure 7.7	White light image (a), WF-AF image (b) and post 2-NBDG image (c) of a hamster cheek pouch are shown. A region of interest in c) is shown by the box around it; d) corresponding histology of the region of interest shown in c) .....	160
Figure 7.8	a) and b) shows generalized linear models when normalized 2-NBDG fluorescence was combined with basal nuclear CoVa in absence and presence of inflammation respectively. Dotted line in both panels shows a representation of the GLM .....	160
Figure 7.9	a) and b) shows generalized linear models when normalized 2-NBDG ratio was combined with ECTI contour in absence and presence of inflammation respectively. Dotted line in both panels shows a representation of the GLM .....	161

Figure A1:	Invasive cancer of larynx. A1a) Three-dimensional volume of normal larynx with MPAM-SHGM; A1b) volume reconstruction of SHGM from extracellular matrix of normal larynx; A1c) MPAM-SHGM volume reconstruction of invasive OSCC of human larynx; A1d) Extracellular collagen SHGM of the invasive OSCC. Red: MPAM; Green: SHGM. Scale bar 50 $\mu$ m. ....	178
Figure. A2:	(a-d) NLOM Micrographs of superficial and basal epithelium from OSCC and corresponding normal mucosa of floor of the mouth. Arrows in c) indicate cytologic features consistent with neoplasia. ....	189
Figure A3:	Coefficient of variation (CoVa) in nuclear area; a) non-tumor/clinically normal and tumor/OSCC biopsies for individual patients; b) all OSCC and normal biopsies combined. ** $p < 0.01$ .....	181

## **List of Abbreviations**

OSCC	Oral Squamous Cell Carcinoma
OED	Oral Epithelial Dysplasia
COE	Conventional Oral Examination
WHO	World Health Organization
NLOM	Nonlinear Optical Microscopy
MPAM	Multiphoton Autofluorescence Microscopy
SHGM	Second Harmonic Generation Microscopy
H&E	Hematoxylin & Eosin
ECM	Extracellular Matrix
BM	Basement Membrane
ECTI	Epithelial-Connective Tissue Interface
LP	Lamina Propria
ROC	Receiver Operator Characteristic
OCT	Optical Coherence Tomography
CRM	Confocal Reflectance Microscopy
CFM	Confocal Fluorescence Microscopy
WF	Wide Field
WF-AF	Wide-Field Autofluorescence
TPEF	Two-photon Excitation Fluorescence
NADH	Reduced Nicotinamide Adenine Di-Nucleotide
FAD	Flavin Adenine Di-Nucleotide
PpIX	Protoporphyrin IX
2-NBDG	2-(N-(7-Nitrobenz-2-oxa-1,3-diazol-4-yl)Amino)-2-Deoxyglucose
DMBA	7,12-Dimethylbenz(a)anthracene
CoV <sub>a</sub>	Coefficient of Variation

# **Chapter 1**

## **Introduction to oral epithelial neoplasms: current detection methods, limitations and opportunities for improvements**

### **1.1 Background: Oral Squamous Cell Carcinoma**

Oral cancer, typically defined as cancer of the mouth and oropharynx, is the sixth most common cancer in the world (1). Approximately 94% of oral cancers are oral squamous cell carcinoma (OSCC) and over 450,000 cases are detected worldwide annually, of which 49,000 are newly diagnosed solely in the US (2). Slightly more than 50% of patients diagnosed with oral cancer survive more than 5 years post-diagnosis and this rate has not improved significantly over the past several decades despite awareness of this disease and increased efforts at detection (3). Survival rate of patients detected with OSCC largely depends on the stage of detection with early detection associated with substantially improved chances of survival (4). As OSCC is often detected at stages beyond regional occurrence when chances of survival are highest, there is a need for development of new and improved techniques for early detection of oral neoplasia, including high-risk precancers having a high chance for transformation and cancers, both of

which are targets for treatment in current clinical management. The need for improved early detection approaches stands for epithelial neoplasms in general, as a common theme found among the various types, including cervical, ovarian, esophageal etc. is that patient outcomes are improved drastically with early detection. The routine way for detection of oral neoplastic lesions to date is white light inspection and subsequent biopsy of suspected lesions. With white light visual guidance, the chances of missing potential neoplastic sites are high - clinical diagnosis of these sites vary between clinicians and the sampling size is limited by the number of biopsies one can perform on a patient. Also, patients may present with several lesions or diffusely spread lesions with varying appearances that makes selection of biopsy site a challenge because white-light visualization only shows surface abnormalities. A limitation is imposed by the difficulty of detecting early lesions by white light inspection (5, 6). Heterogeneity within lesions provides complications toward identification of benign lesions, precancerous lesions or oral epithelial dysplasia (OED) and late stage OSCC.

## **1.2 Current Clinical Approach for Detection of oral epithelial dysplasia (OED) and OSCC:**

The current clinical approach to detect and diagnose OSCC and high risk precursors that have a high chance for transformation (discussed below) such as oral epithelial dysplasia (OED) begin with conventional oral examination (COE), which is inspection of the tissue surface with white light visualization combined with palpation of the oral cavity by an experienced physician. COE is performed to identify suspicious sites including suspicious lesions that may be biopsied immediately or followed over time by visual surveillance. Biopsied lesions are subjected to

histopathologic assessment by a pathologist. Accurate histopathologic diagnoses rely on a number of critical steps: clinical information provided by COE, appropriate biopsy, and a pathologist's interpretation of biopsy results.

**1.2.1 Clinical diagnosis:** In the U.S., the tongue is the most common site (30% cases) for OSCC followed by lip (17%) and floor of mouth (14%). Development of OSCC is a multistep process preceded by different grades of OEDs, in which neoplasia of the epithelium is present but has not yet progressed beyond the basement membrane that separates the epithelium from the underlying stroma, vasculature, and lymph vessels. OEDs have recently been classified as “potentially malignant disorders (PMD)” by the WHO Collaborating Center for Oral Cancer and Precancer (7) and recent recommendations for the treatment of moderate and high grade OEDs have been made based on the risk for malignant transformation (8). While OED itself is a condition that must be defined in histology (e.g. a histological lesion) and is not evident by any one visibly identifiable lesion, there are clinical lesions that may be associated with OED and with early cancer. Such oral cavity lesions typically show up as red (erythroplakia), white (leukoplakia) or mixed colored lesions often without pain or other symptoms. These are known as clinically premalignant lesions that may contain OED or OSCC.

Early stages of oral carcinoma are characterized by focal change in color and subtle change in surface texture including granularity, keratosis, erosion etc. These changes arise from architectural changes that occur underneath the surface due to altered biochemical properties of the epithelium. However, it is important to note that in some cases no obvious signs of premalignant or carcinomas are present on the surface, particularly at the stages of OED, carcinoma-in-situ, or early carcinoma. Progression of early stage cancer to later stages is

characterized by more severe clinical signs such as ulceration, induration, bone invasion, tooth mobility and pain. Tumor invasion and metastasis to lymph nodes are seen in advanced stages increasing the severity to levels less likely to be successfully managed. A clinical examination of oral cavity of patients suspected to have OED or OSCC usually presents a wide range of clinically altered regions that may range from early subtle changes in color, elasticity or surface texture to more pronounced lesions.

**1.2.2 Oral Epithelium and stages of neoplasia:** Figure 1.1 shows a schematic representation the stages of the mucosal epithelium during neoplastic transformation. The expected alterations in tissue architecture from normal (Fig. 1.1a), to mild dysplasia (Fig. 1.1b) to severe dysplasia (Fig. 1.1c), are shown, representing architectural elements that are visualized in histopathology. The top most surface layer of the epithelium is composed of terminally differentiated keratinocytes forming the superficial stratum corneum (9). The underlying cell layers are divided into superficial and basal epithelium. The superficial layer is represented by larger cells while the basal cells are shown as small epithelial cell layer which forms the lower layer of the epithelium. In a normal mucosa cell division takes place primarily in the basal layer, with basal cells undergoing a differentiation process and moving superficially to form the stratum spinosum and finally stratum corneum before being sloughed off the surface (10-12). The extracellular matrix (ECM)/ *lamina propria* (LP) underlying the basal layer is primarily composed of collagen, elastin, and laminin networks and act as a supporting matrix for the epithelium and contains the vascular and lymphatic network of vessels. The epithelium and LP are separated by basement membrane (BM) and this junction is known as the epithelial connective tissue interface (ECTI). In the current understanding, neoplastic transformation



begins in the basal epithelium (13-15); increased and uncontrolled proliferation of basal cells leads to overcrowding of undifferentiated cells in the upper layers, while at the same time secretion of proteases causes remodeling of the ECM (16, 17). There are a number of cytologic, molecular and functional changes that go beyond these architectural changes during neoplastic transformation.

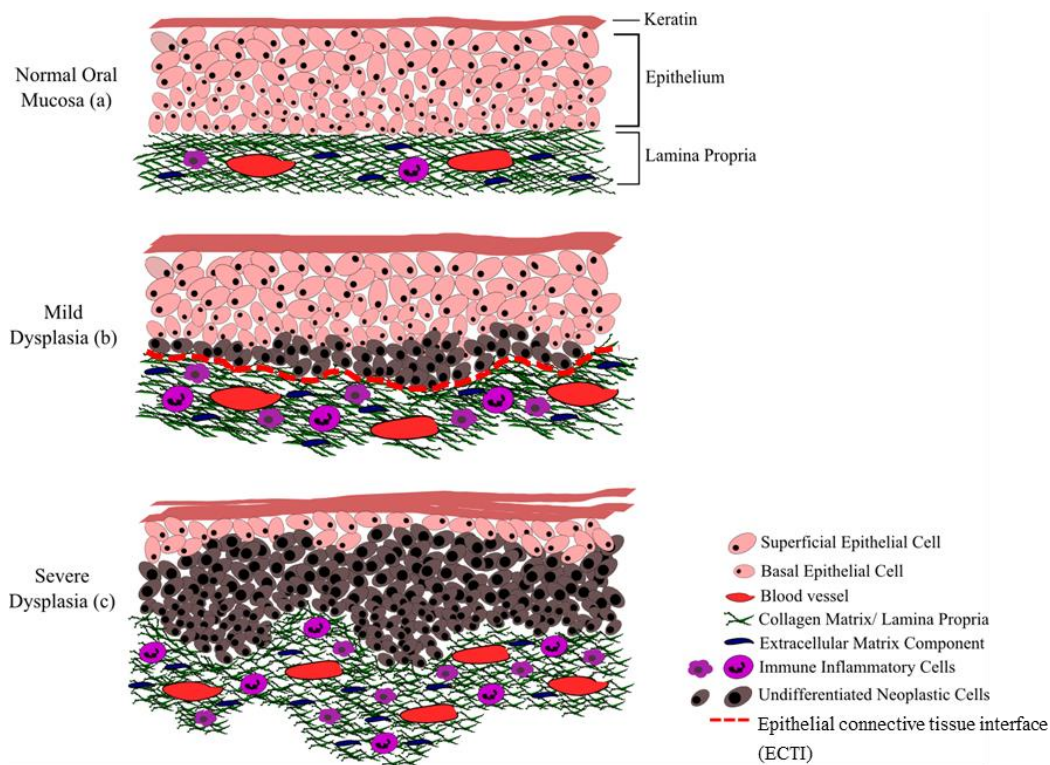


Figure 1.1: Diagram of the basic features of dysplasia seen in a typical histologic examination. Cross-sectional views of a normal mucosa (a), mild dysplasia (b) and severe dysplasia (c) are shown. Published in Pal et al. 2015

As noted, the stages of OED are pathologically divided into mild dysplasia in which neoplastic changes are confined near the basal layer, moderate dysplasia where neoplastic changes extend into the middle one-third of the epithelium and high grade dysplasia (HGD) or severe dysplasia comprising the majority of the epithelium in which abnormal proliferation is seen from the basal layer into the upper third of the epithelium. Carcinoma-in-situ (CIS)

comprises the full extent of the epithelium. In the advanced stages of dysplasia (Fig. 1.1c, “severe dysplasia”) and CIS severe remodeling of the ECM occurs, reflected in the alteration of flat architecture of ECTI by formation of rete ridges as epithelial cells start protruding downwards into the lamina propria without physically disrupting the basement membrane (BM) (18). The normal ECTI is relatively flat in the human buccal mucosa, floor of the mouth and the ventral surface of the tongue. However, in other locations in the oral cavity the presence of rete ridges result in an altered ECTI shape. The process of neoplastic development described here gives rise to multiple cytologic and architectural abnormalities that are conventionally used in histopathologic diagnosis and staging of oral precancer and cancers.

**1.2.3 Histopathologic grading:** The first histological grading method for epithelial neoplasms was introduced by Broder et al. in 1927 that used a scoring system from I to IV with a grade I lesion being highly differentiated epithelium and a grade IV lesion being poorly differentiated epithelium (19). Over the years multiple grading systems have been proposed. Most of these methods used a similar scoring system of grades 1 through 4 with grade 4 being most severe with higher probability for metastasis than a highly differentiated epithelium. In a multivariate survival analysis, the Anneroth’s malignancy grading method was found to be highly significant prognostic factor and therefore is widely accepted in oral cancer diagnosis. Table 1.1 shows a summary of the features assessed in Anneroth’s grading system. Criteria for dysplasia as described by the World Health Organization (WHO) accounts for similar cytologic abnormalities as shown in table 1.1 with additional focus given on architectural changes in the epithelium.

Table 1.1: Anneroth's histological grading criteria

Histologic grading of malignant squamous cell carcinoma				
Morphometric features	1	2	3	4
Degree of keratinization	Highly keratinized (>50% of the cells)	Moderately keratinized (5-20% of the cells)	Minimal keratinization (<5% of the cells)	No keratinization
Nuclear polymorphisms	Little nuclear polymorphism (>75% mature cells)	Moderately abundant nuclear polymorphism (50-75% mature cells)	Abundant nuclear polymorphism (25-50% mature cells)	Extreme nuclear polymorphism (0-25% mature cells)
Number of mitoses	0-1	2-3	4-5	>5

### 1.3 Opportunities for improvements:

The current gold standard for diagnosis of oral malignant and premalignant lesions is biopsy of suspicious lesions and histopathology. Intra-observer and inter-observer variations are often seen during pathological diagnosis of oral malignant and premalignant lesions especially in cases of OED (20). Diagnosis of OSCC requires sufficient sampling by invasive biopsy methods (scalpel or punch biopsy) because of tissue heterogeneity within clinically identified lesions. Additionally histopathological abnormalities may be present in areas with no visible and clinically identifiable lesions making sampling of biopsy sites very critical. Some of the basic measures of accuracy of a diagnostic test are as following:

1. **Sensitivity:** The probability that a test will correctly classify a sample with the disease condition

$$\text{Sensitivity} = \frac{\text{true positives}}{(\text{true positive} + \text{false negative})}$$

2. **Specificity:** The probability that a test will correctly classify a sample without the disease condition

$$\text{Specificity} = \text{true negatives} / (\text{true negative} + \text{false positives})$$

3. **Positive predictive value:** The probability that a positive result indicates the presence of the target pathology
4. **Negative predictive value:** The probability that a negative result indicates the absence of the target pathology

Studies on the performance of COE for oral cancer detection indicate a large range of sensitivities (60-97%) and specificities (75-99%) (21-23). A recent meta-analysis reported specificity of 31% with >90% sensitivity for high risk precancerous lesions, noting COE cannot reliably distinguish these from benign mucosa (24, 25). Benign conditions offer additional complexity to clinical diagnosis of precancerous/premalignant lesions leading to either a false sense of security or over sampling during biopsy. Identification of subtle changes in tissue appearance especially in cases of early precancerous lesions could be complicated and while they could still be identified by an oral cancer specialist, a lack of experience limits early diagnosis by community practitioners or general dentists. Downer et al. has reviewed the performance of visual assessment of oral cancers and observed a large variation in sensitivity (60-97%) and specificity (75-90%) of detection in the literature (21). To improve contrast between normal tissue and precancerous lesions several visual adjuncts are available including the use of toluidine blue which is a vital dye that has been used in oral cancer detection for many years. However, in a review by Patton et al. in 2008 the sensitivity of toluidine blue was found to range from 38-98% while specificity ranged from 9-93% (26). Lack of reliability of toluidine blue staining has limited its regular use in clinics in the USA for detection of oral premalignant and malignant lesions (27).

These limitations in COE sensitivity and specificity as well as variations found between physicians indicate the need for adjunct screening and/or diagnosis methods to attain improved sensitivity, specificity, positive and negative predictive values of tests for oral premalignant and malignant lesions. Methods to detect subtle changes seen in OED and early cancers and to better differentiate neoplasia from benign conditions such as may be present in clinical premalignant lesions which may or may not be neoplastic are needed to achieve better screening for patients with potential oral malignancy. Additionally, there is a requirement to guide clinicians to areas of high potential for neoplastic transformation and better guide biopsies that are performed on a patient to better increase chances of detection. Further, improved methods to guide biopsy may 1) reduce the number of invasive procedures, 2) could reduce pathological evaluation of unnecessarily biopsied lesions and 3) could reduce the mental trauma on patients and their families.

An improvement in detection of indicators of neoplasia is needed. A desired method would target key hallmarks of cancers. There are currently ten 'established' hallmarks of cancer, several of which induce observable microstructural changes in precancerous and cancerous tissue (28). These hallmarks typically describe the process of neoplastic development and have been actively targeted for therapeutic interventions. Several cytologic features such as nuclear and cellular overcrowding, abnormal variations in nuclear and cellular shapes and sizes are observed during conventional histopathologic diagnosis that could indicate presence of known hallmarks such as sustaining proliferative signaling, evading growth suppressors, resisting cell death etc. Other well-established hallmarks such as deregulating cellular energetics, inducing angiogenesis, activation of invasion and metastasis have shown promise in detection of cancers

and needs to be further explored. Use of techniques that reveal changes that may be associated with these known hallmarks that occur with neoplasia presents an opportunity for more reliable indicators of OEDs and OSCC.

#### **1.4 New methods being explored for noninvasive detection of precancer/cancer:**

*In vivo* assessment of microstructural alterations in oral neoplasia has primarily involved optical imaging techniques which offer a noninvasive way to assess the microarchitecture or optical properties of tissue which may be related to both structure and biochemical makeup. Among these are methods that rely on scattering or reflectance of light from complex tissues such as optical coherence tomography (OCT) and confocal reflectance microscopy (CRM) (29, 30); and methods whose image contrast comes from fluorescence such as large-area widefield fluorescence, confocal fluorescence microscopy (CFM) and nonlinear optical microscopy (NLOM) (31-34). These techniques depend on the interaction between live tissue and varying wavelengths of light to detect neoplastic abnormalities noninvasively. Normal white light examination or narrow band illumination (a modality based on reflectance) uses wavelengths in the visible range (400-700 nm) which shows abnormalities on the mucosal surface due to changes in tissue optical properties such as scattering. Fluorescence methods make use of visible light to induce fluorescence from endogenous biomolecules that have been useful in detection of neoplasia, however only on the surface without any depth information. Light in the ultra-violet (UV) region (100-400 nm) could be used to probe for fluorescent biomolecules such as hemoglobin and may act as an indicator of angiogenesis often seen in neoplastic epithelium.

Among other *in vivo* detection methods for neoplasia wide-field (WF) fluorescence imaging under a variety of approaches has been explored extensively in the past, in some cases showing discrimination between normal and neoplastic tissue with high sensitivity but very low specificity in presence of benign lesions. WF fluorescence imaging techniques enables visualization of large surface areas (many centimeters in length) a capability which is important when sites harboring potential neoplasia are first being identified (large areas screening). WF methods rely on fluorescence alterations in neoplastic tissue with contrast provided by autofluorescence or exogenous contrast agents with molecular specificity.

A description of the advantages and limitations of these microscopy and large area optical imaging modalities are discussed in the following section:

**1.4.1 Detection of epithelial neoplasia with OCT and CRM:** OCT with a resolution on the order of ~7-10um may be useful in detecting architectural features epithelial thickness and collagen density of oral mucosa that occur with neoplasia and submucosal fibrosis (35). Studies with OCT imaging of *ex vivo* human OSCC tissue showed sensitivity and specificity of 81.5% and 87% respectively for discrimination of normal and neoplastic tissue (36). Alterations in epithelial thickness, variations in morphology of epithelial-connective tissue interface are observed in oral neoplasia using OCT (37, 38). A limitation of the method is that it does not provide the subcellular resolution needed for assessment of cytologic abnormalities which are associated with neoplasia (39, 40). CRM, providing subcellular resolution, on the other hand has been shown to be useful in detecting cytologic abnormalities by *in vivo* imaging of large multifocal oral lesions (41). CRM allows high resolution imaging of mucosal tissue (42) however has limited imaging depth restricting *in vivo* application of CRM in thick mucosa especially in cases of severe

dysplasia and squamous cell carcinoma. Moreover, both OCT and CRM work on the principle of light scattering in tissue and hence are unable to provide molecular or functional information.

**1.4.2 Confocal fluorescence microscopy in detection of epithelial neoplasms:** Confocal fluorescence microscopy (CFM) allows investigation of neoplastic tissue with exogenous contrast agents (32). Cytologic features like histopathology have been observed in studies involving *in vivo* CFM. Alternatively, exogenous contrast agents such as methylene blue, fluorescein, acriflavin, DNA intercalating molecules have been tested with moderate success for high resolution visualization of neoplastic features in live tissue. However, CFM is limited in imaging depth (42) due to high light scattering of excitation wavelengths from tissues. Fiber based confocal endomicroscopy systems have been developed and investigated for clinical applications with the primary drawback being the need for contrast agents which are in some cases not FDA approved and may also be damaging to DNA integrity and function.

**1.4.3 Nonlinear optical microscopy (NLOM):** NLOM is a general term used to describe fluorescence microscopy in which the detected response (e.g. fluorescence) is nonlinearly related to the illumination, in contrast to methods in which the collected response is linearly proportional to the input as is found in traditional fluorescence microscopy and CFM. In NLOM, fluorescence is generated from higher order light-matter interactions and the dependence of fluorescence intensity on incident light intensity is nonlinear in nature (43). The most common form of NLOM used in biomedical studies is two-photon excitation fluorescence (TPEF) in which two near-infrared photons are absorbed nearly simultaneously (within  $\sim 0.5$  fs) to induce fluorescence emission of a fluorophore (43). Fluorescence is a process involving absorption of photons by a molecule resulting in electronic transitions into high energy states followed by



relaxation to the ground energy state which results in emission of photons at a longer wavelength. TPEF involves a similar process, however requires the near simultaneous absorption of two photons whose energies equate that of a one (traditional) photon fluorescence process (44-46). Fig. 1.2 shows the Jablonski diagram of excitation and emission processes for TPEF where two photons are absorbed by a molecule to produce a single emission photon during the relaxation to the ground electronic state. The two lower energy photons (long wavelength) combine to provide the excitation energy for electronic transitions to a higher state. The electronic relaxation process to return to the ground state does not differ from that of one photon fluorescence. Therefore, in contrast to conventional fluorescence processes, TPEF results in emission of photons having shorter wavelengths (visible light) than those used for excitation (near infrared). In practice, TPEF requires the use of an ultrashort-pulsed near-infrared laser in which the applied excitation wavelength is approximately twice the wavelength normally required for traditional fluorescence of a fluorophore. The delivery of ultrashort pulses at a high repetition rate of light increases the probability of two-photon absorption needed, and the near infrared light provides the photon wavelengths needed for the process. Three-photon fluorescence involves absorption of three photons to induce fluorescence and is relevant in biology samples due to UV fluorophores found in tissues such as aromatic amino acids. Another common nonlinear process based on nonelastic scattering, termed second harmonic generation (SHG), is shown in the Fig. 1.2 in which photons interacting with a material lacking inversion symmetry 'combine energies' to produce a single higher energy (short wavelength) photon. The resulting light following this process has half the wavelength of the illumination light. This process, alternatively termed frequency doubling, has long been used in lasers in which a pump beam illuminates a crystal lacking inversion symmetry to produce

frequency doubled light (Incident wavelength: 800 nm; SHG wavelength: 400 nm). In biological specimens, non-centrosymmetric biomolecules such as collagen fibers and muscle are known to produce SHG signal (47, 48). In this thesis, the term MPM is used to encompass the methods of two and three photon excitation fluorescence, and NLOM is used to describe two and three photon processes and second harmonic generation.

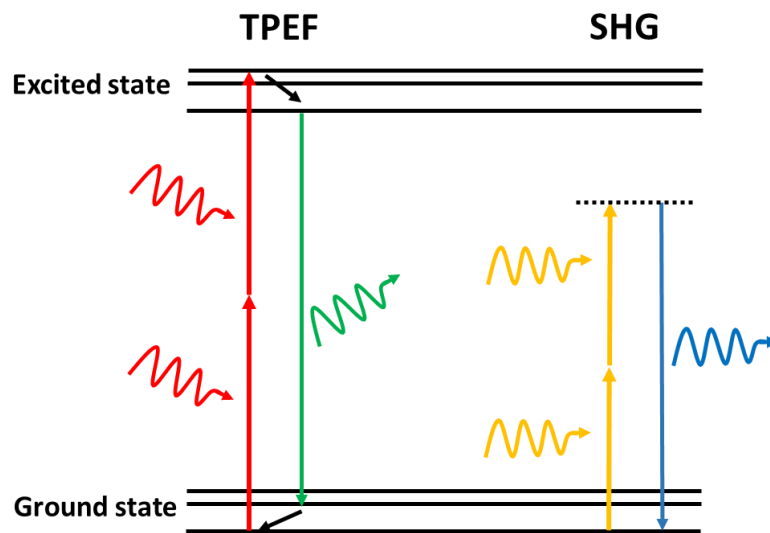


Figure 1.2: Jablonski diagram of common nonlinear processes. Absorption of two photons can lead to fluorescence (left) or second harmonic generation (right). In second harmonic generation (SHG) electronic excitation does not occur.

Details on how formation of an image occurs using NLOM can be found in the literature (46) but briefly involves a laser-scanning microscope configuration. Key to the ability to form an image with depth-resolution is the fact that excitation of multiphoton fluorescence or SHG occurs only at the focal volume of the imaging objective, such that all emission arising from the tissue at any point in time arises from that known volume. Since in NLOM fluorescence efficiency is nonlinearly dependent on excitation light intensity fluorescence emission reduces

rapidly above and below the focal plane confining the fluorescence into a small volume in the order of femto liters. Laser scanning of the illumination point thus allows point-by-point collection of fluorescence or SHG (separated using filters that target the spectral properties of the process) through raster scanning of mirrors and collection of images one plane at a time. Motorized control of the objective allows for its depth movement to collect planes at sequential depths.

**1.4.4 Advantages of NLOM for in vivo imaging:** Use of NIR excitation enables deep tissue imaging for intravital microscopy due to the decreased light scattering that occurs at longer wavelengths. Imaging of thick tissue samples especially in high grade precancers and invasive cancers require higher penetration of excitation light. Higher tissue penetration in NLOM is achieved by lower scattering of NIR excitation light. Additionally, NLOM takes advantage of low nonspecific tissue absorption of excitation light in the NIR wavelength range. This enables NLOM excitation light to penetrate deeper into the tissue for three-dimensional imaging of larger volumes of tissue. This enables an inherent optical sectioning capability of NLOM for three-dimensional imaging without the need for a pin hole. Autofluorescence from NADH and FAD, and SHG from collagen in extracellular matrix provide inherent contrast for live tissue microscopy.

**1.4.5 Use of NLOM in cancer detection and hallmarks of cancer:** NLOM has been investigated for use in detection of cancers for revealing cellular and extracellular indicators of neoplasia that may be helpful in diagnostics (34, 49-52). Noninvasive imaging by NLOM has allowed for layer-by-layer assessment of mucosal microarchitecture (53-55) and been used to identify cellular atypia, metabolic dysregulation, (50, 52, 56, 57) extracellular abnormalities, and

basement membrane (BM) abnormalities in neoplastic oral tissues and cells by several groups. In recent times a major focus of cancer research has been to identify and target cancer hallmarks for diagnostic and therapeutic purposes that are progressively acquired by neoplastic cells (28). These hallmarks are integral to the multistep process of human tumor pathogenesis enabling the cancer cells to ultimately become tumorigenic and develop malignancy. The potential role that label-free NLOM may play in delineating the hallmarks of cancer, taking advantage of deep tissue imaging that enables assessment of full-depth multilayer micro-organization, has been of major interest in recent years. The fact that NLOM may reveal metrics associated with several of the six classic as well as the emerging new hallmarks of cancer, including 1) sustaining proliferative signaling, 2) evading growth suppressors, 3) deregulated cellular energetics, 4) activating invasion and metastasis, and 5) inducing angiogenesis, were investigated indicating potential for in vivo image based detection of cancer. Sustained proliferative signaling and evading growth suppressors were indicated by uncontrolled proliferation of neoplastic cells that led to abnormally high cell density, nuclear and cellular atypia etc. that has been observed in numerous in vivo and ex vivo studies using NLOM. Image based spectroscopy using two-photon excitation have showed alteration in important cellular metabolites (NADH and FAD) indicating deregulation of metabolic pathways (glycolysis, TCA cycle, oxidative phosphorylation, glutamine metabolism) and hence energetics by the metric of optical redox ratio. Combined use of MPAM and SHGM has also allowed for intravital imaging of the dynamic tumor microenvironment comprising of hyperproliferating cancer cells and surrounding extracellular matrix (ECM). In vivo assessment of focal expansion of tumor front, remodeling of basement membrane (BM) and degradation of ECM have been considered as morphometric indication of invasion and metastasis which is supported by biological correlates

such as expression of invasion promoting enzymes (Matrix metalloproteases, Lysyl oxidase etc.). Finally, NLOM has also shown promise in detecting blood vessels and capillaries associated with tumor induced angiogenesis. Owing to its deep-tissue imaging capabilities, NLOM have been employed in identification of new vessel growth, rate of blood flow, compromised vessel permeability that indicate significant alteration in tumor microenvironment and may provide significant information regarding characteristics of primary and metastatic tumors. Therefore, over the years NLOM has proved to be a powerful tool in cancer research by allowing for *in vivo* assessment of microstructural and biomolecular features of tumorigenesis by targeting specific cancer hallmarks identified in biochemical, molecular, and genetic studies.

**1.4.6 Limitations of NLOM:** Similar to all other microscopy techniques NLOM has a limited field-of-view typically in the order of few hundred micro meters. With advanced stitching algorithms larger scanning areas are achieved with NLOM however increase in acquisition time and time required to process large data sets are still limiting its use in a clinical setting. Even with development of fiber based NLOM devices imaging of large areas of oral cavity in the order of several centimeters is not feasible and a large area screening method would help in identifying areas of suspicion to limit number of sites for *in vivo* microscopy.

**1.4.7 Wide-field (WF) fluorescence imaging for quick large area screening:** WF fluorescence imaging techniques typically provide field-of-views in the order of several centimeters and are suitable for a quick assessment of large tissue surfaces. Two modes of WF fluorescence imaging have been tested so far based on the source of fluorescence. WF autofluorescence imaging is based on endogenous fluorescence from inherent fluorophores such as intracellular NADH and FAD, collagen in the extracellular matrix etc. Alternatively,

exogenous contrast based WF fluorescence imaging is generally targeted towards a specific process or a biomarker that is altered under neoplastic conditions. These imaging methods typically utilize a single event or a biomarker that may not be altered in all cases due to tumor heterogeneity and variations in patient population.

**1.4.8 WF autofluorescence (WF-AF) imaging:** WF-AF relies on endogenous fluorescence alterations from neoplastic tissue. Tissue autofluorescence has shown promise in improving visualization of neoplasia and may serve as an adjunct tool for pre-biopsy screening of oral mucosa. Visual identification of lesions is typically performed where neoplastic tissue appeared dark and surrounding normal tissue showed green autofluorescence induced by blue light excitation. Loss of autofluorescence in the visible wavelengths by neoplastic tissue is largely attributed to loss of collagen crosslinks. A commercial system VELscope was recently introduced based on this principle to enhance contrast between potentially neoplastic and non-neoplastic area in the oral cavity. Although a number of studies have suggested use of the VELscope improved detection of suspicious oral lesions with the occasional finding of false positives (58) it should be noted that this device is a screening tool and not for definitive diagnosis. Recent clinical reports indicate such visual aids (e.g. VELscope) improve sensitivity and identify dysplastic lesions missed by conventional oral examination (59, 60). However, because changes in fluorescence are based on endogenous sources altered in cancer as well as benign conditions, high false positive rates (lowered specificity) occur (60-62). When benign conditions (e.g. keratosis or inflammation) are included in the study population, specificity decreases to as low as 15-30% (59, 63-65).

**1.4.9 WF fluorescence imaging using a molecular contrast:** WF fluorescence imaging based on exogenous contrast have been employed in the past to identify areas of abnormal expression of biomarkers or deregulation of important biochemical pathways (66). Most of these contrast agents are investigational with antibodies for biomarkers being conjugated with fluorophores or nanoparticles. These methods involve injection of contrast agents that are not yet FDA approved and hence clinical translation is limited. In recent years considerable efforts have been committed to studies of cell metabolism and metabolic pathways associated with the onset and propagation of cancer (44) improving our current understating of cancer biology but also providing great potential for development of novel diagnostic targets for cancer imaging. One promising fluorescent contrast agent which has emerged is fluorescently is fluorescently labeled deoxyglucose used for monitoring metabolic activity of tumor in pre-clinical studies using *in vivo* and *ex vivo* tissues (67, 68). It should be noted that altered metabolic activity may occur in a variety of benign conditions or other disease states beyond cancer and though promising, use of such an agent will require careful study.

**1.4.10 Limitations of WF fluorescence imaging:** As outlined above, WF fluorescence imaging for identifying areas of potential neoplasia is highly attractive as these methods offer 1) a way in which to image large regions of tissue equivalent to that provided by visual inspection and with 2) an image-contrast that could 'highlight' areas of suspicion. These methods have typically been associated with reasonably high sensitivity compared to visual inspection (27). The greatest limitation that has been encountered by several WF fluorescence approaches has been a lack of specificity, however. In the case of autofluorescence, this limitation occurs because the inherent fluorophores that are detected with the method are not specific to

neoplasia and changes in their fluorescence intensity can occur with inflammation (69) as well as other diseases/benign conditions. These 'nonspecific' changes in autofluorescence occur not only due to similar trends in the fluorophores themselves but also architectural changes that may obscure their signals (e.g. keratosis/thickness changes decreases 'green' autofluorescence arising from the stroma in clinical WF systems in the same way proteolytic degradation of collagen may decrease the signal). Methods in which a molecular contrast agent is used to 'highlight' areas of suspicion could one day provide improvements to the WF fluorescence approach of epithelial neoplasia detection if the given biomarker is specific to neoplasia. Thus far, such methods are investigational and limited primarily to animal studies, with no known optical contrast agent available for use in WF imaging in humans. Further, one may reasonably expect that multiple markers or indicators of neoplasia will be needed for high sensitivity and specificity as many of the currently targeted contrast agents target molecules that can change not only in cancer but other epithelial diseases and even in inflammation. Further, levels of expression of many targeted biomarkers vary by stage and may complicate interpretation (70, 71).

***These disadvantages have limited the use of WF fluorescence imaging as a stand-alone technology.*** However, the high sensitivity provided by these techniques could still offer advantages, particularly if the approach could be combined with complementary approaches that could provide additional metrics associated with neoplasia and enhance the specificity for detection of neoplasia. One such approach that will be considered in the work of this thesis is combining WF imaging with NLOM.



## 1.5 Critical gaps in the field:

The following critical needs have been identified that I believe are needed to improve detection of oral neoplasia:

- 1) An in vivo noninvasive imaging method that can delineate non-neoplastic oral mucosa from neoplastic mucosa in order to better guide clinicians to potential neoplastic areas for improved selection of sites for biopsy. The identification of neoplasia should have high sensitivity and specificity for detection of oral precancers (OED) and cancers.
- 2) Inherent contrast is desired if possible, however the method must surpass the performance of WF-AF methods. Metrics based on those used in pathological assessment or known hallmarks of cancer are desired.
- 3) Reliable detection of benign conditions to reduce the number of unnecessary biopsies that are associated with high physical and psychological trauma.
- 4) Large area pre-screening methods complementing COE are desired which would help clinicians screen surface areas comparable to COE in size.
- 5) Detection methods that reveal features of neoplastic transformation early in the process are required to catch treatable (moderate, high grade, CIS) precancers early enough for effective treatments. Methods that can be applied in patients with a chance for recurrence (those with a history of primary OSCC) is critical due to the higher risk of developing a secondary tumor.

## **1.6 Proposed approach to address these gaps:**

As an attempt to address these gaps with biological and clinical relevance a multimodal, multiscale optical imaging approach was explored in this dissertation to assess performance of a combination of wide-field fluorescence imaging method for high sensitivity prescreening and high resolution subsurface microscopy with NLOM for high specificity detection of features of neoplasia. This research included comparison of oral epithelial dysplasia (OED), a precancerous condition, with inflammation and normal tissue in animal models of cancers and inflammation. Imaging modalities explored in this research also enable functional assessment of live tissue in their native environment opening avenues for simultaneous microstructural and functional assessment of neoplasia.

## **1.7 Thesis Outline**

In this dissertation I have attempted to address the critical gaps mentioned before in order to develop multimodal noninvasive imaging approaches by application of large area screening with WF fluorescence imaging and cellular morphologic/functional assessment with NLOM. The imaging modalities explored in this research has shown potential in identifying key processes leading to neoplasia and a running theme throughout this thesis is application of noninvasive imaging in detection of conventional hallmarks of cancer. The thesis is divided into three primary sections: 1) efforts that further develop microscopic capabilities for optimal

extraction of cytologic, architectural and molecular features in the earliest stages of oral neoplasia (Chapters 2-4); 2) efforts to explore large area detection of oral neoplasia in both inherent contrast and exogenous contrast based techniques (Chapters 5 and 6); and 3) attempts to bring together optimized approaches in high resolution microscopy with large area screening for potential approaches that could address critical gaps in detecting areas of neoplasia and biopsy guidance (Chapter 7).

**Chapter 2** will discuss a systematic evaluation of full depth oral mucosa and sub-mucosa from healthy, inflamed and dysplasia tissue delineated earliest indications of neoplastic transformation. Critical cytologic and extracellular features of neoplasia by noninvasive MPAM-SHGM are described in an animal model of oral epithelial precancer/cancer. These features will be further evaluated for multivariate assessment with wide-field fluorescence imaging modalities in order to develop a multimodal oral neoplasia detection method.

**Chapter 3** will cover a novel approach developed to detect early microstructural changes at the junction of the epithelium and lamina propria where neoplastic events are first seen during neoplastic transformation of oral epithelial mucosa. Beyond the cytologic features described in chapter 2 this chapter will provide insights into the microenvironment at the epithelial-connective tissue interface (ECTI). There is a continuing need to explore the full potential of ECTI architectural assessment to understand the dynamic interplay between epithelium and ECM. In this chapter I have explored a novel NLOM based technique to extract microstructural features from the dynamic remodeling of ECTI in two-dimensions for rapid evaluation and in three-dimensions for assessment of this changing interface in relation to the developing cytologic abnormalities.

**Chapter 4** describes spectral characteristics of *in vivo* autofluorescence in neoplastic epithelium making use of the fact that apart from the microstructural features of neoplasia NLOM can offer biochemical information of intact tissue based on multiphoton autofluorescence spectroscopy. Mitochondrial metabolites such as NADH, FAD and PpIX contribute to specific spectral features that were identified in normal and neoplastic epithelial cells. These features could potentially lead to metabolic functional assessment of neoplastic cells in the native environment and provide cues to detect altered energetics, a critical cancer hallmark.

**Chapter 5** will explore a WF autofluorescence imaging technique in delineating dysplasia and SCC from normal and inflamed tissue that will provide a platform for primary fluorescence based screening for suspicious areas in the oral mucosa. As discussed before there is a need for multiscale imaging with large surface area screening followed by microstructural assessment for detection of oral neoplasia in an inhomogeneous neoplastic microenvironment. Relative fluorescence emission in red and green channels were evaluated for sensitivity and specificity of detection of neoplastic from non-neoplastic oral mucosa in presence of benign lesions (inflammation) with the long term goal being potential combination with NLOM for multiscale imaging.

**Chapter 6** will discuss WF fluorescence imaging of neoplastic tissue with an external contrast agent. While WF autofluorescence is an attractive technique for multiscale imaging with NLOM, clinical application has been limited due to its low specificity in presence of benign lesions. However, exogenous contrast targeted to specific neoplastic events may provide higher specificity of large surface area screening. Therefore, an external contrast based WF

fluorescence imaging technique was explored in chapter 6 where higher metabolic rate in neoplasia was targeted with an optically active glucose analog, 2-NBDG. Topical application of the glucose analog was tested for preferential absorption by neoplastic epithelial cells as expected from Warburg effect. This is the first demonstration of *in vivo* topical application of 2-NBDG as a WF contrast agent for screening of oral mucosa with high sensitivity/specificity for neoplasia.

**Chapter 7** will discuss a multimodal imaging approach by combination of WF imaging and NLOM for noninvasive detection of oral neoplasia. Having investigated critical microstructural and biochemical features of neoplasia with NLOM and large surface area screening with WF fluorescence techniques, information gained from both modalities are brought together in chapter 7 to develop a multiscale imaging approach. The focus of this chapter was to investigate a new potential paradigm in detection of oral precancers and cancers that comprises the benefits of large area screening with WF imaging and microstructural/functional imaging with NLOM. The approaches explored for multimodal delineation of oral neoplasia, specifically at early stages were heavily dependent on optical indications of well-established cancer hallmarks.

**Chapter 8** discusses the overall outcomes of this thesis and potential future research opportunities based on the works presented here.

## Chapter 2

# Nonlinear Optical Microscopy for layer resolved qualitative and quantitative assessment of Neoplastic Oral Mucosa

### 2.1 Introduction:

In the past two decades methods of nonlinear optical microscopy (NLOM) such as multiphoton fluorescence microscopy (MPM) and second harmonic generation microscopy (SHGM) have found numerous biological applications in basic research spanning areas of neuroscience and developmental biology to cancer and others (72-74). It has also been investigated for potential clinical translation in the future. The method is particularly advantageous for *in vivo* microscopy owing to its deep imaging abilities compared to previously available optical microscopy methods, including confocal microscopy. Further, MPM provides detection of microstructural and biochemical alterations directly related to pathologic status of various tissues, with MPM

Results presented in this chapter were partially published in

1. **Remodeling of the epithelial-connective tissue interface (ECTI) in oral epithelial dysplasia as visualized by noninvasive 3D imaging.** Pal R, Shilagard T, Yang J, Villarreal P, Brown T, Qiu S, McCammon S, Resto V and Vargas G. **Cancer Res** June 14 2016 DOI: 10.1158/0008-5472.CAN-16-0252.
2. ***In-Vivo* Nonlinear Optical Microscopy (NLOM) of Epithelial-Connective Tissue Interface (ECTI) Reveals Quantitative Measures of Neoplasia in Hamster Oral Mucosa.** Pal R, Yang J, Ortiz D, Qiu S, Resto V, McCammon S, Vargas G. **PLoS One**. 2015, 10(1): e0116754. doi:10.1371/journal.pone.0116754.

allowing direct visualization of cellular structures with contrast due to a dye or endogenous autofluorescence (termed MPAM). SHGM provides contrast of fibrillar collagen in the lamina propria underlying the epithelium. Together, these two imaging modalities provide complimentary information about three-dimensional microstructure of native tissue.

NLOM has played a vital role in cancer research in the last ~15 years, aiding in the understanding of molecular, cellular and extracellular changes that occur following neoplastic transformation. Brown et al. (75) demonstrated possibilities of multiphoton microscopy beyond the typical depth of 150  $\mu\text{m}$  in imaging physiological functions. Using *in vivo* fluorescent labeling of biomarkers the authors were able to identify aberrations in gene expression, angiogenesis, and tumor cell migration as well as monitor delivery of therapeutic agents. Numerous studies that followed up on *in vivo* imaging of cancer and precancerous (neoplastic) tissues using NLOM provided the foundation for noninvasive intravital microscopy in early diagnostics and therapeutics investigations.

**2.1.1 Brief history of NLOM in oral cancer detection:** As previously described, the current gold standard for oral cancer diagnosis is biopsy of suspicious oral lesions and H&E staining followed by histopathological grading by an experienced pathologist. Currently there is no widely approved and standardized prescreening method to guide clinicians to potential malignant oral lesions or lesions with high risk of malignant transformation. In the past several years NLOM has been investigated as a potential method to image malignant or premalignant (neoplastic) oral lesions made possible by deep tissue high resolution *in vivo* imaging enabling assessment of layer-resolved ( $\sim 1.7 \mu\text{m}$  axial resolution) tissue microarchitecture at subcellular level. The first investigations of NLOM for noninvasive imaging of oral neoplasia were in

hamster studies conducted by Wilder-Smith et al. (33, 76) focusing primarily on stromal components, which showed high correlation ( $\kappa = 0.867$ ) between grading based on NLOM and histopathology. Visual grading was applied based on visually identified features such as breakdown of the regular ECM framework, decreased collagen fiber length, protrusion of capillaries into the epithelial layer, and inflammatory infiltrates. Sun et al. demonstrated that MPAM/SHG when used together could be used to reconstruct the mucosal/submucosal layered structure and that cell nuclei size and epithelial thicknesses measured *in vivo* were in agreement with those measured in histology, validating the use of MPAM for measuring cell features in oral mucosa (55). Skala et al. (54) conducted MPAM imaging of ex vivo biopsies from a hamster model for oral cancer and focused on epithelial features including the thickness of the keratinizing layer and the epithelium as well as cellular metrics. Thickness was reported to increase with increasing grade of neoplasia and consistent with what is seen in histopathology cellular atypia was found. This study also showed loss of the gradient of nuclear area and density with depth in neoplasia indicating a more homogeneous population of undifferentiated cells throughout the depth of the epithelium. Observation of perinuclear autofluorescence in neoplasia hinted at reorganization and reprogramming of mitochondrial networks.

The potential of using SHGM for noninvasive imaging of the extracellular collagen networks in a healthy mucosa was shown by Zhuo et al. in 2007 using a mouse model (77). Images showed normal collagen networks and minor salivary glands in the extracellular matrix (ECM). Vargas et al. combined the methods of MPAM and SHGM for multilayer assessment of oral neoplasia *in vivo* using the hamster model for oral cancer and quantitative measurement of SHG in development of OED (78). In longitudinal studies conducted in the hamster buccal pouch,



reduced collagen density (SHG volume) was found during the process of neoplastic development (78). Finally, quantitative SHG imaging has been conducted using texture analysis with a single parameter, encompassing collagen fiber length, density, thickness (79) and shown to be altered in precancerous tissue compared to normal in animal models.

Beyond the above studies focusing on microarchitectural features, investigations of the use of NLOM have also include the extraction of biochemical signatures based on redox potential through imaging and NLOM spectroscopy. Skala et al demonstrated *in vivo* redox measurement (80) in the hamster model and used fluorescence lifetime MPAM to specifically detect metabolic states of neoplastic and non-neoplastic oral epithelium. Edward et al., conducted multiphoton spectroscopy to interrogate the epithelium in neoplasia also extracting optical redox values that differed between superficial and basal epithelial cells and between normal, moderate and severe dysplasia (53). Assessment of cellular redox ratio with nonlinear microscopy and spectroscopy is an emerging field that provides information about metabolic status of live tissue.

### **2.1.2 Goal of the current study:**

While a number of previous investigations have been conducted to evaluate MPAM or SHGM for identification of image based markers of neoplasia few have combined the two imaging methods to evaluate both epithelial and submucosal changes simultaneously in neoplasia. The few that have combined the imaging methods, did not expressly apply quantitative metrics to determine cellular and ECM parameters for determination of sensitivity

and specificity. The purpose of this study was to investigate the potential of MPAM and SHGM to delineate neoplasia from normal and benign lesions in oral mucosa.

In the studies outlined in this chapter, neoplastic features from epithelium and ECM were assessed and image based metrics determined for those layers to characterize the neoplastic microenvironment in a layer by layer manner. Following are the specific efforts in this study:

1. As an early assessment of NLOM agreement with histopathology, visual grading was applied. Inter-rater agreement between NLOM based visual image grading and the gold standard of histology was determined. An oral cancer grading criteria describe by the World Health Organization (WHO) was followed to grade in vivo NLOM images and H&E stained histological sections of oral epithelial tissue into control and neoplastic (dysplasia and SCC) groups.
2. Cytologic features as representative features identified visually by pathology were quantitatively evaluated. These included basal nuclear density, nuclear area and coefficient of variation in nuclear area (CoVa). In the *lamina propria* collagen density was measured using SHGM to identify degree of ECM remodeling in OED. Sensitivity and specificity of these features were measured using receiver operator characteristic (ROC) curve with results allowing for comparison between parameters.
3. Finally, multiparameter assessments combining metrics from both the epithelium and stroma were conducted to demonstrate utility of simultaneous characterization of multiple parameters.

## 2.2 Materials/Methods:

**2.2.1 Animal Model:** Animal studies were approved by the Institutional Animal Care and Use Committee at the University of Texas Medical Branch and conformed to the Guide for the Care and Use of Laboratory Animals. Four weeks old male Golden Syrian Hamsters (Harlan Laboratories) were purchased for the studies. OED was induced by topical treatment of 0.5% 9,10-dimethyl-1,2-benzanthracene (DMBA) in mineral oil on the left cheek pouch of hamsters three times a week for 8-12 weeks (81). Control animals were treated with mineral oil following the same time course. This model has been used in numerous preclinical studies and has shown histological and molecular similarities to human OED and OSCC (81, 82). In an additional group, Sodium Lauryl Sulfate (SLS) induced inflammation model was used in which hamsters were topically treated for four consecutive days with a solution of 1.4% SLS, 29% calcium pyrophosphate and 18% glycerol in sterilized water (83, 84) and used for imaging studies on the 5th day. Sixteen DMBA-treated, five SLS-treated and thirteen control animals were used providing 24 OED, 17 inflamed and 41 control sites for study. All stages of dysplasia (mild, moderate and severe) were combined into one OED group. Immediately before imaging, animals were anesthetized with intraperitoneal injection of 100-mg/kg ketamine and 2.5-mg/kg xylazine. The buccal cheek pouch was gently pulled out of the oral cavity and stretched, onto a flat sample holder using pins then rinsed with PBS prior to imaging. Following imaging by MPAM-SHGM, imaged sites were biopsied and fixed in 10% neutral-buffered formalin then processed for histopathology by H&E staining. H&E stained sections were graded by an experienced pathologist into normal, inflammation, mild dysplasia, moderate dysplasia, severe dysplasia or carcinoma in situ (CIS) or OSCC.

The DMBA model of oral carcinogenesis is a well-characterized model that shows histological similarities to human OED and OSCC, following a similar multistep progression from normal to increasing grades of dysplasia and carcinoma-in-situ to cancer (81, 82, 85-89). The well documented histological and molecular similarities between this model and human oral precancer/cancer make this a useful model to study morphometric features associated with neoplasia. Additionally, studies have examined the multistep process involving genetic events such as deregulation of oncogenes and tumor suppressor genes in this model (82) and shown parallels in molecular marker alterations (e.g. p53, c-myc, p16, Bcl-2 etc.) to human OED and OSCC (88, 89). The hamster buccal mucosa model shows microstructural similarities to the human buccal mucosa, floor of the mouth and the ventral surface of the tongue (90) which are common sites for neoplastic transformation in humans. It is noted that different areas in the human oral cavity has different microstructure. In human oral cavity, the hard palate, gingiva and the dorsal surface of the tongue are keratinized stratified squamous epithelium while the buccal mucosa, lips, floor of mouth and soft palate are non-keratinized stratified squamous epithelium. Hamster buccal mucosa lacks lymphatics and salivary glands which are integral part of microstructure of human oral cavity including a common site for cancer, floor of mouth, but possess the multilayered structure and vasculature present in human tissue. The layered structure of human oral mucosa varies in epithelial thickness, structure of basement membrane, and presence of rete-processes depending on the anatomical site. Care should be taken to consider these microstructural variations in different anatomical locations as methods explored in this research are considered for their potential for clinical translation.

**2.2.2 MPAM-SHGM System:** The custom-built NLOM system used for MPAM-SHGM is shown in Fig. 2.1. The imaging system utilized a Nd:YVO<sub>4</sub> laser to pump a Ti:Sapphire femtosecond (~100fs, 82MHz) pulsed laser source (Tsunami, Spectra Physics), tunable within the wavelength range of 750-1000 nm. For MPAM, samples were excited with 780 nm wavelength and AF signals were collected through a 450-650 nm broadband emission filter, while 840 nm laser light was used to induce second harmonic generation and signal was collected through a 420/20 nm bandpass filter. An average excitation power of 28 mW was used at the sample with intensity control provided by a variable attenuator using a half wave plate and Glan-Thompson polarizer (Thorlabs, Newton). A long working distance 10X, 0.3 NA air objective (Plan-Neofluar) was used for localization of region of interest and a 40x, 1.2 NA, C-Apochromat, water immersion objective was used for microscopy. This objective provides a field of view of 320X320  $\mu\text{m}$  in X-Y plane and an imaging depth of about 180  $\mu\text{m}$  can be achieved with the current system. Three-dimensional microscopy was performed by obtaining z-stacks using 1  $\mu\text{m}$  z-steps and 8-bit images with 512x512 pixels and 0.625 $\mu\text{m}$  pixel size.

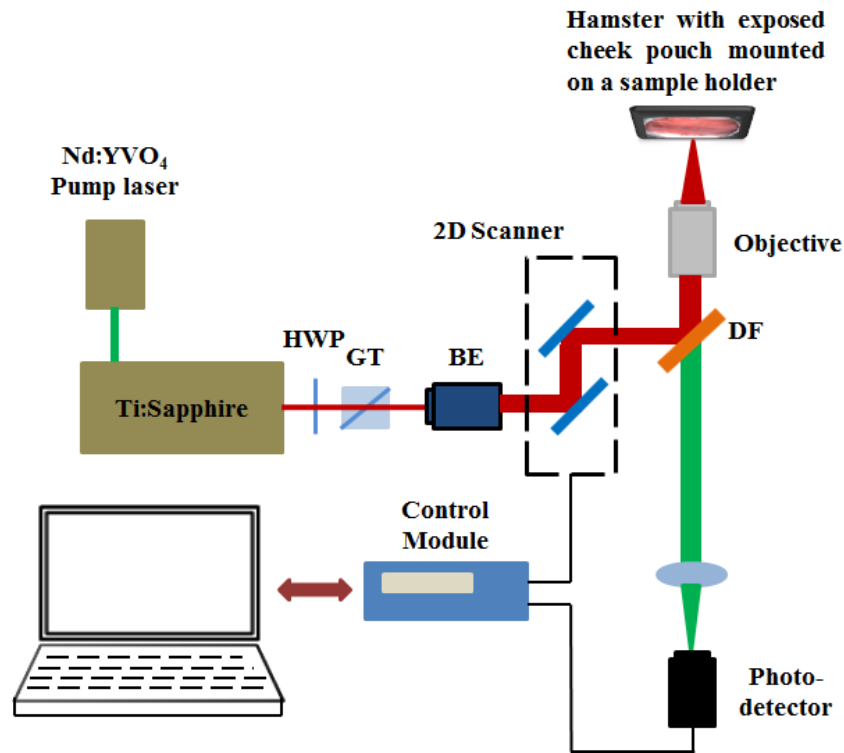


Figure 2.1. Schematic describing the experimental setup for in-vivo multiphoton autofluorescence microscopy (MPAM) and second harmonic generation microscopy (SHGM). HWP: half wave plate; GT: Glans Thompson prism; BE: beam expander; DF: dichroic filter. The hamster is placed on the stage of the inverted microscope with the buccal pouch exposed and facing the objective (90).

**2.2.3 Visual grading of NLOM image stacks and validation:** MPAM and SHGM z-stacks of each imaged site were subjected to visual assessment and graded as normal or neoplasia (dysplasia and squamous cell carcinoma). Image based grading was performed without prior knowledge of histopathological grading of individual sites. Kappa statistical analysis was performed using an online tool (<http://vassarstats.net/kappa.html>) to calculate agreement between histopathology and NLOM based grading. Following are the World Health Organization (WHO) established criteria for epithelial dysplasia that was followed to group samples into two categories (normal/benign and neoplastic):

**Criteria for architectural changes:** 1) irregular epithelial stratification, 2) loss of polarity of basal cells, 3) drop-shaped rete ridges, 4) increased number of mitotic figures, 5) premature keratinization in single cells (dyskeratosis), 6) keratin pearls within rete ridges.

**Criteria for cytologic changes:** 1) abnormal variation in nuclear size (anisonucleosis), 2) abnormal variation in nuclear shape (nuclear pleomorphism), 3) abnormal variation in cell size (anisocytosis), 4) abnormal variation in cell shape (cellular pleomorphism), 5) increased nuclear–cytoplasmic ratio, 6) increased nuclear size, 7) atypical mitotic figures.

## **2.2.4 Image processing and data analysis:**

**2.2.4.1 Thickness of epithelium:** Full thickness of epithelium was measured from cross sectional MPAM-SHGM images and H&E stained sections in ImageJ by measuring length of five vertical lines that were equally spaced and spanned across the epithelium from the end of the keratinizing layer to the top of the lamina propria. Folds and curvatures in the tissue were taken into account during measurements. The average of five thickness measurements was considered as the epithelial thickness.

**2.2.4.2 MPAM-based Cytology:** MPAM-SHGM stacks were evaluated by quantitative measures that could represent cellular crowding, nuclear enlargement, and nuclear pleomorphism, all features present in OED and OSCC and which are graded by pathologists in diagnostics. Quantitative measurements were made for nuclear density and nuclear area at the basal epithelium, and the coefficient of variance of nuclear area calculated as a potential measure of anisonucleosis/nuclear pleomorphism. For quantification of these cytologic features three image planes 5-10  $\mu\text{m}$  apart and showing prominent basal epithelial cells in each image

stack were identified. Three regions of interest (ROIs) were created in each selected plane and nuclear density was found by counting cells within the ROIs to determine number of cells per area. Finally, basal nuclear density of the entire image stack was represented as an average nuclear density of all 9 ROIs. Nuclear area was measured in a similar way from the same 9 ROIs across three image planes by manually delineating the borders of nuclei and calculating the length of major and minor axes. The shape of nuclei of these epithelial cells were treated as ellipsoidal and the area of each nuclei (~20 nuclei from each image plane and ~60 nuclei from each image stack) were determining by using the general formula for area of an ellipse. CoVa is represented as ratio of standard deviation over mean of nuclear area.

**2.2.4.3 Collagen Density:** Collagen density in the lamina propria (LP) was measured using a previously described method (91). SHGM z-stacks were thresholded in ImageJ using Otsu's algorithm. The image plane with maximum positive signal (I) and two image planes 3 $\mu$ m above (I+3) and below (I-3) from each stack were selected for calculation. 246 images from control, inflammation and OED were analyzed. To restrict measurements to collagen and account for dark vessels in the field, binary masks were created for each image and subtracted from thresholded images. For comparison between groups, SHG density in the three planes across the full field of view was calculated for each sample (three image planes per sample) and an average determined per group. For evaluating spatial variation of collagen density, SHG signal density was calculated from regions of interests (ROIs) beneath compromised ECTI in the LP and neighboring LP in the OED group. 40 ROIs from compromised LP and 35 ROIs from neighboring LP were assessed from 24 OEDs.



**2.2.4.4 Statistical analysis:** Statistical comparison between groups were performed by single factor ANOVA followed by the Tukey's *post hoc* test with  $P < 0.05$  considered significant (P value of  $< 0.05$  is represented by a single asterisk '\*' and  $P < 0.01$  by double asterisk '\*\*'). Receiver operator characteristic (ROC) curves were generated using SAS software (SAS Institute Inc.) to calculate area under the curve (AUC), sensitivity and specificity.

## 2.3 Results:

### 2.3.1 *In vivo* NLOM for layer-resolved three-dimensional imaging in hamster buccal

**mucosa:** Figure 2.2 describes an overview of the MPAM-SHGM imaging taking advantage of inherent contrast in the oral mucosa. Three-dimensional volume reconstructions of normal (Fig. 2.2a) and severe dysplasia (Fig. 2.2b) indicates increased epithelial thickness and uneven expansion of the epithelium in dysplasia. Along with the epithelium, the topmost layer of keratin also showed increased thickness in dysplasia. The very thin keratinizing and epithelial layers as well as the flat nature of the ECM, which is seen in a normal mucosa was lost in dysplasia. Single optical sections of normal keratin (Fig. 2.2c), epithelium (Fig. 2.2d) and ECM (Fig. 2.2e) layers are shown in comparison to keratin (Fig. 2.2f), epithelium (Fig. 2.2g), and ECM (Fig. 2.2h) layers from severe dysplasia. Loss of typical honeycomb structure of keratinocytes (Fig. 2.2f; “arrow”), enlarged epithelial nuclei (Fig. 2.2g; “arrows”), and degradation of collagen fibers in the ECM (Fig. 2.2h; “arrows”) that may indicate sites of potential invasion are seen in individual optical sections. Fig. 2.2i shows a cross-sectional view a dysplasia site with corresponding histopathology shown in Fig. 2.2j. The white dotted line in Fig. 2.2i represents epithelial-connective tissue interface (ECTI) which is an important site for tumor invasion which is discussed in more detail in Chapter 3. However, the important point to note here is the striking similarity between *in vivo* NLOM and histopathology. Architectural similarities were seen in all three layers such as thickness of keratinizing and epithelial layers, focal expansion of epithelium, pushing boundary of the ECTI etc.

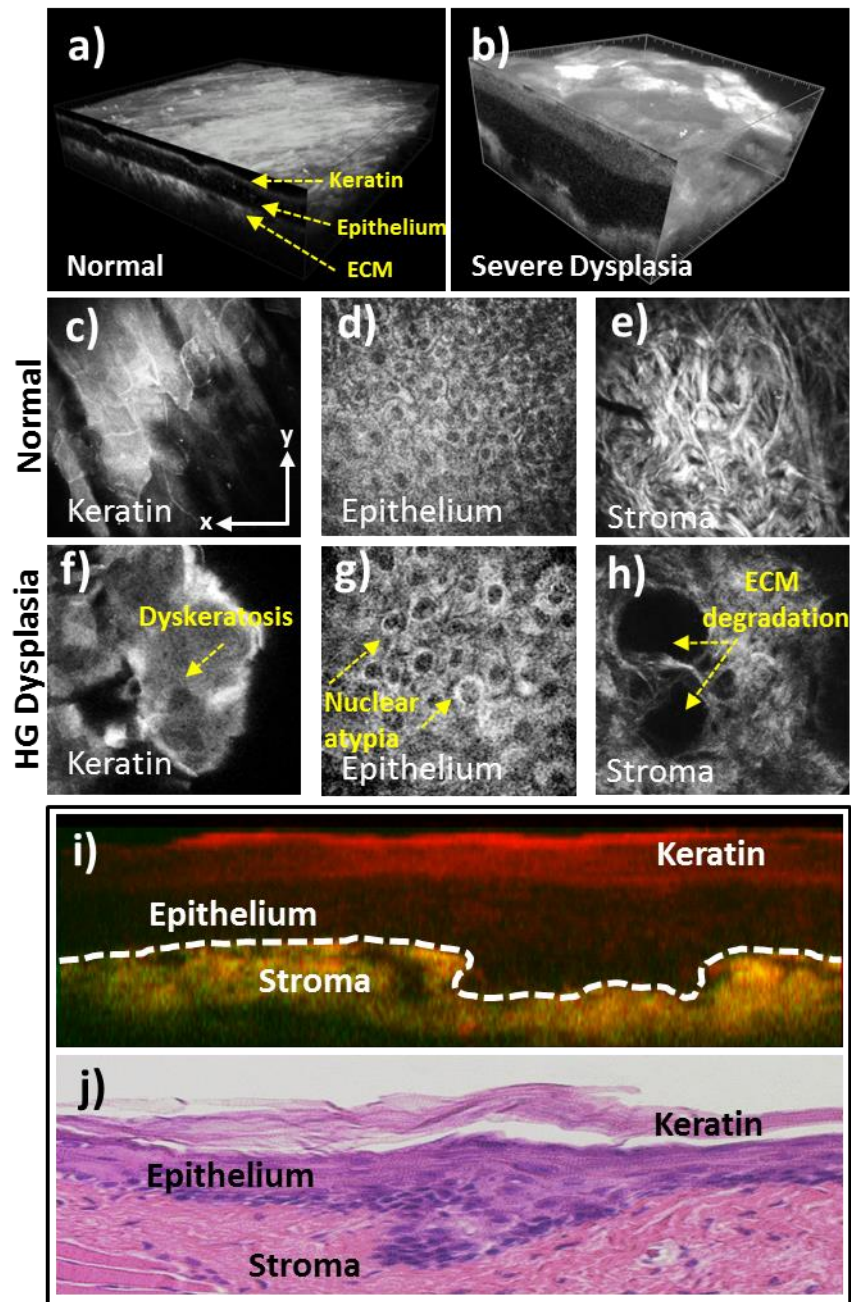


Figure 2.2. In vivo NLOM of hamster buccal mucosa. Volume reconstructions of a normal (a) and a severe dysplasia (b) showing all three tissue layers (keratin, epithelium and stroma); single optical sections of a normal keratinizing layer (c), epithelial cells (d), and stroma (e) are compared with keratin (f), epithelial cells (g) and stroma (h) of a severe

dysplasia. Images shows neoplastic features such as dyskeratosis, enlarged nuclei and ECM degradation in severe dysplasia; *In vivo* cross-section of the same severe dysplasia site is shown (i) with corresponding H&E (j).

**2.3.2 Comparison of cytologic and extracellular atypia observed in NLOM and conventional histopathology:** In a preliminary study including a subset of control (n = 12) and OED (n = 17) samples the level of agreement between NLOM based image grading and histopathologic grading was tested to validate the use of NLOM in detection of commonly used histopathological features of neoplasia in oral epithelial tissue. A comprehensive list of features is described in the methods section that are approved by WHO and were observed in the data set spanning each of the three mucosal layer. Some of the histopathologically important features of cytology (increased basal nuclear density and area, abnormal variation in nuclear shape and size), architecture (epithelial thickness) and *lamina propria* (collagen density) were quantified and are described later in the chapter. Other features were utilized for visual grading only. NLOM based grading of individual sites were performed similar to histopathological grading and samples were graded as normal or neoplasia. Keratin stratification and thickening of keratinizing layer are associated with neoplasia as well as benign conditions and may not be considered a critical indication of neoplasia however these features are almost always present when neoplasia is present in the epithelium.

Table 2.1 shows the number of correlated and non-correlated samples for two grading methods. Cohen's kappa coefficient is a statistical measure of inter-rater agreement for qualitative (categorical) items. Kappa analysis showed high agreement (K = 0.715) of NLOM based grading with gold standard histopathological grading of neoplasia. Results of the

preliminary kappa statistics established the reliability and utility of the imaging method and image assessment criteria for following studies.

Table 2.1: Sample classification based on NLOM and histopathological grading

N = 29 (12 Control; 17 neoplasia)		Pathology	
		Yes	No
MPAM-SHGM	Yes	15	2
	No	2	10

Increased thickness of the epithelium observed in dysplasia (Fig. 2.2 b, i and j) was measured from both NLOM images and histopathology. Variations in epithelial thickness between control oral mucosa and different grades of dysplasia is shown in Fig. 2.3. Epithelial thickness in SCC was not measured since current NLOM imaging capability did not allow for full depth epithelium imaging due to highly keratinized surfaces and severely thickened epithelium. Thickness measures from NLOM (Fig. 2.3a) and histopathologic sections (Fig. 2.3b) showed similar trends. Median epithelial thickness increased gradually from normal to mild, moderate and severe dysplasia with high standard deviations in moderate and severe dysplasia. Large standard deviation in higher grades of dysplasia is consistent with our observation that epithelial thickness is usually non-uniform at these stages due to focal expansion of epithelium. Differences in epithelial thickness between normal and all three OED groups was statistically significant in both NLOM and histopathologic assessments.

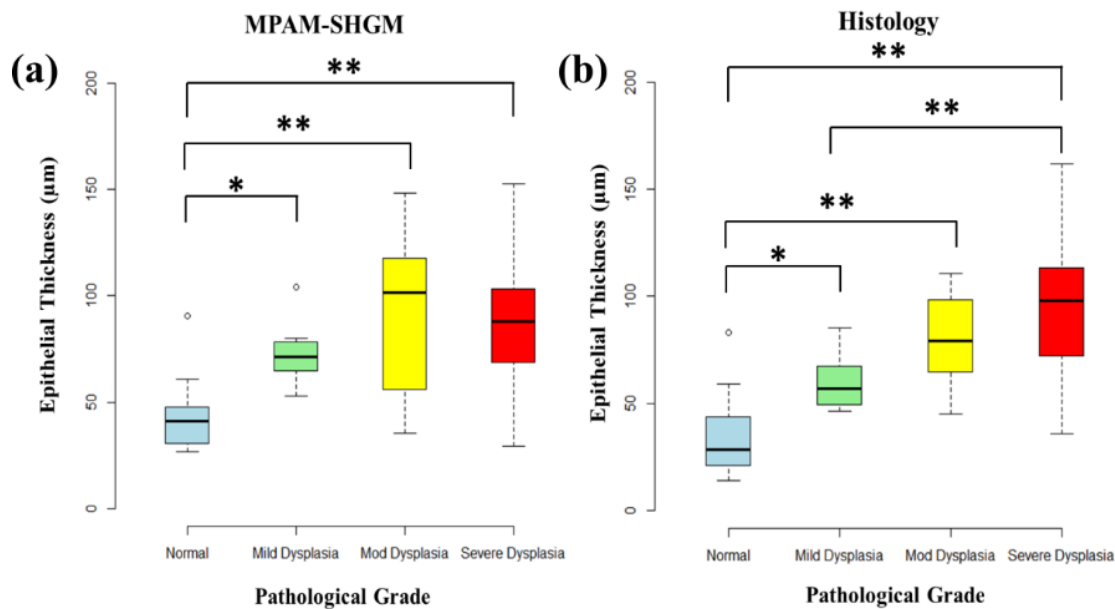


Figure 2.3. Epithelial Thickness measurements from MPAM-SHGM (a) and histology (b) show statistically significant increase in thickness of mild, moderate and severe dysplasia from normal mucosa. Box plot analyses show the median, 25th and 75th percentiles, and outliers for both MPAM-SHGM and histology. “\*” and “\*\*” represent statistical difference between groups at  $p < 0.05$  and  $0.01$  significance respectively. (Pal et al. 2015)

### 2.3.3 Cytologic abnormalities observed by qualitative and quantitative assessment of

**MPAM micrographs in dysplasia:** Figure 2.4 shows single MPAM image planes of superficial epithelium from a normal/control (Fig. 2.4a) hamster mucosa compared against two representative high-grade/severe OED (Fig. 2.4b and 2.4c) at similar depths of 20-25 µm. Normal epithelial cells show a regular mosaic with cells having dark nuclei (diameter: 8-10 µm) and highly autofluorescent cytoplasm (Fig. 2.4a). In OED, overcrowding of immature cells and atypical keratin production known as keratin pearls (Fig. 2.4b, denoted by “\*”) are recognized as features of premalignant changes. Abnormally large nuclei (diameter: 16-18 µm) representing anisonucleosis can be seen in Fig. 2.4c (white arrows). Areas enclosed with white squares shows

comparison of nuclear density between normal and dysplasia. Nuclear density in dysplasia (0.25 nuclei/100  $\mu\text{m}^2$ ) was higher than normal (0.12 nuclei/100  $\mu\text{m}^2$ ) epithelium indicating uncontrolled proliferation and overcrowding of epithelial cells.

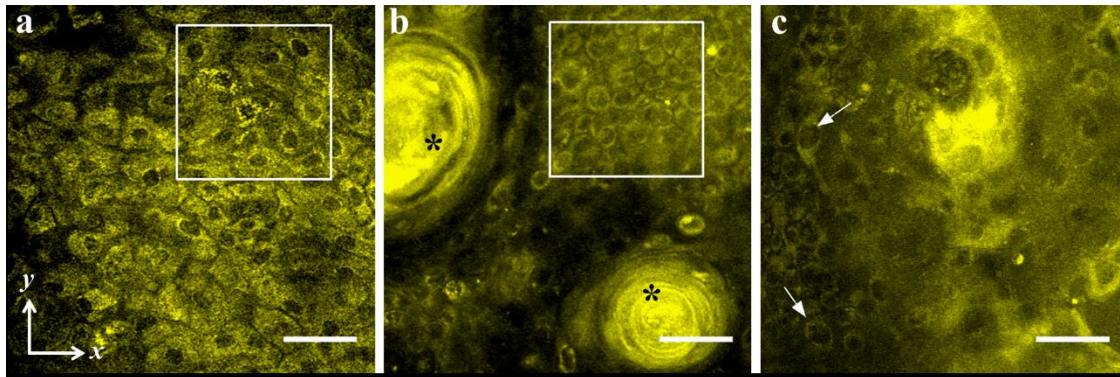


Figure 2.4: x-y micrographs from *in-vivo* MPAM are shown from normal (a), and dysplastic (b,c) epithelium of hamster oral mucosa. White boxes in “a” and “b” shows comparison of nuclear density between a normal and OED. “\*” shows presence of keratin pearls (b) and arrows point towards enlarged nuclei (c) in dysplastic epithelium.

Representative examples of atypical cytology identified in MPAM images are shown in Figure 2.5(a-g). Cytologic abnormalities include presence of mitotic nuclei in superficial epithelium (Fig. 2.5a), nuclear-cellular pleomorphism and anisonucleosis (atypical shape and size of cells and nuclei; Fig. 2.5b-d, white arrows). An interesting feature observed was epithelial cells having single or multiple cytoplasmic finger-like processes (Fig. 2.5b-c “outline”). Clusters of neoplastic cells are also visible in Fig. 2.5d showing loss of normal cell polarity and variation in cell shape and size that are regarded as indicators of OEDs (40).

Linear arrangements of epithelial cells forming Indian file-like patterns (Fig. 2.5f “arrow”) were identified similar to those reported in salivary gland neoplasms (41). Epithelial cells in Fig. 2.5g (arrows) showed perinuclear clustering of fluorescence. Cells with varying degrees of



cytoplasmic fluorescence intensities, could potentially indicate deregulated metabolic rates since the source of fluorescence is cytosolic NADH and FAD and a characteristic previously reported in OED (10).

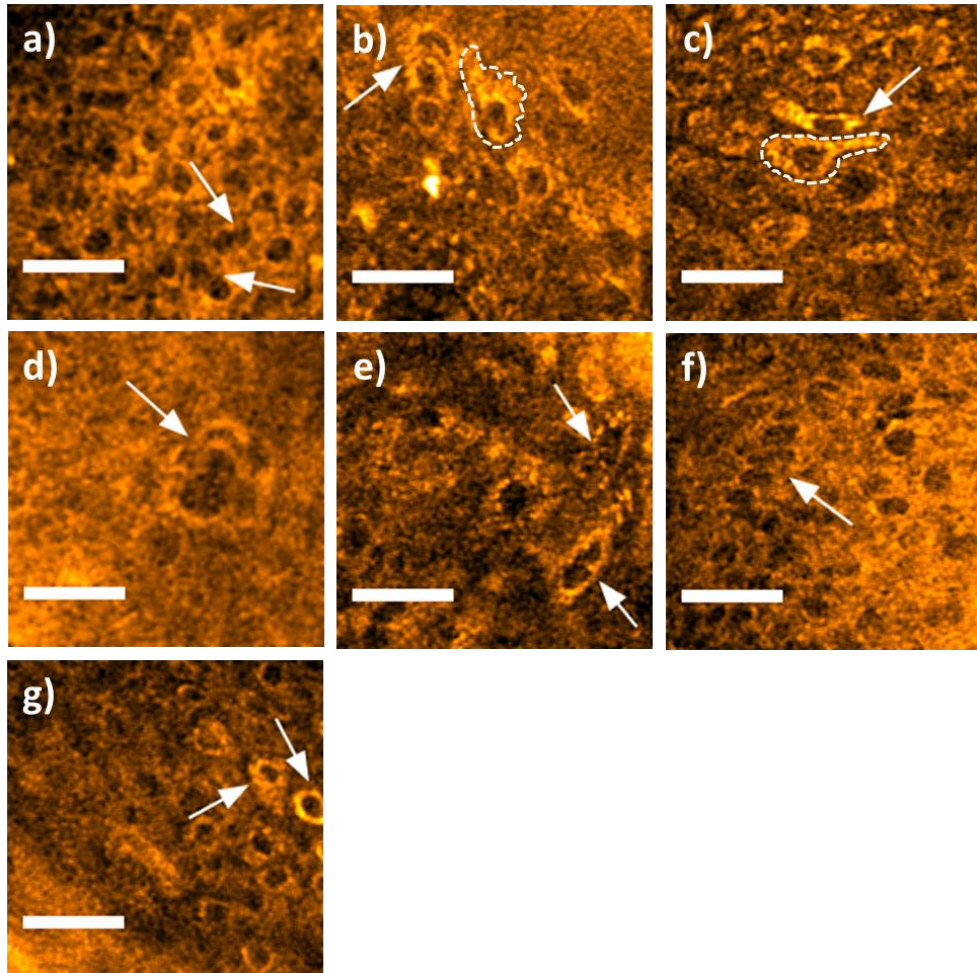


Figure 2.5: a-g) x-y micrographs from MPAM showing cytoplogic atypia in OED. Multiple cytologic features such as increased mitotic figures (a), nuclear and cytoplasmic pleomorphisms (b-c), increase nuclear area (e), irregular polarity (f) and atypical accumulation of autofluorescence around nuclei (g) were observed. Arrows and dotted outlines point towards specific features identified in in-vivo MPAM. Scale bar, 40 $\mu$ m.



Cytologic parameters of nuclear density, nuclear area and coefficient of variation (CoVa) in nuclear area near the ECTI were increased in OED when compared with control (Fig. 2.6a-c). Inflamed tissue was not significantly different from normal by any of three measures. Inflammation was statistically different from OED by nuclear area and CoVa, but not in nuclear density. ROC of basal nuclear density resulted in the lowest AUC (0.78), sensitivity and specificity, with inflammation reducing sensitivity by ~10% (Fig. 2.6d; Table 2.2). Basal nuclear area showed reasonable accuracy (Fig. 2.6e) in differentiating OED from control with an AUC of 0.82 (Table 2.2) irrespective of presence or absence of inflammation. Of the three parameters, CoVa (Fig. 2.6f) had the highest accuracy (AUC=0.99; Table 2.2) irrespective of the presence of inflammation as a potential confounding factor.

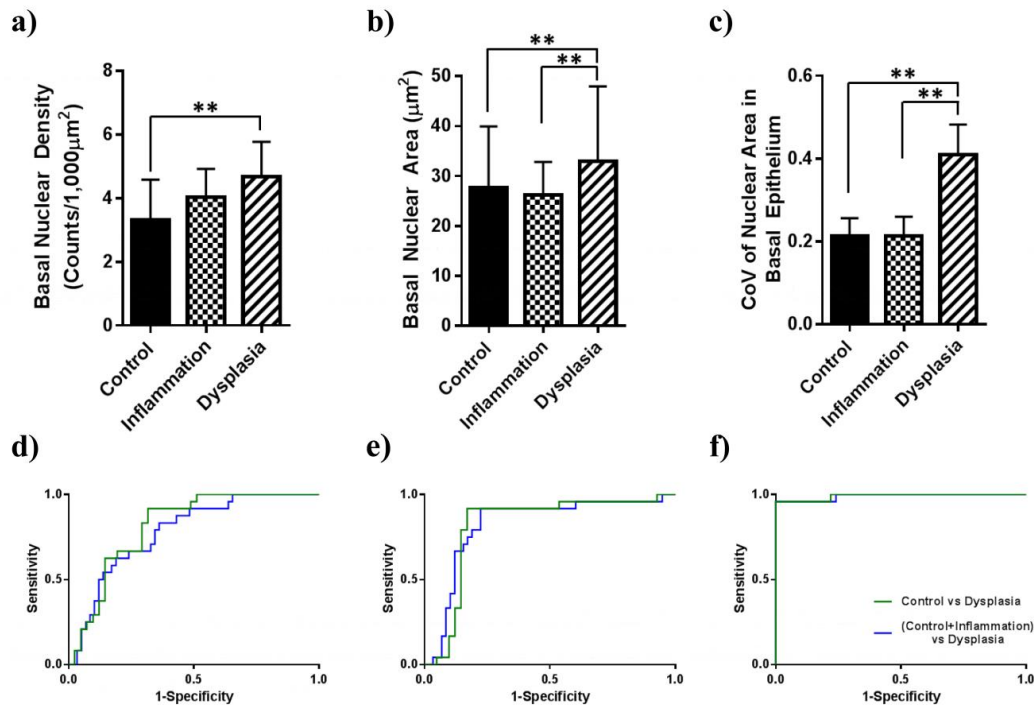


Figure 2.6: Cytologic features of neoplasia measured from MPAM images. Average basal nuclear density (a), basal nuclear area (b) and coefficient of variation (CoVa) of basal nuclear area (c) in control, inflammation and OED are

shown. ROC curves for these parameters are shown in d, e and f respectively. Blue and green ROC curves are for data sets in presence and absence of inflammation as a confounding factor. “\*” and “\*\*” represent  $p < 0.05$  and  $p < 0.01$  respectively.

**2.3.4 Detection of extracellular collagen remodeling in dysplasia using SHGM:** Fig. 2.7a shows an SHGM image plane (single optical section) from control ECM having dense thick fibers of collagen. Fig. 2.7b shows a single SHGM image plane from OED with diffuse SHG signal indicating lack of well-defined collagen fibers. Additionally, SHGM revealed certain areas in the ECM with no appreciable SHG signal. These areas were primarily consisted of areas of matrix compliance and blood vessels. A representative blood vessel is outlined in Fig. 2.7b (dotted outline). After manual masking for blood vessels the remaining areas devoid of SHG indicated collagen degradation/remodeling in the ECM (Fig. 2.7b “\*”).

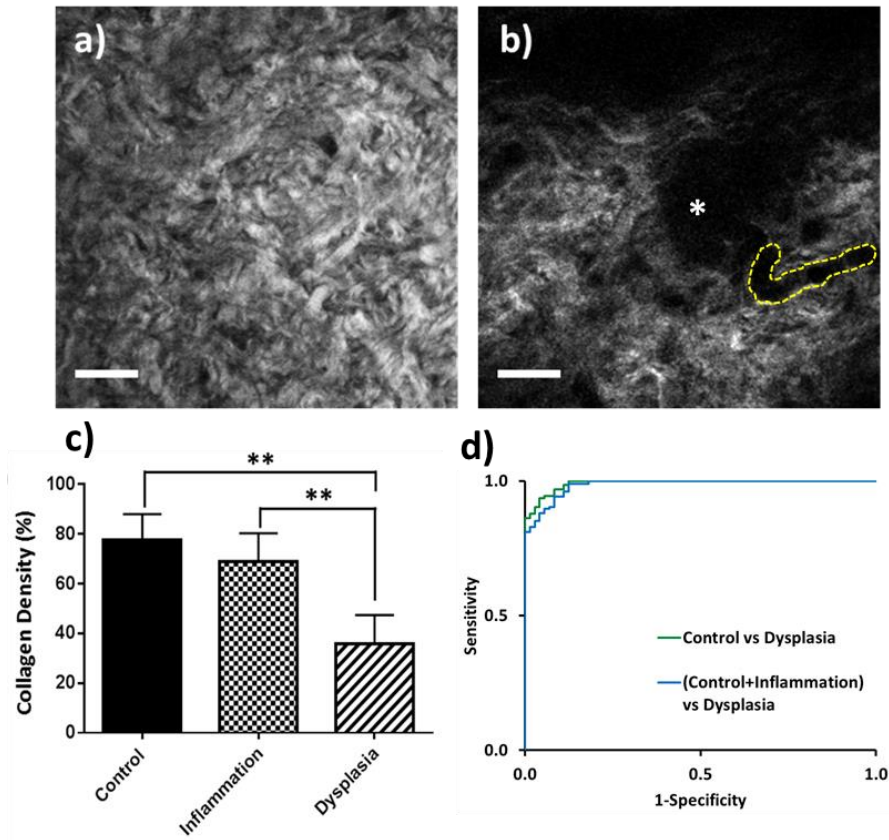


Figure 2.7: Reduction of collagen density in OED. x-y SHGM micrographs of normal (a) and OED (b) are shown in single planes. “\*” in (b) indicates area of degraded collagen. Overall reduction of SHG signal density in OED compared with control and inflammation is shown in c). “\*\*\*” represent  $p < 0.01$ .

Along with cytologic features observed in MPAM, the OED group showed reduced collagen density than control and inflammation primarily because of the presence of large gaps in the ECM. Assessment of total collagen density across three groups showed significantly lower values in OED vs. control and inflammation (Fig. 2.7c). Collagen density in the inflammation group showed lower average value from control group, however this difference was not statistically significant. ROC analysis showed very high (> 90%) sensitivity and specificity (Table 2.2) with or without inclusion of inflammation in the population. Sensitivity and specificity of

collagen density were found to be 94% and 92% respectively with an AUC of 0.98 (Table 2.2) in presence of inflammation.

Table 2.2: Summary of the ROC curve analysis of cytologic features and collagen density quantified from *in vivo* MPAM-SHGM.

Groups		Basal Nuclear Density	Basal Nuclear Area	CoV of Basal Nuclear Area	Collagen Density
Control vs Dysplasia (n=65)	AUC (95% CI)	0.81 (0.71-0.92)	0.82 (0.72-0.93)	0.99 (0.97-1.00)	0.99 (0.98-1.00)
	Sensitivity (%)	83.30%	79.2	95.80%	94.3%
	Specificity (%)	70.70%	85.4	97.60%	94.4%
(Control+Inflammation) vs Dysplasia (n=82)	AUC (95% CI)	0.78 (0.68-0.88)	0.82 (0.72-0.93)	0.99(0.97-1.00)	0.98 (0.97-1.00)
	Sensitivity (%)	70.80%	79.2	95.80%	94.3%
	Specificity (%)	67.20%	81	98.30%	91.7%

### 2.3.5 Combination of cytologic and extracellular features for multivariate analysis

**showing effects of inflammation:** Figure 2.8a and 2.8b shows scatter plots of basal nuclear CoVa and collagen density in absence and presence of inflammation respectively. A preliminary multivariate analysis with basal nuclear CoVa and collagen density showed complete separation of dysplasia from pathologically normal tissue in both cases. Presence of the benign condition had no effect on separation of neoplastic tissue from control when multiple features were used together unlike individual features shown in table 2.2. Fitting to a linear model (dotted line) the multivariate algorithm produced separate clusters for dysplasia and control while inflammation were grouped with control.

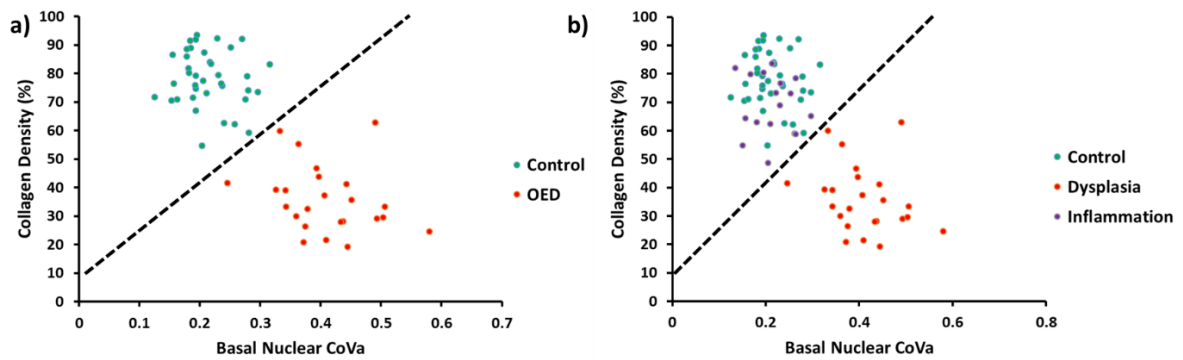


Figure 2.8: Multivariate linear models created by using basal nuclear CoVa and collagen density. a) Scatter plot for control and dysplasia; b) scatter plot for control, inflammation and dysplasia. The dotted straight line represents optimal separation of groups as calculated from the linear model.

## Discussion:

The work presented in this chapter provides a systematic study of neoplastic features seen in noninvasive MPAM-SHGM in a hamster model of oral epithelial precancer/cancer which encompass multiple layers of the tissue. Results show NLOM has the potential for high sensitivity and specificity detection of neoplasia. Several cytologic and extracellular features spanning the full depth of the epithelium were observed and quantified by *in vivo* imaging. Volumetric *in vivo* imaging enabled by NLOM showed high potential for assessment of conventional microstructural features of oral neoplasia with a focus on OED. To the best of my knowledge this is the first study based on *in vivo* NLOM oral epithelial precancers (OEDs) describing quantitative assessment of the epithelium as well as ECM from same sites of interests taking advantage of the endogenous contrast captured by MPAM and SHGM and the first to explore combinations of epithelial and stromal parameters for delineation of neoplasia.

Three-dimensional MPAM/SHGM imaging showed cytologic and architectural features of OED akin to that seen in histopathology (Fig. 2.2) in the hamster model. A visual NLOM feature based grading method for categorizing samples into two categories (normal and dysplasia) showed high correlation with histopathological grading. A comprehensive list of assessed features is shown in Table 2.1 and can be corroborated by previously published results where most of these features have been described in humans or animal models of epithelial cancers (primarily skin, cervical and oral mucosa) using NLOM (34, 92-96).

Epithelial thickness measurements were performed to compare NLOM and histopathological findings. Alteration in epithelial thickness was not envisioned to be a critical neoplastic feature since other benign conditions such as inflammation or hyperplasia shows increased epithelial thickness. Distribution of epithelial thickness measurements for moderate and severe dysplasia was larger than normal and mild dysplasia in both NLOM and histology due to heterogeneity (non-uniform thickness) that results at the lesion site. Highest agreement between NLOM and histology occurred for both normal and severe dysplasia. Differences in epithelial thickness between NLOM imaging and histology for mild and moderate dysplasia may be attributed to the larger sampling area required for biopsy compared to the imaging lateral field-of-view. Both methods (imaging and biopsy) were centered over the most central part of the lesion which generally comprised the most severe pathology relative to the periphery.

MPAM based on autofluorescence provides the ability to visualize cells throughout the full epithelium which then transitions into a fibrous network in the lamina propria as demonstrated in the current study and in previous studies (33, 54, 55, 77). A wide variety of cytologic abnormalities in dysplasia are described in Fig. 2.4 and 2.5. Increased nuclear density,

cellular overcrowding, abundance of mitotic nuclei, nuclear and cellular pleomorphisms are often seen in dysplasia that are not present in control or inflamed epithelium. These features together with increased epithelial thickness are hypothesized to indicate certain hallmarks of cancer. “Sustaining proliferative signaling”, “resisting cell death” and “evading growth suppressors” are the key cancer hallmarks that directly or indirectly induce uncontrolled growth of the epithelial cells which could be correlated to the observed NLOM based features. Although current evidences lack information on expression of molecular markers for these cancer hallmarks, one could hypothesize that abnormally high proliferation rate of the epithelial cells would involve faulty mitoses, heterogeneous population of cells and nuclei with unusual shapes and sizes. Therefore, the *in vivo* cytologic and extra cellular feature analysis method presented here with the help of NLOM is expected to be of major interest for microstructural assessment as well as novel indicators of key cancer hallmarks.

An interesting feature of autofluorescence is shown in Fig. 2.5g where the areas surrounding the nuclei showed higher fluorescence than the rest of the cytoplasm. This observation is consistent with a previous report by Skala et. al. (54). Cellular autofluorescence is primarily generated from NADH and FAD which are localized in mitochondria. Therefore, the perinuclear accumulation of autofluorescence could indicate alteration in mitochondrial distribution in dysplasia. Recent studies in 3D cultured tissue models and human melanoma examining NADH signatures attributed to mitochondria indicate that organizational changes in these signatures occur in epithelial cancers and may be a way to detect metabolic alterations (52, 97).

A unique aspect of this study compared to previous studies to evaluate neoplasia by NLOM is that it included a group having inflammation. Inflammation is known to pose complications in clinical diagnosis of OEDs and by optical methods (98) due to similarities in optical properties (99). ROC curves were calculated with exclusion and inclusion of the inflammation group within the control group. This showed its effect on performance of cytologic and extracellular parameters. Basal nuclear density and basal nuclear area showed reduced performance with inclusion of inflammation - markedly pronounced in the case of basal nuclear density in which sensitivity was by ~10% when inflammation was considered. Presence of epithelial cells at different stages of maturity within the same layer in OED is reflected in increased CoVa in dysplasia. Inflamed epithelium on the other hand has a uniform growth rate, which is indicated in a low CoVa – explaining the lack of effect of inflammation on performance of CoVa.

Delineation of OED from control and inflammation with collagen density as an image based feature also showed high sensitivity and specificity for discrimination between OED from control and inflammation. Inclusion of inflammation in the population reduced the specificity from 94.4% to 91.7% while there was no change in sensitivity, showing the high promise of this parameter. Reduction of collagen density identified in early neoplasia (OED) indicate loss of ECM contents and collagen networks in the ECM. Areas in ECM showing focal loss of collagen was consistently observed only in OEDs and are expected to alter the geometry of the basement membrane (BM) or the epithelial-connective tissue interface (ECTI), which is described in chapter 3. These areas of reduced collagen density are considered to be potential future sites for invasion which could be validated by further assessments of these areas over time.



Qualitative assessment of neoplasia as observed in histopathology is largely dependent on the experience and level of training of the grader (100). Subtle changes in tissue morphology especially in the early stages of neoplasia are often difficult to detect even for an experienced pathologist and even among experienced graders there is high variability. Therefore, methods that provide more objective and quantitative assessment of the microenvironment in neoplasia would be useful for improved detection efforts in particular because if clinical systems are developed that can assess these parameters noninvasively automated algorithms could be established for grading of neoplastic tissue. An attempt to show objective quantitative assessment was performed in this study with multivariate linear model is shown in Fig. 2.8 with the best performing NLOM features basal nuclear CoV and collagen density. These two features together from two separate tissue layers were able to separate all control and inflammation from dysplasia. The linear model emphasizes the high potential of multilayer *in vivo* NLOM for quantitative detection of early indications of neoplasia.

Fiber based NLOM systems are currently being generated and tested for deep tissue *in vivo* imaging with the goal of potential translation in to clinic (101, 102). These imaging systems have shown potential for imaging and detecting cytologic and architectural features *in vivo*. While no systems exist yet for the oral cavity, these efforts have opened new avenues for development of fiber based NLOM systems suitable for oral cavity imaging for noninvasive detection of neoplasia.

In summary, this chapter provided indication for *in vivo* depth resolved NLOM based studies on oral epithelial precancers and cancer. Image based features of neoplasia based on cellular and extracellular atypia were identified from sequential MPAM-SHGM of individual sites

that provided important microstructural information regarding the full epithelium and the lamina propria. This was a first study to assess multiple parameters from each of these layers and evaluate them both separately and together. These features could prove to be useful in future for assessment of neoplasia with multivariate statistics. The ability to detect and differentiate early changes in cytologic and extracellular atypia in a preclinical model provides a powerful way to study processes of early neoplasia and could be developed for imaging of other epithelial sites as well as in human epithelium. As nonlinear optical microscopy approach depths beyond 1 mm (103, 104) potential clinical application has started to look promising and with further development improved diagnostic information is expected.

## Chapter 3

# Three-dimensional visualization of epithelial-connective tissue interface (ECTI) in oral epithelial dysplasia using nonlinear optical microscopy

### 3.1 Introduction:

Application of NLOM in detecting features of oral neoplasia can be extended beyond the assessment of cytologic and extracellular abnormalities. As mentioned earlier MPAM and SHGM when used collectively provides a unique opportunity to model multilayered microstructure of tissues in a label-free manner. MPAM-SHGM from the same tissue volume enables rapid delineation of epithelium from the underlying LP since both layers show autofluorescence while the epithelium lacks SHG. The junction at which SHG signatures begin in depth due to transition

Results presented in this chapter were partially published in

1. **Remodeling of the epithelial-connective tissue interface (ECTI) in oral epithelial dysplasia as visualized by noninvasive 3D imaging.** Pal R, Shilagard T, Yang J, Villarreal P, Brown T, Qiu S, McCammon S, Resto V and Vargas G. **Cancer Res** June 14 2016 DOI: 10.1158/0008-5472.CAN-16-0252.
2. ***In-Vivo* Nonlinear Optical Microscopy (NLOM) of Epithelial-Connective Tissue Interface (ECTI) Reveals Quantitative Measures of Neoplasia in Hamster Oral Mucosa.** Pal R, Yang J, Ortiz D, Qiu S, Resto V, McCammon S, Vargas G. **PLoS One**. 2015, 10(1): e0116754. doi:10.1371/journal.pone.0116754.

into LP represents the epithelial-connective tissue interface (ECTI). Oral epithelial dysplasia (OED), often the precursor of OSCC, is typically differentiated from normal oral mucosa by cellular and extracellular atypia along with architectural alterations. A major architectural change observed in OED is focal expansion of epithelium due to uncontrolled epithelial growth and remodeling of the lamina propria (LP), resulting in transformation of the epithelial-connective tissue interface (ECTI) where the basement membrane (BM) is located.

ECTI plays an integral role in neoplasia, serving as the interface at which malignant cells cross the compromised BM during invasion (105). The ECTI maintains a distinct separation between epithelium and underlying ECM, lymphatics, and vasculature under normal physiologic conditions. During development of OED, the ECM and thus ECTI undergo significant remodeling that appears to support invasion. ECM remodeling in precancers due to compression stress (106) and secretion of matrix proteases (107, 108) by neoplastic foci in the epithelium alters the equilibrium between synthesis and degradation of ECM components. These together results in marked changes in BM/ECTI features including new 'rete-like' features (109) altering ECTI topography, which are useful in pathologic evaluation for diagnosis of neoplastic status (109, 110). These topographical changes result from contributors such as an expanding epithelium at focal sites of hyperproliferation (111), deregulation of ECM dynamics that alter matrix spatial organization (112), and possibly stiffness, inducing pockets of compliance (106).

ECTI has been studied under in vitro conditions, using traditional methods of histology (113, 114) and electron microscopy (115, 116). Two studies involving animal models for OSCC have examined the ECTI 2D shape in histological transverse sections using fractal analysis and showed that OEDs and pre-cancers have a significant increase in irregularities compared to

controls (105, 117). The authors are not aware of any 3D ECTI studies based on histology. Such a study would require extensive processing of many sequential transverse sections, photographed and reconstructed by sophisticated algorithms to provide a 3D view. This has been done in advanced tongue tumors to examine tumor-stroma interface. Study of ECTI as a surface rather than a line-shape in cross-sections has been accomplished by electron microscopy which allowed visualization of the 3D structure of ECTI, including abnormalities in density of connective tissue papillae in humans and animal models of OSCC. However, ECTI shape analysis was not performed. Electron microscopy requires removal of the epithelium and is unable to visualize beyond the ECTI into the LP. Thus, ECTI studies have primarily been under in vitro conditions that require extensive tissue processing, complete destruction of the epithelium, and they do not fully recapitulate the complex 3D organization of the oral mucosa.

Since the ECTI and the processes leading to alterations in ECTI morphology are integral to carcinogenesis, much regarding the process of neoplastic transformation could be learned from methods that allow direct and noninvasive study of this key interface. While difficult to appreciate in transverse histological examination, the ECTI is a surface which extends laterally across the tissue. Volumetric imaging of epithelium using MPAM-SHGM with specificity to visualize the ECTI itself presents an opportunity to investigate how it is altered in OED.

### **3.1.1 Goal of the current study:**

Assessment of ECTI could be useful in the enhanced understanding of early events of epithelial neoplasia. Structural evaluation of the ECTI during the early stages of neoplasia could lead to identification of patterns associated with pre-invasion. This may also provide important

image markers that could be used to develop additional *in vivo* metrics to identify neoplastic sites. Therefore, the overall goal of this study was to assess architectural changes with a focus on ECTI remodeling associated with development of neoplasms in oral epithelial tissue using NLOM as a noninvasive imaging tool. The following are the specific efforts outlined in this study:

- 1) Initial efforts focused on showing that changes in the ECTI occur with OED and could be determined from simple, quick to analyze two-dimensional images in x and z. Two-dimensional assessment of ECTI shape: An image based parameter  $\Delta$ Linearity was introduced as a measure of ECTI shape change.  $\Delta$ Linearity was measured in NLOM and validated with similar measures in histology.
- 2) For a more comprehensive evaluation of the ECTI shape changes that occur in a tissue volume three-dimensional assessment of ECTI shape was performed. An image based parameter ECTI contour was introduced as a measure of remodeling of ECTI surface.
- 3) Spatial relationships of neoplasia-related cytologic abnormalities in neighboring epithelium with ECTI remodeling were assessed and indicated that alterations in ECTI occurred in the context of specific cellular and stromal changes associated with neoplastic change as shown in Chapter 1.

## **3.2 Materials/Methods:**

**3.2.1 Animal Model:** Animal studies were approved by the Institutional Animal Care and Use Committee at the University of Texas Medical Branch and conformed to the Guide for the

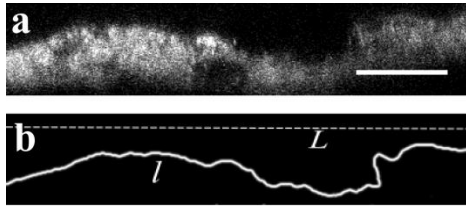
Care and Use of Laboratory Animals. Hamster models for oral neoplasia and inflammation described in chapter 2 were used for the studies presented in this chapter. Control (n=13), inflammation (n=5) and DMBA treated (n=16) hamsters were subjected to *in vivo* multiphoton imaging and spectroscopy. Areas for microscopy and spectroscopy were selected based on visual inspection. *In vivo* NLOM from 41 control, 17 inflamed and 24 dysplasia sites were performed. Imaged sites were biopsied, fixed in 10% neutral buffered formalin and H&E stained for histopathological grading.

**3.2.2 MPAM-SHGM System:** The NLOM system used and methods for *in vivo* microscopy with MPAM and SHGM are described in chapter 2. Briefly 780 nm and 840 nm excitations were used for MPAM and SHGM respectively. Autofluorescence was captured using a broad band emission filter 450-650 nm and SHG was collected through a 420/20 nm bandpass filter. Detection was done by cooled PMTs (R6060, Hamamatsu, Japan). Cross-sections of the regions of interest were also imaged with a built-in z-scanning function in the image acquisition software with the site for acquisition chosen at the center, in the case of a lesion visible by microscopy.

### **3.2.3 Image Processing and Data Analysis:**

**3.2.3.1 Two-dimensional quantitative parameter for rapid evaluation of ECTI remodeling ( $\Delta$ Linearity):** Cross-sectional x-z/y-z views of MPAM-SHGM image stacks were provided by orthogonal view function in ImageJ (NIH). Figure 3.1a shows an example of a SHGM x-z cross-sectional image from a moderately dysplastic mucosa. The ECTI surface was initially identified from co-registered MPAM-SHGM images (55) as the topmost border in SHGM cross-sectional images. These images were thresholded and an edge detection algorithm plugin

was applied to extract the ECTI (“FeatureJ: Edges” plugin in ImageJ). Consistent with known alterations in structure, qualitative observation indicated deviation from a flat surface in cases of dysplasia, resulting in areas where the ECTI curved deeper into the tissue. The expected flat surface of the ECTI in normal buccal mucosa was modeled by a straight line across the cross-sectional image, and a degree of deviation from a flat surface was modeled as a curved surface which deviated in shape from a straight line. A quantitative measure of this deviation was devised and applied to SHGM cross-sections. Mapping of the ECTI and calculation of its length ( $l$ ) was performed (Fig. 3.1b) using a “simple neurite tracer” plugin, also in ImageJ. The measured curved length was then normalized with a theoretical ECTI representing the shortest straight line ( $L$ ) connecting the two ends of the image within the same field of view as shown in Fig. 3.1b.



$$\Delta L = \text{Length of ECTI } (l) - \text{straight line ECTI } (L)$$

$$(\Delta L)_{\text{norm}} = \frac{\text{Length of ECTI } (l) - \text{straight line ECTI } (L)}{\text{straight line ECTI } (L)}$$

Figure 3.1. Cross-sectional x-z SHGM micrograph is shown in (a). Figure (b) shows an ECTI (solid white line) extracted from (a) after the FeatureJ: Edges plugin in ImageJ was applied. The dashed line represents the reference linear distance between the two ends of the image. The equations on the right were used to calculate  $\Delta L_{\text{linearity}}$  ( $\Delta L_{\text{norm}}$ ). Scale bar: 50  $\mu\text{m}$ . (Pal et al. 2015)

### 3.2.3.2 ECTI Contour for three-dimensional quantitative evaluation of

**ECTI remodeling:** MPAM-SHGM images were processed using ImageJ (NIH, Version 1.48u) and Imaris (Bitplane, Version 7.4.2) for 3D volume reconstructions. Because SHG is expected to occur only at this interface and beyond, the ECTI surface was defined as the boundary where SHG



began in depth. For visualization representative z-stacks from each pathological group were median filtered (using a 2x2 matrix) and with adjustment in contrast/brightness in ImageJ to ease visualization of cytologic features, with the same contrast adjustment parameters applied to all z-stacks.

In order to model and quantify surface contour of ECTIs, an ImageJ macro was developed that mapped ECTI surface from SHGM stacks. Steps described were performed on unprocessed images. Briefly, the ImageJ despeckle algorithm (median filter) was applied to each image plane in the stack to reduce salt and pepper noise and Gaussian filtered to smooth the image (radius of 2 pixels). Each stack was considered an x,y,z matrix comprised of columns extending in z that represents pixels at same x-y position as individual columns. Beginning at x,y=0,0 and progressing row by row, columns were sampled at each z position for intensity to identify the depth position where a positive SHG signal occurred (thereby defining the ECTI along each column). Positive SHG signal was determined based on matching or surpassing a threshold intensity value. To insure this position represented the beginning of the LP a 'true signal' was considered as such only if three consecutive pixels along the z-direction were above-threshold intensity. The first of the three pixels was defined as a point on the ECTI surface. After a complete scanning of all 262,144 columns for each stack the ECTI point nearest to the surface (having the smallest depth value) was set as  $z'=0'$  in the local coordinate system creating a temporary reference plane from which each subsequent point on ECTI could be compared. An 8-bit grey scale depth-map was generated based on the distance between the reference plane and each identified surface point on the ECTI (note in this map, each pixel value represents a depth rather than intensity). Z-columns that did not contain signal in any z-depth were assigned a depth,  $z'=0$  in the depth-map defining an interface at the surface. This created false surfaces for

z-columns without any SHG signal, which is accounted for in a normalization step later in the process. Depth-maps containing signal in less than 40% pixels, considered to have poor SHG signal from LP, were excluded (four OED sites from the entire data set excluded based on this criteria) leaving twenty-four OEDs for further analysis. The ImageJ plugin '3D Surface Plot' was used to plot depth-maps in 3D space for representation of the ECTI surface. ECTI surface area was calculated from depth-maps since values in each pixel represent depth from the reference plane. The method implemented for surface area calculation divides a curvature joining four points into two identical triangles and calculates the surface area of each triangle. The sum of the two areas is estimated to be the surface area of the curvature joining the four points. Matrices of 2x2 pixels were defined for the entire depth-map and each matrix divided into two triangles sharing the same hypotenuse. Surface area of each of these triangles was calculated using Heron's formula (118) and the cumulative curved surface area was calculated as a sum of all triangles. The calculated surface area was normalized by the area of the reference plane. This normalization step generated an 'ECTI contour' - a measure of the ECTI curvature.

**3.2.3.3 Histopathology:** H&E stained samples from sites imaged *in-vivo* by MPAM-SHGM were imaged with an Olympus IX71 inverted brightfield microscope using a 20X, 0.75 NA air objective. Samples were graded in four categories (normal, mild dysplasia, moderate dysplasia, severe dysplasia) and sites representing the most central region having the most severe pathological features were selected for quantitative measurements. Grading was performed according to WHO's criteria for architectural and cytological changes in dysplastic epithelium. Two sections closest to the center of lesions encompassing approximately 600 $\mu$ m (twice the

FOV of imaging) were chosen for measurements. This was to maintain consistency with the imaging protocol in which the most central region of a lesion was imaged.

**3.2.3.4 Statistical analysis:** Statistical comparison between groups were performed by single factor ANOVA followed by the Tukey's *post hoc* test with  $P < 0.05$  considered significant ( $P$  value of  $< 0.05$  is represented by a single asterisk '\*' and  $P < 0.01$  by double asterisk '\*\*'). Receiver operator characteristic (ROC) curves were generated using SAS software (SAS Institute Inc.) to calculate area under the curve (AUC), sensitivity and specificity.

### 3.3. Results:

**3.3.1 Visualization of neoplastic abnormalities with ECTI remodeling:** Three-dimensional volumes of MPAM-SHGM overlays for control and OED with corresponding histological sections are shown in Fig. 3.2. Normal buccal epithelium is characterized by a thin layer of keratinocytes (Fig. 3.2a, Left;  $z=4\mu\text{m}$ ) at the surface followed by stratified squamous epithelium. Superficial epithelium (Fig. 3.2a, left;  $z=14\mu\text{m}$ ), composed of highly differentiated epithelial cells with large round nuclei and low nuclear to cytoplasm ratio, and basal epithelium (Fig. 3.2a, left;  $z=19\mu\text{m}$ ) having smaller epithelial cells are shown in planes to the left. Cell nuclei in MPAM images appear as circular regions lacking fluorescence surrounded by autofluorescing cytoplasm. The final layer is LP (Fig. 3.2a, left;  $z=46\mu\text{m}$ ). The 3D multilayer volume reconstruction is shown in Fig. 3.2a, right. Transition between autofluorescence (Epithelium: magenta) and SHG (ECM: green) represents ECTI (Fig. 3.2a), the boundary between epithelium and LP.

Fig. 3.2b shows OED with thickened keratinizing and epithelial layers and remodeled LP. Superficial and basal epithelial layers (Fig. 3.2b, left;  $z=100\mu\text{m}$  and  $140\mu\text{m}$  respectively) showed a heterogeneous population of enlarged cells and nuclei and focal epithelial thickening resembling typical histological features of dysplasia (Fig. 3.2b; inset). These cytologic features are described in detail in chapter 2. Deeper planes in OED traverse across both basal epithelium and LP since focally thickened epithelium results downward bulging of ECTI. Such areas were not observed in control epithelium due to uniform epithelial thickness. Histologic sections of controls and OED showed similar features in cross sections. In

histopathology of OED, focal epithelial thickening was seen along with nuclei of atypical size and shape (pleomorphism).

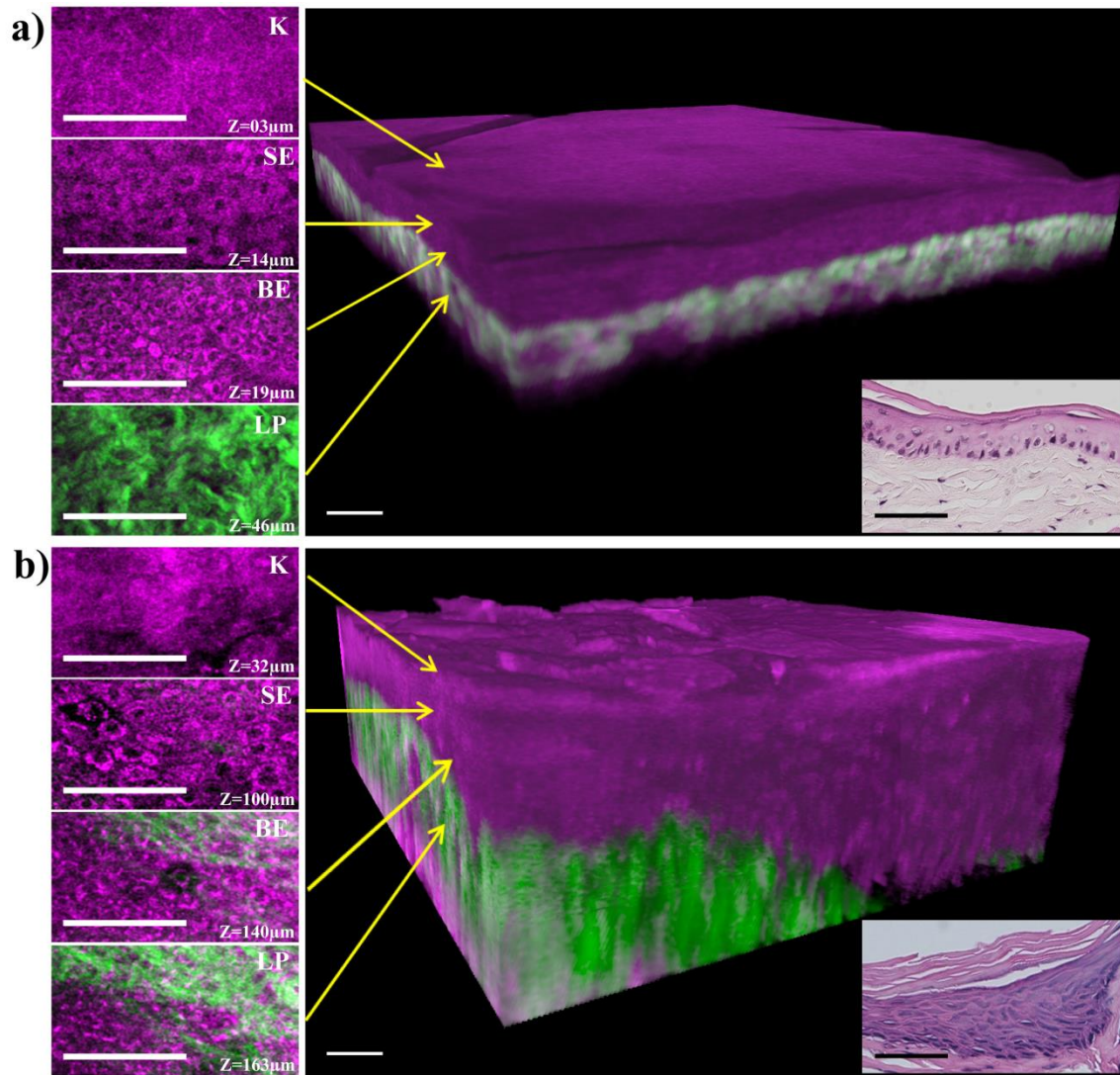


Figure 3.2: Layer resolved volumetric MPAM-SHGM of hamster oral mucosa showed cytologic and microstructural features associated with neoplasia. Single optical sections and three-dimensional volumes of representative control (a), and dysplastic (b) hamster oral epithelium. x-y micrographs from MPAM (magenta) at different depth shows

autofluorescence from keratinizing and epithelial layers. SHG (green) from collagen fibers in the lamina propria is shown in green. Histologic sections of control and dysplasia of corresponding ROIs are shown in respective insets. K: Keratinizing layer, SE: Superficial epithelium, BE: Basal epithelium, LP: Lamina propria. Scale bar, 50µm.

Figure 3.3 shows cross-sectional MPAM-SHGM images along with histology describing a process believed to lead to alterations in the epithelium and ECTI morphology during neoplastic transformation (41) and explained in the chapter 1. Figures 3.3a, c and e shows alterations in tissue architecture from normal (Fig. 3.3a) to mild dysplasia (Fig. 3.3c) to severe dysplasia (Fig. 3.3e). MPAM autofluorescence from the keratinizing stratum corneum, the epithelium and lamina propria is shown in red, while SHGM from the fibrillar collagen network in the lamina propria is shown in green. Autofluorescence from the muscle beneath the ECM (Fig. 3.3a) (shown in red) is comparable to the muscle seen in the deepest layer visible in Fig. 3.3b. A faint green layer in the deep most portion of the MPAM-SHGM composite (Fig. 3.3a) arises from the lamina propria of the opposing side of the folded buccal pouch. In cases of dysplasia (Fig. 3.3c, e) an interesting architectural feature at the junction of the epithelium and ECM (arrows) was observed that was expected to arise due to severe remodeling of the ECM. This feature is reflected in the alteration of flat architecture of epithelial-connective tissue interface (ECTI) by formation of rete ridges as epithelial cells start protruding downwards into the lamina propria without physically disrupting the BM (51). This feature is also appreciated in three-dimensional volumes (Fig. 3.2). Cytological features, such as pleomorphic and atypical cells and nuclei are also depicted in Figure 3.3e (marked “\*\*”) under the grade of severe dysplasia. The transition between epithelium (red) and ECM (green) is considered to represent the ECTI (white arrows in Fig. 3.3a, c, e), where many early dysplastic features are considered to be initiated (4, 45, 46). Cross-sectional views of normal (Fig. 3.3a) and mild dysplasia (Fig. 3.3c) epithelium do not

provide the contrast to visualize individual cell nuclei (epithelial cells are somewhat flattened in this state), but nuclei in the severe dysplasia become enlarged enough and polarized in a direction perpendicular to the surface to be easily visible (Fig. 3.3e, f “\*”).

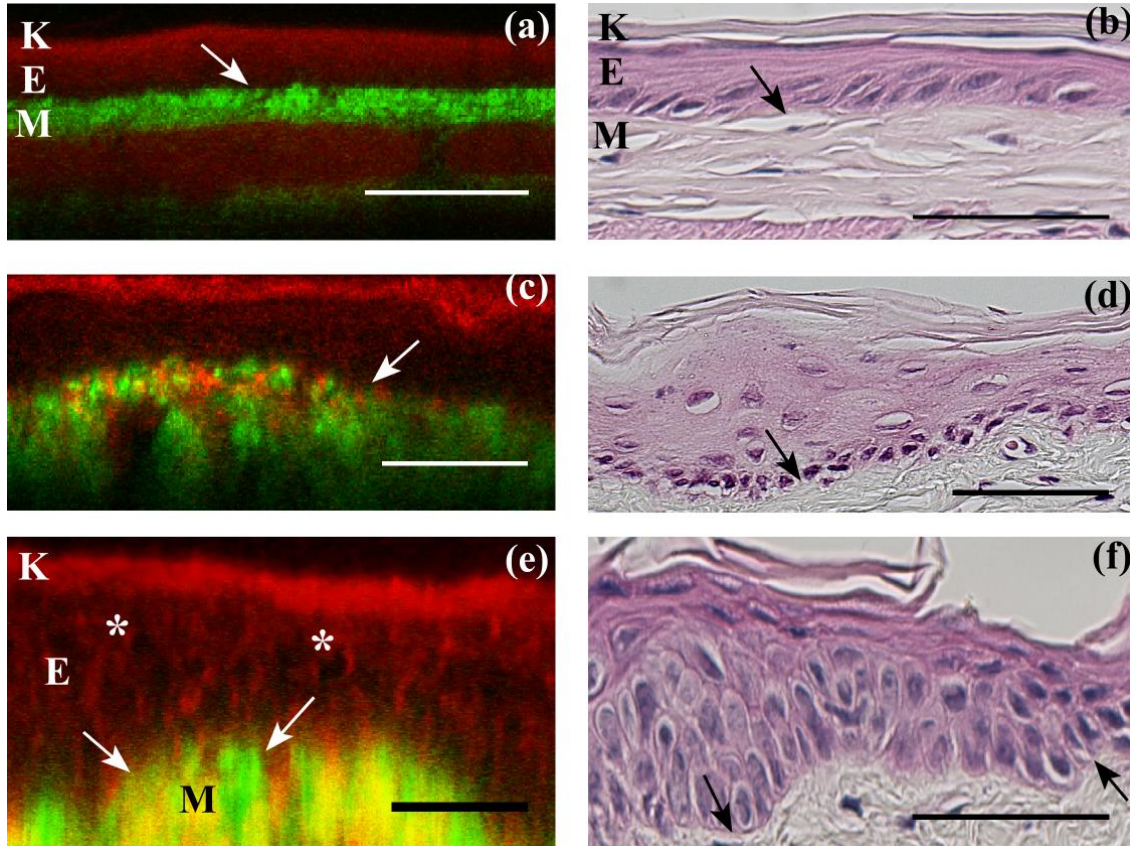


Figure 3.3. Early events during neoplastic transformation. MPAM-SHGM micrographs (a, c, e) and histological sections (b, d, f) of hamster oral mucosa for normal (a, b), mild dysplasia (c, d) and severe dysplasia (e, f) are shown. In-vivo autofluorescence from MPAM (Red) co-registered with SHG (Green) are overlaid to produce cross-sectional MPAM-SHGM micrographs (a, c, e) comparable to histology (b, d, f). K: Keratinizing layer; E: Epithelial layer, M: Lamina propria or ECM. White and black arrows point towards ECTI and “\*” shows enlarged nuclei in dysplastic epithelium. Scale bar: 50 $\mu$ m. (Pal et al. 2015)

Figures 3.3b, d, f shows H&E stained histology sections of the corresponding sites from Figures 3.3a, c, e. Fig. 3.3b shows a normal hamster oral mucosa with characteristic features such as a thin keratinizing layer (~10  $\mu\text{m}$ ) at the top, followed by tightly packed epithelium and a densely packed ECM with the ECTI representing a linear interface (black arrows in Fig. 3.3b, d, f) separating ECM from the epithelium. Fig. 3.3d and 3.3f show features of mild and severe dysplasia respectively, such as increased epithelial thickness, loss of basal cell polarity, abnormal variation in nuclear and cellular shape and size, large number of poorly differentiated cells, and irregular ECTI with rete-ridges. The features seen in Fig. 3.3b, d, f are similar to those revealed by MPAM-SHGM (Fig. 3.3a, c, e).

**3.3.2 2D evaluation of ECTI geometry and quantification of  $\Delta\text{Linearity}$  from cross-sectional MPAM-SHGM:** As described before irregularities in ECTI is an important architectural abnormality seen in dysplasia (Fig. 3.3 “arrows”) and was measured as  $\Delta\text{Linearity}$ . Thirty-three normal sites collected from mineral oil treated hamsters and twenty-seven sites with dysplasia collected from DMBA treated hamsters were analyzed. H&E stained sections and SHGM image cross-sectional images from each site were analyzed for ECTI irregularity (Fig. 3.4). All dysplasia groups showed significantly higher  $\Delta\text{Linearity}$  than normal ECTI for both NLOM (Fig. 3.4a) and histology (Fig. 3.4b) except mild dysplasia in histology, possibly due to a large sampling area in biopsy than microscopy which was approximately twice the size as assurance that the imaged region was sampled by histology. The distributions of  $\Delta\text{Linearity}$  of moderate and severe dysplasia were larger than normal and mild dysplasia similar to epithelial thickness.



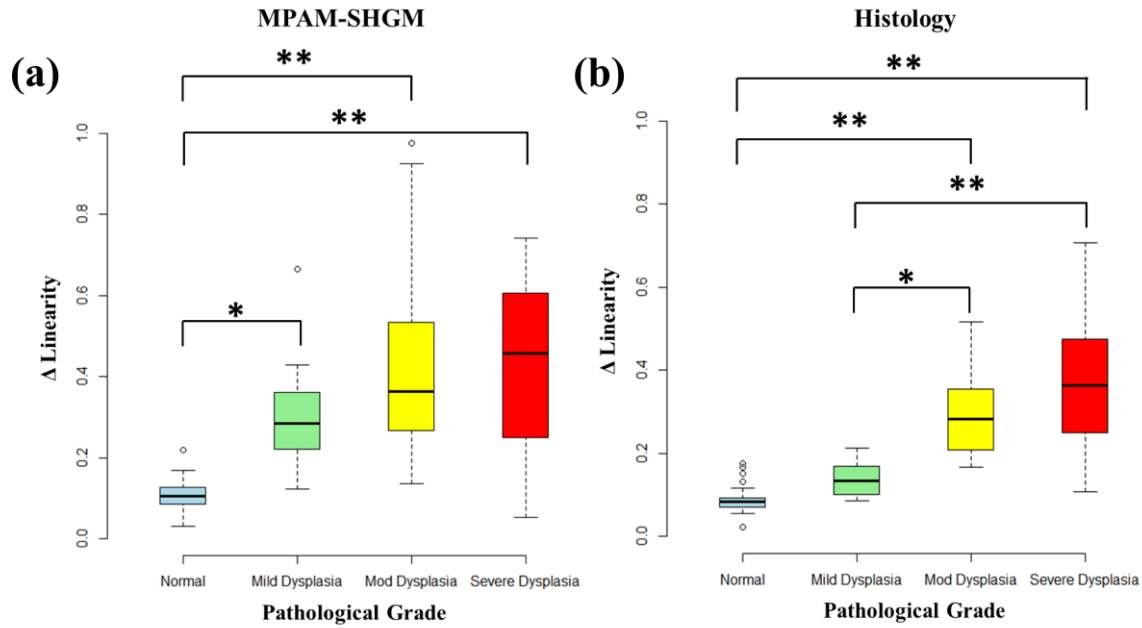


Figure 3.4.  $\Delta L_{\text{norm}}$  measurements from MPAM-SHGM (a) and histology (b) show statistically significant increase in  $\Delta\text{Linearity}$  of mild, moderate and severe dysplasia from normal mucosa. Box plot analyses show the median, 25th and 75th percentiles, and outliers for both MPAM-SHGM and histology. “\*” and “\*\*\*” represent statistical difference between groups at  $p < 0.05$  and  $0.01$  significance respectively.

Average  $\Delta\text{Linearity}$  for normal and all dysplastic grades (Table 3.1) in MPAM-SHGM images were calculated to be  $0.11 \pm 0.04$  for normal,  $0.31 \pm 0.17$  for mild dysplasia,  $0.45 \pm 0.29$  for moderate dysplasia and  $0.41 \pm 0.22$  for severe dysplasia. Similar calculations on histology images revealed ECTI  $\Delta\text{Linearity}$  of  $0.09 \pm 0.03$  for normal,  $0.14 \pm 0.04$  mild dysplasia,  $0.29 \pm 0.1$  for moderate dysplasia, and  $0.38 \pm 0.19$  for severe dysplasia. Average  $\Delta\text{Linearity}$  of dysplastic and normal tissue from MPAM-SHGM and histology are shown in Table 3.1.

Table 3.1: Summary of the statistical analyses performed from  $\Delta$ Linearity measurements carried out on cross-section images from MPAM-SHGM or histopathology. SHGM: Second Harmonic generation Microscopy, SD: Standard Deviation, AUC: Area Under the Curve, TP: True Positive, FP: False Positive, TN: True Negative, FN: False Negative.

Group		$\Delta$ Linearity (SD)	AUC	Sensitivity (%)	Specificity (%)	TP	FP	TN	FN
MPAM-SHGM	Normal	0.11 (0.04)	0.95	87.9	97.6	0.7	0.3	0.96	0.04
	Dysplasia	0.41 (0.24)							
H&E	Normal	0.09 (0.03)	0.96	96.4	85.7	0.59	0.41	0.95	0.05
	Dysplasia	0.28 (0.16)							

As it is believed that the ECTI shape changes are a direct consequence of interactions between neoplastic cells, the basement membrane and ECM of the lamina propria, ROC analysis was performed to test the performance of  $\Delta$ Linearity to differentiate normal from dysplasia. ROC curves for  $\Delta$ Linearity based on MPAM-SHGM and histology were analyzed to differentiate normal from dysplasia (mild, moderated, severe) (Fig. 3.5). An ROC plot represents true positive rate against false positive rate for different possible cut-offs of  $\Delta$ Linearity calculated either from histopathology (Fig. 3.5, green line) or from microscopy (Fig. 3.5, blue line). Table 3 summarizes the results from ROC analysis. As can be seen in Figure 3.5 the ROC curves for MPAM-SHGM and histology are very similar and they produced comparable area under the curve (AUC), which is a measure of accuracy of a test. AUC values from  $\Delta$ Linearity for both MPAM-SHGM and histology are greater than 0.9, considered a successful test. Table 3.1 shows the sensitivity and specificity of  $\Delta$ Linearity for MPAM-SHGM and histology respectively. True positives, false positives, true negatives and false negatives are also shown in Table 3.1 for comparison between MPAM-SHGM and histology.

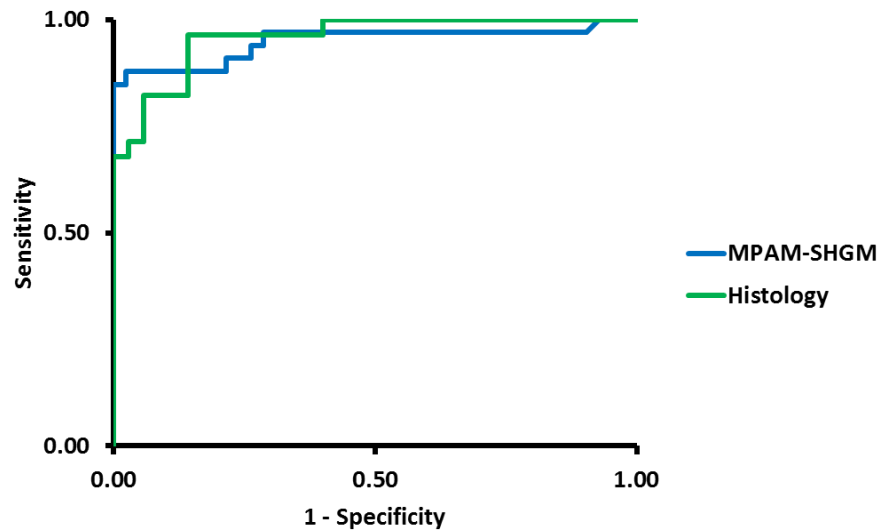


Figure 3.5. ROC curve at 95% confidence for  $\Delta$ Linearity calculated from MPAM-SHGM (Blue) and histological (Green) images. (Adapted from Pal et al., 2015)

ECTI irregularity or in other words  $\Delta$ Linearity provided an excellent platform to study early neoplastic abnormalities in cross-sectional views, however such analysis did not depict the ECTI as a three-dimensional surface, necessary to aptly visualize pockets of matrix compliance in OED. Therefore I examined the ECTI and ECTI associated cytologic abnormalities in three-dimensions utilizing the high-resolution deep tissue three-dimensional imaging capability of NLOM.

### 3.3.3 Three-dimensional visualization of ECTI surface in relation to cytologic atypia:

Figure 3.6 shows regions of interests (ROIs) from control and OED in basal epithelium adjacent to ECTI. Fig. 3.6a shows an LP SHGM image plane from control having dense thick fibers of collagen. Fig. 3.6b is a 3D surface mask of an SHG image stack from control tissue showing a flat topography at the top where basal epithelium meets LP. Fig. 3.6c and 3.6d shows a single image plane and a 3D surface mask respectively of a LP with OED. Areas devoid of SHG indicate

collagen degradation/remodeling in the LP (Fig. 3.6c “\*\*”) with pockets of matrix compliance in 3D surface maps (Fig. 3.6d “\*\*”). Planes which traversed both LP and epithelium at the same depth were observed only in the OED group such as in Fig. 3.6e and 3.6f (top view), where basal epithelial cells with cytologic features consistent with OED are visible along with LP at the same plane. Collagen remodeling (Fig. 3.6e) is indicated by reduced density of collagen fibers and by the expanded epithelial boundary. Cytologic features of neoplasia such as cellular discohesion (Fig. 3.6f “white arrow”), anisonucleosis (Fig. 3.6e “\*\*”) and atypical variation in cell shape (pleomorphism; Fig. 3.6f “black arrow”) are evident in same spatial location as the compromised LP.

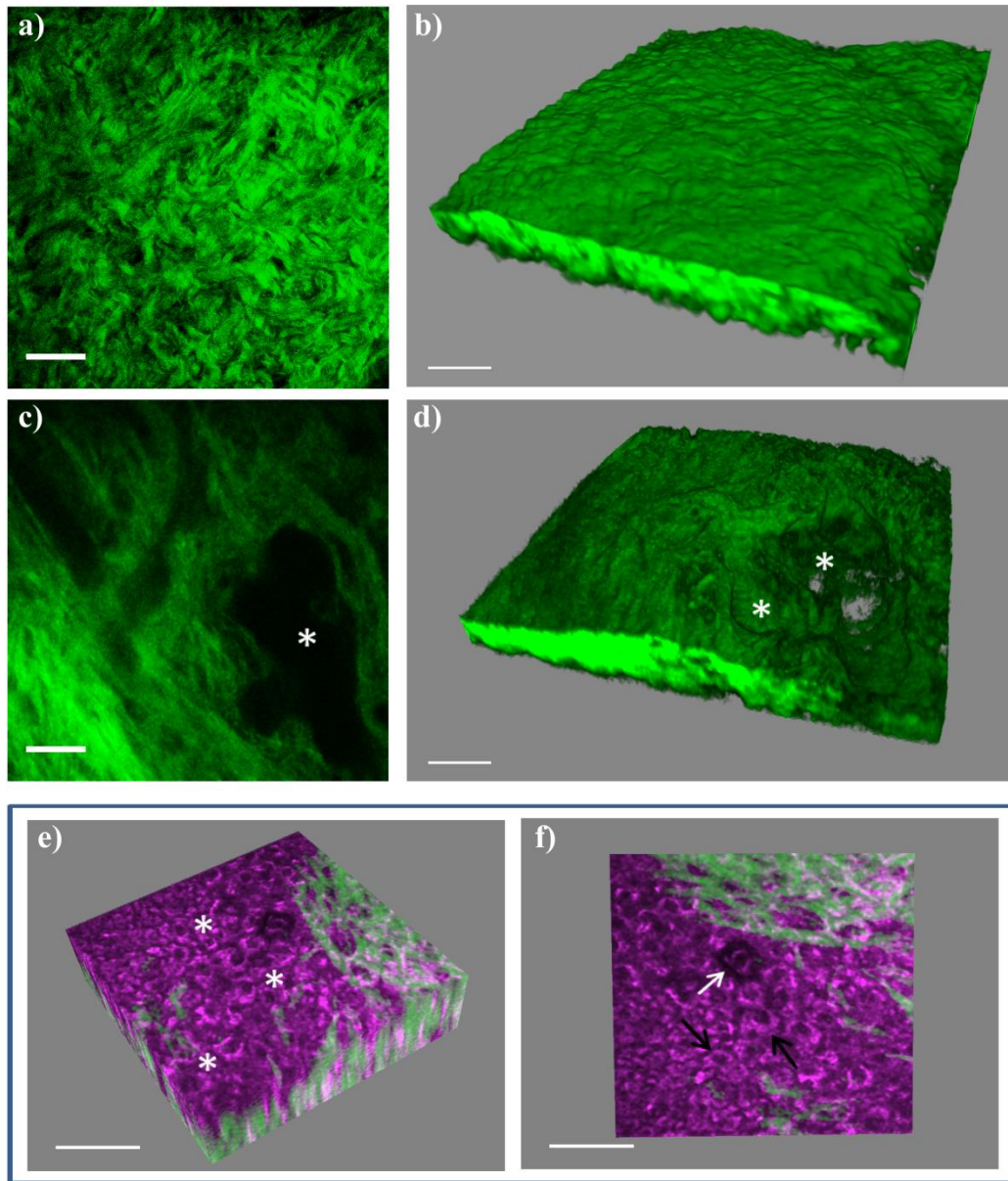


Figure 3.6: Label-free volumetric imaging revealed remodeling of ECM in OED and confirmed presence of neoplastic cells in areas of SHG voids. a) SHGM of a single image plane from a control lamina propria; b) 3D surface map showing the flat topography of a control lamina propria comprising of 130 image planes from SHGM; c) SHGM of a single image plane from an OED lamina propria; d) 3D surface map showing downward bulging of the OED lamina propria comprising of 160 image planes from SHGM; “\*” in (c) and (d) indicates areas of remodeled lamina propria; e) ROI of

co-registered MPAM (magenta) and SHGM (green) from an OED showing presence of epithelial cells having neoplastic cytology ( “\*” and “→” ) near remodeled lamina propria; f) en face view of the ROI shown in (e). Scale bar, 50 $\mu$ m.

**3.3.4 Noninvasive delineation of ECTI contour for quantitative assessment of ECTI remodeling during neoplasia:** Figure 3.7(a-c) shows ECTI surface maps from representative control, inflamed and OED tissues. The color scale (inset, Fig. 3.7a) represents distance of a particular pixel in the surface map from a reference plane at depth of  $z'=0$ . A surface with larger range of colors indicates more irregularities than one showing only few colors.

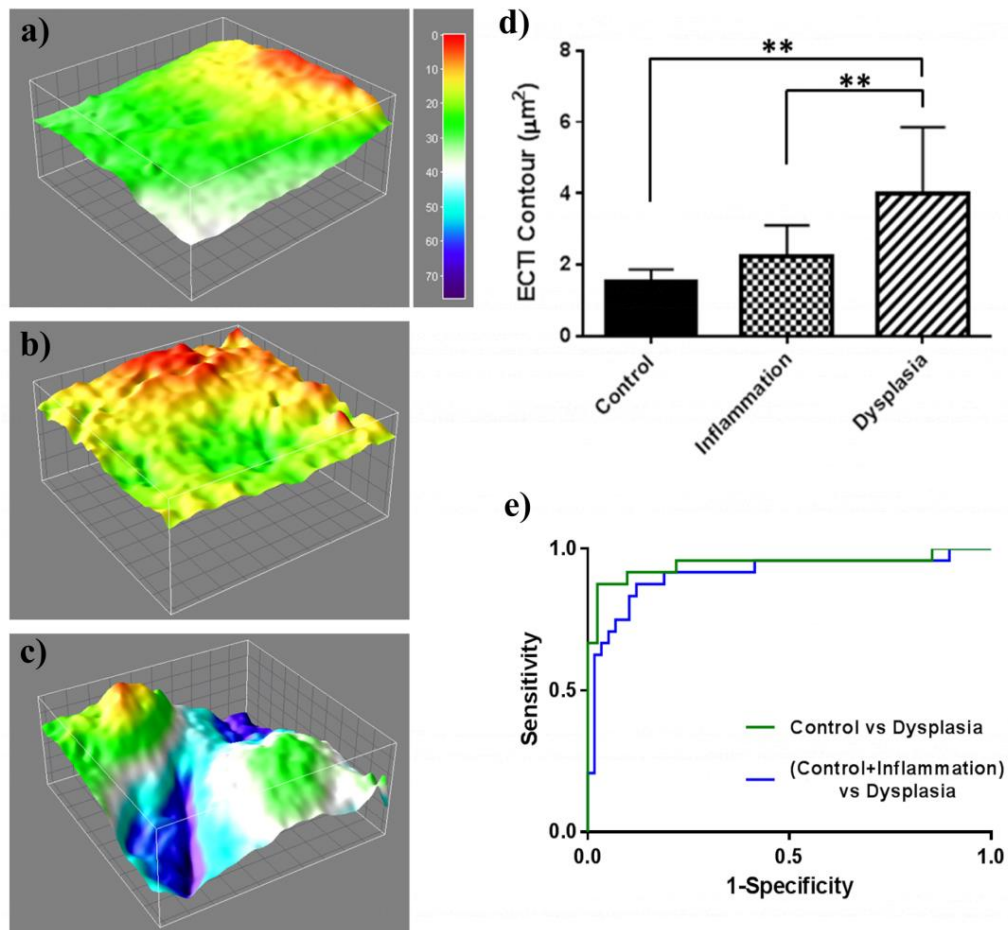


Figure 3.7: Remodeling of ECTI surface maps results in increased ECTI contour in OED. ECTI surface maps generated from SHGM z-stacks for control (a), inflammation (b) and dysplasia (c) show changes in surface topography. Color

scale in (a) indicate changes in depth of the ECTI surface map. Red indicates a point towards the top and blue indicates a point towards the bottom of the surface map. (d) ECTI contour calculated from ECTI surface maps for all three groups. (e) ROC curves of ECTI contour when inflammation is present (blue) or absent (green) in the control group with AUCs 0.91 and 0.95 respectively.

ECTI surfaces in control and inflamed mucosa were relatively flat with average ECTI contour  $1.52 \pm 0.35$  and  $2.22 \pm 0.88$  respectively. ECTI from OED showed major alteration in its surface leading to an elevated ECTI contour ( $4.01 \pm 1.85$ ). The increase in ECTI contour in OED was found to be statistically significant ( $** < 0.01$ ) from control and inflammation (Fig. 3.7d). Inflamed epithelium had a marginal increase from control in ECTI contour however was not statistically significant. Fig. 3.7e shows ROC curves comparing control and OED in the absence and presence of inflammation. The presence of inflammation reduced sensitivity from 91.7% to 87.5% and specificity from 90.2% to 87.9%. Overall, AUCs in absence and presence of inflammation were calculated to be 0.95 and 0.91 respectively (Table 3.2).

Table 3.2: AUC, sensitivity and specificity of ECTI contour in absence and presence of inflammation in study population as measured from ROC analysis.

Statistical Performance of ECTI Contour	Control vs Dysplasia (n=65)	(Control+Inflammation) vs Dysplasia (n=82)
AUC (95% CI)	0.95 (0.87-1.00)	0.91 (0.83-0.99)
Sensitivity (%)	91.70%	87.50%
Specificity (%)	90.20%	87.90%

**3.3.5 ECTI remodeling showed spatial correlation with cytologic abnormalities in neoplasia:** Visual assessment of several cytologic features from MPAM was performed to correlate presence or absence of cytologic abnormalities within sites of ECTI remodeling. As expected a large percentage of OEDs showed presence of at least three cytologic features listed in Table 3.3 and ECTI contour changes were accompanied by neoplastic features (Fig 3.8).

Table 3.3: Visual assessment and distribution of cytological features associated with OED

Parameter	Defining Criteria	Normal (n=41)	Inflammation (n=17)	Dysplasia (n=24)
Epithelial Thickening	Shortest distance from keratinizing layer to ECTI	0	16	22
Anisonucleiosis/ Anisocytosis	Abnormal variation in nuclear and cellular size (e.g. enlargement)	1	3	18
Overcrowding/ Cell Discohesion	Nonuniform intercellular spacing	1	6	13
Pleomorphism	Atypical variation of nuclear and cellular shape	3	3	16
Binucleation	Two nuclei share single cytoplasm as a result of increased mitotic rate and defective cytokinesis	1	3	11

Epithelial thickening was considered abnormal when the epithelium expanded beyond 40  $\mu\text{m}$ , the typical thickness in the hamster cheek pouch model (54, 55, 90). All other features were qualitatively assessed following guidelines presented in (100). The number of samples from each category (control, OED, inflammation) showing these features was calculated and presented in Table 3.3. As shown in Fig. 3.8 more than 90% samples with ECTI deformations were associated with cytologic abnormalities while only less than 10% normal and inflamed samples with no appreciable change in ECTI contour showed such cytologic features.



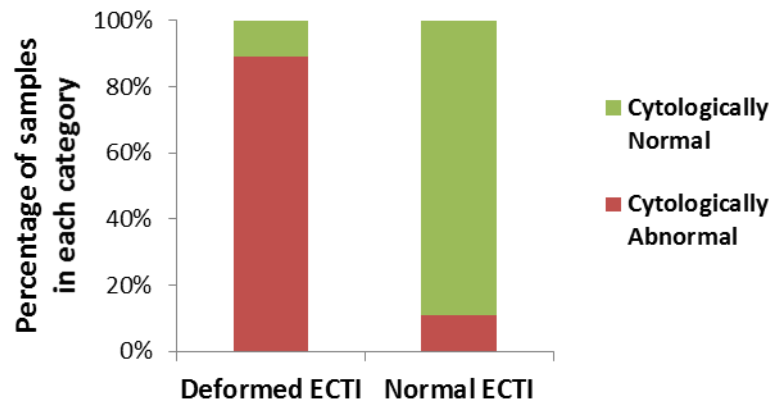


Figure 3.8: Association of cytologic features with ECTI deformation. (Pal et. al. 2016)

**3.3.6 Multivariate statistical model for delineation of neoplasia from normal and benign conditions:** Since basal nuclear CoVa was the highest performing cytologic feature in chapter 2, a multivariate statistical model was created by combining basal nuclear CoVa with ECTI contour. Fig. 3.9a shows the model when only control tissue was compared with OED while Fig. 8b shows the effect of addition of inflammation to the model. The first model (Fig. 3.9a) was able to achieve a perfect separation of OED from control tissue. When inflammation was included in the population as a benign condition the model criteria (intercept and estimate) were re-evaluated and in the process one OED site (Fig. 3.9b; “arrow”) was grouped with the control and benign group. However a simple linear model was not able to achieve any separation between the control and inflammation groups.

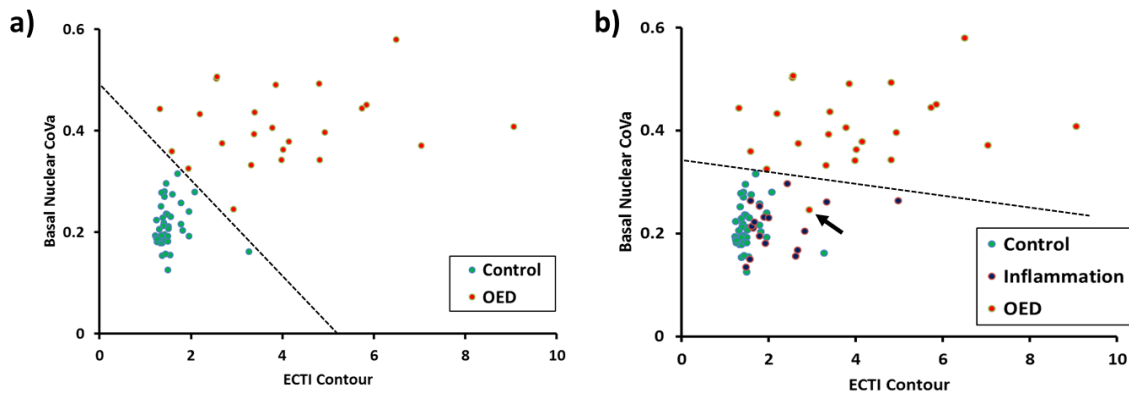


Figure 3.9: Multivariate linear models created by using ECTI Contour and basal nuclear CoVa. a) Scatter plot for control and dysplasia; b) scatter plot for control, inflammation and dysplasia. Dotted straight lines represent optimal separation of groups as calculated from the linear model. The arrow in b) indicate the only miss-classified OED in presence of inflammation.

### 3.4 Discussion:

Noninvasive characterization of ECTI remodeling is expected to lead to the better understanding of the initial processes that leads to neoplasia and ultimately invasion. NLOM allowed for the ECTI to be represented as a 2D cross section (similar to histology), as well as a 3D surface expanding beyond limited views provided by traditional histopathology. ECTI in OED was characterized by downward bulging of the epithelium similar to a well-delineated pushing margin seen in pre-invasive OSCC (119) resulting in a contour change/deformation and quantified as ECTI contour. Results indicated delineation of OED from control/benign tissue in a hamster model of OED and inflammation. ECTI deformations were found to occur along with

basal cellular atypia as measured by nuclear density, nuclear area and CoVa, and with collagen remodeling measured by collagen density.

**3.4.1 ECTI remodeling quantified as  $\Delta$ Linearity in neoplasia:** The significance of ECTI shape is based on the potential central role this interface serves in neoplastic transformation. There are indications that early pathological events leading to neoplastic transformation of basal epithelium initiate structural alterations in the ECTI (120). Based on the observation that the ECTI shape went from relatively flat to curved, forming rete-ridges (Fig. 3.3: arrows) with OED, a parameter representing deviation of ECTI from absolute linearity ( $\Delta$ Linearity) was introduced. With more rete ridges present in OED (Fig. 3.3 and 3.4), the average  $\Delta$ Linearity between two given points on the ECTI surface increased relative to a flat appearance observed in normal mucosa. ROC analysis showed the potential of  $\Delta$ Linearity to differentiate dysplastic abnormality from normal mucosa with AUC and sensitivity/ specificity comparable to analysis based on H&E (Fig. 3.5 and Table 3.1). Such quantitative assessment of ECTI remodeling was based on cross-sectional MPAM-SHGM imaging which provides a method for quick screening of the oral mucosa. It is clear from Fig. 3.3 that characteristics of remodeling of ECTI during neoplastic development were strikingly similar in both MPAM-SHGM and histopathology. However, identification of cytologic features associated with abnormal ECTI from MPAM-SHGM cross-sections can be difficult due to low contrast presented by autofluorescence especially by normal and low grade dysplasia.

**3.4.2 Volumetric assessment of ECTI remodeling:** In addition to  $\Delta$ Linearity measured from MPAM-SHGM cross-sections the ECTI contour also increased (Fig. 3.7) with increasing degree of remodeling and formation of new rete-like features in OED. Average ECTI contour in

inflamed tissue was higher than control (Fig. 3.5d) and may be attributed to vasculature near the surface of LP. Future studies may include vessel masks to blend vessel surfaces with ECTI surface and reduce artifacts in ECTI contour. ROC curves calculated with exclusion and inclusion of inflammation within the control group showed its effect on performance of ECTI contour. As mentioned in chapter 1 inflammation can pose complications in clinical diagnosis of OEDs and by optical methods (98) due to similarities in optical properties (99). Performance of ECTI contour in delineation of OED from normal/inflamed mucosa was superior to nuclear density and area as shown in chapter 2. ECTI contour showed sensitivity/specificity comparable to CoVa and collagen density (Chapter 2) with slightly lower AUC. However, 95% confidence interval of all three parameters overlapped significantly, indicating comparable differentiating power for OED despite inflammation. Identification of cellular atypia and collagen remodeling accompanying ECTI deformation highlights the relevance of ECTI contour as a reliable indicator of OED. As expected, inflammation induced epithelial thickening but showed no significant change in ECTI contour, collagen density or evident cellular atypia in visual assessments.

#### **3.4.3 Advantages and challenges of volumetric assessment of ECTI remodeling:**

Overall advantages of ECTI contour were that it allowed for assessment of deformation and the algorithm developed was fairly straightforward, using freely accessible software (ImageJ). The primary challenge in determining ECTI contour was identifying pixels with SHG signals indicative of collagen contribution with high accuracy which was ensured by requiring at least three consecutive depth locations showing a positive SHG signal. This algorithm is adaptable to other image stacks with a hard interface, as seen in SHGM. More advanced edge detection algorithms could be developed in future when detection of subtle changes in fluorescence intensities is

necessary as has been done for OCT or CRM (37, 121). Given that depth of imaging encompasses the epithelium and LP, the algorithm could be readily applied in similar mucosal structures and in those in which rete-like ridges extend in depth. The general approach could also be applied in cases involving bulb-like rete ridges; in such cases, each z-column may contain more than one transition, requiring an algorithm to detect each major transition as an edge and defining the pixels that lie on the epithelial side versus stromal side. A second challenge that may be encountered in human neoplasia could be the depths needed to reach the ECTI. While human oral mucosa can range in thickness from ~200  $\mu\text{m}$  to several hundred microns accessible to NLOM, in neoplasia these depths may be increased substantially, potentially limiting ECTI analysis. Future studies will need to be conducted to evaluate the full potential for ECTI analysis in human neoplasia.

**3.4.4 Association of ECTI remodeling and cytologic atypia:** Qualitative analysis revealed the vast majority of samples having ECTI deformation also showed additional architectural and cellular atypia. Three neoplastic cytologic features related to features in histology were identified from images in 96% OED samples. Importantly, in about 90% cases those features occurred along with increased ECTI contour (Fig. 3.8), indicating presence of ECTI surface deformation whenever neoplastic cytology is present. The link between these features and ECTI contour is anticipated due to known modulation of each other's microenvironment. Since all stages of OED were grouped, it is possible that these percentages are on the lower end since changes in mild OED may be more difficult to identify in micrographs. To demonstrate the feasibility of multivariate assessment of oral neoplasia ECTI contour and basal nuclear CoVa were utilized as important NLOM based signatures of neoplasia. As shown in Fig. 3.9 information

gained from analysis of a cytologic feature and ECTI remodeling provided reasonable delineation of neoplasia from normal tissue even in presence of benign conditions. These results help re-emphasizing on the fact that multiple image based features would be required to accurately identify neoplastic processes just like in cases of histopathologic assessment.

**3.4.5 Conventional methods to study ECTI remodeling and their limitations:** Studies resulting in direct assessment of irregularities in ECTI morphology have been restricted to histological evaluation and in some part electron microscopy (53, 105, 115, 116, 122-124). Studies have been reported in which density (87) or shape (124) of rete ridges from histological sections under normal and dysplastic conditions were quantified. Others have demonstrated ECTI irregularities in histology by looking at tissue complexity based on fractal geometry calculations (105, 117). While histopathology provides assessment of cellular and architectural atypia together, it is typically in cross-section and requires tissue removal. Examination of the ECTI by electron microscopy also revealed irregular ECTI with discontinuities and prominent focal thickening of the BM during epithelial dysplasia and invasive carcinoma (115, 116). With electron microscopy the 3D ECTI surface is appreciated however it requires removal of epithelium excluding assessment of cytologic abnormalities. All of these studies required tissue removal and extensive processing of the excised tissue to extract ECTI parameters.

**3.4.6 Advantages of NLOM based study of ECTI remodeling:** A key advantage of the method presented in the current study is that the method allows direct imaging of the ECTI without disruption to the epithelium and requires no exogenous stains. Further, delineation of the ECTI is without ambiguity as there is no SHG signal in the epithelium, arising only from noncentrosymmetric molecules in the lamina propria (fibrillar collagen), and creating a 'hard'

interface defining the transition from a region of no SHG signal (epithelium) to one with strong SHG signal (lamina propria). Independent optical signatures arising from epithelium and fibrillar collagen in MPAM and SHGM, respectively, help in accurate segmentation of ECTI in 3D while preserving the mucosal structural integrity, important in assessing the interplay between epithelium and LP across the ECTI. This ability to extract independent signal contrasts is an advantage over reflectance based techniques, such as OCT and CRM discussed in the introduction, due to a clear contrast between epithelium (lacking SHG) and LP (strong SHG). While ECTI in oral mucosa may be segmented in OCT (29, 125), cytologic features are beyond the current capability due to resolution limits. Further study with CRM will be needed to examine ECTI demarcation in oral mucosa which is unpigmented and presents lower contrast between epithelium and LP than skin (particularly dark skin) in which dermal-epidermal junction has been delineated in 3D (121).

To conclude, I showed that ECTI topography changes from flat to curved surface, increasing  $\Delta$ Linearity and surface area (ECTI contour) in OEDs. I also showed cytologic features consistent with neoplasia in basal epithelium were associated with increased ECTI contour as was collagen remodeling. The significance of this work is that a new approach utilizing NLOM for *in vivo* imaging has been shown for observing and quantifying ECTI topography in three-dimensions without tissue perturbation. The ability to noninvasively study topographical changes at the ECTI along with cellular and extracellular atypia expands the possibilities for investigation of early neoplastic transformation in OED and could potentially lead to development of novel diagnostic approaches.

## Chapter 4

# Spectroscopic characterization of Oral Epithelial Dysplasia and Squamous Cell Carcinoma using Multiphoton Autofluorescence Micro-spectroscopy

### 4.1 Introduction:

In addition to microstructural assessments using NLOM, there is a potential to extract spectroscopic features that can augment the understanding of the biochemical neoplastic microenvironment, such as evaluation of metabolic dysregulation in neoplasia. The origin of autofluorescence interrogated in previous chapters arises in large part from metabolites such as NADH and FAD and images are composed based on those contrast signatures. Extraction of the specific spectroscopic features of those signatures could be useful toward improved understanding of signals comprised within obtained images and could potentially be used to extract metabolic-related parameters from images or be could be used in concert with image base MPAM to evaluate signatures altered with neoplasia. While tissue spectroscopy has been widely studied in the context of neoplasia, traditional single-photon fluorescence used for these

Results presented in this chapter are currently under review in Lasers in Surgery and Medicine

1. **Spectroscopic characterization of Oral Epithelial Dysplasia and Squamous Cell Carcinoma using Multiphoton Autofluorescence Micro-spectroscopy.** Rahul Pal, Kert Edward, Liang Ma, Suimin Qiu, Gracie Vargas.



studies samples tissue volumes that encompass millimeters in depth (126-129). There are few studies examining multiphoton autofluorescence spectroscopy (MPAS) in oral mucosa. A study in mouse normal oral mucosa established a general characteristic for emission spectra by MPAM (77). One study (53), established the potential to identify redox potential differences between normal and OED mucosa as well as showed parallels to earlier single photon spectroscopy assessments in oral neoplasia. The study did not include oral squamous cell carcinoma (OSCC) with OED. A significant advantage of MPAS is the ability to gain depth-resolved fluorescence to spatially localize spectroscopic signatures to the subcellular scale which can be used to complement image-based information. This helps to better delineate the origin and interdependence of spectral contributors.

Fluorescence from native biomolecules such as NADH, FAD, collagen, porphyrins and aromatic amino acids show altered homeostasis during neoplasia and have been examined extensively for their potential to reveal indication of neoplastic transformation by a variety of optical approaches. Biochemical assessment of metabolic activity in the form of redox potential can be performed using MPAM with isolation of autofluorescence from the metabolic coenzymes NADH and FAD (34, 130). NADH and FAD play an important role in metabolism by acting as electron carriers between key metabolic pathways and maintaining the intracellular redox balance. The ability to evaluate metabolic and biochemical features based on endogenous fluorophores has made MPAM and MPAS a valuable tool in cancer research including investigations examining the potential for early and noninvasive detection of neoplasia in skin (131, 132) and oral mucosa (76, 78).

MPAS has been applied to the study of normal and neoplastic epithelium in recent studies focused on skin and oral mucosa. A recent study explored multiphoton spectral properties in a mouse model for skin SCC (133). Palero et al. (126) conducted spectral imaging of murine skin examining emission spectra due to collagen, elastin, phospholipids, intracellular NADH and FAD etc. in the 400-600 nm range induced by excitation with 764 nm. Two multiphoton spectroscopic studies in the oral mucosa includes a study by Zhuo et al. who reported multiphoton autofluorescence spectroscopy of normal oral mucosa (77) with a characteristic primary 'blue-green' emission peak centered at 485-495 nm occurring at the epithelium with 810 nm excitation. The primary emission from epithelium was attributed to the metabolic cofactors NADH and FAD. Edward et al. reported MPAS in oral dysplasia and established the potential to identify redox potential differences between normal and OED mucosa as well as showed parallels to traditional single photon spectroscopy assessments in oral neoplasia but did not examine squamous cell carcinoma (SCC) (53). This study, evaluating emission wavelengths from 400-650 nm arising from excitation wavelengths ranging from 780 to 890 nm found that a significant decrease in autofluorescence intensity occurs with dysplasia, consistent with literature in single photon autofluorescence spectroscopy, and demonstrated depth-dependent redox which was maximal in the basal layer. Additionally, spectral shifts in the primary blue-green peak comprising signatures from the metabolic coenzymes NADH and FAD were found to occur, with the greatest change occurring in both superficial and basal epithelium at 780 and 800 nm excitations.

In each of these studies investigations focused on the primary emission within the 400-600 nm range, with major signatures attributed to NADH and FAD. NADH and FAD play a major

role in cellular metabolism and as mentioned above may be used to extract an optical redox value. Another important metabolite that has not been evaluated in epithelial neoplasia using MPAS is protoporphyrin IX (PpIX), a highly autofluorescent metabolic intermediate of heme biosynthetic pathway and characterized by a sharp peak centered at 635 nm (134, 135) when excited by blue light in the single-photon fluorescence scenario. PpIX has been reported to contribute to changes in autofluorescence with neoplasia and in at least one single-photon fluorescence spectroscopy study was investigated for noninvasive detection of oral precancerous lesions. With cancer becoming increasingly recognized as a metabolic disease, the ability to extract signatures arising from key metabolites could lead to improved detection strategies. For example changes in PpIX are reported to occur in hypoxia (136). Varying degrees of hypoxia leads to deregulation of mitochondrial and cytosolic metabolism (137) hence altering intracellular proportions of NADH, FAD and PpIX. Thus enhanced knowledge of these fluorophore contributions to imaging signals could help with improved understanding of the tumor microenvironment as well as identification of new optical markers indicative of OED or SCC.

#### **4.1.1 Goal of the current study:**

The overall goal of this study was to evaluate multiphoton spectral characteristics specifically from neoplastic epithelial cells (focusing primarily on the intracellular cytosolic space) in both OED and OSCC. Here I report my findings on autofluorescence changes in a hamster model of neoplastic oral mucosa using *in vivo* multiphoton spectroscopy (MPAS). Following are the specific goals of this study:

- 1) Evaluate the spectral characteristics of the cytosolic space of OED and early OSCC epithelial cells in the spectral range from ~425-650nm, encompassing a) the broad blue-green autofluorescence peak attributed to the coenzymes NADH and FAD (~460-560 nm) as well as b) the red spectral peak (~630 nm) for PpIX fluorescence in neoplastic tissue.
- 2) Extracted quantitative values from spectra at these two regions, including a ratiometric blue-green and red metric.

Knowledge gained from these MPAS characteristics will be helpful to future studies examining the contributors to the microscopy images obtained by multiphoton autofluorescence microscopy explored in Chapters 2 and 3. Further they could contribute to the growing body of knowledge regarding changes in metabolic signatures with neoplasia and could be extended for 1) basic scientific questions regarding spectral/metabolic alterations in transformation and 2) identifying new spectral/image based metrics of dysfunction in neoplasia.

## **4.2 Materials/Methods:**

**4.2.1 Animal Model:** All studies were approved by the Institutional Animal Care and Use Committee at the University of Texas Medical branch. Hamster models for oral neoplasia and inflammation described in previous chapters were used for the studies presented in this chapter. Control (n=5) and DMBA treated (n=17) hamsters were subjected to *in vivo* multiphoton imaging and spectroscopy. Areas for microscopy and spectroscopy were selected based on visual inspection. Multiphoton imaging and spectroscopy from 21 control, 11 dysplasia and 10 SCC sites were performed. Imaged sites were biopsied, fixed in 10% neutral buffered formalin and H&E stained for histopathological grading.

**4.2.2 Microscopy/Spectroscopy:** A previously described (Chapters 2 and 3) custom-built MPAM system with an incorporated spectrometer was used for this study (53). Regions of interests (ROIs) were determined using a 10X, 0.3NA air objective (Plan-Neofluar) with a long working distance, while a 40X 1.2NA C-Apochromat water immersion objective was used for both multiphoton microscopy and spectroscopy. The spectrometer contained a spectrograph (Acton Research Corporation, Spectra Pro 150) and a calibrated EM CCD (Newton, Andor, Ireland) for detection and recording of spectra. For each site, multiphoton fluorescence image was taken from the epithelium at 780nm excitation and ROIs for spectroscopy were selected based on the images. Multiphoton spectroscopy was performed on ROIs selected from cytoplasm in epithelial cells using 780 nm excitation and autofluorescence spectra were collected with a spectral resolution of 0.1 nm per pixel in the spectral window of 200-700 nm and an integration time of 10 seconds. The entrance slit separation was 0.25 mm for all measurements and a 300 g/mm grating was used. The system was calibrated using a Mercury-argon light source before experiments were performed. Spectral properties of all optical parts of the system were determined and used for correction of all emission spectra. Recorded spectra were background corrected and processed for removal of sharp spikes due to cosmic rays. A flat field correction was also performed for the wavelength dependence of the CCD camera using standard fluorophores. A translation mirror was used to direct fluorescence emission from sample to either the PMT for microscopy or the spectrometer.

**4.2.3 Histopathology:** For histopathological grading, H&E stained sections were imaged using an Olympus IX71 inverted brightfield microscope with a 20X, 0.75 NA air objective.

Grading was performed according to WHO criteria for oral premalignant and malignant lesions (100). Mild, moderate and severe dysplasia were categorized into one OED group.

**4.2.4 Data Analysis:** Data was processed using codes written in Matlab. Single factor ANOVA followed by Tukey's post hoc test for  $p < 0.05$  (\*) and  $p < 0.01$  (\*\*) was performed to assess statistical significance of intensity differences between groups.

### 4.3 Results:

Representative images from in vivo multiphoton autofluorescence microscopy (MPAM) of hamster oral epithelium are shown in Fig. 4.1 for 780 nm excitation. Since the source of autofluorescence in epithelial cells are primarily NADH and FAD which are abundant in cytoplasm, these cells are visualized as dark ellipsoidal nuclei surrounded by bright cytoplasm (Fig. 4.1a “\*” and “→” respectively). Moderate dysplasia (Fig. 4.1b) and SCC (Fig. 4.1c) epithelium showed an overall nuclear enlargement (“\*” in Fig. 4.1b), nuclear and cellular pleomorphism with progression of neoplasia when compared with control epithelium (Fig. 4.1a). Uniform organization of epithelial cells was seen in control epithelium while dysplasia and SCC was indicated by loss of cellular arrangement and atypical distribution of large and small nuclei in single image planes. This is an indication of loss of epithelial differentiation leading to abnormal variation in nuclear shape and size. The SCC epithelium shows scattered bright signal

(Fig. 4.1c “→”) which is expected to originate from premature keratinization in undifferentiated epithelial cells. Images from MPAM were utilized to direct spectroscopic assessment and ROIs for MPAS were selected from clearly visible cytoplasm in the epithelium.

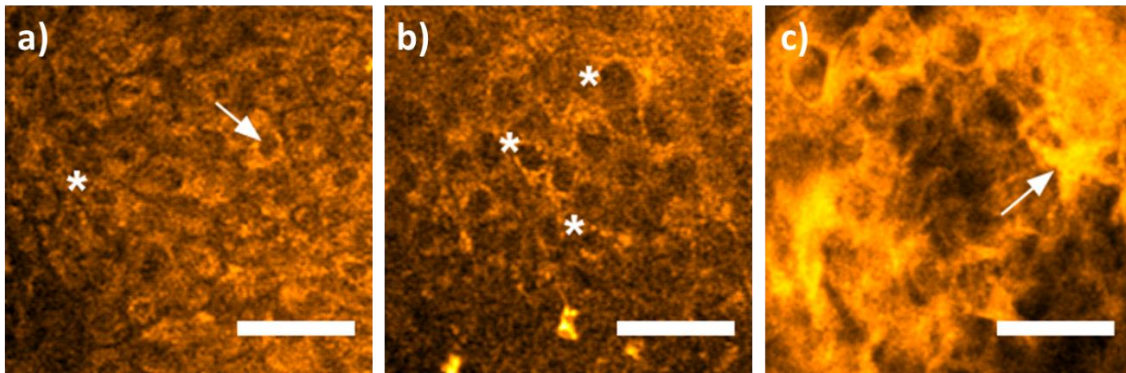


Figure 4.1: Two-photon autofluorescence images of control (a), moderate dysplasia (b), and SCC (c) epithelium at 780 nm excitation. “\*” and “→” in (a) indicates cytoplasm and nucleus respectively, and “\*” in (b) indicates pleomorphic nuclei. “→” in (c) indicates premature keratinization. Scale bar: 50  $\mu$ m.

Spectroscopic features of autofluorescence emission from the epithelium of control (blue), dysplasia (red and yellow) and SCC (green) are shown in Figure 4.2. Comparing these autofluorescence spectra it is evident that there are differences in spectral peak locations and intensities between control, dysplasia and SCC. Representative emission spectra recorded in the 400-650 nm spectral range indicates a broad peak centered around 480-520 nm for all three groups (Fig. 4.2a) of tissues. This blue peak is characteristic of cytoplasmic NADH and FAD autofluorescence and is typical for all epithelial tissues. Control epithelium showed one major peak in the blue spectral range and no further peak was seen at longer wavelengths. Dysplasia and SCC showed less autofluorescence in the same spectral range compared to control spectra. To compare spectral shape characteristic spectra from Fig. 4.2a were normalized to their peak

intensities and shown in Fig. 4.2b. Normalized spectra showed an overall red shift of the main blue peak in dysplasia and SCC. In dysplasia blue shifted spectra were also present, but the majority of samples were red shifted although the overall spectral line shape in the blue-green region stayed same for all three groups.

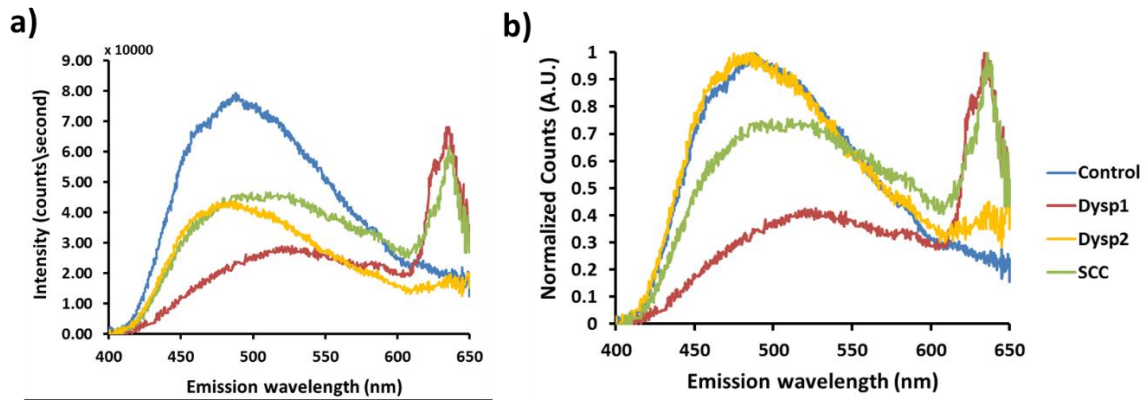


Figure 4.2: In vivo two-photon autofluorescence spectra obtained from control, dysplasia and SCC from epithelium of hamster cheek pouch mucosa using 780 nm excitation; (a) raw intensity profile showing comparison between control (blue), two representative dysplasia (red and yellow) and SCC (green) epithelium; (b) same spectra as in (a) normalized to their peak intensities.

Apart from the peak shift in blue-green spectral range a new peak at 635 nm at the wavelength expected for Protoporphyrin IX (PpIX) was evident in SCC and in some cases of dysplasia. It is clear from Fig. 4.2 that SCC produces more autofluorescence than control at 635 nm (red peak), which is expected to arise from PpIX fluorescence. Although, there was a large variation in absolute intensity it was the dominant peak in most SCC epithelium. Two representative spectra of dysplasia are shown in Fig. 4.2 where one is highly fluorescent (red) in the PpIX region while the other one (yellow) showed marginally increased fluorescence than



control in the same region. Nine out of ten SCC and six out of eleven dysplasia tissues evaluated showed this distinct secondary peak.

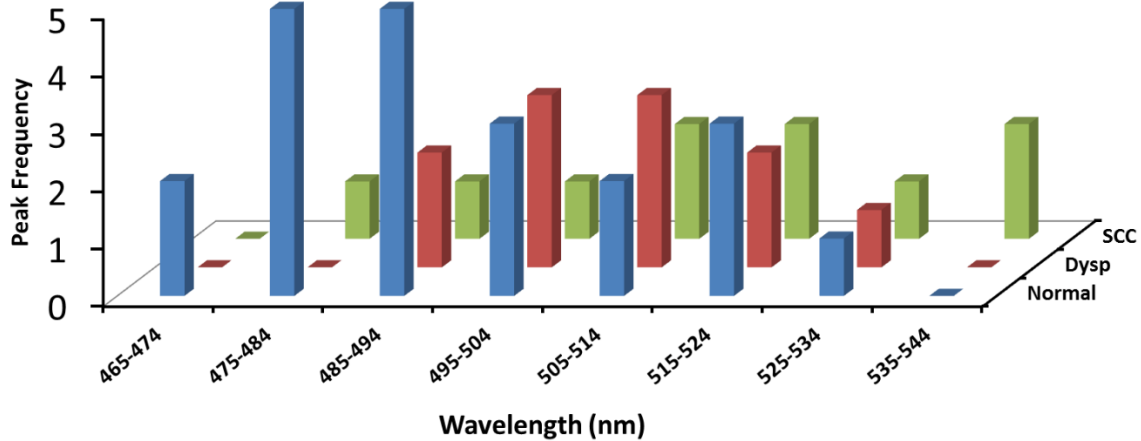


Figure 4.3: Distribution of autofluorescence peaks in the 456 nm to 545 nm ranges is shown for all three pathological groups. Histograms indicate most samples in the control (blue) group showed a blue-green peak in lower wavelengths while in dysplasia (red) and SCC (green) showed a wider distribution of the blue-green peak, which was often in the longer wavelengths than control.

A histogram distribution of blue-green autofluorescence peak for all three pathological groups is shown in Figure 4.3. As our data suggest there was a larger variation in peak distribution in dysplasia and SCC than in control (Fig. 4.3). Also, for most dysplasia and SCC, blue-green peaks were shifted to longer central wavelengths than control. Median blue-green peak for dysplasia and SCC were 513 nm and 514.5 nm respectively while for control tissue the blue-green peak was centered at 488 nm. Median peak location was used instead of average, since average peak was less reliable due to high within-group variance in dysplasia and SCC.

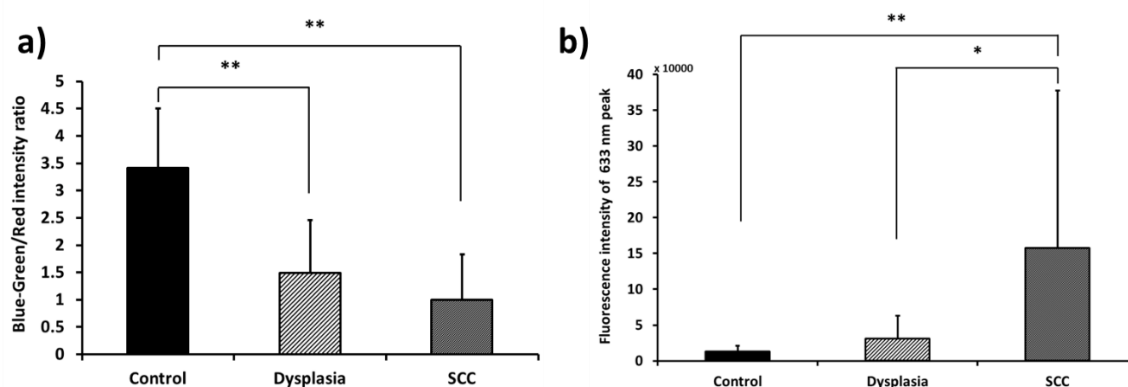


Figure 4.4: (a) Difference in peak fluorescence intensity at 635 nm emission between control, dysplasia and SCC; (b) Difference in blue/red intensity ratio between control, dysplasia and SCC. \*  $p < 0.05$  and \*\*  $p < 0.01$ .

Peak intensity of all samples at 635 nm emission wavelength was calculated and compared as shown in Figure 4.4a. SCC showed statistically significant increase in peak intensity from control and dysplasia. The standard deviation of 635 nm peak intensity in SCC was also very high presumably because of heterogeneity in the tumor microenvironment. In order to quantify relative change in fluorescence between blue (480-520 nm) and red (635 nm) fluorescence a ratio parameter was introduced which is shown in Fig. 4.4b. Since control tissue did not show the distinct secondary peak for PpIX, the blue/red intensity ratio in control was significantly higher than dysplasia and SCC. The 635 nm peak intensity alone (Fig. 4.4a) was sufficient to allow for differentiation between SCC and control tissue, but it was not sufficient to separate dysplasia and control. However, when used in conjunction with the blue-green peak intensity (Blue-green/Red intensity ratio) (Fig. 4.4b) the discrimination between dysplasia and control became greater and statistically significant.

## 4.4 Discussion:

The application of NLOM explored in this study goes beyond conventional microstructural assessment of neoplastic tissue and focuses on spectroscopic features of metabolic changes that are associated with neoplasia. With the origin of signals investigated being the cytoplasm of epithelial cells and spectral characteristic of NADH, FAD, and PpIX, obtained data showing alterations in these spectra could be indicative of intracellular metabolic deregulation, which is an important cancer hallmark. Results of this study demonstrate the potential of MPAS for delineating neoplastic (dysplastic and OSCC) from non-neoplastic oral mucosa based on spectroscopic signatures arising specifically from the metabolic deregulation in neoplasia. Observed spectroscopic changes included differences in intensities of fluorescence from these metabolites as well as spectral shifts in the NADH/FAD band in which the wavelength of the main emission peak changed between control, dysplasia and OSCC epithelium.

**4.4.1 Reduced NADH-FAD autofluorescence in oral epithelial neoplasia:** With excitation at 780 nm the overall autofluorescence intensity of epithelial cells in the blue-green spectral region was less in neoplastic tissue than control a finding that is consistent with the literature involving traditional single-photon fluorescence spectroscopy and imaging (138-140). Autofluorescence spectroscopy of neoplastic epithelium in the past has shown reduced fluorescence intensity in the blue-green spectral region (127, 141). This is particularly important in cancer research since the major contributors for autofluorescence in blue-green region are endogenous metabolic cofactors NADH and FAD (53, 142) and with the help of optical sectioning capability of MPAS we were able to localize these changes in the cytoplasm rather than in a large volume that is seen in single photon spectroscopy. Reduction in overall fluorescence

intensity in the blue-green emission window may be an indication of altered metabolic activities in dysplasia and SCC. Other likely scenarios for reduced fluorescence in single photon spectroscopy are epithelial thickening, remodeling of collagen in extracellular matrix, and increased hemoglobin absorption with increased microvascular density (129). Multiphoton spectroscopy ensures collection of spectral information isolated to an optical plane, such as the epithelium in this case, excluding contribution from these other factors.

**4.4.2 Spectral peak shifts in NADH-FAD autofluorescence:** Another feature observed in autofluorescence spectra in this study is a shift of the blue-green peak to longer wavelengths in dysplasia and SCC. Similar red shift in SCC was also reported in single photon autofluorescence spectroscopy for multiple excitation wavelengths ranging from 330 nm to 470 nm (129, 143). However, these studies did not evaluate peak shifts in dysplasia. Although in our study median peaks in dysplasia and SCC were red shifted with respect to control, average peak for dysplasia did not show significant red shift from control. In a previous study, our group reported a blue shift of the primary blue-green peak in moderate and severe dysplasia, rather than the red shift seen in SCC and in some cases of dysplasia (53). The direction of spectral shifts are likely a consequence of metabolic factors such as shifts to higher or lower redox potential (higher NADH relative to FAD in higher redox potential) which could vary in various microenvironments (e.g. hypoxia, nutrient availability). Another scenario that may result in shifts to longer wavelengths could be a thickened keratinizing layer with increased scattering from keratin (144). Future studies to further understand the noted shifts could examine these factors.

**4.4.3 Potential application to detection efforts:** While of a limited dataset the findings of this study indicate the potential for use of the blue-green/red ratio and red peaks for

indicating presence of neoplasia. This spectroscopic information will likely have to be combined with cytology and microstructural parameters such as those discussed in Chapters 2 and 3. As noted before spectral based metrics explored in this study could be indicative of alterations in metabolic activities during neoplastic transformation and thus may help identify molecular signatures in the native tissue environment. A combined effort with MPAM, SHGM and MPAS would therefore be able to provide cytologic, microstructural and biochemical information about neoplastic transformation which may be helpful in clinics for better delineation of neoplasia from normal mucosa or benign lesions.

#### **4.4.4 Autofluorescence spectra and potential relationship to study of metabolism:**

Since NADH and FAD are key players in mitochondrial metabolism, measurement of relative contribution of NADH and FAD from multiphoton spectra could inform about redox potential or metabolic status of individual epithelial cells. Multiphoton image based (145) and multiphoton spectroscopy based (53) estimation of redox potential has shown promise in ex vivo and in vivo studies of oral neoplasia. However, beyond estimation of redox potential multiphoton autofluorescence spectra may be correlated to an important cancer hallmark, deregulation of energy metabolism. Alteration in relative amount of NADH and FAD autofluorescence could indicate alterations in activities of glycolysis, TCA cycle and oxidative phosphorylation and eventually provide cues to cancer hallmarks such as metabolic defects characteristics of neoplastic development. Recent studies in ex vivo engineered tissue and skin have explored the relationship of detected NADH from MPAM images with such metabolic contributors (52, 97).

**4.4.5 Cytoplasmic autofluorescence spectra showed presence of PpIX:** A sharp peak at 635 nm was present in all OSCC and a subset of dysplasia samples. This emission peak matches

the expected wavelength and shape of PpIX, reported extensively in the literature for single photon autofluorescence spectroscopic detection of oral neoplasia (141, 143, 146). An expected secondary peak at 705 nm was not detected in the optical setup as optical components in this system blocked detection of fluorescence above 650 nm. PpIX fluorescence has not previously been reported by the method of multiphoton imaging or spectroscopy. In the past, increased red fluorescence typically within 630-640 nm has been observed in SCC (127, 129, 141) with single photon excitation at 405 nm or 410 nm. De Veld et al. showed the presence of a peak at 638 nm in the center of tumors but not in the periphery where tissues were dysplastic or benign (141, 147). These are attributed to PpIX. Since typical single-photon fluorescence samples volumes of tissue that encompass epithelium and sub-epithelium together, many have attributed PpIX fluorescence in tumors from animals and humans has been demonstrated to be of bacterial origin. The PpIX fluorescence has also been suggested to be of endogenous origin since bacterial cultures from tumors with this characteristic red fluorescence did not show the characteristic PpIX fluorescence (148). Instead, tumors injected with these organisms produced PpIX fluorescence, which indicated requirement of a host-microbe interaction. Finally, endogenous PpIX which is produced in mitochondria of epithelial cells has also been shown to be altered in oral cancer (134, 149, 150) and is supported by our spectroscopic assessment of cytoplasm of neoplastic epithelial cells.

**4.4.6 Intracellular dynamics of NADH, FAD and PpIX in a heterogeneous tumor microenvironment:** Three important metabolites described above, NADH, FAD and PpIX, may be correlated and interdependent based on the tumor microenvironment and metabolic status. In tumors, due to hypoxic microenvironment energy production primarily relies on glycolysis

(Warburg effect) while more energy efficient mitochondrial metabolic processes are downregulated (151). As a result, neoplastic cells show increased levels of NADH leading to a loss of the tight regulation of NADH/FAD balance and altering the autofluorescence spectra. On the other hand depending on the degree of hypoxia neoplastic tissues might be severely deprived of nutrients leading to downregulation of glycolysis and activation of mitochondrial metabolism. Energy production in these cases relies on carbon sources other than glucose such as glutamine (152). As a result, the NADH/FAD balance is affected with oxidation of NADH and  $\text{FADH}_2$ . Since PpIX is also produced in the mitochondria, and known to be altered by hypoxia, relative amounts of cellular NADH, FAD to PpIX is expected to fluctuate as a result of the hypoxic nature. Further understanding of how variations in tumor microenvironment affects the levels of NADH, FAD, PpIX and the overall autofluorescence spectra can be examined in future studies. For example, studies could be conceptualized that examine the effect of hypoxia on these signatures, akin to studies examining effects on NADH signatures under hypoxic conditions (52, 97).

In conclusion, this study describes MPAS characteristic features of epithelial cells in OED and OSCC *in vivo* tissues, and showed that spectral parameters differed in a statistically significant manner between normal and neoplasia. These parameters could potentially be incorporated into MPM methods to evaluate presence of neoplasia, potentially coupled to imaging presented in Chapters 2 and 3. Of note, the study found an emission peak at 635 nm, which we attribute to PpIX which also was helpful in delineating neoplasia from normal. The PpIX-like fluorescence was identified in the cytoplasm of neoplastic epithelial cells, indicating an endogenous origin of this fluorophore. Characterization of spectral properties for dysplasia and

SCC epithelium using multiphoton excitation may serve as a platform for future studies combining MPAM and MPAS for multimodal detection of epithelial neoplasia. Further development to extract contributions from individual metabolites of NADH, FAD, and PpIX may also be helpful for examining the tumor metabolic microenvironment including potentially studying heterogeneities that are known to occur. Future efforts in this area should be focused on examining areas beyond cells to study heterogeneities that likely exist within neoplastic areas and better characterize the OED and OSCC neoplastic microenvironment.

**Acknowledgements:**

The work of this Chapter has been submitted and reviewed for publication and is in revision. I would like to thank Dr. Kert Edward for his contributions in building the MPAS instrumentation for spectroscopy and for data acquired for this study.



## **Chapter 5**

### **Large Area (Wide-field) Autofluorescence (WF-AF)**

### **Imaging in the Hamster Model for Oral Epithelial Neoplasia**

#### **5.1 Introduction:**

NLOM as described in previous chapters provided microstructural and biochemical metrics for detection of oral neoplasia that performed with high sensitivity and specificity even in presence of benign conditions. Sensitivity and specificity values greater than 85% were found for promising parameters. However, as evident, NLOM is a microscopic method and is thus limited in field-of-view, restricting the potential use for on-site screening for neoplastic abnormalities over the areas needed for clinical translation (on the order of cm). Large area imaging methods that could potentially be applied in conjunction with *in vivo* NLOM were explored in this chapter. A desired method should have high sensitivity to locate areas of suspicion since MPAM is expected to provide high Se and Sp. The efforts in this chapter were designed to test the performance of wide-field autofluorescence (WF-AF) alone in detecting

altered fluorescence properties of neoplastic tissue and for potential further exploration in Chapter 6 where it was studied alongside NLOM. The current chapter will discuss the findings on wide-field autofluorescence imaging method which is based on changes in autofluorescence in the green and red spectral regions.

Several adjunct methods to white light examination of oral precancers and cancers have been proposed so far including methods based on wide-field reflectance and fluorescence. One such method was provided by ViziLite (Zila Pharmaceuticals, Inc., AZ, USA) which utilized blue light illumination with detection of reflected light for indication of oral lesions. Epstein et al. and Kerr et al. performed initial studies on performance of ViziLite and reported multiple lesions being identified with the help of ViziLite that were not detected by conventional white light examination (153, 154). However, others have reported no change in diagnosis with or without the use of ViziLite (155). Lesions identified with ViziLite were also detected in white light examination and it was demonstrated that differentiation between benign lesions and premalignant or malignant lesions was not possible, which remained an important issue in oral cancer diagnosis even in the present clinical setup (1).

Alternatively detection of tissue autofluorescence has shown promise as an adjunct method to improve contrast between normal and neoplastic tissue. There are a variety of inherent fluorophores in the epithelium or stroma that show fluorescence properties when excited by UV or visible light and can be detected even with the naked eye. As discussed in previous chapters, it is well known that tissue autofluorescence is sensitive to functional and structural changes associated with neoplastic transformation in the oral mucosa. A US FDA approved clinical device named VELscope (LED Dental, Inc., White Rock, BC, Canada) was

introduced to improve discrimination of neoplastic tissue from surrounding normal oral mucosa. The working principle of this device is based on the fact that neoplastic tissue shows significantly less autofluorescence across a variety of excitation wavelength in the UV and visible region. The loss of autofluorescence is typically attributed to the loss of crosslinks in the collagen matrix underneath the neoplastic oral epithelium (27). However, fluorescence spectroscopic studies as described in the previous chapter also shows loss of autofluorescence from cellular NADH and FAD under conditions of neoplasia or preneoplasia (129). Lane et al. (156) conducted a study in 2006 to assess the performance of VELscope in direct visualization of oral precancerous lesions and found a sensitivity of 98% and specificity of 100%.

However, follow up studies suggested that there was no difference in outcome between VELscope and white light examination (157). Importantly, 72% lesions with reduced fluorescence identified through VELscope were diagnosed as benign or inflammation making differentiation of benign lesions from true neoplasia difficult. In a recent study by Mehrotra et al. the sensitivity and specificity of VELscope was found to be merely 50% and 38.9% respectively (158) raising questions about the performance of this adjunct tool especially in presence of benign conditions, a significant one being inflammation. Therefore, the literature indicates VELscope may be useful for surveillance of lesions identified by COE, but further research is still required to establish its value as a general screening tool. It is also noted that existing commercial devices based on single 'color' fluorescence rely solely on visual information without quantification and outcomes are dependent on the experience level of the examiner.

Improvements to commercial devices may include methods for improved quantification as well as incorporation of multiple emission bands representing different

fluorophores, in a sense akin to spectroscopic studies. Recent efforts in humans have in fact shown improvement is possible in WF-AF imaging by collection of red and green autofluorescence with quantification of these signals relative to each other (31, 159, 160). In a study involving human subjects normalized red-to-green fluorescence intensity ratio resulting from 405 nm excitation, was shown to have the highest performance in differentiating dysplasia and OSCC from normal oral mucosa compared to values related to single wavelength emission. Although highly promising, these results did not account for the benign conditions that are typically associated with neoplastic oral mucosa. Loss of autofluorescence in the green spectrum is usually associated with reduced collagen cross links in the stroma as well as changes in relative amounts of NADH and FAD in the epithelium. Additionally, neoplastic tissue showed increased fluorescence in the red spectrum and while not identified as such in these studies could have been due to accumulation of protoporphyrin IX (PpIX) discussed in Chapter 4.

### **5.1.1 Goal of the current study:**

The overall goal of this study was to explore the potential of wide-field autofluorescence (WF-AF) imaging to detect neoplastic changes in oral epithelial tissue *in vivo* with the long term vision being potential combination with *in vivo* NLOM for a bimodal and multiscale imaging approach in early detection of oral epithelial neoplasia. This chapter presents WF-AF imaging results on detection of OED and OSCC with groups also representing benign inflammation. Following are the specific studies performed:

- 1) Establish the use of red-to-green autofluorescence (R/G) in detection of control and neoplastic tissue in the hamster model for OED and OSCC, setting the stage for combination of WF-AF with microscopic approaches explored in early chapters.
- 2) Assess the performance of WF-AF in experiments that included inflammation as a benign condition as well as neoplasia, using receiver operator curve (ROC) statistics to determine potential sensitivity and specificity. The inclusion of the inflammation group is important to begin exploring advantages and limitations of explored methods.

## 5.2 Materials/Methods:

**5.2.1 Animal Model:** Hamster models for oral neoplasia and inflammation described in previous chapters were used for the studies presented in this chapter. Control (n=7), inflammation (n=4) and DMBA treated (n=13) hamsters were subjected to *in vivo* WF-AF imaging.

**5.2.2 WF-AF Imaging System:** A diagram of the custom built WF-AF imaging system is depicted in Fig. 5.1. A collimated LED light source (M405L3-C1, ThorLabs, Newton) with 405 nm emission was used as source of excitation. The excitation beam was directed on the sample by placing a dichroic filter (510 nm LP) at 45° angle to the imaging surface. Fluorescence emission from samples were collected through a 435 nm LP filter and images were captured using a color Nikon DS Fi1 camera attached to a AF Micro NIKKOR 60mm 1:2.8 lens. With the current system a ~5cm diameter illumination field was achieved which was sufficient to image most hamster cheek pouches except the edges of the field of view (FOV).

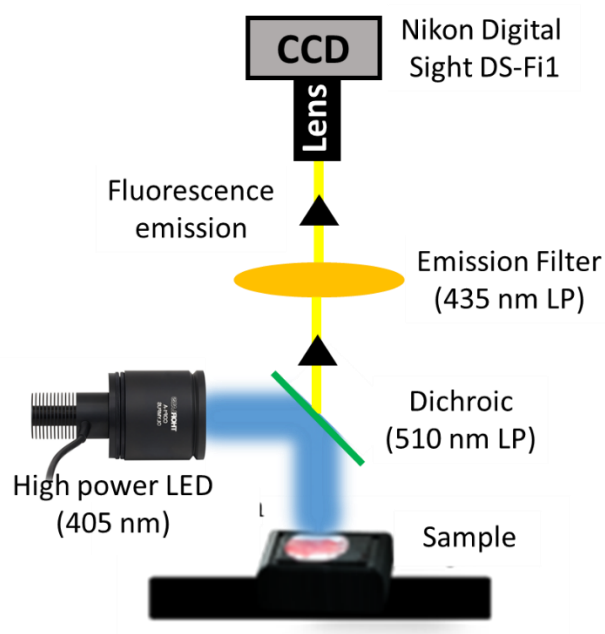


Figure 5.1: Diagram of the WF-AF imaging system for live hamster cheek pouch imaging.

**5.2.3 *In vivo* WF-AF imaging:** Hamsters were anesthetized and cheek pouch were prepared for *in vivo* imaging using methods described in chapter 2. The exposed cheek pouch was placed directly under the dichroic filter and autofluorescence images were captured as 24 bit RGB images for 405 nm excitation. Multiple images with several exposure and gain settings were captured for each cheek pouch and the image with least number of saturated pixels was selected for analysis. A part of the sample holder that was used to hold the mucosa tissue was imaged each time which served as an internal control for any variation in illumination and used for normalizing intensity measurements. White light images of the cheek pouch were also captured with room light as reference to localize and record sites of biopsy and image analysis.

**5.2.4 Image Analysis:** Captured WF-AF images were opened in ImageJ and red and green channels were separated using the Bayer mask of the camera. The following criteria were used for selection of sites for analysis:

- 1) Sites with visible tumors, increased autofluorescence in red channel, basal level autofluorescence (to test for false negatives) in red channel
- 2) White light visual examination: sites were selected based on surface roughness, color or swelling with or without guidance by WF-AF
- 3) Location on the cheek pouch: sites near the edges of the pouch or any injury caused during sample preparation for imaging were avoided
- 4) Sites contaminated by blood (advanced tumors tend to bleed easily) were avoided
- 5) Folds in tissue: sites with visible folds were excluded from analysis

Based on these criteria, 3-5 sites were selected from each cheek pouch providing 86 sites (36 control, 15 inflammation, 25 dysplasia and 10 OSCC) for analysis. Three regions of interests (ROIs) of size 20x20 pixels were created within each site and average intensities in each ROI for red ( $I_{R1}$ ,  $I_{R2}$ ,  $I_{R3}$ ) and green ( $I_{G1}$ ,  $I_{G2}$ ,  $I_{G3}$ ) channels were measured. A ratio of red to green intensities for each ROI ( $I_{RG1}$ ,  $I_{RG2}$ ,  $I_{RG3}$ ) were then calculated. Similarly, five ROIs were created and red to green intensity ratios were measured ( $I_{C-RG1}$ ,  $I_{C-RG2}$ , ...  $I_{C-RG5}$ ) within the sample holder region that served as an internal control in this study. An average red to green intensity ratio ( $[\sum I_{C-RG1} + I_{C-RG2} + \dots + I_{C-RG5}]/5$ ) of the internal control was then used as a normalization factor to normalize red to green intensity ratios ( $I_{RG1}$ ,  $I_{RG2}$ ,  $I_{RG3}$ ) measured from tissue sites. This normalization step was performed by dividing the individual red to green (R/G) intensity ratio of each ROI by the average R/G intensity ratio of the internal control. The resulting normalized R/G intensity ratio

for three ROIs from each site were averaged to obtain the normalized R/G intensity ratio ( $I_{RG, Norm}$ ).

**5.2.5 Statistical Analysis:** Statistical comparisons between groups were performed using methods described in previous chapters. Briefly single factor ANOVA followed by the Tukey's *post hoc* test were performed with  $P < 0.05$  considered significant ( $P$  value of  $< 0.05$  is represented by a single asterisk '\*' and  $P < 0.01$  by double asterisk '\*\*'). Receiver operator characteristic (ROC) curves were generated using SAS software (SAS Institute Inc.) to calculate area under the curve (AUC), sensitivity and specificity.



### 5.3 Results:

The resolution of the WF-AF imaging system was tested by imaging a U.S. Air Force (USAF) resolution target. A photograph of the resolution target is shown in Fig. 5.2. Line spacing of 24.8  $\mu\text{m}$  in group 4 and element 3 was easily discriminated at the highest magnification. The shadow at the back of the elements is due to the thickness of the target and not inherent to the imaging system.

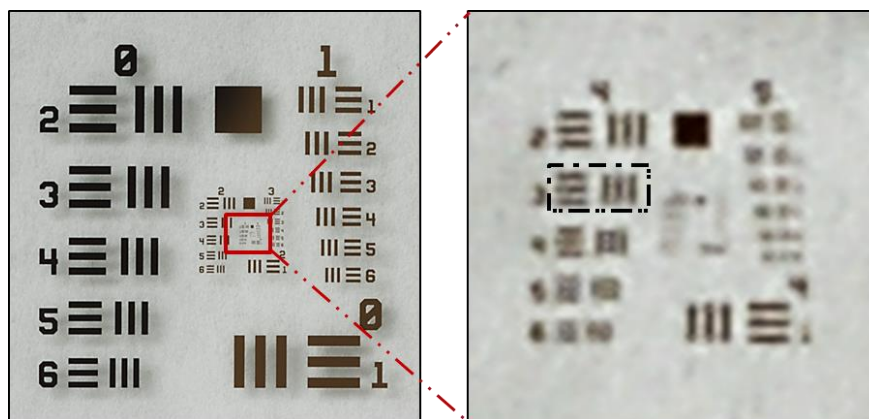


Figure 5.2: USAF resolution target (left) with zoomed in image on the right shows line spacing at group 4 and element 3 (dotted outline) was easily discriminated.

White light visual examination followed by WF-AF imaging in the hamster cheek pouch model revealed several unique autofluorescence features of individual tumors and precancerous lesions. Preliminary screening of the cheek pouch using a white light examination (Fig. 5.3a) identified several large and small exophytic tumors (indicated by arrows) which were also visible in the WF-AF image (Fig. 5.3b) except for few necrotic tumors (Fig. 5.3a; yellow arrow). The necrotic tumors showed up as non-fluorescent dark regions while non-necrotic tumors were highly fluorescent in the red channel (Fig. 5.3c; outline white box). The green

channel (Fig. 5.3d) in general showed low fluorescence. Only red and green channels are shown since the major fluorescence changes have been suggested to occur in these two spectral regions and the excitation wavelength (405 nm) is in the blue channel.

In addition to the obvious non-necrotic tumors certain areas adjacent to the tumors became visible in the red fluorescence channel (Fig. 5.3b and 5.3c; marked '\*'). These previously unidentified and potentially neoplastic areas were confirmed to be dysplasia by the gold standard histopathology. The cheek pouch mucosa also contained clinically normal areas with no observable variation in fluorescence in either channel (Fig. 5.3b, 5.3d and 5.3d; dotted white box). These areas were diagnosed as normal after histopathological grading.

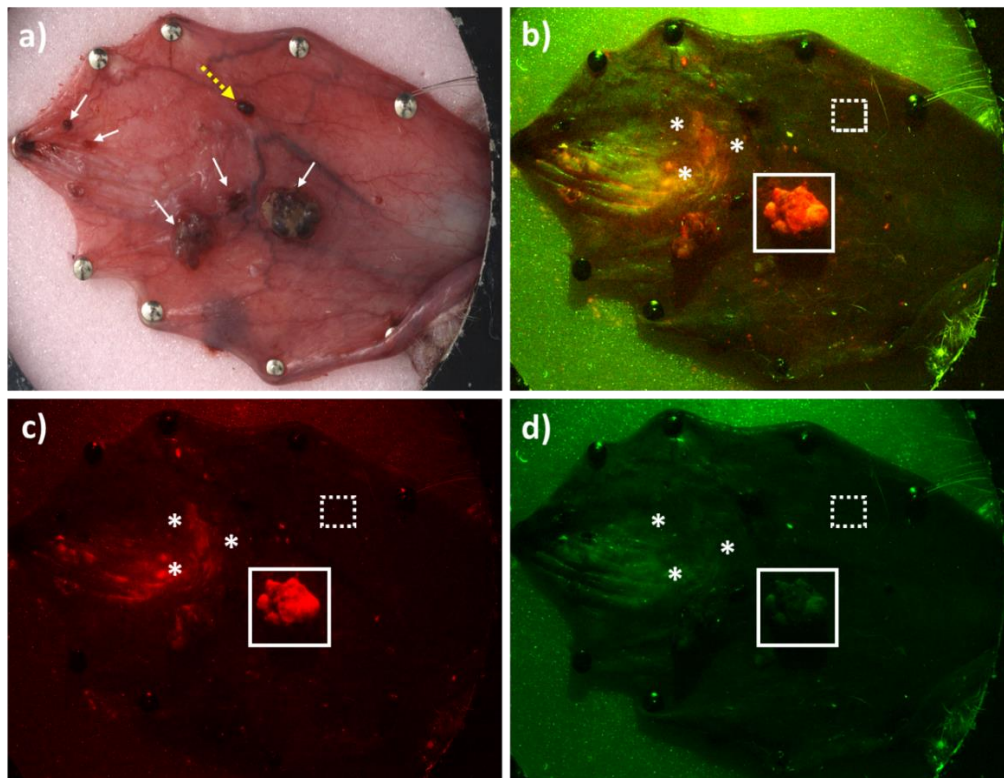


Figure 5.3: Representative white light and WF-AF images of a DMBA treated hamster cheek pouch are shown. a) White light image; b) composite of red and green autofluorescence; c) red autofluorescence and d) green

autofluorescence. Examples of a large tumor (white box), dysplasia ('\*'), a necrotic tumor ('yellow dashed →'), several other exophilic tumors ('solid arrows') and a normal area (dashed box) are outlined.

Figure 5.4 shows representative white light and WF-AF images from a control and an inflamed cheek pouch mucosa. Although the difference between the control and the inflamed mucosa (Fig. 5.4a and 5.4c) based on white light visual inspection was not as pronounced as was seen in the DMBA treated mucosa, the surface of the inflamed mucosa showed increased roughness and the color changed from light pink to more reddish tone. Since the inflammation model involved application of SLS to the entire cheek pouch inflammation was seen to occur throughout the mucosa. WF-AF imaging the control mucosa (Fig. 5.4b) showed little to no fluorescence in the red channel while the entire mucosa exhibited moderate green fluorescence with no variations within different areas. Therefore there was no apparent contrast between areas in the control cheek pouch mucosa when looked at the red-green intensity images. On the contrary, there was slight increase in red fluorescence in the inflamed mucosa which can be seen in the Fig. 5.4d as a reddish hue as compared to the control mucosa (Fig. 5.4b).

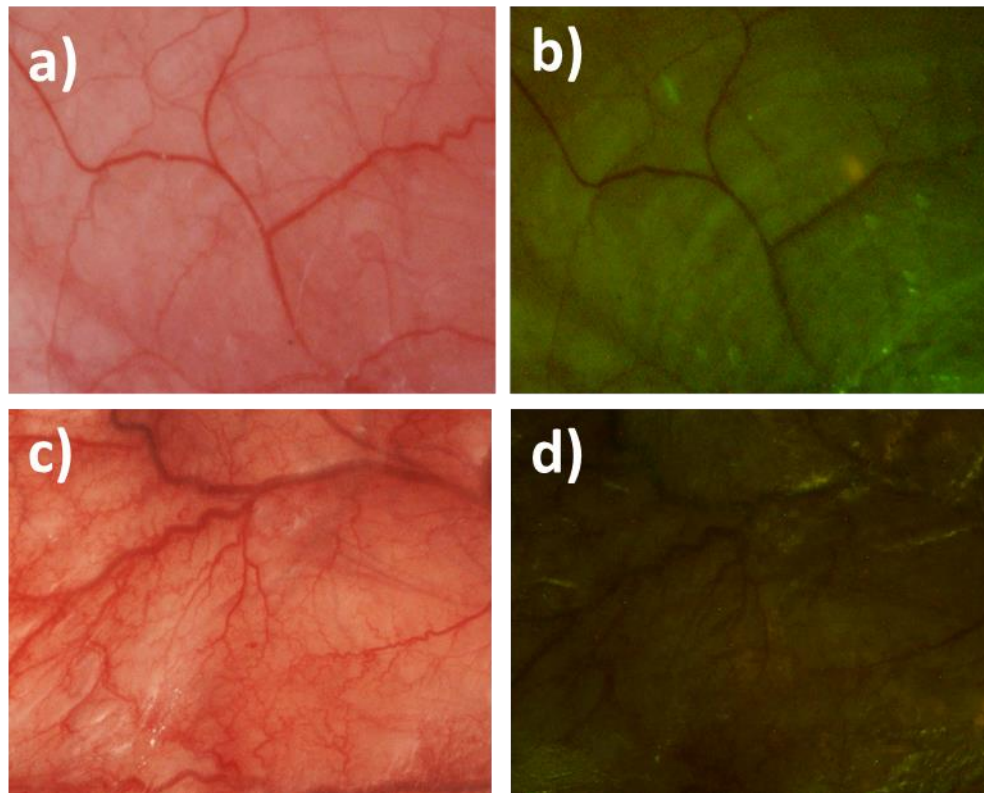


Figure 5.4: (a) and (b) are representative white light and WF-AF images respectively of a control cheek pouch mucosa. (c) and (d) shows white light and WF-AF images respectively of an inflamed cheek pouch mucosa.

The results for normalized R/G intensity ratio measurement is shown in the bar graph in Fig. 5.5. Averaged  $I_{RG, norm}$  was plotted for each group and results showed a gradual increase in  $I_{RG, norm}$  from control to inflammation to dysplasia and SCC with SCC having the highest  $I_{RG, norm}$ . It was noted that the standard deviation for dysplasia and SCC groups were also very high. The increase in  $I_{RG, norm}$  for dysplasia and SCC from control tissue was statistically significant however there was no significant difference between dysplasia and SCC based on quantitative assessment of WF-AF imaging. The  $I_{RG, norm}$  for inflammation was also higher than control, however, it was not statistically significant and the average value was in between control and dysplasia. It was expected that this would complicate the differentiation of control and dysplasia

and therefore an ROC analysis was performed with or without the presence of inflammation in the study group.

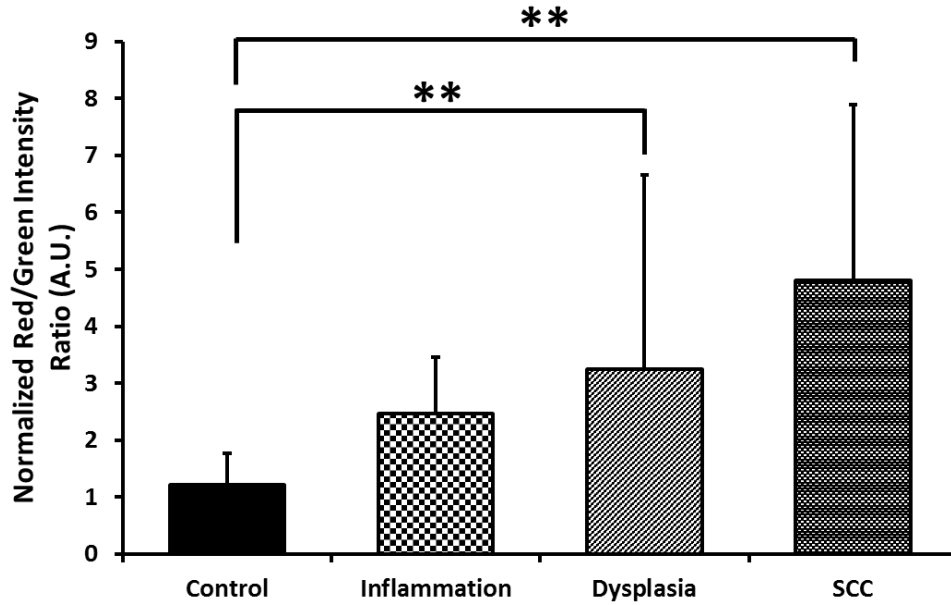


Figure 5.5: Normalized R/G intensity ratio is shown for control, inflammation, dysplasia and SCC tissue. \*\*  $P < 0.01$

The following data sets were created for ROC curve analysis to calculate performance of the WF-AF image parameter  $I_{RG, \text{norm}}$  in distinguishing normal/control oral mucosa from neoplastic oral mucosa;

1. Normal (Control) and neoplastic (dysplasia and SCC)
2. Normal (control and inflammation) and neoplastic (dysplasia and SCC)

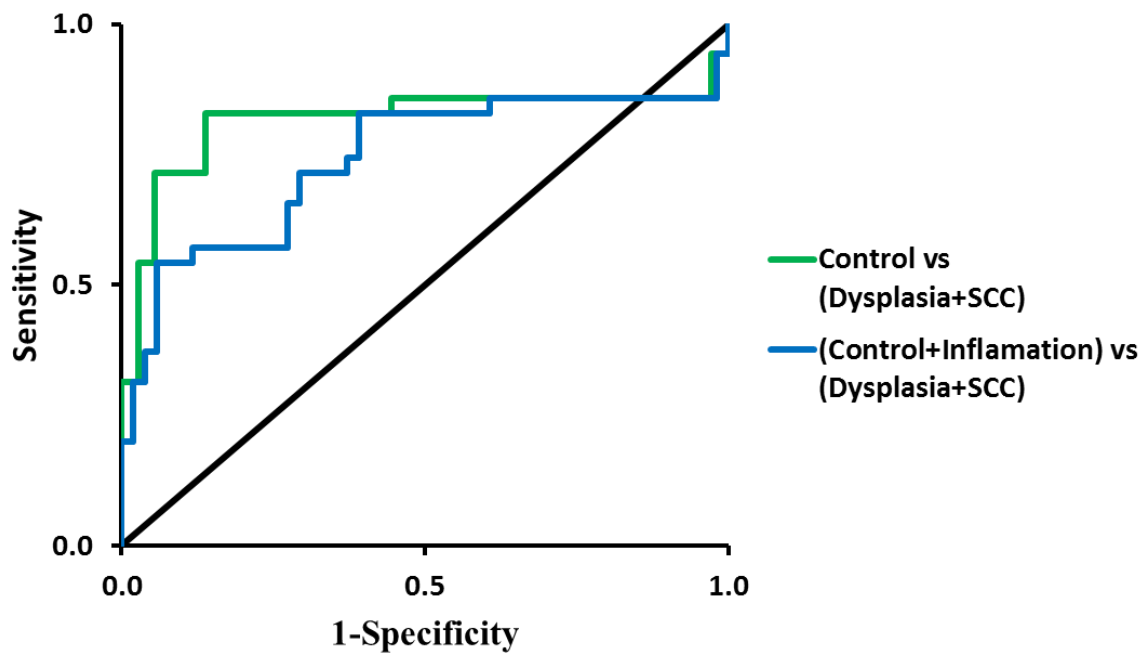


Figure 5.6: ROC curves showing the performance of the WF-AF imaging with (blue curve) or without (green curve) the inclusion of inflammation in the study.

ROC curves showed (Fig. 5.6) significant loss in performance when inflammation was present (blue curve) compared to when inflammation was excluded (green curve) from the study. This loss in overall performance can be appreciated from the area under the curve (AUC) values shown in table 5.1.

Table 5.1: AUC, sensitivity and specificity for normalized R/G values with or without the presence of inflammation in the study group.

Group	AUC	Sensitivity (%)	Specificity (%)
Control vs (Dysplasia + SCC)	0.82	83	86
(Control + Inflammation) vs (Dysplasia + SCC)	0.74	83	61

Neoplastic abnormalities were often associated with increased red fluorescence and high R/G values (Fig 5.3b), but several false positives based on visual identification of lesions were obtained and quantitative analysis showed poor-moderate discrimination (AUC: 0.815 and 0.739 without and with benign condition/inflammation respectively) by WF fluorescence alone. Sensitivity/Specificity as calculated (Table 5.1) from ROC curves showed high sensitivity (83%) with or without benign conditions (inflammation), but poor specificity when inflammation was included (only 61%) in the study set compared to without inflammation (86%).

## 5.4 Discussion:

WF-AF imaging is a label-free imaging technique that indicates alterations in tissue autofluorescence associated with neoplasia at a macroscopic scale which is typically in the order of several centimeters in contrast to previously described NLOM or other optical microscopy techniques that operates at a much smaller scale (few hundred microns). Therefore, if sufficient sensitivity and specificity is shown, WF-AF imaging could potentially be employed as a noninvasive screening method adjunct to white light inspection for oral epithelial abnormalities. Results presented in this chapter show significantly elevated red/green intensity ratio for dysplasia and SCC from control and based on only neoplastic and control mucosa reasonable discriminating power of  $I_{RG, norm}$  parameter was observed. However, inclusion of inflammation in the control group, to mimic a more realistic situation of the actual clinical problem, reduced the performance of the WF-AF based method significantly indicating WF-AF imaging alone may not

have the discriminating power to separate neoplastic from non-neoplastic oral mucosa with high degree of accuracy.

**5.4.1. Complications of white light clinical diagnosis with benign conditions:** White light visual examination of the hamster oral precancer/cancer revealed typical clinical features of neoplasia such as small or large exophylic tumors, red or white colored lesions with no visible outward growth, thickened and fragile surface keratinization and areas of increased surface roughness. Histopathological diagnosis revealed that certain visual features such as surface roughness, fragile keratinizing layer, discolored epithelium etc. could potentially indicate both neoplasia as well as benign conditions like inflammation or hyperplasia. The animal model for inflammation used in this study corroborates this observation by presenting cheek pouches with rough surfaces and altered color. This is a limitation of white light examination that has been pointed out again and again in the literature (161-163) with numerous efforts being put into optical fluorescence imaging (164). Inflammation and other benign conditions impose a limitation in clinical diagnosis because of their similar appearance to early neoplastic oral lesions. A clinical data survey in 2012 indicated that ~75% oral biopsies at the University of Texas Dental Branch were pathologically normal or benign (27) highlighting the need for adjunct noninvasive methods for screening of oral lesions.

**5.4.2 Autofluorescence induced by blue light excitation:** It has been previously reported by several groups that with blue light excitation (400-460 nm) tissue autofluorescence changes during neoplastic transformation and could provide a useful adjunct to white light inspection in screening of high-grade oral lesions (147, 165, 166). Fluorescence induced by blue light showed superior contrast of oral lesions than a conventional white light visual examination.



Reduction in green autofluorescence with blue light excitation often extended beyond clinical tumor margins up to 25 mm as seen in a study by Poh et al. (167). In this study 405 nm excitation wavelength was used to test autofluorescence changes in neoplasia following indication in the literature (159) that it could provide improved contrast between normal and neoplastic tissue over other blue light excitations.

**5.4.3 Elevated red autofluorescence in neoplasia:** Increased red autofluorescence by 405 nm excitation for dysplasia and SCC was observed in the animal model used in the studies presented here (Fig. 5.3). Additionally, multiple lesions that were unidentified in conventional white light visual examination showed increased red fluorescence (Fig. 5.3b; marked ‘\*’) and were categorized as dysplasia after histopathologic diagnosis which indicated high sensitivity of WF-AF imaging in detecting certain false negatives. Similar increase in red autofluorescence for SCC with 410 nm excitation is well documented in the literature (134, 168, 169). Ingrams et al. (170) reported very high sensitivity and specificity (90% and 91% respectively) of differentiation of normal and dysplasia/SCC mucosa based on the presence of red fluorescence. Red fluorescence in epithelial tissue due to 405 nm excitation is generally attribute to protoporphyrin IX (PpIX) whose origin in the tissue has been debated. Although it is not clear whether accumulataion of PpIX is due to endogenous metabolic abnormalities or bacterial contamination at the surface of the tissue, my recent studies on two photon autofluorescence spectroscopy (Chapter 4) indicated an epithelial cytoplasmic origin of this fluorescence in dysplasia and SCC.

**5.4.4 Performance of red to green intensity ratio:** R/G intensity ratio from regions of interests were measured (Fig. 5.5) following methods similar to those of Roblyer et al. (159) to

test the performance of quantitative WF-AF imaging in the animal model in presence of benign conditions. Control tissue showed R/G intensity ratio close to 1 indicating little difference in fluorescence between red and green channel. Similar to my expectations, R/G intensity ratio for dysplasia and SCC was significantly higher than control mucosa, but there was no statistically significant difference between dysplasia and SCC. This was possibly due to high level of heterogeneity in the neoplastic tissue that led to large standard deviations in R/G intensity ratios. Additionally, as discussed previously, alterations in fluorophores targeted by WF techniques are altered both in OED and in OSCC. While there was a trend toward more differences in OSCC, as a group this was not statistically significant.

**5.4.5 Performance of red to green intensity ratio in presence of inflammation:** WF-AF imaging however provided high sensitivity and specificity of differentiation of normal and neoplasia, but failed to show such high specificity when inflammation was present (Fig. 5.6 and Table 5.1) as a confounding factor. Although not statistically significant average R/G intensity ratio for inflammation was found to be in between control and dysplasia (Fig. 5.5) which made it difficult to differentiate control and dysplasia based on R/G intensity ratio only. Since changes in fluorescence are based on endogenous sources (collagen, NADH, FAD, PpIX etc.) that are altered in neoplasia as well as in inflammation and other benign conditions including hyperkeratinization, high false positive rates (lowered specificity) may occur (59-61). Studies have shown when benign conditions (e.g. keratosis or inflammation) are included in the study population, specificity decreases to as low as 15-30% (59-61). Studies by Roblyer et al. (159, 160) reported improved sensitivity and specificity using the R/G intensity ratio (channels separated by Bayer mask) over white light examination. Specifically digital image capture providing

objective quantification was found to be superior to visual aids alone. Benign conditions were not closely examined, but since AF change is due to biochemical changes not specific to neoplasia, it is expected that these would lower specificity as found with commercial WF-AF visualization devices. This disadvantage will limit WF-AF as a stand-alone technology, but the high sensitivity of WF-AF to neoplastic change and large area screening capability in oral mucosa makes it a technology worth considering if improved specificity could be provided with a complementary method that retains the advantage of noninvasive imaging.

In conclusion, results presented in this chapter indicate that WF-AF imaging with 405 nm excitation may improve delineation of normal and neoplastic oral mucosa by increasing optical contrast of neoplasia beyond what is normally observed in visual inspection as reported in the literature. While R/G did not optimally delineate OED from OSCC, our objective in this study was to delineate control normal from neoplasia which included OED and OSCC. The method did appear to provide this delineation. A second objective was to evaluate the degree to which inflammation reduced performance. As expected, inflammation lead to a reduction in specificity an expected outcome as signatures assessed by AF are shared between these conditions – and an outcome showing WF-AF alone will not suffice for identifying neoplasia as desired for improved biopsy guidance and detection. With sensitivity for detecting indicators of neoplasia (OED + OSCC) from normal mucosa remaining at 83% despite presence of inflammation and the ability to ‘screen’ large regions of tissue comparable to visual inspection, the method of WF-AF remains a viable method for further investigation as a ‘pre-screening’ tool to guide the method of NLOM. Although it is possible to obtain high sensitivity and specificity in NLOM alone and showing in previous chapters, there are practical limitations of performing microscopy in large

regions of human oral mucosa even if encompassed in a compact endoscopic instrument. Therefore, a multiscale imaging approach that combines the high sensitivity quantitative WF-AF imaging with the detailed inspection by NLOM (shown in previous chapters to provide high sensitivity and specificity) could be a promising combination to improve delineation of neoplastic oral mucosa from normal and benign conditions for biopsy guidance. This hypothesis is examined more closely in the 7<sup>th</sup> chapter of this dissertation.

## Chapter 6

# Wide-field fluorescence imaging using a topical fluorescent probe for intracellular glucose uptake in the Hamster Model for Oral Epithelial Neoplasia

### 6.1 Introduction:

While wide-field autofluorescence imaging is an attractive large area imaging modality that could provide guidance for detailed microscopic imaging with NLOM, an alternative approach that could be considered is the use of an external contrast agent that may provide molecular level feedback and possible improved sensitivity and specificity. Molecular imaging provides information about biochemical and metabolic status that can serve additional metrics that may be incorporated for detection of early neoplasia and invasive tumors. So far molecular imaging has contributed to our understanding of biological processes that accompany early neoplastic changes leading to invasive carcinoma (171). Clinical translation of these molecular imaging techniques has been limited partly due to the lack of FDA approved contrast agents and preclinical studies. *In vivo* molecular imaging can detect changes in established biomarkers in

native condition and may help in risk assessment of neoplastic tissue. This could be helpful both at the stage of detection and before any surgical procedure is applied.

One example of clinical use of molecular imaging is positron emission tomography (PET) that utilizes  $^{18}\text{F}$ FDG (fluorodeoxy glucose) as contrast agent. Neoplastic tissues have higher glucose demand due to higher metabolic rates compared to healthy tissues. Non-neoplastic healthy tissue rely primarily on mitochondrial oxidative phosphorylation to generate ATP, while neoplastic cells has been observed to switch to glycolysis as their primary source of energy even in the presence of sufficient oxygen supply (Figure 6.1). Due to their high energy demand, tumors show higher rate of glycolysis than normal tissue. This is known as the Warburg effect and has been studied extensively after it was first postulated in the 1920s.

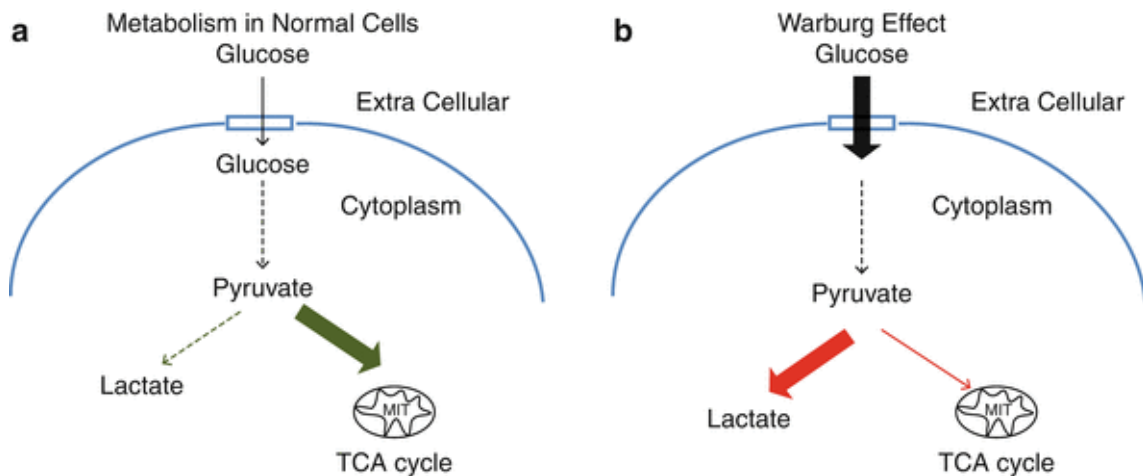


Figure 6.1: a) Glucose metabolism in normal cells. End product of glycolysis (Pyruvate) is utilized by mitochondria for oxidative phosphorylation as indicated by a bold green arrow. b) Neoplastic tumor cells have a higher rate of glucose uptake, glycolysis and lactate production indicated by bold back and red arrows.

To meet the energy demand of highly proliferating neoplastic cells glucose consumption by those cells increase, this is supported by the over-expression of glucose transporters (GluTs)

and hexokinase enzymes in neoplastic cells. In PET imaging  $^{18}\text{F}$ FDG is used as a reporter of glucose uptake where radioactive  $^{18}\text{F}$  provides contrast for tracking. Neoplastic cells expressing higher levels of GluTs show higher uptake of  $^{18}\text{F}$ FDG *in vivo* than non-neoplastic cells and the differential uptake of  $^{18}\text{F}$ FDG is imaged by PET. PET imaging is routinely used in clinic for cancer detection and is clinically important in deep tissue imaging of glucose metabolism; nonetheless it suffers from significant limitations due to radioactive radiations and low spatial resolution ( $0.3\text{-}1\text{ cm}^3$ ) (172) in detection of early neoplasia.

Optical molecular imaging is an alternative approach, which utilizes optically active molecules for *in vivo* biomarker imaging. As an alternative to  $^{18}\text{F}$ FDG an optically active fluorescent analog of glucose would be suitable for molecular imaging and targeting increased glucose metabolism in neoplasia. Ideally a glucose sensor should possess following features:

- a) Suitable molecular weight compared to glucose
- b) Low cytotoxicity
- c) Competition by glucose for cellular uptake
- d) Resistance to quenching or photo-bleaching
- e) Ability of the probe to be metabolized by the cell/tissue

The first known fluorescently active glucose bioprobe was 6-(N-(7-nitrobenz-2-oxa-1,3-diazol-4-yl)amino)-2-deoxyglucose (6-NBDG) which was developed in 1985 (173). The fluorochrome was attached to the C-6 position of D-glucose and it was the first glucose analog developed to study glucose transport systems in living organisms. Although 6-NBDG provided an efficient way of assessing activity of GluTs and glucose transport across cell membranes, it was not suitable to study cell metabolism. Modification at C-6 position in 6-NBDG inhibited the C-6

phosphorylation by glycolytic enzyme Hexokinase, which led 6-NBDG to accumulate within the cells. Therefore another glucose analog, 2-(N-(7-nitrobenz-2-oxa-1,3-diazol-4-yl)amino)-2-deoxyglucose (2-NBDG) was developed (Fig. 6.2a), which is also an optical equivalent of  $^{18}\text{F}$ FDG that is not associated with inherent limitations of  $^{18}\text{F}$ FDG. Fig. 6.2b shows the excitation and emission spectra of 2-NBDG. In this case the fluorochrome was attached to the C-2 position of D-glucose to keep C-6 free for Hexokinase mediated phosphorylation. Studies in bacteria has shown that 2-NBDG 6-phosphate gets converted back into 2-NBDG by glucose-6-phosphatase and finally is degraded into non-fluorescent products by the glycolytic pathway (174). Therefore decay of 2-NBDG fluorescence is a measure of glycolytic activity of live tissues and could indicate differences in metabolic activities between normal and neoplastic tissue.

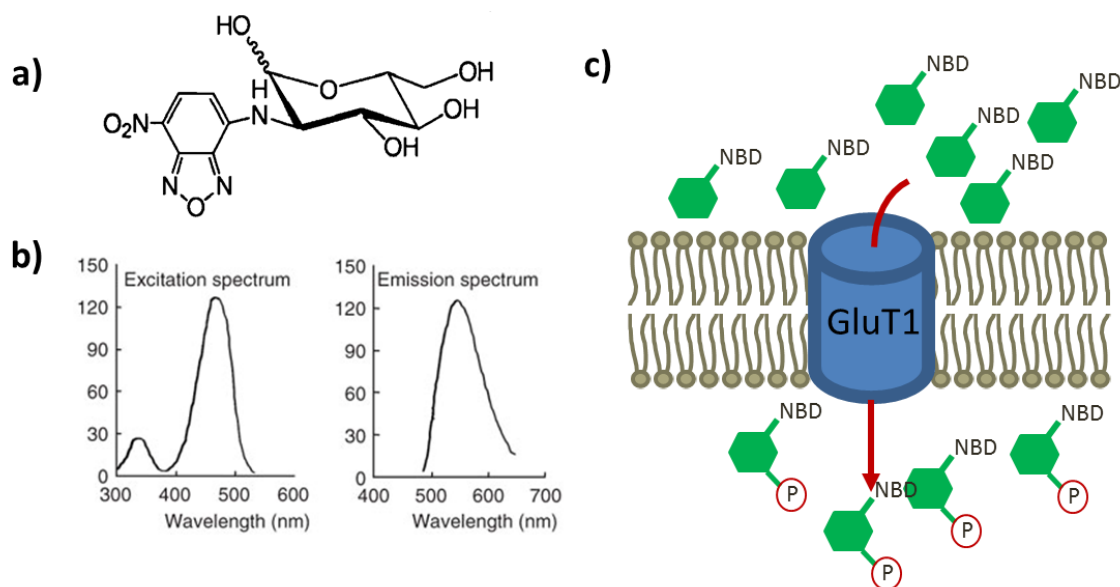


Figure 6.2: a) Chemical structure of 2-NBDG. b) Excitation and emission spectra of 2-NBDG. c) 2-NBDG is internalized by glucose transporter 1 (GluT1) and subsequently phosphorylated by glycolytic enzyme hexokinase.



2-NBDG has been used in numerous studies including diabetes, brain research and to some extent in cancer research (175-177). 2-NBDG staining of *ex vivo* tissue as well as injection into live animal has been shown to improve contrast between normal and tumors. The unique design of 2-NBDG makes it metabolically active and thus prevent it from getting accumulated once inside the target cell. This glucose probe has been shown to have an intracellular transport mechanism involving GluTs (Fig. 6.2c) since intracellular uptake of 2-NBDG was inhibited by D-glucose and not by L-glucose in *E. coli*. It is also non-radioactive unlike  $^{18}\text{F}$ FDG which is routinely used in the clinic for tumor diagnosis. These features make 2-NBDG a compelling candidate for non-invasive tumor targeting. 2-NBDG preferentially accumulates in the neoplastic cells compared to normal cells and could provide an optical image based marker for detection of neoplastic tissue. 2-NBDG can be used to perform wide-field fluorescence imaging at a higher spatial resolution than PET, which is important for detection of epithelial neoplasms. The molecular weight of 2-NBDG is 330 Da that makes it suitable for topical delivery in epithelial tissue without the need for IV injection.

As mentioned earlier metabolic status of a tumor microenvironment is altered from normal tissue and highly heterogeneous, which makes metabolic deregulation an important cancer hallmark. Since 2-NBDG application helps in identifying areas of higher glucose uptake, assessment of 2-NBDG uptake could indicate alterations in metabolic activities in the complex microenvironment in precancerous lesions when visual lesion identification is difficult. ***This study was undertaken to demonstrate topical application of 2-NBDG to improve optical contrast between normal and neoplastic tissue by targeting a well-documented cancer***

**hallmark.** As in the previous study, inflammation was included to assess potential advantages and limitations of WF imaging.

### **6.1.1 Goal of the current study:**

The overall goal of this study was to assess the feasibility of optical imaging using a fluorescently active glucose sensor to study deregulation of glucose metabolism in neoplastic tissue and provide a novel way of optical assessment of a cancer hallmark. Additionally, the wide-field imaging method utilizing 2-NBDG was assessed with the long term vision that it could be applied as an alternative to WF-AF with NLOM imaging for a new multiscale approach to assessing neoplasia in the epithelium. In this study, I have evaluated the contrast properties of topical delivery of 2-NBDG in the hamster model of oral neoplasia. The specific goals were to

- a) Test *in vivo* topical application of 2-NBDG and visualize the uptake of 2-NBDG by wide-field fluorescence imaging. All known previous studies have investigated this contrast agent in *ex vivo* tissues or by *in vivo* injection, but no topical applications are known to have been published. Topical application would make potential clinical translation of this and similar agents more feasible than those requiring immediate systemic delivery.
- b) Compare uptake of 2-NBDG between normal, dysplasia and OSCC tissue and test sensitivity and specificity of 2-NBDG based contrast using ROC analysis.
- c) Measure 2-NBDG uptake in benign conditions such as in inflamed tissue using the hamster model of inflammation described earlier and test sensitivity and

specificity of 2-NBDG fluorescence with or without the presence of inflammation as a potential confounding factor.

## **6.2 Materials and Methods:**

**6.2.1 Sample preparation and background imaging:** Control and DMBA treated hamsters were anesthetized with IP injection of ketamine/Xylazine (60-70 mg/kg + 5-10 mg/kg) and cheek pouches were prepared for imaging using a protocol described before. A white light image of the pouch was taken for reference. For fluorescence imaging of 2-NBDG I have modified the excitation source and emission filter in the wide-field fluorescence imaging system (Figure 6.3) already described in chapter 3. Briefly, detection of fluorescence was achieved using an AF Micro NIKKOR 60mm 1:2.8 lens attached to a Nikon DS Fi1 camera. A high power 470nm LED (ThorLabs) was used as excitation source and a 550nm BP (Edmund Optics) filter was used as emission filter. A long pass 510nm dichroic (Edmund Optics) filter was used to direct the excitation light onto the sample at a right angle to avoid artifacts due to shadows from large exophytic tumors. Pre-2-NBDG stain background fluorescence images of each hamster cheek pouch were taken with multiple combinations of exposure and gain. These images were used for normalization of 2-NBDG fluorescence after staining.

**6.2.2 2-NBDG topical application:** 1ml of 1mg/ml 2-NBDG in sterile PBS (pH 7.4) was carefully applied on each cheek pouch sample at room temperature in the dark for 30 minutes. After 30 minutes of incubation samples were rinsed for 2 minutes with sterile room temperature PBS (pH 7.4) and any excess 2-NBDG was wiped off the tissue surface using sterile

gauze. Finally the tissue was rinsed again sterile PBS for 1 minute to keep the tissue moist during experiment. Animals were then transferred to the wide-field fluorescence imaging system and imaged.

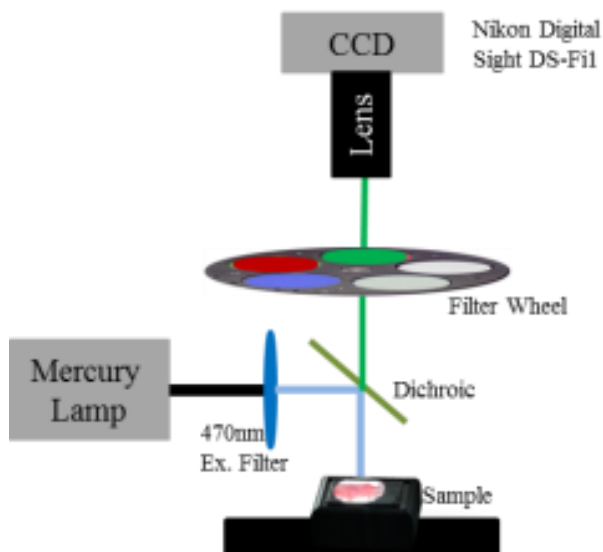


Figure 6.3: Wide-field fluorescence imaging setup for 2-NBDG imaging.

**6.2.3 2-NBDG decay:** A kinetic study was performed with a small set of DMBA treated hamsters (n=3) to optimize image parameters and time of imaging. The first time point after 2-NBDG application was 5 minutes since it takes about 5 minutes to rinse the tissue and reposition under the imaging system. Images at six more time points were taken at 10, 20, 30, 60, 90 and 120 minutes. All images were taken at the same exposure and gain settings of the camera.

**6.2.4 2-NBDG uptake by epithelial cells:** 2-NBDG uptake by epithelial cells by topical application was confirmed by topical treatment of 2-NBDG on hamster buccal mucosa for 30 minutes in the dark followed by layer resolved two-photon microscopy and confocal microscopy. Tissue biopsies before and after 2-NBDG topical application were imaged in a two-photon

microscope with 800nm excitation and a broad band emission 500-700nm. Images were taken from superficial and basal cell layers to identify the depth of penetration of 2-NBDG when applied topically.

Biopsy samples before and after topical application of 2-NBDG were also imaged using a confocal microscope to identify spectral characteristic of fluorescence signal. Lambda stacks were collected using 488nm excitation and emission spectra from 510nm-670nm with 5nm band-width. Laser power was kept unchanged between samples to allow for intensity based comparisons.

**6.2.5 Differential 2-NBDG uptake across pathological groups:** 2-NBDG was applied topically on control (n=6), inflamed (n=4), and DMBA (n=12) treated hamster oral mucosa using a protocol described earlier in this chapter and wide-field fluorescence images were taken at 60 minutes time point. A total of 26 normal, 19 inflammation, 36 OED and 23 OSCC sites were imaged. Fold increase in 2-NBDG signal was calculated by comparing background fluorescence signal with post 2-NBDG signal for each ROI. After the imaging, biopsies were taken from each ROI and processed for histopathology. ROIs for biopsy and image analysis were selected based on following criteria:

- a) Physical appearance under white light examination: areas with visible surface abnormalities in texture, color and swelling were included
- b) At least 5 mm away from the edge of the tissue or pins used to secure the tissue on the sample holder
- c) Away from clearly visible folds in the tissue (due to possible surface accumulation of fluorophores in folded tissue)

- d) Avoiding sites of injuries (such as during sample preparation) and areas covered in blood
- e) Away from areas of high reflectance.

**6.2.6 Image Analysis:** Three smaller ROIs (r1, r2, and r3) were chosen from each ROI (R1) and average intensities for each smaller ROIs were calculated ( $I_{r1,ave}$ ;  $I_{r2,ave}$ ;  $I_{r3,ave}$ ) using imageJ. Average intensity of R1 is then expressed as ( $I_{R1} = [I_{r1,ave} + I_{r2,ave} + I_{r3,ave}]/3$ ). Average intensities for each ROI was calculated from pre and post 2-NBDG images and a fold increase in fluorescence ( $\Delta F_{2-NBDG}$ ) is calculated as  $I_{R1,Post}/I_{R1,Pre}$ .  $\Delta F_{2-NBDG}$  is then compared between pathological groups and statistical comparison was done by ANOVA and Tukey's post hoc analysis. Receiver operator characteristic (ROC) curves were created for 2-NBDG fluorescence using statistical software SPSS and the ROC curves were used to calculate area under the curve (AUC), sensitivity and specificity.

## Results:

A pilot study was performed to validate feasibility of topical application of 2-NBDG on hamster oral mucosa. Figure 6.4 shows time resolved wide-field imaging of 2-NBDG fluorescence after topical application of 2-NBDG for 30 minutes. The pre-2-NBDG background image showed very small amount of autofluorescence at the excitation (470 nm) and emission (550 nm BP) appropriate for 2-NBDG fluorescence. Imaging was performed 5, 10, 20, 30, 60, 90 and 120 minutes after the 30 minutes incubation with 2-NBDG (Figure 6.4a). Images showed maximum fluorescence at 10 minutes time point and gradually decreased over the time course of two hours. After the initial increase in fluorescence which is an indication of rate of glucose uptake the gradual decrease in fluorescence over time is indicative of glucose consumption by the epithelium under investigation. The decay of 2-NBDG fluorescence was linear for both tumor ( $R^2 = 0.98$ ) and normal ( $R^2 = 0.99$ ) sites. The slope of the curve from 10 min (maximum 2-NBDG fluorescence) to 120 min will indicate the rate of glucose metabolism. In my preliminary kinetic studies, tumors showed a slope of -0.79 which is almost twice as fast as normal areas with a slope of -0.41. This observation was expected because tumors have a higher rate of glucose metabolism than normal epithelium. Average fluorescence in SCC at 60 min post 2-NBDG time point was still higher than fluorescence in normal epithelium at 5 min time point. Therefore, 60 min time point was selected for imaging in later experiments and analysis.

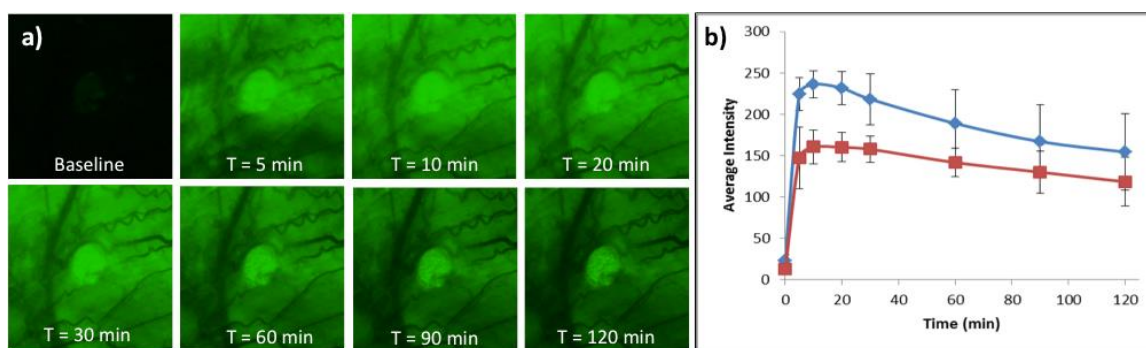


Figure 6.4: *In vivo* uptake of 2-NBDG. **a)** Time course of 2-NBDG fluorescence with wide-field fluorescence imaging of a DMBA treated hamster oral mucosa. **b)** Average 2-NBDG fluorescence intensities measured at each imaged time point from multiple ROIs showed the decay kinetics of intracellular 2-NBDG. Blue: tumors; Red: normal.

Biopsies were taken from non-2-NBDG epithelium and 2-NBDG stained epithelium, and lambda stacks were imaged to identify spectral characteristics of 2-NBDG fluorescence from epithelial cells. Figure 6.5a shows a baseline confocal image from non-2-NBDG epithelium and 6.5b shows a 2-NBDG stained epithelium imaged with 488 nm excitation and 545-500 nm band pass emission. 2-NBDG stained epithelium showed much stronger fluorescence than non-2-NBDG epithelium at the same emission channel. Spectral profile calculated by measuring average intensities from a lambda stack of a non-2-NBDG epithelium showed weak autofluorescence peak around 520 nm as expected due to NADH and FAD. However, a strong peak at 550 nm was seen in 2-NBDG stained epithelium, which indicates penetration of 2-NBDG into the epithelium.



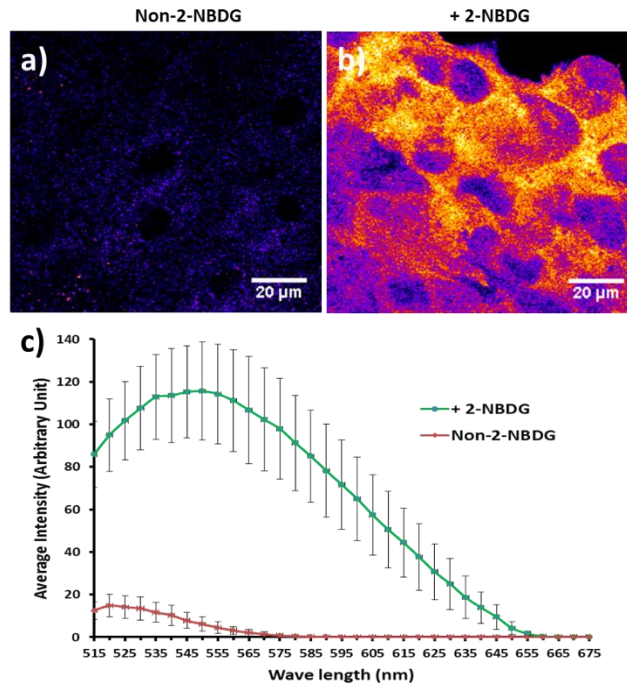


Figure 6.5: Confocal images of hamster oral mucosa before **(a)** and after **(b)** 2-NBDG topical application. **(c)** Analysis of Lambda stacks showed a small autofluorescence peak in native tissue (red) while a large fluorescence peak for 2-NBDG centered around 550 nm was found in the epithelium topically treated with 2-NBDG.

Two-photon fluorescence imaging experiments were also performed to assess the depth of penetration of 2-NBDG by topical delivery. Two-photon autofluorescence images were taken from superficial (Figure 6.6a) and basal epithelium (Figure 6.6b) of intact hamster oral mucosa before 2-NBDG topical application. Images taken after 2-NBDG application showed significantly brighter epithelial cells in both superficial (Figure 6.6b) and basal (Figure 6.6d) epithelial layers. This indicates penetration of 2-NBDG into the basal epithelium with 30 minutes topical application of 2-NBDG and therefore makes it a suitable method for targeting altered glucose uptake by neoplastic cells to enhance contrast between normal and neoplastic tissue in hamster oral mucosa.

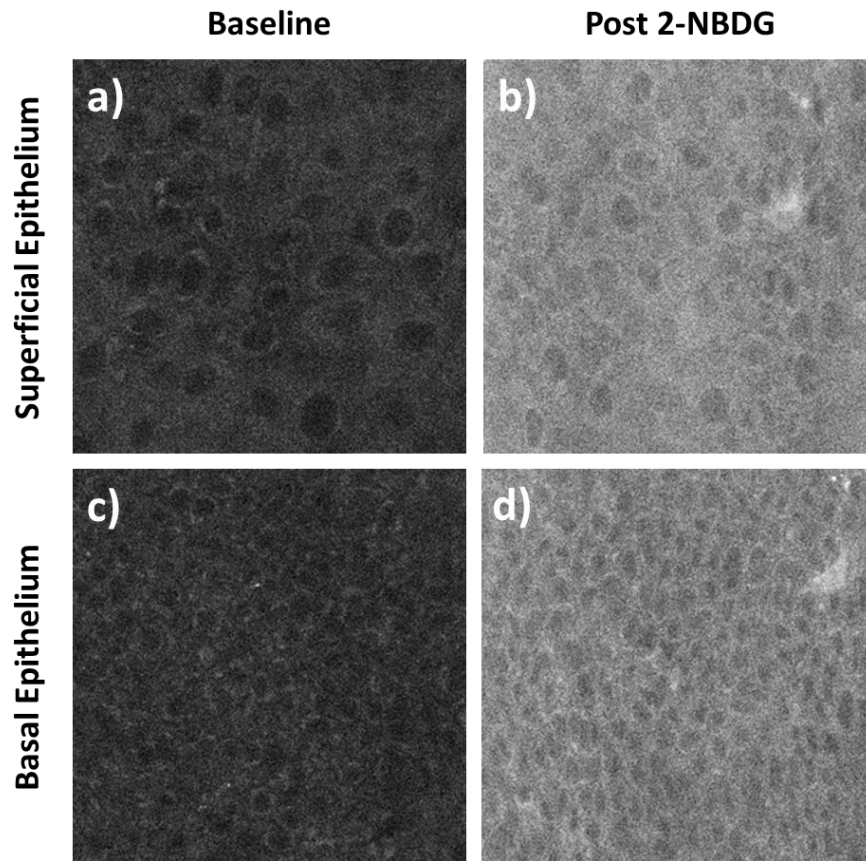


Figure 6.6: Micrographs from two-photon microscopy before and after topical application of 2-NBDG. Both superficial and basal epithelial layers showed increased fluorescence after 2-NBDG staining indicating penetration of 2-NBDG into the basal epithelium.

Figure 6.7a shows an example of a white light image of a normal cheek pouch mucosa with no visible abnormality. Figure 6.7b and 6.7c shows wide-field fluorescence images before and after 2-NBDG was topically applied on the same cheek pouch mucosa. 2-NBDG application increases fluorescence evenly over the entire FOV and does not show any contrast between different areas indicating uniform uptake of 2-NBDG and no abnormal metabolic behavior. Figure 6.7d shows histology of the ROI outlined in Fig. 6.7c. Normal pathology of the mucosa was confirmed by histopathologic examination.

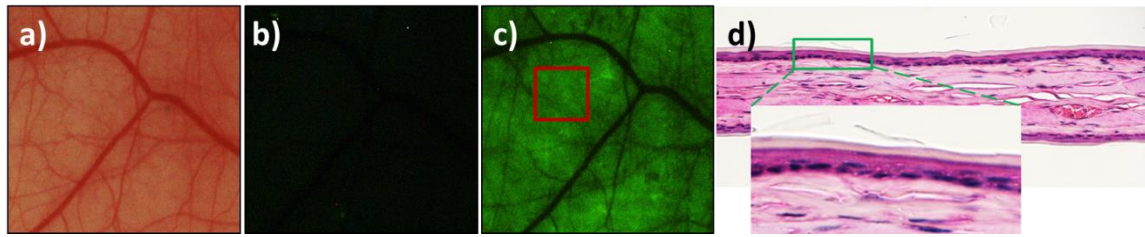


Figure 6.7: White light (a) pre-stained (b) and post-stained (c) images of a normal hamster cheek pouch are shown. (d) H&E stained cross-section of the ROI (c: red box) normal histopathologic features.

Figure 6.8 shows an example of an SCC where the exophytic tumor is easily visible under white light (Fig. 6.8a). While pre-2-NBDG baseline image (Fig. 6.8b) showed almost no fluorescence the post 2-NBDG stained image (Fig. 6.8c) showed significantly high fluorescence with a preferential accumulation of 2-NBDG within the tumor. Histopathologic assessment of the tumor (Fig. 6.8d) showed features of poorly differentiated squamous cell carcinoma such as complete loss of cell polarity, nuclear and cellular pleomorphisms etc.

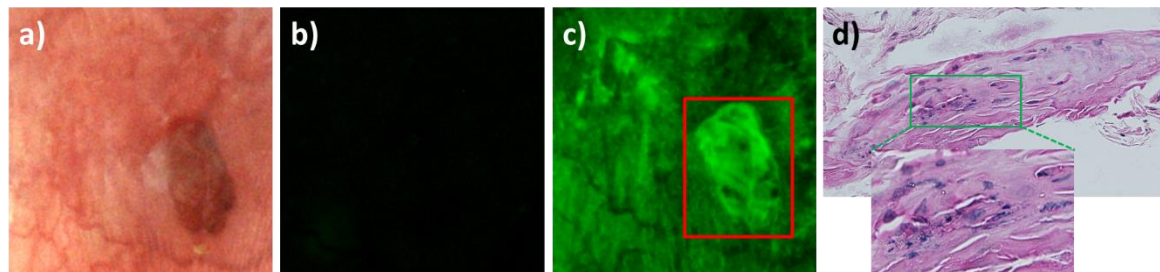


Figure 6.8: White light (a) pre-stained (b) and post-stained (c) images of a tumor are shown. MPAM-SHGM cross-section is shown in (c) and H&E stained cross-section in (d) confirms the pathology.

Figures 6.7 and 6.8 showed two extreme cases where the pathology of the tissue could be anticipated and the uptake of 2-NBDG correlated with histopathology. Figure 6.9 shows a rather complex situation where areas surrounding a tumor are expected to be at a high risk of being pre-cancerous but a while light examination showed no visual surface abnormalities (Figure 6.9a:

arrow). While wide-field fluorescence imaging before 2-NBDG application (Figure 6.9b) showed little fluorescence as expected, certain areas surrounding the tumor showed unusually high 2-NBDG fluorescence (Figure 6.9c) which led us to identify the area as an ROI. Corresponding histopathology (Figure 6.9d) of the ROI revealed abnormal cytology and microstructure of a moderate dysplasia.

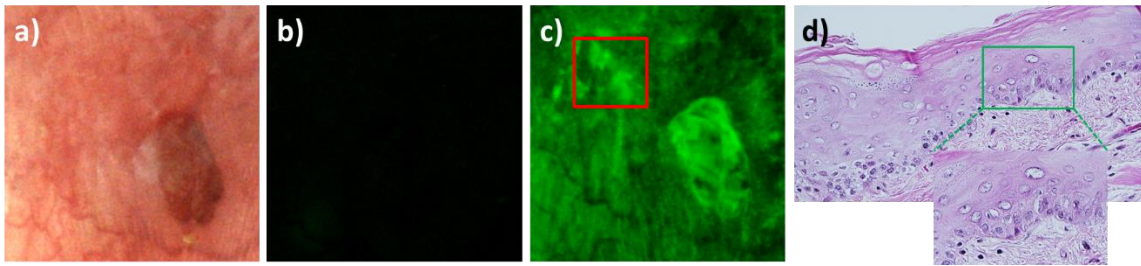


Figure 6.9: White light (a) pre-stained (b) and post-stained (c) images of a tumor associated epithelium is shown. The region of suspicion is outlined at the top left corner of the tissue in (c). H&E stained cross-section in (d) confirms the pathology to be moderate dysplasia.

Figure 6.10 describes another example where a pre-cancerous lesion was found away from regions of gross surface abnormalities. The tissue appeared normal under white light (Figure 6.10a) examination whereas the 2-NBDG stained image showed a region of increased uptake of 2-NBDG (Figure 6.10c). H&E stained cross-section (Figure 6.10d) showed cytologic features indicating moderate dysplasia. This finding is particularly important since abnormal uptake of 2-NBDG revealed an area of moderate dysplasia that was rather unsuspecting under a conventional white light examination.

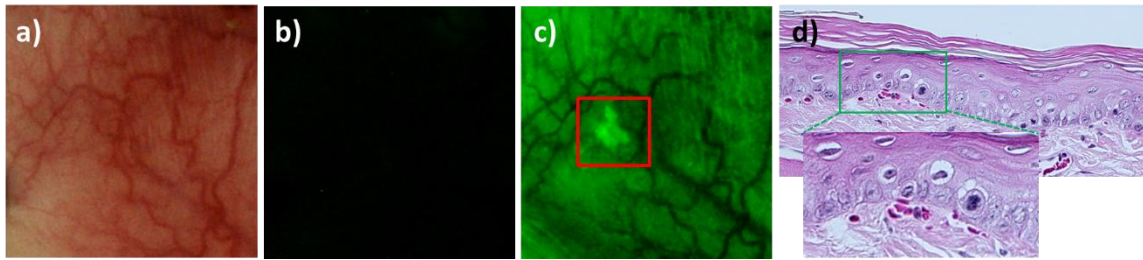


Figure 6.10: White light (a) pre-stained (b) and post-stained (c) images of a moderate dysplasia are shown. The region of high 2-NBDG uptake in (c) is outlined. d) H&E stained section of the ROI.

2-NBDG fluorescence intensity normalized by baseline fluorescence for each ROI was measured for statistical comparison between normal, inflammation, dysplasia and SCC (Fig. 6.11a). Results showed statistically significant increase in 2-NBDG uptake in dysplasia and SCC from normal tissue. Uptake of 2-NBDG in SCC was also significantly higher than dysplasia. However, 2-NBDG fluorescence for inflammation was not significantly different from normal or dysplasia. When looked at different grades of dysplasia separately there was no statistically identifiable trend of 2-NBDG uptake between mild, moderate and severe dysplasia (Figure 6.11b). A frequency histogram for each pathological group (Figure 6.11c) showed the distribution of 2-NBDG signal. The distribution for normal tissue was narrow as expected, but for dysplasia and SCC it was wide ranging from normal to five or six times higher than normal with most samples showing up in the higher end of the distribution. As seen in the distribution 2-NBDG signal from inflammation (red bars) overlapped with both normal (blue bars) and dysplasia (green bars). The effect of this overlap on the performance of 2-NBDG uptake as a measure of neoplastic abnormality can be seen in the ROC curves (Figure 6.11d), results from which is summarized in Table 6.1.

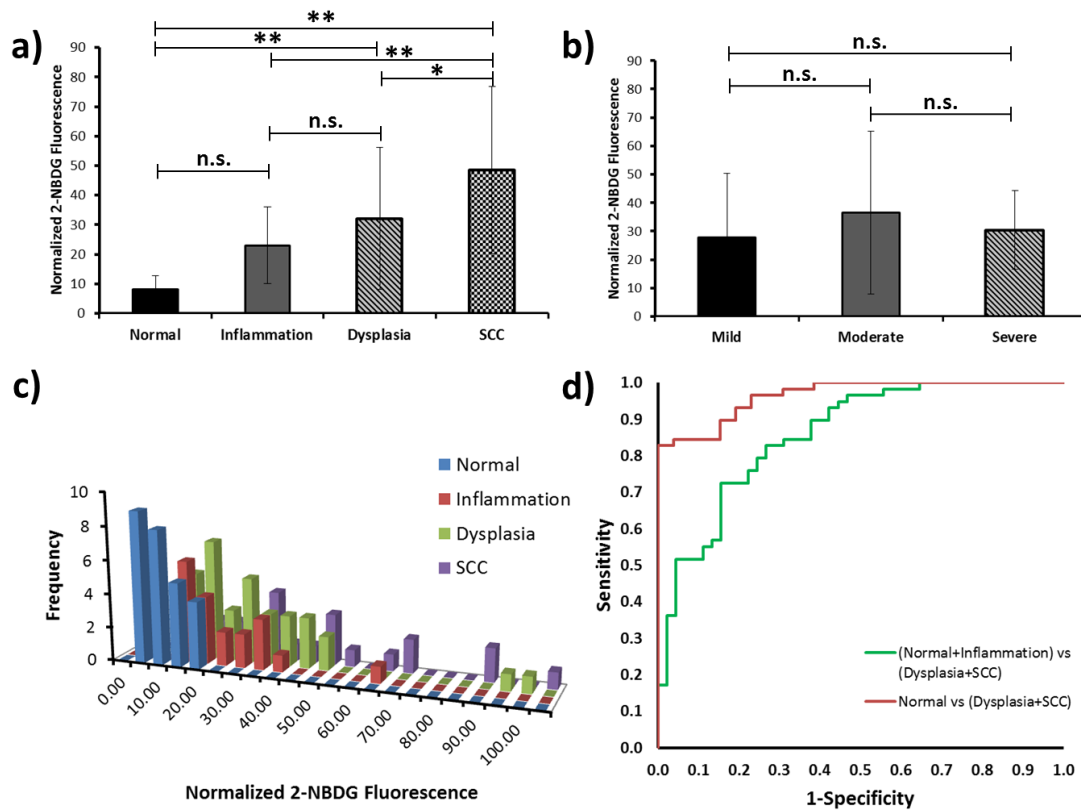


Figure 6.11: a) Normalized 2-NBDG fluorescence intensity as measured from wide-field imaging for normal, inflammation, dysplasia and SCC tissue. b) Normalized 2-NBDG fluorescence for mild, moderate and severe dysplasia. c) Distribution of 2-NBDG uptake for each sample across pathological groups. d) ROC curves using normalized 2-NBDG fluorescence with or without inflammation in the normal group. \*  $p < 0.05$ , \*\*  $p < 0.01$ , n.s.  $p > 0.05$ .

The inclusion of inflammation as a benign condition with normal data set (green ROC curve) reduced the overall performance of wide-field imaging based on 2-NBDG fluorescence significantly from the data set when inflammation was not present (red ROC curve). Although the area under the curve was still reasonably high (0.86) in presence of inflammation, the sensitivity decreased from 0.90 to 0.83 while specificity decreased 0.85 to 0.73.

Table 6.1: Summary of ROC statistical analysis of normalized 2-NBDG fluorescence quantified from wide-field imaging.

Group	AUC	Sensitivity (%)	Specificity (%)
Control vs (Dysplasia + SCC)	0.97	90	85
(Control + Inflammation) vs (Dysplasia + SCC)	0.86	83	73

## Discussion:

### 6.4.1 *In vivo* topical application of 2-NBDG in identification of oral epithelial neoplasia:

In this study, topical application of 2-NBDG was tested as a source of contrast to delineate normal and inflammation from dysplasia and SCC in the *in vivo* hamster model for inflammation, OED and OSCC. To the best of my knowledge this is the first study that assessed the potential of *in vivo* topical application of a fluorescently active glucose analog to target deregulation of glucose metabolism in precancers and cancers. Topical delivery of contrast agents is particularly important in epithelial cancers since it provides a potentially rapid and accurate localization of the contrast agent to the epithelial tissue and avoids the need for *in vivo* systemic injection of the chemical agent. Additionally, systemic injection as a method of delivery of contrast agents has limitations such as nonspecific accumulation in liver or kidney. This requires injection of high concentration of contrast agents to achieve sufficient localization of those agents in the site of interest. Experiments performed in this study indicates 1ml of 1mg/ml 2-NBDG, which is five times lower than concentrations used in systemic injection based studies (178, 179), when applied topically provided sufficient contrast between normal and neoplastic tissue.

In these results, it is shown that 2-NBDG applied topically did result in differential fluorescence intensity between normal oral mucosa and transformed (neoplastic) mucosa, resulting in a high AUC for detection in ROC analysis. One limitation of the study is that a direct comparison was not made between topical application and systemic 2-NBDG applications by injection. There were limitations of systemic injection of 2-NBDG in the hamster model. Since hamsters do not have long tails, tail veins are not accessible for intravenous (I.V.) injection. Sublingual injection was a possible route, but in pilot tests resulted in topical contamination of the cheek pouch with 2-NBDG. When 2-NBDG applied topically was shown to penetrate in to the basal cells (Fig. 6.6) and displayed decay kinetics that differed between normal and neoplasia (Fig. 6.4, as well as unpublished results from the lab), no further attempts at *in vivo* injection studies were made.

Clinical application of the topical method for 2-NBDG would require further evaluation of pharmacokinetic properties of the contrast agent. Evidence from the literature suggests glucose transporter mediated internalization of 2-NBDG in normal and cancerous cells while no toxic effect has been shown so far in *in vivo* studies (180). In studies conducted in *E. coli*, after internalization 2-NBDG was shown to be rapidly phosphorylated and then degraded into non-fluorescent derivatives (174). Demonstration of intracellular fate, distribution and excretion in animal models would help in optimization of 2-NBDG topical application methods. Further, there will be a need to evaluate and decrease time of topical application such that use is practical in a clinical setting.

**6.4.2 Decay of 2-NBDG fluorescence over time after *in vivo* uptake in oral mucosa:** A pilot study on decay of 2-NBDG fluorescence *in vivo* showed a dynamic nature of the signal. The



uptake kinetics of 2-NBDG was not determined because topical application of 2-NBDG meant the fluorophore was present on the tissue surface and in image fields during the time this kinetics would be studied. Interestingly fluorescence reached maxima at 10 min after the end of 30 min incubation in 2-NBDG (Figure 6.4b). After the 10 min time point 2-NBDG fluorescence decayed with time for both normal and SCC - significant observations being that while overall the neoplastic sites had higher 2-NBDG fluorescence (greater uptake) at any one timepoint, the decay kinetics differed, such that decay (interpreted as utilization) occurred faster for neoplastic sites than normal. At 5 min post 2-NBDG time point average fluorescence signal from SCC sites were higher than normal sites and stayed higher in SCC at the end of the experiment (120 min time point) although the rate of fluorescence decay was higher in SCC than normal tissue. The slope of fluorescence decay curves for SCC was almost two times higher than normal tissue. This was expected since cancerous tissue has higher glucose metabolic rate than normal epithelium and therefore metabolizes 2-NBDG to non-fluorescent products faster. It is noted that ongoing studies by a colleague (P. Villarreal) in the lab are expanding these decay kinetic studies, with early results indicating a consistency with this observation in decay responses.

**6.4.3 Uptake of 2-NBDG by epithelial cells and penetration into basal cell layer:** An additional effort was undertaken to show penetrance of 2-NBDG into the epithelium following topical application. Confocal and two-photon fluorescence microscopy experiments were performed to identify the source and location of fluorescence signal after topical application of 2-NBDG (Figure 6.5 and 6.6). This was important since 2-NBDG was expected to accumulate on the surface of the tissue due to heterogeneous surface topography of human oral cavity which could lead to nonspecific accumulation of 2-NBDG. In hamster oral mucosa, after several careful

saline washes to remove excess 2-NBDG from the surface, 2-NBDG fluorescence from superficial and basal epithelium was confirmed using confocal and two-photon excitation microscopy of the intact tissue. This differed from tissues lacking topical application and which showed no background fluorescence beyond very weak autofluorescence. If 2-NBDG was accumulating only on the surface, one would not localize the signal to basal cells in the intact tissue. Experiments performed here demonstrate in vivo topical application of 2-NBDG in an animal model.

It is noted that changes in tissue composition and architecture such as epithelial thickening, hyper-keratinization may influence the penetration depth of 2-NBDG by topical application especially in human oral mucosa. Due to relatively small molecular weight of 2-NBDG and recent developments in mucoadhesive formulations (181) penetration of 2-NBDG in thick tissue it is expected that such potential limitations could be overcome. Many steps are required for potential optimization, including time of application needed and studies will still need to be done to identify the optimum dose and diffusion rate of 2-NBDG in humans. Nonetheless, the current study provides an indication that topical 2-NBDG could potentially work to delineate highly metabolic sites from normal.

**6.4.4. 2-NBDG uptake across all groups:** In this study, 2-NBDG fluorescence for each ROI was calculated as a fold increase from the baseline fluorescence of the same ROI. This normalization of fluorescence intensity was necessary to account for variations in baseline fluorescence from different animals and different sites within each animal. 2-NBDG uptake as indicated by fold increase in fluorescence intensity was seen to increase from normal to inflammation, dysplasia and SCC with SCC showing maximum uptake of 2-NBDG (Figure 6.11a).

In the animal model used for these studies SCCs are usually exophylic in nature and are easily identified under conventional white light examination. In humans this is not the case with SCCs usually presenting under surfaces that appear relatively flat – thus while 2-NBDG may not be needed to visualize tumors of the hamster mucosa the increased contrast found in SCC would highly benefit the human cancer scenario that involves flat lesions. Unlike the exophylic tumors in the hamster model, lesions with different grades of dysplasia and inflammation on the other hand do not always show visible surface abnormalities in this model. It was in these cases that the increase in image contrast afforded by 2-NBDG was most evidently an advantage over white light inspection. Quantitatively, 2-NBDG intensity increased with all stages of neoplasia (OED and SCC), but was also seen to increase in inflammation relative to normal, although not as much as neoplasia. Careful investigation of 2-NBDG stained oral mucosa revealed several instances of high 2-NBDG uptake in tissue which appeared visually normal. One striking example is shown in Figure 6.10, in which a visually normal region showed significant uptake of 2-NBDG relative to the surrounding tissue and was found by histology to in fact be neoplastic (OED). This was a significant finding as 2-NBDG showed potential to identify metabolic abnormalities associated with abnormal pathology even when clinical diagnosis was difficult. One way that application of the 2-NBDG may prove to be important is by its ability to identify false negatives.

**6.4.5 Performance of 2-NBDG based wide-field imaging in absence and presence of benign conditions:** ROC curves calculated for 2-NBDG fluorescence in absence and presence of inflammation in the normal group indicated its effect on sensitivity and specificity. This is relevant as inflammation can pose complications in clinical diagnosis of dysplasia and is often a confounding factor in conventional oral examination due to similarities in optical properties that

are shared between conditions. Inflammation along with other benign lesions are known to alter metabolic activity in epithelial tissue which was expected to affect 2-NBDG uptake. Results suggest loss of sensitivity and specificity (AUC reduced from 0.97 to 0.86) when inflammation was mixed in the data set since 2-NBDG fluorescence uptake in inflammation overlapped with both normal and dysplasia, although not statistically significant (Figure 6.11a and 6.11c). The loss of sensitivity and specificity was not as pronounced as in the case of wide-field autofluorescence imaging shown in Chapter 5.

In the studies presented here 2-NBDG has been used as an optical contrast agent to monitor metabolic status (hallmark of cancer) of tissues using wide-field fluorescence imaging. This imaging modality provides indication of alteration in glycolytic activity in native tissue at a large surface area, usually in the order of several centimeters. This is essential while looking for abnormalities in oral and oropharyngeal tissue. Although wide-field fluorescence imaging of 2-NBDG provides an excellent platform for screening based on metabolic behavior, this approach lacks spatial and depth resolution to enable assessment of subsurface microstructural and cytologic alterations akin to clinical pathology or other markers that are needed to identify neoplasia with both high Sensitivity and Specificity. In the chapters 2, 3 and 4 methods based on nonlinear optical microscopy and spectroscopy were established and tested for identification of microstructural and cytologic features of neoplasia. Recognizing the limitation of restricted field-of-view provided by microscopy (on the order of hundreds of micrometers and limited to millimeters even with mosaic stitching), widefield imaging was explored to identify and narrow down the regions to which subsurface assessment could be performed with NLOM. In this chapter, I present a potential widefield approach that provides topical contrast as an alternative

to inherent WF imaging based on endogenous autofluorescence. Advantages over WF-AF include the use of a molecular contrast agent that can be applied topically and is associated with the cancer hallmark of dysregulated metabolism (e.g. Warburg effect). Further, taking inflammation into account, Sensitivity (0.83 in both cases) was comparable with improved Specificity (0.73 vs. 0.61) over WF-AF. A limitation is the need for a contrast agent which could delay adoption by clinicians/FDA approval. Further, studies in human tissues will need to be conducted to assess if these advantages in Specificity and Sensitivity hold beyond the animal model.

In conclusion, uptake of 2-NBDG in oral epithelial tissue by topical application is a simple method to monitor neoplasia. Methods described here also provide insights into one of the life's fundamental processes: glucose metabolism. Studies presented here open several new avenues for exploring metabolic abnormalities under different physiologic and pathologic conditions. I have established the feasibility of topical application of 2-NBDG in identifying metabolically active regions in a large tissue, which is expected to provide necessary platform for preclinical studies using live animals. In vivo monitoring of glucose consumption by optical imaging will be of great advantage in image based diagnosis of cancers, precancers and other metabolic disorders. With regard to the goals of this thesis, the method presented here warrant further study to determine if it could be used as a first-pass approach to 'highlight' areas of suspicion for complementary NLOM to determine if such areas are neoplastic and should be biopsied.

## Chapter 7

# Multimodal noninvasive imaging for multiscale detection of oral epithelial neoplasia using wide-field fluorescence imaging and nonlinear optical microscopy

### 7.1 Introduction:

In this dissertation so far two types of imaging have been tested for their potential in delineating oral neoplasia from normal and benign epithelial tissue. Multiple cytologic, architectural and spectroscopic features were identified (chapters 2, 3 and 4) by NLOM based image assessment methods. These NLOM features were largely associated with neoplasia *in vivo* and could indicate standard hallmarks of cancer, with results indicating high sensitivity and specificity for detection of neoplasia, using standard pathology as the gold standard. However, as noted before NLOM is limited by the imaging field of view and would require additional wide-field imaging to guide us to areas of suspicion with high sensitivity for depth resolved microstructural imaging. On the other hand, widefield approaches having high sensitivity but lacking specificity offer the potential to screen large areas but without the ability to detect specific metrics of neoplasia based on subsurface cellular and molecular features. As a potential solution to better identify and delineate areas of neoplasia and to better guide biopsy sites, a

multimodal imaging approach combining *in vivo* wide-field fluorescence imaging and NLOM was tested in this chapter to combine strengths of both modalities.

The need for evaluating *in vivo* indications of neoplasia to identify potentially malignant lesions has led to the development of several noninvasive techniques with a focus on multimodal imaging. Two or more imaging modalities that could be used simultaneously or sequentially with capability to provide complimentary information are typically employed in a multimodal imaging approach. Efforts in optical imaging techniques to develop multimodal *in vivo* imaging systems include fluorescence life time microscopy (FLIM) and confocal reflectance microscopy (182), optical coherence tomography (OCT) and fluorescence imaging (183), FLIM and OCT (184) etc. These modalities provide biochemical as well as microstructural information about neoplastic abnormalities in live tissue that are otherwise not observed in single modality imaging. All are recent efforts and still under investigation. It is likely that an approach that offers a sense of molecular changes (fluorescence by FLIM for example) paired with a high-resolution method that also has the depth of imaging needed to image human tissue may present viable approaches (OCT has the desired imaging depth but lacks subcellular resolution while CRM has the resolution but may lack the depth). The choice of WF imaging with NLOM in the current work was guided by the high performance of NLOM as shown in early chapters (subcellular resolution to large depths with contrast based on endogenous molecules that change with neoplasia and features that mimic those seen in pathology all together resulting in high sensitivity and specificity) with the fact that WF imaging is already a clinically viable approach in which clinical instruments based on endogenous fluorescence already exist commercially.

The current study was performed to test efficacy of a multimodal imaging approach by using clinically viable wide-field fluorescence imaging and subsurface high-resolution NLOM to overcome the inherent limitations of both imaging modalities. Two wide-field fluorescence imaging techniques 1) wide-field autofluorescence (WF-AF) and 2) wide-field exogenous contrast based fluorescence (WFF) with a glucose sensor were tested for potential combination with NLOM. The WFF method was specifically targeted towards higher metabolic rate in neoplasia while WF-AF investigated changes in inherent fluorescence. Both of these methods indicate deregulation of metabolic processes in neoplasia and provides a quick screening of large surface area which is important especially in oral mucosa due to the presence of large heterogeneous lesions. However, both methods are associated with one common limitation, which is low resolution and inability to assess subsurface cytologic and microstructural abnormalities. To achieve detection of neoplasia with accuracy comparable to histopathology, one would require high-resolution deep tissue microscopy in addition to wide-field imaging. Therefore, in the overall multimodal approach the lack of resolution and imaging depth of wide-field imaging was compensated by NLOM while the inherent low field of view provided by NLOM was compensated by large area preliminary screening with wide-field imaging.

#### **7.1.1 Goal of the current study:**

The overall goal of this proof-of-principle study was to assess the potential performances of multiscale imaging combining wide-field fluorescence imaging techniques described in chapters 5 and 6 with subsurface high-resolution NLOM described in chapters 2, 3 and 4. Large area screening achieved by wide-field fluorescence (endogenous or exogenous contrast) imaging was complimented by layer-resolved NLOM that provided subsurface



microstructural information at subcellular resolution for assessment of cytologic and architectural abnormalities consistent with neoplasia. Instrumentation that combined these modalities was not constructed at this point as the goal of this work was to test the concept of multiscale imaging for further development. The specific goals of this chapter are as follows:

- 1) Test performance of univariate and multivariate models of WF-AF imaging combined with NLOM based features of neoplasia for effective delineation of normal and neoplastic tissue.
- 2) Examine the potential of univariate and multivariate models of WF-2NBDG imaging for glucose uptake combined with NLOM based features of neoplasia for effective delineation of normal and neoplastic tissue.
- 3) Test the effect of inflammation on performances of each statistical model to assess effectiveness of the multimodal approach with large area screening and microstructural assessment of neoplasia.

It is noted that for the assessments contained in this chapter, parameters derived from both WF and NLOM methods were obtained together and were analyzed, under the assumption that if a combined instrument were developed, automated algorithms could be developed to quickly analyze metrics obtained by both methods. This may differ from an approach in which only those areas visually highlighted by WF imaging would be evaluated by NLOM. The first scenario was chosen, to fully explore advantages and disadvantages of the combined techniques and possibly follow a more realistic first application of a multimodal approach in which a clinician chooses to test highlighted and un-highlighted areas that appear abnormal visually by

COE. Further studies will be required to explore a second scenario in which NLOM is guided solely by WF imaging.

## **7.2 Materials and Methods:**

**7.2.1 Animal model:** The previously described hamster models of oral precancer/cancer and inflammation were used for this study. Control (n = 7), inflammation (n = 4) and DMBA treated (n = 10) hamsters were anesthetized and prepared for *in vivo* imaging as described in previous chapters.

**7.2.2 *In vivo* multiscale wide-field and NLOM imaging:** WF-AF imaging was performed first using the method described in Chapter 5, followed by imaging of 2-NBDG uptake as described in Chapter 6 in the same animals. Sites selected by WF imaging were imaged by *in vivo* NLOM with MPAM and SHGM following established imaging protocols described in previous chapters (Chapters 2 and 3). For selection, all sites positive for any one wide-field imaging modality or both modalities were selected for microscopy. Sites that appeared abnormal by COE but not by WF imaging were also included in the study. Additional sites that showed no visual abnormality were selected to test false negative rates.

**7.2.3 Statistical analysis with generalized linear model:** Two wide-field image based parameters R/G intensity ratio and 2-NBDG fluorescence were individually combined with ECTI contour, basal nuclear density, basal nuclear area and basal nuclear CoVa using a generalized linear model in the statistical software R. Generalized linear model (GLM) is a variation of linear regression that accounts for response variables that do not show a normal distribution (185). This is achieved by using an additional argument “family” to describe the error distribution and

the link function in a regular linear regression model. GLM could be used when the responses variable is categorical having two possible outcomes (in this case normal or neoplastic). When the binary outcome variable is indicated by  $Y_i$  and modeled with a binomial family distribution the probability of either outcome is  $P(Y_i=1) = \pi_i$ . In a GLM this probability is modeled as a function of multiple variables. A GLM for two variables  $x$  and  $y$  is described by the following equation where  $\epsilon$ ,  $\alpha$  and  $\beta$  are coefficients of the model.

$$\text{logit}(\pi_i) = \epsilon + \alpha * x + \beta * y$$

For this study GLM with two variables including one wide-field image based (R/G ratio or 2-NBDG fluorescence) and one NLOM based (ECTI contour, basal nuclear density, basal nuclear area or basal nuclear CoVa) were created and coefficients for each variable were calculated from each model. P-values were also calculated to test significance of the GLM. Multivariate models using forward selection method were also created using R/G intensity ratio and cytologic features with addition of one cytologic parameter in each cycle until the largest separation between neoplastic and non-neoplastic tissue is found.

### 7.3 Results:

Figure 7.1 describes a potential work flow for combination of WF-AF imaging and NLOM. White light image of a DMBA treated hamster cheek pouch mucosa is shown in Fig. 7.1a. An advanced tumor is indicated by “\*” and surrounding areas showed alteration in color with visible white patches. WF-AF imaging (Fig. 7.1b) revealed increased red autofluorescence in the tumor indicated in Fig. 7.1a. Certain areas in the tumor however were dark due to light absorption from bleeding during sample preparation. Apart from the tumor there were small lesions that also showed alteration in autofluorescence and one such area is shown by a square outline in Fig. 7.1b. After selection of multiple such areas *in vivo* NLOM was performed in selected potentially neoplastic sites. Micrographs in Fig. 7.1c from NLOM showed cytologic abnormalities that were consistent with histopathology (Fig. 7.1d). After assessment of NLOM images keratinizing and extracellular collagen layers did not show any significant alterations while the epithelial layer showed cytologic atypia consistent with epithelial neoplasms. Corresponding histopathology corroborated with findings from NLOM indicated presence of moderate dysplasia.

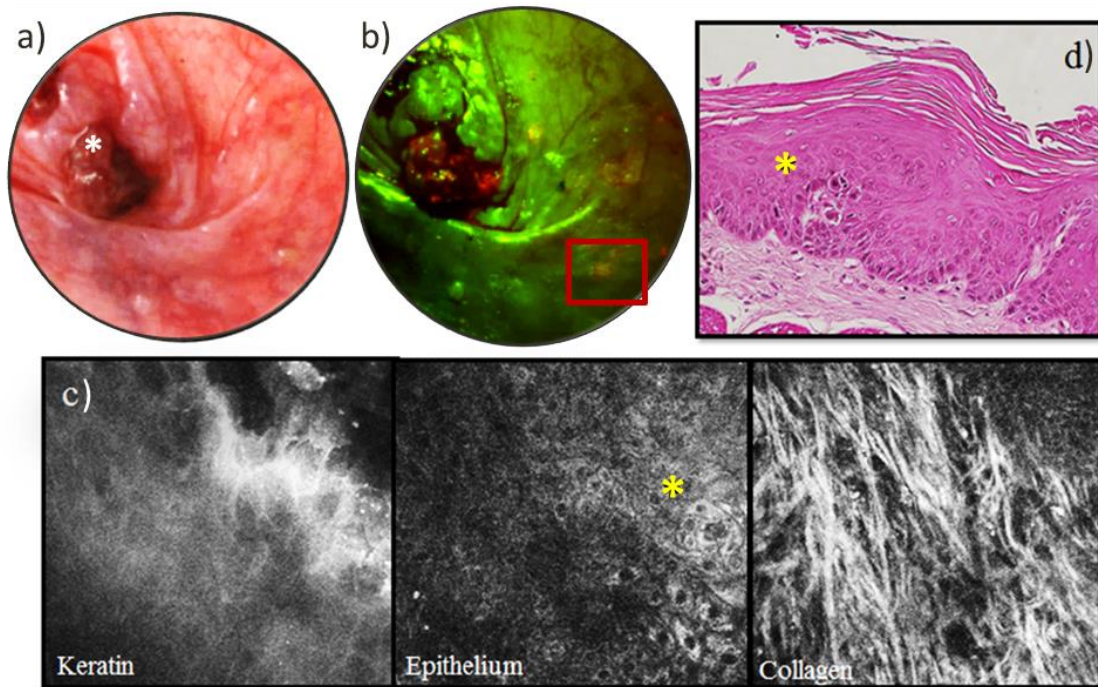


Figure 7.1: Multimodal imaging approach with sequential WF-AF imaging and *in vivo* NLOM is shown; a) white light image of a DMBA treated hamster oral mucosa; b) WF-AF image of the same mucosa; c) NLOM of the region of interest shown by red colored box in b). Single x-y micrographs from the keratinizing layer, epithelium and stroma is shown in three panels. d) H&E stained section of the imaged site. “\*” in a) shows an advanced tumor and “\*” in c) and d) indicates a cluster of neoplastic cells. It should be noted that similar cytologic features were observed in NLOM and histopathology.

**7.3.1 Potential for multivariate statistical assessment of WF-AF and NLOM based features of neoplasia:** Results from generalized linear models with multiscale imaging of WF-AF and NLOM are shown in Fig. 7.2. Four NLOM cytologic parameters (ECTI contour, basal nuclear density, basal nuclear area or basal nuclear CoVa) were tested for combination with WF-AF based parameter normalized R/G intensity ratio. ECTI contour and basal nuclear CoVa showed significant discrimination ( $p\text{-value} < 0.01$ ) between control and oral epithelial dysplasia (OED) in presence of inflammation. P-values for combination of basal nuclear density and basal nuclear

area with normalized R/G intensity ratio were 0.18 and 0.20 respectively which led to the exclusion of these two cytologic features from further statistical analyses and multivariate modeling. Fig. 7.2a and 7.2b shows GLM generated for WF-AF combined with basal nuclear CoVa in absence and presence of inflammation. It can be seen in Fig. 7.2b that after inclusion of the benign condition the coefficients of the model (represented by change in location of the dotted line) has changed. Out of 59 sites analyzed one site was miss-classified irrespective of presence of benign condition. Pathologically this site was a mild dysplasia which are typical associated with low risk for transformation into malignancy. The models for normalized R/G intensity ratio and basal nuclear CoVa in absence and presence of inflammation are described by the following equations:

$$\text{logit}(\pi_i) = -16.43 + 1.08 \cdot \text{RG} + 48.74 \cdot \text{CoVa} \dots\dots\dots \text{(Without inflammation)}$$

$$\text{logit}(\pi_i) = -17.98 + 0.68 \cdot \text{RG} + 55.25 \cdot \text{CoVa} \dots\dots\dots \text{(With inflammation)}$$

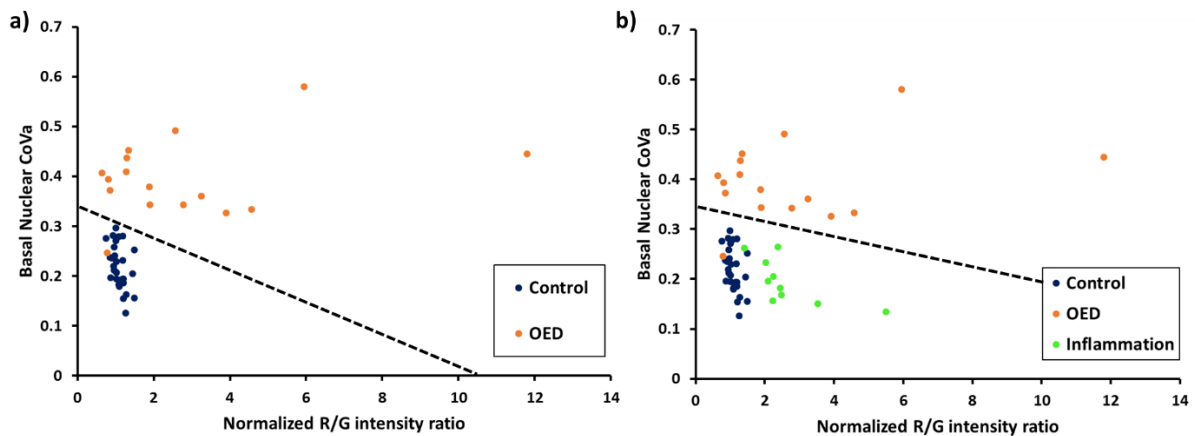


Figure 7.2: Generalize linear model by combining normalized R/G intensity ratio with basal nuclear CoVa in absence (a) and presence of inflammation (b). The dotted line in each panel shows a representation of the GLM.

Sensitivity and specificity of these models indiscriminating OED from normal tissue was measured from ROC curves shown in Fig. 7.3. GLMs for combined R/G intensity ratio and basal nuclear CoVa showed an AUC of 0.98 irrespective of inclusion or exclusion of inflammation. Sensitivity and specificity values (94% and 97% respectively) were also same for both cases. AUC of the GLM in presence of inflammation is significantly higher than the AUC for R/G intensity ratio (“AUC=0.74” as shown in chapter 5) as a stand alone paramter.

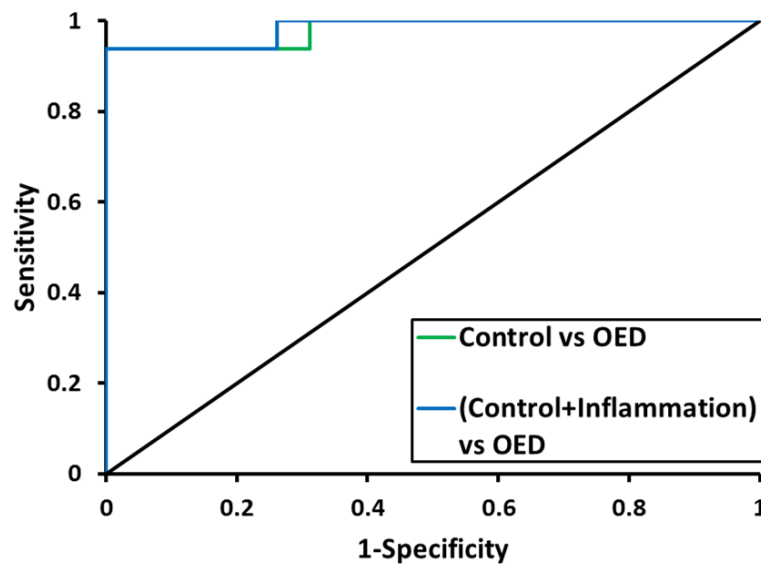


Figure 7.3: ROC curves for the generalized linear models of combined R/G intensity ratio and basal nuclear CoVa are shown in absence and presence of inflammation.

Fig. 7.4a and 7.4b shows GLM results when WF-AF was combined with the other NLOM parameter with significant p-value, ECTI contour. Results showed miss-classification of sites in both models in absence (Fig. 7.4a) and presence (Fig. 7.4b) of the benign condition. In this model 6 sites out of 59 were miss-classified when inflammation was present as compared to only one miss-classified site in the model with basal nuclear CoVa (Fig. 7.2b). Comparing Fig. 7.2b and 7.4b classification of normal and neoplastic sites was better when R/G intensity ratio

was combined with basal nuclear CoVa (Fig. 7.2) than when it was combined with ECTI contour (Fig. 7.4). The models for normalized R/G intensity ratio and ECTI contour in absence and presence of inflammation are described by the following equations:

$$\text{logit}(\pi_i) = -13.93 + 2.84 \cdot \text{RG} + 3.81 \cdot \text{ECTI contour} \dots\dots\dots \text{(Without inflammation)}$$

$$\text{logit}(\pi_i) = -6.63 + 0.58 \cdot \text{RG} + 1.71 \cdot \text{ECTI contour} \dots\dots\dots \text{(With inflammation)}$$

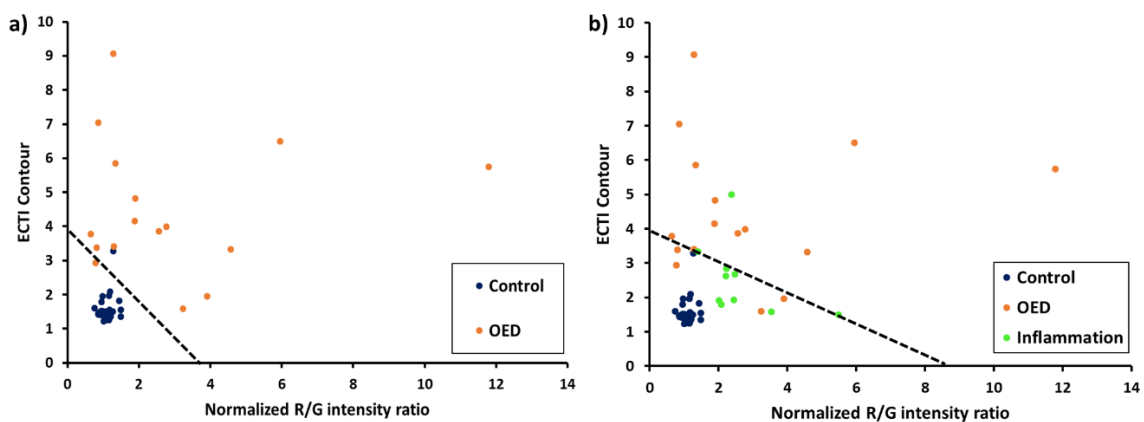


Figure 7.4: a) and b) shows generalized linear models when normalized R/G intensity ratios were combined with ECTI contour in absence and presence of inflammation respectively. The dotted line in each panel shows a representation of the GLM.

GLMs for R/G intensity ratio and ECTI contour parameters showed high sensitivity (94%) and specificity (97%) with an AUC of 0.99 when only control sites were compared with OED as shown by the ROC curves in Fig. 7.5. However, in presence of inflammation the overall performance was reduced (AUC = 0.95) with sensitivity and specificity values of 81% and 86% respectively. Performances of these GLMs in absence of inflammation were comparable between basal nuclear CoVa and ECTI contour. Inclusion of inflammation however resulted in reduction of performance of GLM with ECTI contour while the performance of GLM was



unaffected by presence of inflammation when basal nuclear CoVa was combined with R/G intensity ratio (Fig. 7.3).

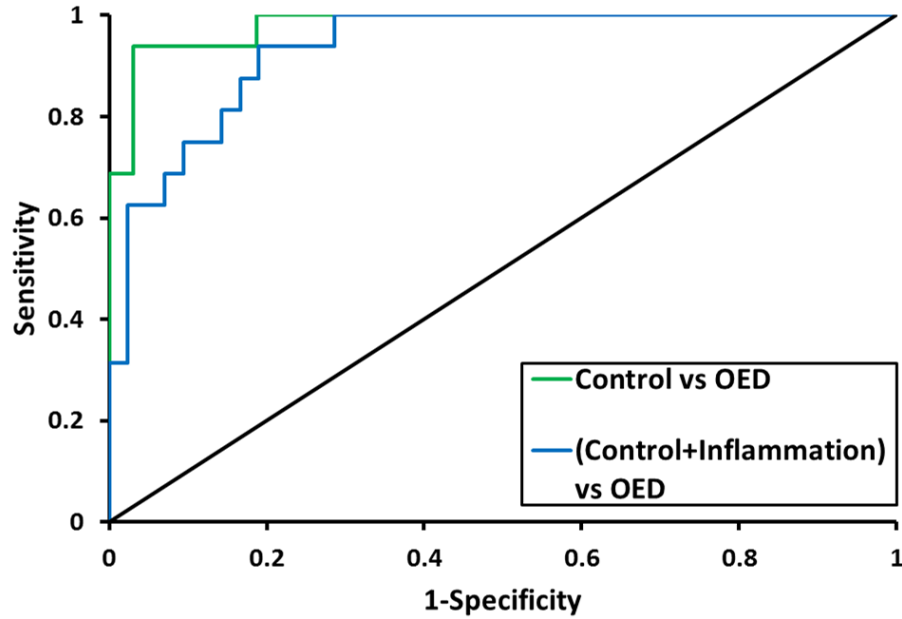


Figure 7.5: ROC curves for the generalized linear models of combined R/G intensity ratio and ECTI contour are shown in absence and presence of inflammation.

**7.3.2 Three parameter multivariate model:** A multivariate model using forward selection method for WF-AF and NLOM based parameters were also tested to develop more robust algorithms and the results are shown in Table 7.1. A statistical model with normalized R/G intensity ratio, ECTI contour and basal nuclear CoVa was found significant ( $p$ -value  $< 0.05$ ) in presence of benign condition. To test statistical performance of the multivariate model with three image parameters ROC analysis was performed which is shown in Fig. 7.6.

Table 1: Statistical models for multivariate linear regression of normalized R/G intensity ratio in combination with NLOM based cytologic parameters. Corresponding intercept, estimate and p-values shown.

Cytologic parameter tested with R/G	Intercept	Estimate	P
Multivariate Model	0.44		0.02
ECTI Contour		0.20	
Basal Nuclear CoVa		3.52	

In absence and presence of inflammation in the study population the multivariate model showed an AUC of 0.99. While sensitivity stayed unchanged at 94%, specificity of this model improved from 94% to 97% in presence of inflammation. Comparing ROCs and statistical performances it is clear that a model with three parameters including one wide-field imaging and two NLOM based parameters was more successful than single parameters from individual imaging modalities in discriminating OED from normal tissue in presence of inflammation.

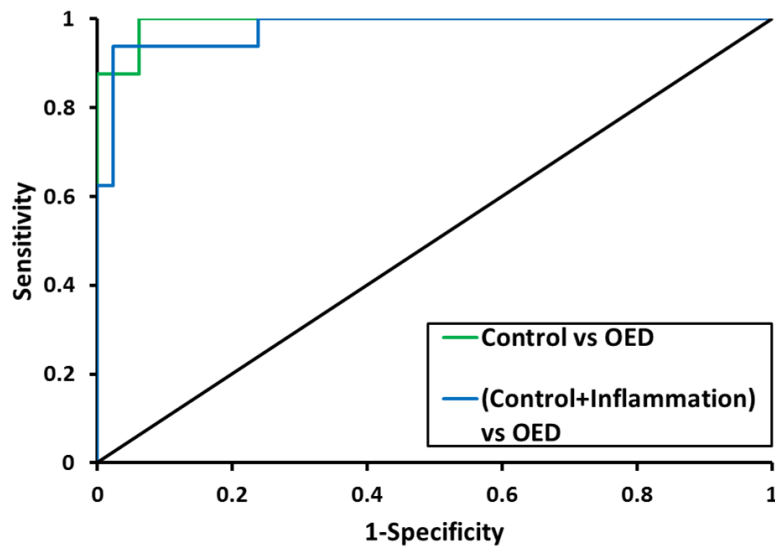


Figure 7.6: ROC curves for the multivariate model of combined R/G intensity ratio, basal nuclear CoVa and ECTI contour are shown in absence and presence of inflammation.

**7.3.3 Potential for combining a glucose analog (2-NBDG) based WF fluorescence imaging with NLOM based features of neoplasia (Pilot study):** Figure 7.7 describes a unique feature of WF imaging by 2-NBDG topical application. Wide-field images show cropped hamster buccal mucosa where no surface abnormality was visible in white light examination (Fig. 7.7a) and in WF-AF imaging (Fig. 7.7b). Interestingly after 2-NBDG application a small site was visible with higher accumulation of the glucose analog than the surrounding tissue. Follow up NLOM and histopathology showed cytologic features of mild dysplasia. Only histological section is shown in Fig. 7.7d for simplicity.

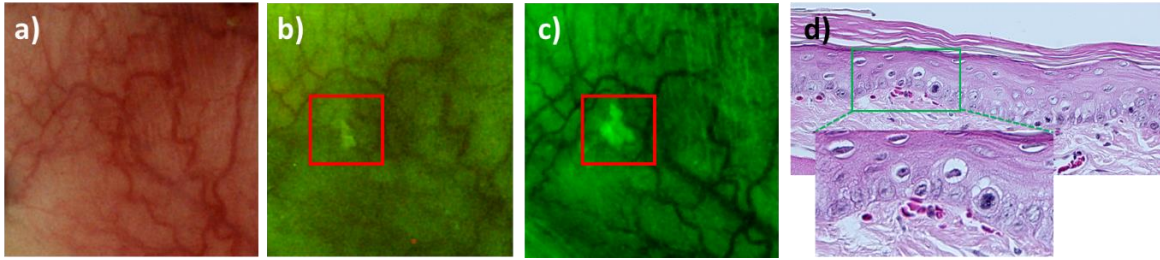


Figure 7.7: White light image (a), WF-AF image (b) and post 2-NBDG image (c) of a hamster cheek pouch are shown. A region of interest in c) is shown by the box around it; d) corresponding histology of the region of interest shown in c).

In a preliminary effort to test combinations of 2-NBDG based WF imaging and NLOM features scatter plots for normalized 2-NBDG fluorescence and basal nuclear CoVa were created in absence (Fig. 7.8a) and presence (Fig. 7.8b) of inflammation. Plots showed larger distribution of OED and inflammation while control sites were clustered together showing low 2-NBDG fluorescence emission and CoVa in basal nuclear size. A GLM efficiently separated OED from control irrespective of the presence of inflammation in the population as shown by the dotted line in Fig. 7.8a and 7.8b.

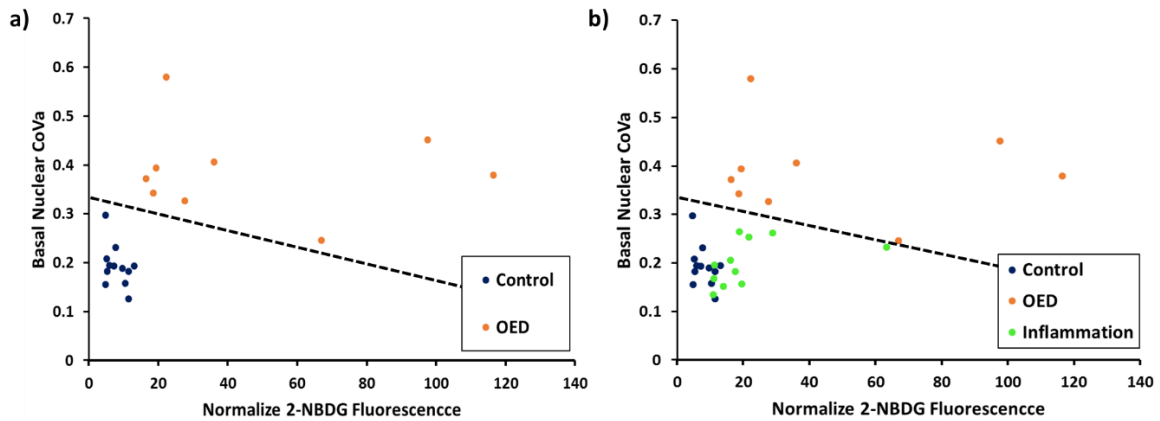


Figure 7.8: a) and b) shows generalized linear models when normalized 2-NBDG fluorescence was combined with basal nuclear CoVa in absence and presence of inflammation respectively. Dotted line in both panels shows a representation of the GLM.

Similar to WF-AF imaging a GLM for normalized 2-NBDG fluorescence was also tested with ECTI contour and the results are shown in Fig. 7.9. A GLM seemed to have separated OED and control tissue in absence of inflammation (Fig. 7.9a) however inclusion of inflammation altered the coefficients of the model in a way such that it allowed miss-grouped OEDs and inflammations as indicated by green points toward the right and orange points towards the left of the GLM (dotted line) in Fig. 7.9b. Additionally, when the models shown in Fig. 7.8b and 7.9b in presence of inflammation were compared 2-NBDG fluorescence uptake seemed to be more efficient in separating OED from control and inflammation in combination with basal nuclear CoVa than with ECTI contour.

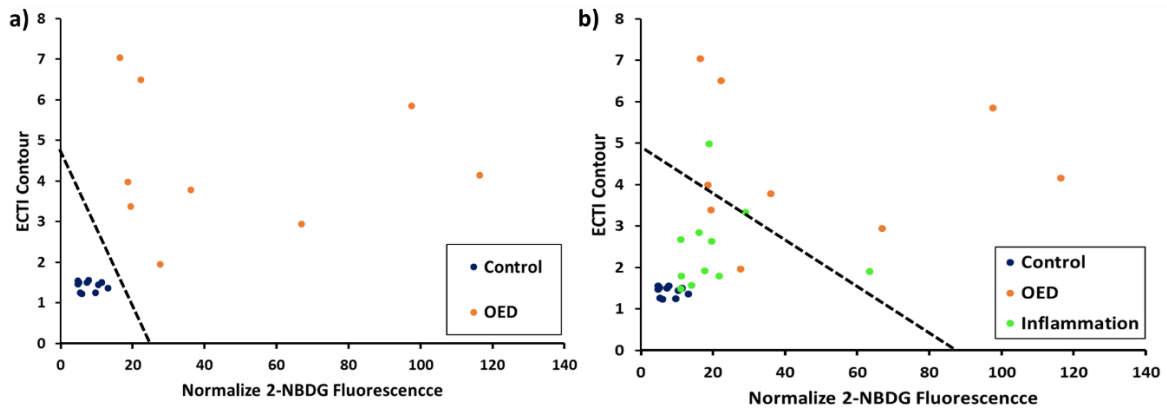


Figure 7.9: a) and b) shows generalized linear models when normalized 2-NBDG ratio was combined with ECTI contour in absence and presence of inflammation respectively. Dotted line in both panels shows a representation of the GLM.

## 7.4 Discussion:

The overall goal of this dissertation was explored in this chapter by testing combinations of WF fluorescence imaging with NLOM based features of neoplasia. Generalized linear models and multivariate linear models created by using one WF image based feature and one or more NLOM based features showed potential for discriminating neoplastic from non-neoplastic tissue in a heterogeneous sample population where inflammation was also present. Results presented in this chapter show the feasibility of a multiscale optical imaging approach for *in vivo* detection of oral epithelial neoplasia using quantitative features obtained from each modality.

Rigorous assessment of quantitative features of neoplasia obtained from NLOM have showed (Chapters 2, 3 and 4) high sensitivity and specificity. Limited field-of-view provided by NLOM would require for a prescreening of an oral cavity by a high sensitivity WF imaging modality. Since one probable approach for multimodal imaging would be where sites for NLOM will be detected based on alterations in WF fluorescence intensities, a WF imaging modality with high sensitivity was desired for effecting pairing with NLOM. For both WF fluorescence imaging approaches tested sensitivity was 83% (chapters 5 and 6) in presence of benign conditions, which made them suitable candidates for large area prescreening. An overall approach shown in Fig. 7.1 describes a potential workflow for combination of two imaging modalities. Areas of suspicion selected from white light examination and WF-AF imaging are subjected to *in vivo* NLOM and qualitative assessments showed cytologic features of neoplasia that correlated between NLOM and histopathology. In another approach metrics from both imaging modalities could be combined and evaluated simultaneously using automated algorithms to assess metrics from WF imaging and NLOM. This approach would require much larger sampling by NLOM but

could potentially show higher sensitivity and specificity than a sequential approach where NLOM is guided solely by WF imaging.

In an approach in which NLOM is guided by WF-AF imaging, performance of detection will inherently rely on fluorescence alterations observed in WF-AF imaging, and the approach relies on having high sensitivity. Improved specificity of this approach will however be reliant on efficacy of NLOM in detecting neoplastic features that are consistent with histopathology or hallmarks of cancer. Scatter plots shown in Fig. 7.2 and 7.4 shows a broad distribution of OED when WF-AF image parameter was combined with basal nuclear CoVa or ECTI contour respectively. This was expected because of the inherent heterogeneity of neoplasia. Additionally, the OED group consisted of dysplasia from all three stages (mild, moderate and severe), which possibly increased intra-group variability. As observed in Fig. 7.2, one dysplasia site was grouped with non-neoplastic group which was later found to be a case of mild dysplasia. Therefore, in the GLM of WF-AF and basal nuclear CoVa all high risk precancers were correctly identified which was reflected in an AUC of 0.98 in presence of inflammation. Similarly, combination of WF-AF with ECTI contour also showed a high AUC (0.95) however sensitivity (81%) and specificity (86%) values in presence of inflammation were slightly lower than the last GLM.

A multivariate model with forward selection of variables showed effective discrimination with AUC of 0.99 between neoplastic from non-neoplastic tissue in a heterogeneous sample population. This multivariate model was created with a combination of R/G intensity ratio, basal nuclear CoVa and ECTI contour. ROC analyses showed improved AUC of the model than individual R/G intensity ratio (AUC = 0.74) and ECTI contour (AUC = 0.91). Although basal nuclear CoVa alone (AUC = 0.99) performed as good as the multivariate model,

without a prescreening technique to guide NLOM detection of suspicious areas would be challenging.

A pilot study to test combination of WF 2-NBDG fluorescence imaging with NLOM was also performed that showed similar trends to WF-AF imaging. In depth statistical analyses however was not performed due to limited number of samples. GLMs for 2-NBDG fluorescence were created in combination with basal nuclear CoVa (Fig. 7.8) or ECTI contour (Fig. 7.9) and in both cases the model showed complete separation of neoplasia from non-neoplastic tissue when inflammation was not included (Fig. 7.8a and 7.9a). With inclusion of inflammation, the model for basal nuclear CoVa did not change at all (Fig. 7.8b), but it was greatly affected in the case of ECTI contour (Fig. 7.9b) to account for a broad distribution of inflamed sites. Although a complete statistical assessment of WF 2-NBDG fluorescence imaging in combination with NLOM was not performed Fig. 7.7 shows the potential strength of this technique as a prescreening tool. A dysplasia site was detected after 2-NBDG topical application from an area in the oral mucosa where white light examination and WF-AF did not reveal any observable feature to indicate presence of neoplasia. Further studies will be required to assess the full potential of 2-NBDG topical application in identifying these tissue sites that remain undetected by other prescreening methods.

In this proof-of-principle study sites chosen for NLOM were not entirely guided by WF imaging. WF positive and negative sites were included in the study to test the true sensitivity and specificity of this approach. In an approach where NLOM is entirely guided by fluorescence alterations from WF imaging, sensitivity of the approach would be limited by WF imaging and identification of false negatives could be reliant on COE. However, with the development of fast



laser scanning systems and new algorithms for real time mosaicking large are NLOM is becoming practical (186). A future application of this approach would be to develop multiscale imaging systems with automated algorithms for on spot assessment of quantitative metrics obtained from both methods. Studies shown in this dissertation indicated a viable approach for multiscale imaging with clinical instruments for WF autofluorescence imaging already commercially available.

In conclusion, results presented in this chapter shows the feasibility of a multiscale imaging approach for combined large area assessment and subsurface microscopic evaluation of neoplastic oral mucosa. Some of the major clinical challenges such as inability to detect *in vivo* cytologic and microstructural alterations, lack of contrast for low grade dysplasia, frequent identification of benign conditions as neoplasia could be avoided with this approach which is expected to lead to improvements in clinical management of oral cancer patients. Additionally, this approach could also be useful in long term monitoring of oral mucosal tissue in high risk population (patients with a history of tobacco or alcohol use or past history of oral cancer). Findings presented here will direct future research to develop novel diagnostic approaches for high risk oral precancers and cancers with high confidence in a heterogeneous microenvironment.

#### **Acknowledgements:**

I would like to thank Dr. Yong-fang Kuo and Dr. Yongquan Dong in the Office of Biostatistics at UTMB, Galveston for their help in statistical analysis.

# Chapter 8

## Summary, Future directions and Conclusions

### 8.1 Summary:

In summary, this work has explored new approaches for identifying image-based markers of epithelial neoplasia based on the deep in vivo microscopy method of NLOM and explored a strategy by which large area fluorescence could help highlight potentially suspicious sites for applying NLOM microscopy. This novel multiscale and multimodal approach provides a manner for large area screening with WF fluorescence imaging and subsurface microstructural assessment of select regions with noninvasive NLOM. Identification of image-based markers of neoplasia was driven by quantitative assessment of parameters with much focus placed on metrics associated with known pathological and biological hallmarks of neoplasia. After careful assessment of quantitative features of neoplasia using both imaging modalities image based parameters were identified and tested for potential combination into a single workflow with multivariate algorithms for robust and objective tissue classification. The work presented in this dissertation provides a strategy for multiscale fluorescence imaging that could be developed into a multimodal imaging device in the future. With the need for methods that can better guide where biopsies should be obtained in patients suspected of neoplasia, such as tool could lead to better clinical management. While this could include patients being screened in the clinic eventually, patients who could benefit most are those in which development of a tumor is high – in head and neck patients, recurrence occurs in more than 50% of patients within two

years of a successful treatment for a primary tumor (187, 188). There is no way to know when or where a secondary occurrence may occur, only that the chances are high. A tool that can be used to screen this population of patients could make a significant impact. Additionally, assessment of tumor/neoplastic tissue margin is clinically important during surgical resection. This aspect of clinical management of oral cancer was not explored in this research and needs to be considered in future efforts. The work of this thesis has established a potential route by which such a tool could be developed though more research will be required.

Methods of NLOM such as MPAM and SHGM were explored in chapters 2, 3 and 4 for a systematic quantitative multi-layer evaluation of early processes of neoplastic development in the oral mucosa. Mild, moderate and severe dysplasia sites were imaged with MPAM and SHGM *in vivo* in the animal model and several cytologic, extracellular and spectroscopic features were assessed with demonstration of novel ECTI features. Some of these features such as basal nuclear CoVa, ECTI contour and collagen density showed high sensitivity (87-95%) and specificity (88-98%) of discrimination between neoplastic and non-neoplastic tissue in a complex environment with presence of inflammation. These NLOM based features were demonstrated to be suitable for detection of neoplasia as standalone features as well as in combinations as shown in multivariate analyses (Fig. 2.8 and 3.9). Rigorous statistical tests for evaluation of sensitivity and specificity of MPAM spectroscopy based features were not performed due to limited number of samples. Since spectroscopy based features indicate intracellular balance of NADH and FAD, assessment of redox status in a tumor microenvironment may be correlated to its overall metabolic state which is shown by differential accumulation of the WF contrast agent 2-NBDG.

There is strong indication from the literature that NLOM can be made compact and portable such that realization of an intraoral NLOM device could be developed. A commercial NLOM for clinical imaging in skin is already available (189, 190) though that configuration based on an articulated arm is too bulky for the oral cavity. More compact fiber-based systems are also being developed in a number of labs (191-193). Finally, new lasers are becoming available for deeper imaging to >1mm (194-196). Nonetheless, despite the promise of developing a compact portable device, a challenge that will need to be overcome is the limited fields of view available to microscopy and the fact that choosing sites for these small fields would be limited by the method of visual inspection by COE alone. The development of improved electronics and image stitching algorithms for high-resolution imaging of large tissue areas are becoming realistic (197), but this would only partially address the challenge and still not be sufficient for full oral cavity inspection. The approach presented in this work aims to address these challenges, suggesting that COE could be supported by large area fluorescence to identify on a large scale, sites that are highly likely to harbor neoplasia.

Two approaches for large area fluorescence were approached, one based on endogenous fluorescence and similar to commercial devices but providing two spectral regions and quantitative assessment of parameters which the literature indicates to be superior to visual assessment of single color fluorescence. A second approach employed a fluorescent glucose analog to highlight areas of high glycolytic activity expected in neoplasia. Both methods of WF imaging (autofluorescence and exogenous contrast based) were used to improve contrast between normal and neoplastic areas from white light examination. Both approaches provided

high sensitivity and specificity. Though inflammation reduced specificity in both modalities, values were higher than studies have found for COE.

In this study WF imaging was considered as a potential tool to highlight areas of suspicion, and while both sensitivity and specificity are important, a criterion established was that the method have high sensitivity – in that even if it resulted in a high false positive rate (expected as shown in the literature), the ability to evaluate the tissue with NLOM shown in early chapters to maintain high sensitivity and specificity despite inflammation, could address the limitation of false positives. A high sensitivity screening method is often associated with large number of false positives which is shown in chapter 5 by the reduction of specificity when benign condition was present in the sample population. However, follow up NLOM is expected to reduce the number of false positives and the effect of benign conditions on image based detection techniques as shown in chapters 2, 3 and 4.

It was difficult to estimate the number of false negatives which such as neoplastic tissue without any observable alterations in WF fluorescence. These hard to catch OED/precancerous lesions may require a close attention while testing WF imaging approaches in future studies. One way to detect these lesions could be by using multiple WF imaging methods. One such example is shown in Figure 7 of chapter 7 where a small lesion with a histopathological diagnosis of mild dysplasia was seen after topical application of 2-NBDG while white light examination and WF-AF imaging did not reveal any detectable alteration in fluorescence.

Preliminary multimodal approaches explored in chapter 7 also indicated improved specificity and hence reduced false positives when WF and NLOM imaging modalities were quantitatively combined into a single algorithm. The analysis approach involved the use of

metrics from both imaging modalities together with a vision of potential combination of these imaging modalities into a single device for near simultaneous imaging. With recent developments in NLOM techniques, future efforts could enable faster large area scanning leading to possible multiscale imaging in near real time manner to make such simultaneous quantitative metrics possible. This approach assumes a clinician would choose areas that are highlighted by WF imaging as well as seemingly negative areas, potentially guided by visual cues, which is likely realistic. An alternative manner in which the combination of these methods can be explored is in a scenario in which NLOM is strictly guided by WF-AF, meaning NLOM imaging is conducted only of 'highlighted' sites. In that latter scenario, as mentioned in chapter 7, the sensitivity and to some degree specificity could be dictated by WF imaging. As the data suggests in chapters 5 and 6, both WF imaging techniques explored in this dissertation showed high sensitivity (> 80%) even in presence of confounding factors such as inflammation. Performance was superior than expected for COE as reported in the literature indicating sensitivity and specificity below 60%, indicating these are viable approaches for combination with NLOM. However, imaging and clinical workflow as well as improvements to the combined method Se and Sp should continue to be optimized in order to maximize the potential benefits of optical imaging for guiding biopsy selection.

One running theme of this dissertation is image based identification of cancer hallmarks - possible correlations of image features of neoplasia with well-established hallmarks of cancers were explored. Contrast for NLOM imaging was primarily based on autofluorescence from mitochondrial metabolites NADH, FAD and to some extent PpIX in higher grade dysplasia and SCC. Similarly contrast for WF-AF imaging relies on endogenous NADH, FAD, PpIX and collagen

fluorescence while an exogenous contrast was provided by 2-NBDG with molecular specificity to areas of higher glucose uptake. It is easily noted that these endogenous and exogenous fluorophores have potential to indicate metabolic status of a tissue which if altered is an important hallmark of cancer (“deregulating cellular energetics”). As described before in chapter 2 NLOM based identification of nuclear and cellular atypia could indicate uncontrolled epithelial proliferation which that may suggest actions of other cancer hallmarks such as “sustaining proliferative signaling”, “resisting cell death” and “evading growth suppressor”. Finally, focal thickening of epithelium, remodeling of ECTI and reduced collagen density as shown by quantitative features from *in vivo* NLOM suggests initial processes for a cancer hallmark, “activating invasion and metastasis”. These hallmarks were observed in the pre-invasive dysplasia stages when therapeutic interventions are typically successful.

As with the current clinical standard for diagnosis by pathology, it is likely that multiple parameters arising from the epithelium, ECTI and *lamina propria* will need to be evaluated together to inform as to the pathological status of human oral mucosa. In an attempt to observe the potential of WF fluorescence imaging and NLOM in distinguishing OEDs from normal tissue multivariate algorithms were tested by combining optical signatures of neoplasia. Several potential combinations of features were tested. In chapter 2, combination of collagen density with basal nuclear CoVa was tested, while in chapter 3 basal nuclear CoVa was combined with ECTI contour. In both cases reasonable classification of neoplastic tissue was seen in presence of benign conditions. However, as noted before (Chapter 1) NLOM is inherently restricted by the field-of-view that can be scanned during clinical examinations and adjunct methods for large area screening would be valuable in directing clinicians to areas of interests for follow up

microscopy. Therefore, a multimodal imaging approach to combine NLOM with a prescreening method by WF fluorescence imaging was evaluated in this dissertation. Preliminary studies with generalized linear models and multivariate classification algorithms as described in chapter 7, showed sufficient power for distinguishing neoplasia from normal and benign tissue. However, It will be of interest to explore multivariate combinations in animal models and humans (54, 93, 198) by principal component analysis or ten-fold cross validation including cytologic, biochemical and microstructural abnormalities detected in NLOM and large area screening as described in the following chapters. Careful investigation of these parameters collectively with cytologic and microstructural features presented here could provide a more comprehensive assessment of neoplastic alterations.

## **8.2 Future directions:**

The research presented in this dissertation has established a proof-of-concept multiscale imaging approach for detection of oral epithelial neoplasms. Concepts developed in this dissertation are expected to be beneficial in further development of multimodal image based cancer detection method as well as future research on understanding how neoplastic changes occur in epithelium. One may envision several directions that future research in this area could lead to.

**8.2.1 *In vivo* assessment of intracellular biochemical and metabolic events in neoplastic tissue:** Since NLOM based microstructural imaging relies on contrast from cellular metabolites such as NADH, FAD and PpIX assessment of fluorescence properties and spectral



characteristics of these fluorophores in native tissue could indicate the overall metabolic status of the tissue under surveillance. As described in chapter 4 *in vivo* spectroscopic assessment of neoplastic tissue showed variations in cytoplasmic autofluorescence which may be correlated to altered metabolic activity and potentially indicate levels of glycolysis and mitochondrial metabolism. It would therefore be important to further study the changes in these metabolites using fluorescence imaging and spectroscopy during development of neoplasia. Cellular redox parameters have been assessed under oxidative stress conditions and in cancer cell lines based on NADH and FAD fluorescence captured by NLOM (34, 199). While redox parameter has shown significant association with cancer induced metabolic deregulation it has not been studied in the context of a complex and heterogeneous microenvironment seen in a developing neoplastic tissue. Future efforts aimed towards understanding the fluorescence properties of these cellular metabolites under various stress conditions could help in detection of neoplastic processes with specificity to biochemical alterations.

**8.2.2 Continuous efforts in wide-field fluorescence imaging with external contrast agent for improved molecular specificity:** This dissertation explored a novel *in vivo* topical application method of contrast based wide-field fluorescence imaging with the long term goal being potential combination with NLOM based detection of neoplasia. Due to the lack of power a rigorous statistical assessment of 2-NBDG along with NLOM features was not performed. However, preliminary results shown in chapters 6 and 7 indicated promise for possible combination of these two modalities in a dual modality approach. Therefore, future studies with larger sample sizes may be required for in depth assessment of multiscale imaging with preliminary screening provided by 2-NBDG application. Additionally, since 2-NBDG is not FDA

approved for human use yet, which limits its *in vivo* use but may be tested in fresh biopsies from patients. Alternatively other optically active deoxy-glucose analogs may also be explored for potential multimodal imaging with microscopy techniques. Near infra-red active deoxy-glucose analogs have been developed (200) for improved depth of imaging which could prove to be useful in combination with confocal reflectance microscopy or OCT imaging. These molecular probes were not explored in this research because of potential interference with NLOM. There is also potential for targeting additional biomarkers such as MMP2, Integrin, EGFR etc. as a source of contrast for wide-field fluorescence imaging. However, low specificity and heterogeneity of expression of these biomarkers are not always a reliable indicator of neoplasia. Nonetheless this research established a platform for multiscale imaging approaches using wide-field imaging and microscopy. Future efforts are still required to identify the optimum imaging modalities, image parameters and features of neoplasia for the development of an effective biopsy guidance method that could be translated into clinics.

**8.2.3 Assessment of noninvasive NLOM in human oral mucosa:** Investigating NLOM based microstructural and biochemical features of neoplasia as potential diagnostic metrics would require additional effort, including demonstration in human mucosa. The hamster model provided the ability for noninvasive *in-vivo* imaging in a buccal mucosa which is similar in microstructure to the human buccal mucosa, floor of the mouth and the ventral surface of the tongue in human oral cavity (87), all common sites for neoplastic transformation. The objective lens chosen for NLOM studies was most appropriate for hamster buccal mucosa, however depths beyond the approximate ~200  $\mu\text{m}$  evaluated in this study would be needed for humans with epithelial thickening beyond this limit (e.g. high grade OED). SHGM has been performed on

human oral mucosa (201) and feasible using longer working distance objectives. It is anticipated that information gained from NLOM could be used to develop improved diagnostic approaches either by other optical methods reliant on understanding of cellular/structural changes or even directly using NLOM through endoscopy (202). The application of depth resolved optical imaging to human epithelial tissues (30, 203) including MPAM and SHGM (93, 201) and recent advancements that are pushing the depth limits of NLOM and miniaturization (186) support the feasibility of using NLOM in human tissue in the future.

It will also be of interest to examine the application of NLOM based features to other sites of the human oral cavity. Different anatomical locations of the oral cavity have different microstructure such as non-keratinized stratified squamous epithelium of the cheek and keratinized stratified squamous epithelium of the hard palate show rete-processes in the ECTI under normal condition (204). Other cytologic and architectural features also vary from one anatomic location to other. In addition to oral mucosa future research in other common sites for epithelial neoplasms such as in esophagus or cervicovaginal areas could also benefit from the concepts of multiscale imaging developed in this dissertation. Careful assessment of individual tissue types would be required for effective feature selection and potential combination with wide-field imaging modalities.

**8.2.4 Development of compact multimodal imaging device for screening of oral mucosa:** This dissertation described a viable noninvasive fluorescence imaging strategy for multiscale image acquisition and analysis of oral precancers and cancers in an animal model. However, further tests of this approach in a clinical setting would require development of a compact hand held system capable of performing wide-field fluorescence imaging as well as

NLOM. Development of such a device will involve significant efforts in engineering and rigorous testing. An endoscopic multimodal imaging probe will enable us to access otherwise difficult to reach sites in the oral cavity especially back of the throat, larynx etc. However, combining these two imaging modalities into a single system could be challenging in terms of achieving the optimum field of view for wide-field screening and being able to acquire high-resolution subsurface microscopy. A combined dual modality system may compromise the resolution and imaging depth of NLOM to some extent, but a tradeoff between performances of two modalities could lead to an effective screening device for oral precancers and cancers. With optical fiber based NLOM endoscopic systems being currently developed (205, 206) for deep tissue imaging with high resolution it would be an important step forward to combine wide-field imaging capabilities to these systems and test their performances in ex vivo human tissue and eventually in vivo translation into clinics.

### **8.3 Conclusions:**

A technique for *in vivo* measurement of optical signatures of neoplasia was described in this dissertation that works on an approach based on large area preliminary screening followed by subsurface microstructural assessment of oral mucosal tissue. Preliminary tests indicated potential for this multimodal approach, however, clinical application of this approach would require demonstration of full potential of optical imaging of live tissue and in depth understanding of biological significances of optical signatures were beyond the scope of this dissertation.

## **Appendix: Potential translation of NLOM in *ex vivo* human oral squamous cell carcinoma**

I would like to thank Tyra Brown and Paula Villarreal for their contributions in sample collection, image acquisition and analysis that are included in this chapter.

The results contained in this Appendix represent results from pilot assessments to evaluate the potential translation of NLOM to imaging of oral neoplasia in humans. Studies on *ex vivo* human tissues were approved by the institutional review board (IRB) and supported by the Cancer Prevention Research Institute of Texas.

Pilot NLOM studies on *ex vivo* human oral cavity and oropharyngeal tissues showed promise for depth resolved assessment of neoplastic cytologic features similar to ones observed in *in vivo* hamster studies as well as conventional histopathology of OSCC.

**Human Tissues:** Studies on *ex vivo* human tissues were approved by the institutional review board (IRB) of the University of Texas Medical Branch protocol #11-256 (Microscopic Imaging of Resected Head and Neck Cancer Tissues) in which tissues not needed for diagnosis (considered discarded tissues) were obtained from resected specimens of patients undergoing therapeutic surgical resections for oral cancer. Samples from discarded portions included sections that appeared clinically normal and visually consistent with OSCC. Samples were placed immediately in dye-free DMEM media and imaged.

Tissues collected from resected OSCC tissues included floor of the mouth ( $n = 3$ ) and larynx ( $n = 3$ ). For each patient areas appearing clinically normal and an OSCC area were obtained and imaged fresh with NLOM. Three-dimensional layer resolved MPAM-SHGM was performed (Fig. A1) from three regions of interest for each sample and cytologic features were assessed by qualitative and quantitative methods that were established in hamster studies described in Chapters 2 and 3.

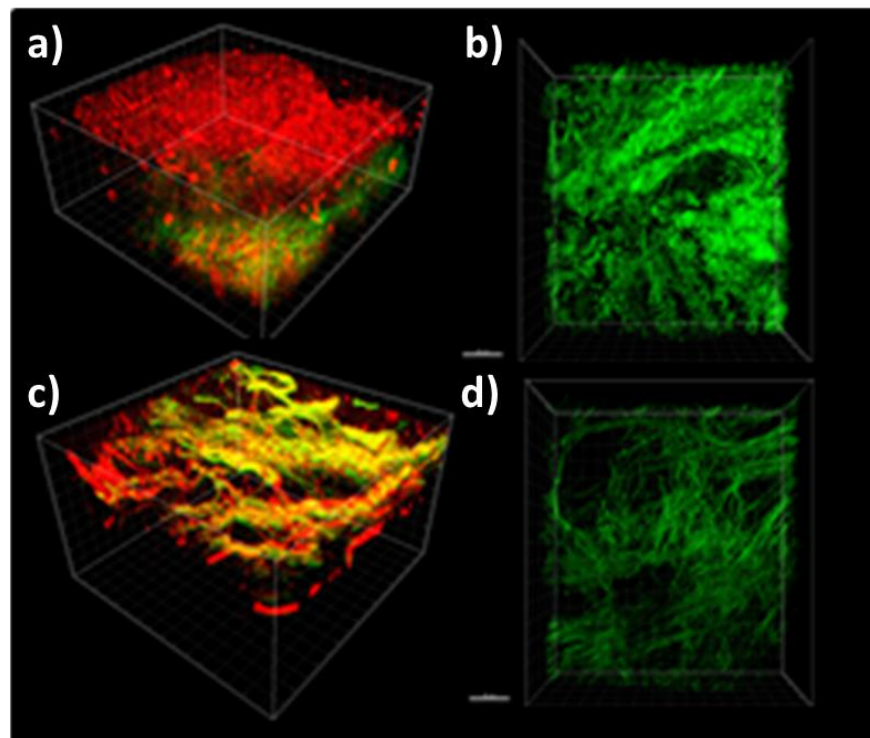


Figure A1: Invasive cancer of larynx. A1a) Three-dimensional volume of normal larynx with MPAM-SHGM; A1b) volume reconstruction of SHGM from extracellular matrix of normal larynx; A1c) MPAM-SHGM volume reconstruction of invasive OSCC of human larynx; A1d) Extracellular collagen SHGM of the invasive OSCC. Red: MPAM; Green: SHGM. Scale bar 50  $\mu\text{m}$ .

Fig. A1 represents three-dimensional volumes obtained from NLOM of normal (Fig. A1a and A1b) and invasive OSCC (Fig. A1c and A1d) in human larynx tissue. Fig. A1a shows epithelial

organization while thick collagen fibers were observed in the extracellular matrix (Fig. A1b). OSCC showed loss of organized epithelial cells (Fig. A1c) as well as abnormalities in the extracellular matrix (Fig. A1d) such as reduced density of collagen and thin collagen fibers that are consistent with invasive OSCC.

Fig. A2 shows micrographs from OSCC and corresponding normal epithelium with abnormal cytology in OSCC indicated by arrows. In the basal epithelial layer, nuclear and cellular overcrowding was observed in OSCC (Fig. A2d) when compared with normal mucosa (Fig. A2b).

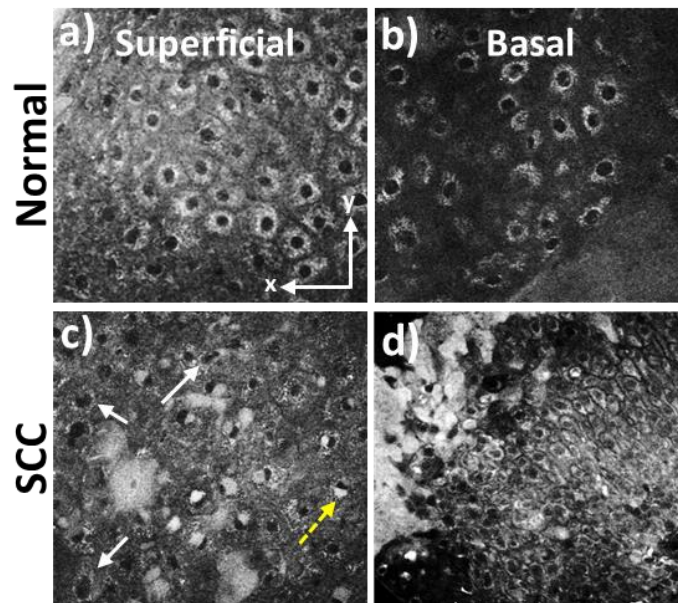


Fig. A2: (a-d) NLOM Micrographs of superficial and basal epithelium from OSCC and corresponding normal mucosa of floor of the mouth. Arrows in c) indicate cytologic features consistent with neoplasia including different sized nuclei and increased numbers of multinucleated cells.

Cytologic features of neoplasia that were observed in hamster studies were also observed in the human OSCC. Table 1 provides a summary of NLOM based cytologic features observed in clinical samples. Anisonucleosis/anisocytosis and nuclear pleomorphisms were most

consistent and promising in both tissue types studied (floor of the mouth and larynx). Multinucleated epithelial cells were observed in OSCC that may indicate increased rate of mitoses. Additional features of neoplasia such as premature keratinization, nucleated keratinocytes, perinuclear localization of mitochondrial autofluorescence (dotted arrow in Fig. A2c) potentially indicating clustering of mitochondria were also observed.

Table A1: Cytologic features identified by NLOM in ex vivo human OSCC from floor of mouth

Cytologic Feature	N (n=6)	C (n=6)
Anisonucleosis/Anisocytosis <sup>1</sup>	0	6
Overcrowding/Discohesion	1	3
Nuclear pleomorphism <sup>2</sup>	1	6
Multinucleated cells	3	5

C, squamous cell carcinoma; N, normal oral epithelium.

<sup>1</sup>Defined as abnormal variation in nuclear size.

<sup>2</sup>Defined as abnormal variation in nuclear shape.

Coefficient of variation (CoVa) in nuclear area as published recently in hamster studies (207) was also measured from NLOM images of floor of mouth biopsies. Fig. A3a shows CoVa in nuclear area from non-tumor/clinically normal and tumor/OSCC sites for each patient. CoVa for all three patients was increased in OSCC compared to corresponding normal epithelium. Fig. A3b shows average CoVa values for all non-tumor/clinically normal and tumor/OSCC indicating statistically significant increase in abnormal variation in nuclear size in OSCC.



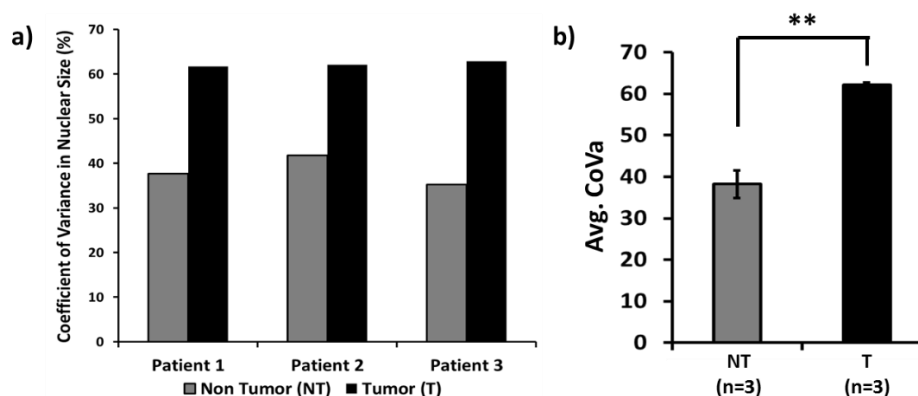


Figure A3: Coefficient of variation (CoVa) in nuclear area; a) non-tumor/clinically normal and tumor/OSCC biopsies for individual patients; b) all OSCC and normal biopsies combined. \*\*  $p < 0.01$

Analysis of samples is ongoing at the time of writing of this thesis. Further, histological evaluation is underway. Hematoxylin and eosin staining of tissues sections has been performed and are awaiting pathological confirmation of results.

Preliminary results presented here indicated potential clinical translation of the methods explored in this research using NLOM. Studies based on the hamster model of oral neoplasia established a platform for cytologic and microstructural assessment of neoplastic transformations in an *in vivo* system. Recent results on *ex vivo* biopsies from human OSCC is showing promise for similar NLOM based cytologic features in detection of neoplasia. The samples used in this study were from patients undergoing therapeutic resections so the presence of advanced cancer was already known. The advantage of this is that despite any depth imaging limitations optical methods may encounter, features near the 'surface' of the tissue within a few hundred micrometers may be quantitatively evaluated and at least in these preliminary assessments show potential for delineating normal from neoplasia. The tissues can also represent multiple stages, with samples that appear as 'clinically' normal potentially having

abnormalities due to transition areas between normal and cancer that will be revealed in histology. These studies are ongoing and assessment of other microscopic and widefield imaging capabilities discussed in the chapters of this thesis are planned in future efforts.

## References:

1. Vigneswaran N, Williams MD. Epidemiologic trends in head and neck cancer and aids in diagnosis. *Oral and maxillofacial surgery clinics of North America*. 2014;26(2):123-41. Epub 2014/05/06. doi: 10.1016/j.coms.2014.01.001. PubMed PMID: 24794262; PMCID: PMC4040236.
2. Foundation TOC. [www.oralcancerfoundation.org](http://www.oralcancerfoundation.org).
3. Neville BW, Day TA. Oral cancer and precancerous lesions. *CA: a cancer journal for clinicians*. 2002;52(4):195-215. Epub 2002/07/26. PubMed PMID: 12139232.
4. Silverman S, Jr., Gorsky M. Epidemiologic and demographic update in oral cancer: California and national data--1973 to 1985. *J Am Dent Assoc*. 1990;120(5):495-9. Epub 1990/05/01. PubMed PMID: 2335670.
5. Artese L, Rubini C, Ferrero G, Fioroni M, Santinelli A, Piattelli A. Microvessel density (MVD) and vascular endothelial growth factor expression (VEGF) in human oral squamous cell carcinoma. *Anticancer research*. 2001;21(1B):689-95. Epub 2001/04/13. PubMed PMID: 11299827.
6. White WM, Rajadhyaksha M, Gonzalez S, Fabian RL, Anderson RR. Noninvasive imaging of human oral mucosa in vivo by confocal reflectance microscopy. *The Laryngoscope*. 1999;109(10):1709-17. Epub 1999/10/16. doi: 10.1097/00005537-199910000-00029. PubMed PMID: 10522947.
7. Napier SS, Speight PM. Natural history of potentially malignant oral lesions and conditions: an overview of the literature. *Journal of oral pathology & medicine : official publication of the International Association of Oral Pathologists and the American Academy of Oral Pathology*. 2008;37(1):1-10. Epub 2007/12/25. doi: 10.1111/j.1600-0714.2007.00579.x. PubMed PMID: 18154571.
8. Mortazavi H, Baharvand M, Mehdipour M. Oral potentially malignant disorders: an overview of more than 20 entities. *Journal of dental research, dental clinics, dental prospects*. 2014;8(1):6-14. Epub 2014/07/16. doi: 10.5681/jodddd.2014.002. PubMed PMID: 25024833; PMCID: PMC4091702.
9. Sloan P, Picardo M, Schor SL. The structure and function of oral mucosa. *Dental update*. 1991;18(5):208-12. Epub 1991/06/01. PubMed PMID: 1884872.
10. Winning TA, Townsend GC. Oral mucosal embryology and histology. *Clinics in dermatology*. 2000;18(5):499-511. Epub 2001/01/03. PubMed PMID: 11134845.
11. Squier CA, Kremer MJ. Biology of oral mucosa and esophagus. *Journal of the National Cancer Institute Monographs*. 2001(29):7-15. Epub 2001/11/06. PubMed PMID: 11694559.
12. Dale BA, Salonen J, Jones AH. New approaches and concepts in the study of differentiation of oral epithelia. *Critical reviews in oral biology and medicine : an official publication of the American Association of Oral Biologists*. 1990;1(3):167-90. Epub 1990/01/01. PubMed PMID: 1717003.
13. Rich AM, Nataatmadja MI, Reade PC. Basal cell nuclear size in experimental oral mucosal carcinogenesis. *British journal of cancer*. 1991;64(1):96-8. Epub 1991/07/01. PubMed PMID: 1906729; PMCID: 1977312.
14. Potten CS, Morris RJ. Epithelial stem cells in vivo. *Journal of cell science Supplement*. 1988;10:45-62. Epub 1988/01/01. PubMed PMID: 3077942.

15. Boysen M, Reith A. Discrimination of various epithelia by simple morphometric evaluation of the basal cell layer. A light microscopic analysis of pseudostratified, metaplastic and dysplastic nasal epithelium in nickel workers. *Virchows Archiv B, Cell pathology including molecular pathology*. 1983;42(2):173-84. Epub 1983/01/01. PubMed PMID: 6133390.
16. Sutinen M, Kainulainen T, Hurskainen T, Vesterlund E, Alexander JP, Overall CM, Sorsa T, Salo T. Expression of matrix metalloproteinases (MMP-1 and -2) and their inhibitors (TIMP-1, -2 and -3) in oral lichen planus, dysplasia, squamous cell carcinoma and lymph node metastasis. *British journal of cancer*. 1998;77(12):2239-45. Epub 1998/07/02. PubMed PMID: 9649139; PMCID: 2150416.
17. Zhang Y, Wang C, Mizukami H, Itoh H, Kusama M, Ozawa K, Jinbu Y. Increased expression and activation of matrix metalloproteinase-2 (MMP-2) in O-1N: hamster oral squamous cell carcinoma with high potential lymph node metastasis. *Journal of experimental & clinical cancer research : CR*. 2006;25(3):417-23. Epub 2006/12/16. PubMed PMID: 17167983.
18. Rivera C, Venegas B. Histological and molecular aspects of oral squamous cell carcinoma (Review). *Oncology letters*. 2014;8(1):7-11. Epub 2014/06/25. doi: 10.3892/ol.2014.2103. PubMed PMID: 24959211; PMCID: PMC4063640.
19. Ankur Bhargava SS, Monali Chalishazar. Histopathological Grading Systems In Oral Squamous Cell Carcinoma: A Review *International Journal of Oral Health*. 2010;2(4).
20. Mehrotra R, Gupta DK. Exciting new advances in oral cancer diagnosis: avenues to early detection. *Head & neck oncology*. 2011;3:33. Epub 2011/07/30. doi: 10.1186/1758-3284-3-33. PubMed PMID: 21798030; PMCID: PMC3170277.
21. Downer MC, Moles DR, Palmer S, Speight PM. A systematic review of test performance in screening for oral cancer and precancer. *Oral oncology*. 2004;40(3):264-73. Epub 2004/01/30. PubMed PMID: 14747057.
22. Awan KH, Morgan PR, Warnakulasuriya S. Assessing the accuracy of autofluorescence, chemiluminescence and toluidine blue as diagnostic tools for oral potentially malignant disorders--a clinicopathological evaluation. *Clinical oral investigations*. 2015;19(9):2267-72. Epub 2015/03/26. doi: 10.1007/s00784-015-1457-9. PubMed PMID: 25804887.
23. Bobdey S, Balasubramaniam G, Kumar A, Jain A. Cancer Screening: Should Cancer Screening be Essential Component of Primary Health Care in Developing Countries? *International journal of preventive medicine*. 2015;6:56. Epub 2015/08/04. doi: 10.4103/2008-7802.160053. PubMed PMID: 26236443; PMCID: 4505397.
24. Ye X, Zhang J, Tan Y, Chen G, Zhou G. Meta-analysis of two computer-assisted screening methods for diagnosing oral precancer and cancer. *Oral oncology*. 2015;51(11):966-75. Epub 2015/09/20. doi: 10.1016/j.oraloncology.2015.09.002. PubMed PMID: 26384539.
25. Luo X, Xu H, He M, Han Q, Wang H, Sun C, Li J, Jiang L, Zhou Y, Dan H, Feng X, Zeng X, Chen Q. Accuracy of autofluorescence in diagnosing oral squamous cell carcinoma and oral potentially malignant disorders: a comparative study with aero-digestive lesions. *Scientific reports*. 2016;6:29943. Epub 2016/07/16. doi: 10.1038/srep29943. PubMed PMID: 27416981; PMCID: 4945954.
26. Patton LL, Epstein JB, Kerr AR. Adjunctive techniques for oral cancer examination and lesion diagnosis: a systematic review of the literature. *J Am Dent Assoc*. 2008;139(7):896-905; quiz 93-4. Epub 2008/07/03. PubMed PMID: 18594075.

27. Shin D, Vigneswaran N, Gillenwater A, Richards-Kortum R. Advances in fluorescence imaging techniques to detect oral cancer and its precursors. *Future Oncol.* 2010;6(7):1143-54. Epub 2010/07/14. doi: 10.2217/fon.10.79. PubMed PMID: 20624126; PMCID: 2929485.
28. Hanahan D, Weinberg RA. Hallmarks of cancer: the next generation. *Cell.* 2011;144(5):646-74. doi: 10.1016/j.cell.2011.02.013. PubMed PMID: 21376230.
29. Lee CK, Chi TT, Wu CT, Tsai MT, Chiang CP, Yang CC. Diagnosis of oral precancer with optical coherence tomography. *Biomed Opt Express.* 2012;3(7):1632-46. Epub 2012/07/19. doi: 10.1364/BOE.3.001632. PubMed PMID: 22808434; PMCID: 3395487.
30. Kurugol S, Dy JG, Rajadhyaksha M, Gossage KW, Weissman J, Brooks DH. Semi-automated Algorithm for Localization of Dermal/ Epidermal Junction in Reflectance Confocal Microscopy Images of Human Skin. *Proceedings of SPIE--the International Society for Optical Engineering.* 2011;7904:7901A. Epub 2011/06/29. doi: 10.1117/12.875392. PubMed PMID: 21709746; PMCID: 3120112.
31. Roblyer D, Kurachi C, Stepanek V, Schwarz RA, Williams MD, El-Naggar AK, Lee JJ, Gillenwater AM, Richards-Kortum R. Comparison of multispectral wide-field optical imaging modalities to maximize image contrast for objective discrimination of oral neoplasia. *Journal of biomedical optics.* 2010;15(6):066017. Epub 2011/01/05. doi: 10.1117/1.3516593. PubMed PMID: 21198191; PMCID: PMC3013151.
32. Obstoy B, Salaun M, Veresezan L, Sesboue R, Bohn P, Boland FX, Thiberville L. Safety and performance analysis of acriflavine and methylene blue for in vivo imaging of precancerous lesions using fibered confocal fluorescence microscopy (FCFM): an experimental study. *BMC pulmonary medicine.* 2015;15:30. Epub 2015/04/17. doi: 10.1186/s12890-015-0020-4. PubMed PMID: 25880748; PMCID: PMC4382935.
33. Wilder-Smith P, Osann K, Hanna N, El Abbadi N, Brenner M, Messadi D, Krasieva T. In vivo multiphoton fluorescence imaging: a novel approach to oral malignancy. *Lasers in surgery and medicine.* 2004;35(2):96-103. doi: 10.1002/lsm.20079. PubMed PMID: 15334611.
34. Skala MC, Riching KM, Gendron-Fitzpatrick A, Eickhoff J, Eliceiri KW, White JG, Ramanujam N. In vivo multiphoton microscopy of NADH and FAD redox states, fluorescence lifetimes, and cellular morphology in precancerous epithelia. *Proceedings of the National Academy of Sciences of the United States of America.* 2007;104(49):19494-9. Epub 2007/11/29. doi: 10.1073/pnas.0708425104. PubMed PMID: 18042710; PMCID: 2148317.
35. Sharma P, Verma Y, Sahu K, Kumar S, Varma AV, Kumawat J, Gupta PK. Human ex-vivo oral tissue imaging using spectral domain polarization sensitive optical coherence tomography. *Lasers Med Sci.* 2017;32(1):143-50. Epub 2016/11/04. doi: 10.1007/s10103-016-2096-3. PubMed PMID: 27807650.
36. Hamdoon Z, Jerjes W, McKenzie G, Jay A, Hopper C. Optical coherence tomography in the assessment of oral squamous cell carcinoma resection margins. *Photodiagnosis and photodynamic therapy.* 2016;13:211-7. Epub 2015/07/27. doi: 10.1016/j.pdpdt.2015.07.170. PubMed PMID: 26210067.
37. Pande P, Shrestha S, Park J, Serafino MJ, Gimenez-Conti I, Brandon J, Cheng YS, Applegate BE, Jo JA. Automated classification of optical coherence tomography images for the diagnosis of oral malignancy in the hamster cheek pouch. *Journal of biomedical optics.* 2014;19(8):086022. doi: 10.1117/1.JBO.19.8.086022. PubMed PMID: 25162909; PMCID: PMC4145245.

38. Tsai MT, Lee HC, Lu CW, Wang YM, Lee CK, Yang CC, Chiang CP. Delineation of an oral cancer lesion with swept-source optical coherence tomography. *Journal of biomedical optics*. 2008;13(4):044012. Epub 2008/11/22. doi: 10.1117/1.2960632. PubMed PMID: 19021340.
39. Wang HW, Chen Y. Clinical applications of optical coherence tomography in urology. *Intravital*. 2014;3(1):e28770. Epub 2014/04/30. doi: 10.4161/intv.28770. PubMed PMID: 28243507; PMCID: PMC5312717.
40. Hsieh YS, Ho YC, Lee SY, Chuang CC, Tsai JC, Lin KF, Sun CW. Dental optical coherence tomography. *Sensors (Basel, Switzerland)*. 2013;13(7):8928-49. Epub 2013/07/17. doi: 10.3390/s130708928. PubMed PMID: 23857261; PMCID: PMC3758630.
41. Cinotti E, Labeille B, Cambazard F, Thuret G, Gain P, Perrot JL. Reflectance confocal microscopy for mucosal diseases. *Giornale italiano di dermatologia e venereologia : organo ufficiale, Societa italiana di dermatologia e sifilografia*. 2015;150(5):585-93. Epub 2015/06/24. PubMed PMID: 26099354.
42. Abbaci M, Breuskin I, Casiraghi O, De Leeuw F, Ferchiou M, Temam S, Laplace-Builhe C. Confocal laser endomicroscopy for non-invasive head and neck cancer imaging: a comprehensive review. *Oral oncology*. 2014;50(8):711-6. Epub 2014/06/17. doi: 10.1016/j.oraloncology.2014.05.002. PubMed PMID: 24932530.
43. Helmchen F, Denk W. Deep tissue two-photon microscopy. *Nature methods*. 2005;2(12):932-40. Epub 2005/11/22. doi: 10.1038/nmeth818. PubMed PMID: 16299478.
44. Zipfel WR, Williams RM, Webb WW. Nonlinear magic: multiphoton microscopy in the biosciences. *Nature biotechnology*. 2003;21(11):1369-77. Epub 2003/11/05. doi: 10.1038/nbt899. PubMed PMID: 14595365.
45. Williams RM, Zipfel WR, Webb WW. Multiphoton microscopy in biological research. *Current opinion in chemical biology*. 2001;5(5):603-8. Epub 2001/10/02. PubMed PMID: 11578936.
46. Gratton E, Barry NP, Beretta S, Celli A. Multiphoton fluorescence microscopy. *Methods (San Diego, Calif)*. 2001;25(1):103-10. Epub 2001/09/18. doi: 10.1006/meth.2001.1219. PubMed PMID: 11559001.
47. Campagnola P. Second harmonic generation imaging microscopy: applications to diseases diagnostics. *Analytical chemistry*. 2011;83(9):3224-31. Epub 2011/03/31. doi: 10.1021/ac1032325. PubMed PMID: 21446646; PMCID: PMC3104727.
48. Bianchini P, Diaspro A. Three-dimensional (3D) backward and forward second harmonic generation (SHG) microscopy of biological tissues. *Journal of biophotonics*. 2008;1(6):443-50. Epub 2009/04/04. doi: 10.1002/jbio.200810060. PubMed PMID: 19343670.
49. Adur J, Carvalho HF, Cesar CL, Casco VH. Nonlinear optical microscopy signal processing strategies in cancer. *Cancer informatics*. 2014;13:67-76. Epub 2014/04/17. doi: 10.4137/cin.s12419. PubMed PMID: 24737930; PMCID: PMC3981479.
50. Shah AT, Demory Beckler M, Walsh AJ, Jones WP, Pohlmann PR, Skala MC. Optical metabolic imaging of treatment response in human head and neck squamous cell carcinoma. *PLoS One*. 2014;9(3):e90746. Epub 2014/03/07. doi: 10.1371/journal.pone.0090746. PubMed PMID: 24595244; PMCID: PMC3942493.
51. Xu X, Cheng J, Thrall MJ, Liu Z, Wang X, Wong ST. Multimodal non-linear optical imaging for label-free differentiation of lung cancerous lesions from normal and desmoplastic tissues. *Biomed Opt Express*. 2013;4(12):2855-68. Epub 2014/01/11. doi: 10.1364/boe.4.002855. PubMed PMID: 24409386; PMCID: PMC3862152.

52. Xylas J, Varone A, Quinn KP, Pouli D, McLaughlin-Drubin ME, Thieu HT, Garcia-Moliner ML, House M, Hunter M, Munger K, Georgakoudi I. Noninvasive assessment of mitochondrial organization in three-dimensional tissues reveals changes associated with cancer development. *International journal of cancer*. 2015;136(2):322-32. Epub 2014/05/28. doi: 10.1002/ijc.28992. PubMed PMID: 24862444; PMCID: PMC4837461.
53. Edward K, Qiu S, Resto V, McCammon S, Vargas G. In vivo layer-resolved characterization of oral dysplasia via nonlinear optical micro-spectroscopy. *Biomed Opt Express*. 2012;3(7):1579-93. doi: 10.1364/BOE.3.001579. PubMed PMID: 22808430; PMCID: PMC3395483.
54. Skala MC, Squirrell JM, Vrotsos KM, Eickhoff JC, Gendron-Fitzpatrick A, Eliceiri KW, Ramanujam N. Multiphoton microscopy of endogenous fluorescence differentiates normal, precancerous, and cancerous squamous epithelial tissues. *Cancer Res*. 2005;65(4):1180-6. Epub 2005/03/01. doi: 10.1158/0008-5472.can-04-3031. PubMed PMID: 15735001.
55. Sun J, Shilagard T, Bell B, Motamedi M, Vargas G. In vivo multimodal nonlinear optical imaging of mucosal tissue. *Optics express*. 2004;12(11):2478-86. Epub 2004/05/31. PubMed PMID: 19475084.
56. Quinn KP, Bellas E, Fourligas N, Lee K, Kaplan DL, Georgakoudi I. Characterization of metabolic changes associated with the functional development of 3D engineered tissues by non-invasive, dynamic measurement of individual cell redox ratios. *Biomaterials*. 2012;33(21):5341-8. Epub 2012/05/09. doi: 10.1016/j.biomaterials.2012.04.024. PubMed PMID: 22560200; PMCID: PMC3387752.
57. Varone A, Xylas J, Quinn KP, Pouli D, Sridharan G, McLaughlin-Drubin ME, Alonzo C, Lee K, Munger K, Georgakoudi I. Endogenous two-photon fluorescence imaging elucidates metabolic changes related to enhanced glycolysis and glutamine consumption in precancerous epithelial tissues. *Cancer Res*. 2014;74(11):3067-75. Epub 2014/04/02. doi: 10.1158/0008-5472.can-13-2713. PubMed PMID: 24686167; PMCID: PMC4837452.
58. Paulis M. The influence of patient education by the dental hygienist: acceptance of the fluorescence oral cancer exam. *Journal of dental hygiene : JDH*. 2009;83(3):134-40. Epub 2009/09/03. PubMed PMID: 19723432.
59. Bhatia N, Lalla Y, Vu AN, Farah CS. Advances in optical adjunctive AIDS for visualisation and detection of oral malignant and potentially malignant lesions. *International journal of dentistry*. 2013;2013:194029. Epub 2013/10/01. doi: 10.1155/2013/194029. PubMed PMID: 24078812; PMCID: PMC3775423.
60. Nagi R, Reddy-Kantharaj YB, Rakesh N, Janardhan-Reddy S, Sahu S. Efficacy of light based detection systems for early detection of oral cancer and oral potentially malignant disorders: Systematic review. *Medicina oral, patologia oral y cirugia bucal*. 2016;21(4):e447-55. Epub 2016/03/08. PubMed PMID: 26946209; PMCID: PMC4920458.
61. Ohnishi Y, Fujii T, Ugaki Y, Yasui H, Watanabe M, Dateoka S, Kakudo K. Usefulness of a fluorescence visualization system for the detection of oral precancerous and early cancerous lesions. *Oncology reports*. 2016;36(1):514-20. Epub 2016/04/29. doi: 10.3892/or.2016.4776. PubMed PMID: 27121913.
62. Awan KH, Morgan PR, Warnakulasuriya S. Evaluation of an autofluorescence based imaging system (VELscope) in the detection of oral potentially malignant disorders and benign keratoses. *Oral oncology*. 2011;47(4):274-7. Epub 2011/03/15. doi: 10.1016/j.oraloncology.2011.02.001. PubMed PMID: 21396880.

63. Awan KH, Patil S. Efficacy of Autofluorescence Imaging as an Adjunctive Technique for Examination and Detection of Oral Potentially Malignant Disorders: A Systematic Review. *The journal of contemporary dental practice*. 2015;16(9):744-9. Epub 2015/11/03. PubMed PMID: 26522601.
64. Hanken H, Kraatz J, Smeets R, Heiland M, Assaf AT, Blessmann M, Eichhorn W, Clauditz TS, Grobe A, Kolk A, Rana M. The detection of oral pre- malignant lesions with an autofluorescence based imaging system (VELscope) - a single blinded clinical evaluation. *Head & face medicine*. 2013;9:23. Epub 2013/08/24. doi: 10.1186/1746-160x-9-23. PubMed PMID: 23967796; PMCID: PMC3851797.
65. Scheer M, Fuss J, Derman MA, Kreppel M, Neugebauer J, Rothamel D, Drebber U, Zoeller JE. Autofluorescence imaging in recurrent oral squamous cell carcinoma. *Oral and maxillofacial surgery*. 2016;20(1):27-33. Epub 2015/08/13. doi: 10.1007/s10006-015-0520-7. PubMed PMID: 26267490.
66. Keereweer S, Mol IM, Vahrmeijer AL, Van Driel PB, Baatenburg de Jong RJ, Kerrebijn JD, Lowik CW. Dual wavelength tumor targeting for detection of hypopharyngeal cancer using near-infrared optical imaging in an animal model. *International journal of cancer*. 2012;131(7):1633-40. Epub 2012/01/12. doi: 10.1002/ijc.27430. PubMed PMID: 22234729.
67. Rajaram N, Frees AE, Fontanella AN, Zhong J, Hansen K, Dewhirst MW, Ramanujam N. Delivery rate affects uptake of a fluorescent glucose analog in murine metastatic breast cancer. *PLoS One*. 2013;8(10):e76524. Epub 2013/11/10. doi: 10.1371/journal.pone.0076524. PubMed PMID: 24204635; PMCID: PMC3799786.
68. Sheth RA, Josephson L, Mahmood U. Evaluation and clinically relevant applications of a fluorescent imaging analog to fluorodeoxyglucose positron emission tomography. *Journal of biomedical optics*. 2009;14(6):064014. Epub 2010/01/12. doi: 10.1117/1.3259364. PubMed PMID: 20059252; PMCID: PMC2794415.
69. Farah CS, McCullough MJ. A pilot case control study on the efficacy of acetic acid wash and chemiluminescent illumination (ViziLite) in the visualisation of oral mucosal white lesions. *Oral oncology*. 2007;43(8):820-4. Epub 2006/12/16. doi: 10.1016/j.oraloncology.2006.10.005. PubMed PMID: 17169603.
70. Santosh AB, Jones T, Harvey J. A review on oral cancer biomarkers: Understanding the past and learning from the present. *Journal of cancer research and therapeutics*. 2016;12(2):486-92. Epub 2016/07/28. doi: 10.4103/0973-1482.176414. PubMed PMID: 27461598.
71. Radhika T, Jeddy N, Nithya S, Muthumeenakshi RM. Salivary biomarkers in oral squamous cell carcinoma - An insight. *Journal of oral biology and craniofacial research*. 2016;6(Suppl 1):S51-s4. Epub 2016/12/03. doi: 10.1016/j.jobcr.2016.07.003. PubMed PMID: 27900251; PMCID: PMC5122805.
72. Svoboda K, Yasuda R. Principles of two-photon excitation microscopy and its applications to neuroscience. *Neuron*. 2006;50(6):823-39. doi: 10.1016/j.neuron.2006.05.019. PubMed PMID: 16772166.
73. Supatto W, Truong TV, Debarre D, Beaurepaire E. Advances in multiphoton microscopy for imaging embryos. *Current opinion in genetics & development*. 2011;21(5):538-48. Epub 2011/09/16. doi: 10.1016/j.gde.2011.08.003. PubMed PMID: 21917444; PMCID: 3241964.



74. Wyckoff J, Gligorijevic B, Entenberg D, Segall J, Condeelis J. High-resolution multiphoton imaging of tumors in vivo. *Cold Spring Harbor protocols*. 2011;2011(10):1167-84. Epub 2011/10/05. doi: 10.1101/pdb.top065904. PubMed PMID: 21969629; PMCID: 4000043.
75. Brown EB, Campbell RB, Tsuzuki Y, Xu L, Carmeliet P, Fukumura D, Jain RK. In vivo measurement of gene expression, angiogenesis and physiological function in tumors using multiphoton laser scanning microscopy. *Nature medicine*. 2001;7(7):864-8. Epub 2001/07/04. doi: 10.1038/89997. PubMed PMID: 11433354.
76. Wilder-Smith P, Krasieva T, Jung WG, Zhang J, Chen Z, Osann K, Tromberg B. Noninvasive imaging of oral premalignancy and malignancy. *Journal of biomedical optics*. 2005;10(5):051601. Epub 2005/11/19. doi: 10.1117/1.2098930. PubMed PMID: 16292949.
77. Zhuo S, Chen J, Jiang X, Xie S, Chen R, Cao N, Zou Q, Xiong S. The layered-resolved microstructure and spectroscopy of mouse oral mucosa using multiphoton microscopy. *Physics in medicine and biology*. 2007;52(16):4967-80. doi: 10.1088/0031-9155/52/16/017. PubMed PMID: 17671347.
78. Vargas G, Shilagard T, Ho KH, McCammon S. Multiphoton autofluorescence microscopy and second harmonic generation microscopy of oral epithelial neoplasms. *Conf Proc IEEE Eng Med Biol Soc*. 2009;2009:6311-3. Epub 2009/12/08. doi: 10.1109/iembs.2009.5332783. PubMed PMID: 19963923; PMCID: 2829879.
79. Teh SK, Zheng W, Li S, Li D, Zeng Y, Yang Y, Qu JY. Multimodal nonlinear optical microscopy improves the accuracy of early diagnosis of squamous intraepithelial neoplasia. *Journal of biomedical optics*. 2013;18(3):036001. Epub 2013/03/05. doi: 10.1117/1.jbo.18.3.036001. PubMed PMID: 23455959.
80. Skala MC, Riching KM, Bird DK, Gendron-Fitzpatrick A, Eickhoff J, Eliceiri KW, Keely PJ, Ramanujam N. In vivo multiphoton fluorescence lifetime imaging of protein-bound and free nicotinamide adenine dinucleotide in normal and precancerous epithelia. *Journal of biomedical optics*. 2007;12(2):024014. Epub 2007/05/05. doi: 10.1117/1.2717503. PubMed PMID: 17477729; PMCID: PMC2743958.
81. Gimenez-Conti I. The hamster cheek pouch carcinogenesis model. *Acta odontologica latinoamericana : AOL*. 1993;7(1):3-12. Epub 1993/01/01. PubMed PMID: 11885256.
82. Vairaktaris E, Spyridonidou S, Papakosta V, Vylliotis A, Lazaris A, Perrea D, Yapijakis C, Patsouris E. The hamster model of sequential oral oncogenesis. *Oral oncology*. 2008;44(4):315-24. Epub 2007/12/07. doi: 10.1016/j.oraloncology.2007.08.015. PubMed PMID: 18061531.
83. Baert JH, Veys RJ, Ampe K, De Boever JA. The effect of sodium lauryl sulphate and triclosan on hamster cheek pouch mucosa. *International journal of experimental pathology*. 1996;77(2):73-8. Epub 1996/04/01. PubMed PMID: 8762865; PMCID: PMC2691625.
84. Veys RJ, Baert JH, De Boever JA. Histological changes in the hamster cheek pouch epithelium induced by topical application of sodium lauryl sulphate. *International journal of experimental pathology*. 1994;75(3):203-9. Epub 1994/06/01. PubMed PMID: 8086317; PMCID: PMC2001810.
85. Pena A, Strupler M, Boulesteix T, Schanne-Klein M. Spectroscopic analysis of keratin endogenous signal for skin multiphoton microscopy. *Optics express*. 2005;13(16):6268-74. Epub 2005/08/08. PubMed PMID: 19498639.
86. White FH, Gohari K, Smith CJ. Histological and ultrastructural morphology of 7,12 dimethylbenz(alpha)-anthracene carcinogenesis in hamster cheek pouch epithelium. *Diagnostic histopathology*. 1981;4(4):307-33. Epub 1981/10/01. PubMed PMID: 6802623.

87. de Souza FL, Oliveira M, Nunes MB, Serafim LH, Azambuja AA, Braga LM, Saur L, de Souza MA, Xavier LL. Sunitinib Improves Some Clinical Aspects and Reverts DMBA-Induced Hyperplastic Lesions in Hamster Buccal Pouch. *ISRN otolaryngology*. 2014;2014:859621. Epub 2014/04/03. doi: 10.1155/2014/859621. PubMed PMID: 24693453; PMCID: 3945207.
88. Derka S, Vairaktaris E, Papakosta V, Vassiliou S, Acil Y, Vylliotis A, Spyridonidou S, Lazaris AC, Mourouzis C, Kokkori A, Moulavasili P, Perrea D, Donta I, Yapijakis C, Patsouris E. Cell proliferation and apoptosis culminate in early stages of oral oncogenesis. *Oral oncology*. 2006;42(5):540-50. Epub 2006/02/09. doi: 10.1016/j.oraloncology.2005.10.008. PubMed PMID: 16464633.
89. Papakosta V, Vairaktaris E, Vylliotis A, Derka S, Nkenke E, Vassiliou S, Lazaris A, Mourouzis C, Rallis G, Spyridonidou S, Anagnostopoulou S, Perrea D, Donta I, Yapijakis C, Patsouris E. The co-expression of c-myc and p53 increases and reaches a plateau early in oral oncogenesis. *Anticancer research*. 2006;26(4b):2957-62. Epub 2006/08/05. PubMed PMID: 16886620.
90. Pal R, Yang J, Ortiz D, Qiu S, Resto V, McCammon S, Vargas G. In-vivo nonlinear optical microscopy (NLOM) of epithelial-connective tissue interface (ECTI) reveals quantitative measures of neoplasia in hamster oral mucosa. *PLoS One*. 2015;10(1):e0116754. doi: 10.1371/journal.pone.0116754. PubMed PMID: 25633927; PMCID: PMC4310593.
91. Walsh AJ, Cook RS, Lee JH, Arteaga CL, Skala MC. Collagen density and alignment in responsive and resistant trastuzumab-treated breast cancer xenografts. *Journal of biomedical optics*. 2015;20(2):26004. Epub 2015/02/24. doi: 10.1117/1.JBO.20.2.026004. PubMed PMID: 25700233; PMCID: 4335617.
92. Paoli J, Smedh M, Wennberg AM, Ericson MB. Multiphoton laser scanning microscopy on non-melanoma skin cancer: morphologic features for future non-invasive diagnostics. *The Journal of investigative dermatology*. 2008;128(5):1248-55. Epub 2007/11/09. doi: 10.1038/sj.jid.5701139. PubMed PMID: 17989735.
93. Balu M, Kelly KM, Zachary CB, Harris RM, Krasieva TB, Konig K, Durkin AJ, Tromberg BJ. Distinguishing between benign and malignant melanocytic nevi by in vivo multiphoton microscopy. *Cancer Res*. 2014;74(10):2688-97. Epub 2014/04/02. doi: 10.1158/0008-5472.CAN-13-2582. PubMed PMID: 24686168; PMCID: 4024350.
94. Cicchi R, Kapsokalyvas D, Troiano M, Campolmi P, Morini C, Massi D, Cannarozzo G, Lotti T, Pavone FS. In vivo non-invasive monitoring of collagen remodelling by two-photon microscopy after micro-ablative fractional laser resurfacing. *Journal of biophotonics*. 2014;7(11-12):914-25. Epub 2013/12/18. doi: 10.1002/jbio.201300124. PubMed PMID: 24339127.
95. Cicchi R, Sturiale A, Nesi G, Kapsokalyvas D, Alemanno G, Tonelli F, Pavone FS. Multiphoton morpho-functional imaging of healthy colon mucosa, adenomatous polyp and adenocarcinoma. *Biomed Opt Express*. 2013;4(7):1204-13. Epub 2013/07/13. doi: 10.1364/boe.4.001204. PubMed PMID: 23847743; PMCID: PMC3704099.
96. Zhuo S, Chen J, Xie S, Zheng L, Zhu X, Jiang X. Stromal optical properties: differentiating normal and cancerous stroma. *Lasers Med Sci*. 2010;25(6):911-3. Epub 2010/08/17. doi: 10.1007/s10103-010-0824-7. PubMed PMID: 20711743.
97. Pouli D, Balu M, Alonzo CA, Liu Z, Quinn KP, Rius-Diaz F, Harris RM, Kelly KM, Tromberg BJ, Georgakoudi I. Imaging mitochondrial dynamics in human skin reveals depth-dependent hypoxia and malignant potential for diagnosis. *Science translational medicine*.

2016;8(367):367ra169. Epub 2016/12/03. doi: 10.1126/scitranslmed.aag2202. PubMed PMID: 27903865; PMCID: PMC5176339.

98. Kordbacheh F, Bhatia N, Farah CS. Patterns of differentially expressed genes in oral mucosal lesions subjected to autofluorescence. *Oral diseases*. 2016. Epub 2016/01/11. doi: 10.1111/odi.12438. PubMed PMID: 26749103.

99. Jones KB, Jordan R. White lesions in the oral cavity: clinical presentation, diagnosis, and treatment. *Semin Cutan Med Surg*. 2015;34(4):161-70. doi: 10.12788/j.sder.2015.0180. PubMed PMID: 26650693.

100. Poh CF, Ng S, Berean KW, Williams PM, Rosin MP, Zhang L. Biopsy and histopathologic diagnosis of oral premalignant and malignant lesions. *J Can Dent Assoc*. 2008;74(3):283-8. Epub 2008/04/05. PubMed PMID: 18387269.

101. Lefort C, Hamzeh H, Louradour F, Pain F, Haidar DA. Characterization, comparison, and choice of a commercial double-clad fiber for nonlinear endomicroscopy. *Journal of biomedical optics*. 2014;19(7):076005. Epub 2014/07/09. doi: 10.1117/1.jbo.19.7.076005. PubMed PMID: 25003753.

102. Warren SC, Kim Y, Stone JM, Mitchell C, Knight JC, Neil MA, Paterson C, French PM, Dunsby C. Adaptive multiphoton endomicroscopy through a dynamically deformed multicore optical fiber using proximal detection. *Optics express*. 2016;24(19):21474-84. Epub 2016/09/24. doi: 10.1364/oe.24.021474. PubMed PMID: 27661887.

103. Kobat D, Horton NG, Xu C. In vivo two-photon microscopy to 1.6-mm depth in mouse cortex. *Journal of biomedical optics*. 2011;16(10):106014. Epub 2011/10/28. doi: 10.1117/1.3646209. PubMed PMID: 22029361.

104. Dombeck DA, Harvey CD, Tian L, Looger LL, Tank DW. Functional imaging of hippocampal place cells at cellular resolution during virtual navigation. *Nature neuroscience*. 2010;13(11):1433-40. Epub 2010/10/05. doi: 10.1038/nn.2648. PubMed PMID: 20890294; PMCID: 2967725.

105. Landini G, Hirayama Y, Li TJ, Kitano M. Increased fractal complexity of the epithelial-connective tissue interface in the tongue of 4NQO-treated rats. *Pathology, research and practice*. 2000;196(4):251-8. Epub 2000/04/27. doi: 10.1016/S0344-0338(00)80074-6. PubMed PMID: 10782469.

106. Paszek MJ, Weaver VM. The tension mounts: mechanics meets morphogenesis and malignancy. *Journal of mammary gland biology and neoplasia*. 2004;9(4):325-42. Epub 2005/04/20. doi: 10.1007/s10911-004-1404-x. PubMed PMID: 15838603.

107. Ramos-DeSimone N, Hahn-Dantona E, Siple J, Nagase H, French DL, Quigley JP. Activation of matrix metalloproteinase-9 (MMP-9) via a converging plasmin/stromelysin-1 cascade enhances tumor cell invasion. *The Journal of biological chemistry*. 1999;274(19):13066-76. Epub 1999/05/01. PubMed PMID: 10224058.

108. Liotta LA, Stetler-Stevenson WG. Tumor invasion and metastasis: an imbalance of positive and negative regulation. *Cancer Res*. 1991;51(18 Suppl):5054s-9s. Epub 1991/09/15. PubMed PMID: 1884381.

109. Wenig BM. Squamous cell carcinoma of the upper aerodigestive tract: precursors and problematic variants. *Modern pathology : an official journal of the United States and Canadian Academy of Pathology, Inc*. 2002;15(3):229-54. Epub 2002/03/21. doi: 10.1038/modpathol.3880520. PubMed PMID: 11904340.

110. Tilakaratne WM, Sherriff M, Morgan PR, Odell EW. Grading oral epithelial dysplasia: analysis of individual features. *Journal of oral pathology & medicine : official publication of the International Association of Oral Pathologists and the American Academy of Oral Pathology*. 2011;40(7):533-40. Epub 2011/04/20. doi: 10.1111/j.1600-0714.2011.01033.x. PubMed PMID: 21501232.
111. Syafriadi M, Cheng J, Jen KY, Ida-Yonemochi H, Suzuki M, Saku T. Two-phase appearance of oral epithelial dysplasia resulting from focal proliferation of parabasal cells and apoptosis of prickles. *Journal of oral pathology & medicine : official publication of the International Association of Oral Pathologists and the American Academy of Oral Pathology*. 2005;34(3):140-9. Epub 2005/02/04. doi: 10.1111/j.1600-0714.2004.00283.x. PubMed PMID: 15689227.
112. Agrawal U, Rai H, Jain AK. Morphological and ultrastructural characteristics of extracellular matrix changes in oral squamous cell carcinoma. *Indian journal of dental research : official publication of Indian Society for Dental Research*. 2011;22(1):16-21. Epub 2011/04/29. doi: 10.4103/0970-9290.79968. PubMed PMID: 21525671.
113. Fedele S. Diagnostic aids in the screening of oral cancer. *Head & neck oncology*. 2009;1:5. Epub 2009/03/17. doi: 10.1186/1758-3284-1-5. PubMed PMID: 19284694; PMCID: PMC2654034.
114. Arbyn M, Sankaranarayanan R, Muwonge R, Keita N, Dolo A, Mbalawa CG, Nouhou H, Sakande B, Wesley R, Somanathan T, Sharma A, Shastri S, Basu P. Pooled analysis of the accuracy of five cervical cancer screening tests assessed in eleven studies in Africa and India. *International journal of cancer*. 2008;123(1):153-60. Epub 2008/04/12. doi: 10.1002/ijc.23489. PubMed PMID: 18404671.
115. Paulsen F, Thale A. Epithelial-connective tissue boundary in the oral part of the human soft palate. *Journal of anatomy*. 1998;193 ( Pt 3):457-67. Epub 1999/01/07. PubMed PMID: 9877301; PMCID: 1467866.
116. Wilson DF, Jiang DJ, Pierce AM, Wiebkin OW. Oral cancer: role of the basement membrane in invasion. *Australian dental journal*. 1999;44(2):93-7. Epub 1999/08/19. PubMed PMID: 10452163.
117. Landini G, Rippin JW. Fractal dimensions of the epithelial-connective tissue interfaces in premalignant and malignant epithelial lesions of the floor of the mouth. *Analytical and quantitative cytology and histology / the International Academy of Cytology [and] American Society of Cytology*. 1993;15(2):144-9. Epub 1993/04/01. PubMed PMID: 8318129.
118. Margot Vullieza MAG, Aurélien Souto-Lebela, Yann Quinsata, Claire Lartiguea, Steven P. Kordellb, Adam C. Lemoineb, Christopher A. Brownb, editor. Multi-scale Curvature Analysis and Correlations with the Fatigue Limit on Steel Surfaces after Milling. 2nd CIRP Conference on Surface Integrity (CSI); 2014 21 May 2014; Elsevier B.V.
119. Crissman JD, Liu WY, Gluckman JL, Cummings G. Prognostic value of histopathologic parameters in squamous cell carcinoma of the oropharynx. *Cancer*. 1984;54(12):2995-3001. Epub 1984/12/15. PubMed PMID: 6498773.
120. Mueller MM, Fusenig NE. Friends or foes - bipolar effects of the tumour stroma in cancer. *Nature reviews Cancer*. 2004;4(11):839-49. Epub 2004/11/02. doi: 10.1038/nrc1477. PubMed PMID: 15516957.
121. Kurugol S, Kose K, Park B, Dy JG, Brooks DH, Rajadhyaksha M. Automated delineation of dermal-epidermal junction in reflectance confocal microscopy image stacks of human skin. *The*

- Journal of investigative dermatology. 2015;135(3):710-7. Epub 2014/09/04. doi: 10.1038/jid.2014.379. PubMed PMID: 25184959; PMCID: 4323765.
122. Johnson NW. The role of histopathology in diagnosis and prognosis of oral squamous cell carcinoma. *Proceedings of the Royal Society of Medicine*. 1976;69(10):740-7. Epub 1976/10/01. PubMed PMID: 792881; PMCID: 1864634.
  123. Akhter M, Hossain S, Rahman QB, Molla MR. A study on histological grading of oral squamous cell carcinoma and its co-relationship with regional metastasis. *Journal of oral and maxillofacial pathology : JOMFP*. 2011;15(2):168-76. Epub 2012/04/25. doi: 10.4103/0973-029X.84485. PubMed PMID: 22529575; PMCID: 3329698.
  124. Sami MM, Saito M, Muramatsu S, Mikami T, Al-Eryani K, Sawair FA, Eid RA, Cheng J, Kikuchi H, Saku T. Twin-pair rete ridge analysis: a computer-aided method for facilitating objective histopathological distinction between epithelial dysplasia and carcinoma in-situ of the oral mucosa. *Oral Medicine & Pathology*. 2010;14(3):89-97. doi: 10.3353/omp.14.89.
  125. Alex A, Povazay B, Hofer B, Popov S, Glittenberg C, Binder S, Drexler W. Multispectral in vivo three-dimensional optical coherence tomography of human skin. *Journal of biomedical optics*. 2010;15(2):026025. Epub 2010/05/13. doi: 10.1117/1.3400665. PubMed PMID: 20459270.
  126. Palero JA, de Bruijn HS, van der Ploeg van den Heuvel A, Sterenborg HJ, Gerritsen HC. Spectrally resolved multiphoton imaging of in vivo and excised mouse skin tissues. *Biophysical journal*. 2007;93(3):992-1007. doi: 10.1529/biophysj.106.099457. PubMed PMID: 17449667; PMCID: 1913153.
  127. Gillenwater A, Jacob R, Ganeshappa R, Kemp B, El-Naggar AK, Palmer JL, Clayman G, Mitchell MF, Richards-Kortum R. Noninvasive diagnosis of oral neoplasia based on fluorescence spectroscopy and native tissue autofluorescence. *Archives of otolaryngology--head & neck surgery*. 1998;124(11):1251-8. PubMed PMID: 9821929.
  128. Skala MC, Palmer GM, Zhu C, Liu Q, Vrotsos KM, Marshek-Stone CL, Gendron-Fitzpatrick A, Ramanujam N. Investigation of fiber-optic probe designs for optical spectroscopic diagnosis of epithelial pre-cancers. *Lasers in surgery and medicine*. 2004;34(1):25-38. doi: 10.1002/lsm.10239. PubMed PMID: 14755422; PMCID: 2768119.
  129. Schwarz RA, Gao W, Daye D, Williams MD, Richards-Kortum R, Gillenwater AM. Autofluorescence and diffuse reflectance spectroscopy of oral epithelial tissue using a depth-sensitive fiber-optic probe. *Applied optics*. 2008;47(6):825-34. PubMed PMID: 18288232; PMCID: 2773166.
  130. Rice WL, Kaplan DL, Georgakoudi I. Two-photon microscopy for non-invasive, quantitative monitoring of stem cell differentiation. *PLoS One*. 2010;5(4):e10075. doi: 10.1371/journal.pone.0010075. PubMed PMID: 20419124; PMCID: 2855700.
  131. Balu M, Zachary CB, Harris RM, Krasieva TB, Konig K, Tromberg BJ, Kelly KM. In Vivo Multiphoton Microscopy of Basal Cell Carcinoma. *JAMA dermatology*. 2015;151(10):1068-74. Epub 2015/04/25. doi: 10.1001/jamadermatol.2015.0453. PubMed PMID: 25909650; PMCID: 4607557.
  132. Tsai TH, Jee SH, Dong CY, Lin SJ. Multiphoton microscopy in dermatological imaging. *Journal of dermatological science*. 2009;56(1):1-8. Epub 2009/08/25. doi: 10.1016/j.jdermsci.2009.06.008. PubMed PMID: 19699614.
  133. Thomas G, van Voskuilen J, Truong H, Song JY, Gerritsen HC, Sterenborg HJ. In vivo nonlinear spectral imaging as a tool to monitor early spectroscopic and metabolic changes in a

- murine cutaneous squamous cell carcinoma model. *Biomed Opt Express*. 2014;5(12):4281-99. Epub 2015/01/13. doi: 10.1364/BOE.5.004281. PubMed PMID: 25574438; PMCID: 4285605.
134. Inaguma M, Hashimoto K. Porphyrin-like fluorescence in oral cancer: In vivo fluorescence spectral characterization of lesions by use of a near-ultraviolet excited autofluorescence diagnosis system and separation of fluorescent extracts by capillary electrophoresis. *Cancer*. 1999;86(11):2201-11. PubMed PMID: 10590358.
  135. Ghadially FN. Red fluorescence of experimentally induced and human tumours. *The Journal of pathology and bacteriology*. 1960;80:345-51. Epub 1960/10/01. PubMed PMID: 13704882.
  136. Otsuka S, Matsumoto K, Nakajima M, Tanaka T, Ogura S. Oxygen Availability for Porphyrin Biosynthesis Enzymes Determines the Production of Protoporphyrin IX (PpIX) during Hypoxia. *PLoS One*. 2015;10(12):e0146026. doi: 10.1371/journal.pone.0146026. PubMed PMID: 26717566; PMCID: 4705112.
  137. Eales KL, Hollinshead KE, Tennant DA. Hypoxia and metabolic adaptation of cancer cells. *Oncogenesis*. 2016;5:e190. doi: 10.1038/oncsis.2015.50. PubMed PMID: 26807645; PMCID: PMC4728679.
  138. Venugopal C, Nazeer SS, Balan A, Jayasree RS. Autofluorescence spectroscopy augmented by multivariate analysis as a potential noninvasive tool for early diagnosis of oral cavity disorders. *Photomedicine and laser surgery*. 2013;31(12):605-12. doi: 10.1089/pho.2013.3547. PubMed PMID: 24251928.
  139. Pavlova I, Weber CR, Schwarz RA, Williams MD, Gillenwater AM, Richards-Kortum R. Fluorescence spectroscopy of oral tissue: Monte Carlo modeling with site-specific tissue properties. *Journal of biomedical optics*. 2009;14(1):014009. doi: 10.1117/1.3065544. PubMed PMID: 19256697; PMCID: 2722954.
  140. De Veld DC, Witjes MJ, Sterenborg HJ, Roodenburg JL. The status of in vivo autofluorescence spectroscopy and imaging for oral oncology. *Oral oncology*. 2005;41(2):117-31. doi: 10.1016/j.oraloncology.2004.07.007. PubMed PMID: 15695112.
  141. de Veld DC, Skurichina M, Witjes MJ, Duin RP, Sterenborg HJ, Roodenburg JL. Clinical study for classification of benign, dysplastic, and malignant oral lesions using autofluorescence spectroscopy. *Journal of biomedical optics*. 2004;9(5):940-50. doi: 10.1117/1.1782611. PubMed PMID: 15447015.
  142. Drezek R, Brookner C, Pavlova I, Boiko I, Malpica A, Lotan R, Follen M, Richards-Kortum R. Autofluorescence microscopy of fresh cervical-tissue sections reveals alterations in tissue biochemistry with dysplasia. *Photochem Photobiol*. 2001;73(6):636-41. Epub 2001/06/26. PubMed PMID: 11421069.
  143. Vengadesan N, Aruna P, Ganesan S. Characterization of native fluorescence from DMBA-treated hamster cheek pouch buccal mucosa for measuring tissue transformation. *British journal of cancer*. 1998;77(3):391-5. PubMed PMID: 9472633; PMCID: 2151305.
  144. Wu Y, Qu JY. Autofluorescence spectroscopy of epithelial tissues. *Journal of biomedical optics*. 2006;11(5):054023. Epub 2006/11/10. doi: 10.1117/1.2362741. PubMed PMID: 17092172.
  145. Skala M, Ramanujam N. Multiphoton redox ratio imaging for metabolic monitoring in vivo. *Methods in molecular biology (Clifton, NJ)*. 2010;594:155-62. Epub 2010/01/15. doi: 10.1007/978-1-60761-411-1\_11. PubMed PMID: 20072916; PMCID: PMC2874879.

146. Yuvaraj M, Udayakumar K, Jayanth V, Prakasa Rao A, Bharanidharan G, Koteeswaran D, Munusamy BD, Murali Krishna C, Ganesan S. Fluorescence spectroscopic characterization of salivary metabolites of oral cancer patients. *J Photochem Photobiol B*. 2014;130:153-60. doi: 10.1016/j.jphotobiol.2013.11.006. PubMed PMID: 24333763.
147. de Veld DC, Bakker Schut TC, Skurichina M, Witjes MJ, Van der Wal JE, Roodenburg JL, Sterenberg HJ. Autofluorescence and Raman microspectroscopy of tissue sections of oral lesions. *Lasers Med Sci*. 2005;19(4):203-9. doi: 10.1007/s10103-004-0325-7. PubMed PMID: 15772873.
148. Sharvill D. Trichophyton sulphureum ringworm; infections in an adult scalp, a newborn infant, and three nurses. *British medical journal*. 1955;2(4936):415-7. Epub 1955/08/13. PubMed PMID: 13240128; PMCID: 1980478.
149. Silveira L, Jr., Paleckis LG, Nicolau RA, Nogueira GV, Busanello RZ, Mardegan DA, Fonseca SM, Zangaro RA, Pacheco MT. [Detection of induced neoplastic lesions in the oral mucosa of hamsters using fluorescence spectroscopy]. *Revista da Associacao Medica Brasileira*. 2004;50(3):297-301. doi: /S0104-42302004000300038. PubMed PMID: 15499483.
150. Wang CY, Tsai T, Chiang CP, Chen HM, Chen CT. Improved diagnosis of oral premalignant lesions in submucous fibrosis patients with 5-aminolevulinic acid induced PpIX fluorescence. *Journal of biomedical optics*. 2009;14(4):044026. doi: 10.1117/1.3200934. PubMed PMID: 19725737.
151. Kim JW, Dang CV. Cancer's molecular sweet tooth and the Warburg effect. *Cancer Res*. 2006;66(18):8927-30. Epub 2006/09/20. doi: 10.1158/0008-5472.can-06-1501. PubMed PMID: 16982728.
152. Metallo CM, Gameiro PA, Bell EL, Mattaini KR, Yang J, Hiller K, Jewell CM, Johnson ZR, Irvine DJ, Guarente L, Kelleher JK, Vander Heiden MG, Iliopoulos O, Stephanopoulos G. Reductive glutamine metabolism by IDH1 mediates lipogenesis under hypoxia. *Nature*. 2011;481(7381):380-4. Epub 2011/11/22. doi: 10.1038/nature10602. PubMed PMID: 22101433; PMCID: 3710581.
153. Epstein JB, Gorsky M, Lonky S, Silverman S, Jr., Epstein JD, Bride M. The efficacy of oral lumenoscopy (ViziLite) in visualizing oral mucosal lesions. *Special care in dentistry : official publication of the American Association of Hospital Dentists, the Academy of Dentistry for the Handicapped, and the American Society for Geriatric Dentistry*. 2006;26(4):171-4. Epub 2006/08/25. PubMed PMID: 16927741.
154. Kerr AR, Sirois DA, Epstein JB. Clinical evaluation of chemiluminescent lighting: an adjunct for oral mucosal examinations. *The Journal of clinical dentistry*. 2006;17(3):59-63. Epub 2006/10/07. PubMed PMID: 17022366.
155. Ram S, Siar CH. Chemiluminescence as a diagnostic aid in the detection of oral cancer and potentially malignant epithelial lesions. *International journal of oral and maxillofacial surgery*. 2005;34(5):521-7. Epub 2005/08/02. doi: 10.1016/j.ijom.2004.10.008. PubMed PMID: 16053872.
156. Lane PM, Gilhuly T, Whitehead P, Zeng H, Poh CF, Ng S, Williams PM, Zhang L, Rosin MP, MacAulay CE. Simple device for the direct visualization of oral-cavity tissue fluorescence. *Journal of biomedical optics*. 2006;11(2):024006. Epub 2006/05/06. doi: 10.1117/1.2193157. PubMed PMID: 16674196.
157. Huber MA. Assessment of the VELscope as an adjunctive examination tool. *Texas dental journal*. 2009;126(6):528-35. Epub 2009/07/31. PubMed PMID: 19639920.

158. Mehrotra R, Singh M, Thomas S, Nair P, Pandya S, Nigam NS, Shukla P. A cross-sectional study evaluating chemiluminescence and autofluorescence in the detection of clinically innocuous precancerous and cancerous oral lesions. *J Am Dent Assoc.* 2010;141(2):151-6. Epub 2010/02/04. PubMed PMID: 20123872.
159. Roblyer D, Richards-Kortum R, Sokolov K, El-Naggar AK, Williams MD, Kurachi C, Gillenwater AM. Multispectral optical imaging device for in vivo detection of oral neoplasia. *Journal of biomedical optics.* 2008;13(2):024019. Epub 2008/05/10. doi: 10.1117/1.2904658. PubMed PMID: 18465982; PMCID: PMC3970814.
160. Roblyer D, Kurachi C, Stepanek V, Williams MD, El-Naggar AK, Lee JJ, Gillenwater AM, Richards-Kortum R. Objective detection and delineation of oral neoplasia using autofluorescence imaging. *Cancer prevention research (Philadelphia, Pa).* 2009;2(5):423-31. Epub 2009/04/30. doi: 10.1158/1940-6207.capr-08-0229. PubMed PMID: 19401530; PMCID: PMC2719708.
161. Burzynski NJ, Firriolo FJ, Butters JM, Sorrell CL. Evaluation of oral cancer screening. *Journal of cancer education : the official journal of the American Association for Cancer Education.* 1997;12(2):95-9. Epub 1997/07/01. doi: 10.1080/08858199709528462. PubMed PMID: 9229272.
162. Bouquot JE. Common oral lesions found during a mass screening examination. *J Am Dent Assoc.* 1986;112(1):50-7. Epub 1986/01/01. PubMed PMID: 3455995.
163. Malaovalla AM, Silverman S, Mani NJ, Bilimoria KF, Smith LW. Oral cancer in 57,518 industrial workers of Gujarat, India: a prevalence and followup study. *Cancer.* 1976;37(4):1882-6. Epub 1976/04/01. PubMed PMID: 946594.
164. Lingen MW, Kalmar JR, Karrison T, Speight PM. Critical evaluation of diagnostic aids for the detection of oral cancer. *Oral oncology.* 2008;44(1):10-22. Epub 2007/09/11. doi: 10.1016/j.oraloncology.2007.06.011. PubMed PMID: 17825602; PMCID: PMC2424250.
165. Svistun E, Alizadeh-Naderi R, El-Naggar A, Jacob R, Gillenwater A, Richards-Kortum R. Vision enhancement system for detection of oral cavity neoplasia based on autofluorescence. *Head & neck.* 2004;26(3):205-15. Epub 2004/03/05. doi: 10.1002/hed.10381. PubMed PMID: 14999795.
166. Utzinger U, Bueeler M, Oh S, Heintzelman DL, Svistun ES, Abd-El-Barr M, Gillenwater A, Richards-Kortum R. Optimal visual perception and detection of oral cavity neoplasia. *IEEE transactions on bio-medical engineering.* 2003;50(3):396-9. Epub 2003/04/03. doi: 10.1109/tbme.2003.808832. PubMed PMID: 12669997.
167. Poh CF, MacAulay CE, Zhang L, Rosin MP. Tracing the "at-risk" oral mucosa field with autofluorescence: steps toward clinical impact. *Cancer prevention research (Philadelphia, Pa).* 2009;2(5):401-4. Epub 2009/04/30. doi: 10.1158/1940-6207.capr-09-0060. PubMed PMID: 19401533; PMCID: PMC2726429.
168. Onizawa K, Saginoya H, Furuya Y, Yoshida H, Fukuda H. Usefulness of fluorescence photography for diagnosis of oral cancer. *International journal of oral and maxillofacial surgery.* 1999;28(3):206-10. Epub 1999/06/04. PubMed PMID: 10355944.
169. Betz CS, Stepp H, Janda P, Arbogast S, Grevers G, Baumgartner R, Leunig A. A comparative study of normal inspection, autofluorescence and 5-ALA-induced PPIX fluorescence for oral cancer diagnosis. *International journal of cancer.* 2002;97(2):245-52. Epub 2002/01/05. PubMed PMID: 11774271.



170. Ingrams DR, Dhingra JK, Roy K, Perrault DF, Jr., Bottrill ID, Kabani S, Rebeiz EE, Pankratov MM, Shapshay SM, Manoharan R, Itzkan I, Feld MS. Autofluorescence characteristics of oral mucosa. *Head & neck*. 1997;19(1):27-32. Epub 1997/01/01. PubMed PMID: 9030941.
171. Olivo M, Bhuvaneswari R, Keogh I. Advances in bio-optical imaging for the diagnosis of early oral cancer. *Pharmaceutics*. 2011;3(3):354-78. Epub 2011/01/01. doi: 10.3390/pharmaceutics3030354. PubMed PMID: 24310585; PMCID: PMC3857071.
172. Nitin N, Carlson AL, Muldoon T, El-Naggar AK, Gillenwater A, Richards-Kortum R. Molecular imaging of glucose uptake in oral neoplasia following topical application of fluorescently labeled deoxy-glucose. *International journal of cancer*. 2009;124(11):2634-42. Epub 2009/01/29. doi: 10.1002/ijc.24222. PubMed PMID: 19173294; PMCID: PMC2700039.
173. Speizer L, Haugland R, Kutchai H. Asymmetric transport of a fluorescent glucose analogue by human erythrocytes. *Biochimica et biophysica acta*. 1985;815(1):75-84. Epub 1985/04/26. PubMed PMID: 4039191.
174. Yoshioka K, Saito M, Oh KB, Nemoto Y, Matsuoka H, Natsume M, Abe H. Intracellular fate of 2-NBDG, a fluorescent probe for glucose uptake activity, in *Escherichia coli* cells. *Bioscience, biotechnology, and biochemistry*. 1996;60(11):1899-901. Epub 1996/11/01. doi: 10.1271/bbb.60.1899. PubMed PMID: 8987871.
175. Zhang WY, Lee JJ, Kim IS, Kim Y, Myung CS. Stimulation of glucose uptake and improvement of insulin resistance by aromadendrin. *Pharmacology*. 2011;88(5-6):266-74. Epub 2011/11/08. doi: 10.1159/000331862. PubMed PMID: 22056597.
176. Itoh Y, Abe T, Takaoka R, Tanahashi N. Fluorometric determination of glucose utilization in neurons in vitro and in vivo. *Journal of cerebral blood flow and metabolism : official journal of the International Society of Cerebral Blood Flow and Metabolism*. 2004;24(9):993-1003. Epub 2004/09/10. doi: 10.1097/01.wcb.0000127661.07591.de. PubMed PMID: 15356420.
177. Zhao Y, Liu H, Riker AI, Fodstad O, Ledoux SP, Wilson GL, Tan M. Emerging metabolic targets in cancer therapy. *Frontiers in bioscience (Landmark edition)*. 2011;16:1844-60. Epub 2011/01/05. PubMed PMID: 21196269; PMCID: PMC3117434.
178. Mor A, Aizman E, George J, Kloog Y. Ras inhibition induces insulin sensitivity and glucose uptake. *PLoS One*. 2011;6(6):e21712. Epub 2011/07/09. doi: 10.1371/journal.pone.0021712. PubMed PMID: 21738773; PMCID: PMC3126849.
179. Thekkekk N, Maru DM, Polydorides AD, Bhutani MS, Anandasabapathy S, Richards-Kortum R. Pre-clinical evaluation of fluorescent deoxyglucose as a topical contrast agent for the detection of Barrett's-associated neoplasia during confocal imaging. *Technology in cancer research & treatment*. 2011;10(5):431-41. Epub 2011/09/08. doi: 10.7785/tcrt.2012.500220. PubMed PMID: 21895028; PMCID: PMC4527376.
180. Natarajan A, Srienc F. Dynamics of glucose uptake by single *Escherichia coli* cells. *Metabolic engineering*. 1999;1(4):320-33. Epub 2000/08/11. doi: 10.1006/mben.1999.0125. PubMed PMID: 10937825.
181. Laffleur F. Mucoadhesive polymers for buccal drug delivery. *Drug development and industrial pharmacy*. 2014;40(5):591-8. Epub 2014/03/01. doi: 10.3109/03639045.2014.892959. PubMed PMID: 24576266.
182. Jabbour JM, Cheng S, Malik BH, Cuenca R, Jo JA, Wright J, Cheng YS, Maitland KC. Fluorescence lifetime imaging and reflectance confocal microscopy for multiscale imaging of oral precancer. *Journal of biomedical optics*. 2013;18(4):046012. Epub 2013/04/19. doi: 10.1117/1.jbo.18.4.046012. PubMed PMID: 23595826; PMCID: PMC3628018.

183. Hucker WJ, Ripplinger CM, Fleming CP, Fedorov VV, Rollins AM, Efimov IR. Bimodal biophotonic imaging of the structure-function relationship in cardiac tissue. *Journal of biomedical optics*. 2008;13(5):054012. Epub 2008/11/22. doi: 10.1117/1.2975826. PubMed PMID: 19021392; PMCID: PMC2719892.
184. Park J, Jo JA, Shrestha S, Pande P, Wan Q, Applegate BE. A dual-modality optical coherence tomography and fluorescence lifetime imaging microscopy system for simultaneous morphological and biochemical tissue characterization. *Biomed Opt Express*. 2010;1(1):186-200. Epub 2011/01/25. doi: 10.1364/boe.1.000186. PubMed PMID: 21258457; PMCID: PMC3005181.
185. Song L, Langfelder P, Horvath S. Random generalized linear model: a highly accurate and interpretable ensemble predictor. *BMC bioinformatics*. 2013;14:5. Epub 2013/01/18. doi: 10.1186/1471-2105-14-5. PubMed PMID: 23323760; PMCID: PMC3645958.
186. Hoover EE, Squier JA. Advances in multiphoton microscopy technology. *Nature photonics*. 2013;7(2):93-101. Epub 2013/12/07. doi: 10.1038/nphoton.2012.361. PubMed PMID: 24307915; PMCID: 3846297.
187. DeConde A, Miller ME, Palla B, Lai C, Elashoff D, Chhetri D, St John MA. Squamous cell carcinoma of buccal mucosa: a 40-year review. *American journal of otolaryngology*. 2012;33(6):673-7. Epub 2012/06/12. doi: 10.1016/j.amjoto.2012.04.006. PubMed PMID: 22681929.
188. Wang W, Han S, Yao Z, Li X, Huang P, Zhang M, Chen Y, He J. A study of epidemiologic and recurrence factors of oral cancer. *Journal of oral and maxillofacial surgery : official journal of the American Association of Oral and Maxillofacial Surgeons*. 2012;70(9):2205-10. Epub 2012/01/03. doi: 10.1016/j.joms.2011.09.040. PubMed PMID: 22209101.
189. Huang Y, Lui H, Zhao J, Wu Z, Zeng H. Precise Spatially Selective Photothermalolysis Using Modulated Femtosecond Lasers and Real-time Multimodal Microscopy Monitoring. *Theranostics*. 2017;7(3):513-22. Epub 2017/03/04. doi: 10.7150/thno.17596. PubMed PMID: 28255346; PMCID: PMC5327629.
190. Kantelhardt SR, Kalasauskas D, Konig K, Kim E, Weinigel M, Uchugonova A, Giese A. In vivo multiphoton tomography and fluorescence lifetime imaging of human brain tumor tissue. *Journal of neuro-oncology*. 2016;127(3):473-82. Epub 2016/02/03. doi: 10.1007/s11060-016-2062-8. PubMed PMID: 26830089.
191. Zhao Y, Sheng M, Huang L, Tang S. Design of a fiber-optic multiphoton microscopy handheld probe. *Biomed Opt Express*. 2016;7(9):3425-37. Epub 2016/10/05. doi: 10.1364/boe.7.003425. PubMed PMID: 27699109; PMCID: PMC5030021.
192. Liu W, Li C, Zhang Z, Kartner FX, Chang G. Self-phase modulation enabled, wavelength-tunable ultrafast fiber laser sources: an energy scalable approach. *Optics express*. 2016;24(14):15328-40. Epub 2016/07/15. doi: 10.1364/oe.24.015328. PubMed PMID: 27410809.
193. Huang L, Mills AK, Zhao Y, Jones DJ, Tang S. Miniature fiber-optic multiphoton microscopy system using frequency-doubled femtosecond Er-doped fiber laser. *Biomed Opt Express*. 2016;7(5):1948-56. Epub 2016/05/28. doi: 10.1364/boe.7.001948. PubMed PMID: 27231633; PMCID: PMC4871093.
194. Kobat D, Horton NG, Xu C. In vivo two-photon microscopy to 1.6-mm depth in mouse cortex. *Journal of biomedical optics*. 2011;16(10):106014. Epub 2011/10/28. doi: 10.1117/1.3646209. PubMed PMID: 22029361.
195. Dombeck DA, Harvey CD, Tian L, Looger LL, Tank DW. Functional imaging of hippocampal place cells at cellular resolution during virtual navigation. *Nature neuroscience*.

- 2010;13(11):1433-40. Epub 2010/10/05. doi: 10.1038/nn.2648. PubMed PMID: 20890294; PMCID: PMC2967725.
196. Durr NJ, Weisspfennig CT, Holfeld BA, Ben-Yakar A. Maximum imaging depth of two-photon autofluorescence microscopy in epithelial tissues. *Journal of biomedical optics*. 2011;16(2):026008. Epub 2011/03/03. doi: 10.1117/1.3548646. PubMed PMID: 21361692; PMCID: PMC3061332.
  197. Bedard N, Quang T, Schmeler K, Richards-Kortum R, Tkaczyk TS. Real-time video mosaicing with a high-resolution microendoscope. *Biomed Opt Express*. 2012;3(10):2428-35. Epub 2012/10/20. doi: 10.1364/boe.3.002428. PubMed PMID: 23082285; PMCID: PMC3469983.
  198. Wu Y, Fu F, Lian Y, Chen J, Wang C, Nie Y, Zheng L, Zhuo S. Monitoring morphological alterations during invasive ductal breast carcinoma progression using multiphoton microscopy. *Lasers Med Sci*. 2015;30(3):1109-15. Epub 2015/01/27. doi: 10.1007/s10103-015-1712-y. PubMed PMID: 25616712.
  199. Quinn KP, Sridharan GV, Hayden RS, Kaplan DL, Lee K, Georgakoudi I. Quantitative metabolic imaging using endogenous fluorescence to detect stem cell differentiation. *Scientific reports*. 2013;3:3432. Epub 2013/12/07. doi: 10.1038/srep03432. PubMed PMID: 24305550; PMCID: PMC3851884.
  200. Kim WH, Lee J, Jung DW, Williams DR. Visualizing sweetness: increasingly diverse applications for fluorescent-tagged glucose bioprobes and their recent structural modifications. *Sensors (Basel, Switzerland)*. 2012;12(4):5005-27. Epub 2012/06/06. doi: 10.3390/s120405005. PubMed PMID: 22666073; PMCID: PMC3355456.
  201. Tsai MR, Chen SY, Shieh DB, Lou PJ, Sun CK. In vivo optical virtual biopsy of human oral mucosa with harmonic generation microscopy. *Biomed Opt Express*. 2011;2(8):2317-28. doi: 10.1364/BOE.2.002317. PubMed PMID: 21833368; PMCID: PMC3149529.
  202. Brown CM, Rivera DR, Pavlova I, Ouzounov DG, Williams WO, Mohanan S, Webb WW, Xu C. In vivo imaging of unstained tissues using a compact and flexible multiphoton microendoscope. *Journal of biomedical optics*. 2012;17(4):040505. Epub 2012/05/09. doi: 10.1117/1.JBO.17.4.040505. PubMed PMID: 22559671; PMCID: 3382343.
  203. DeCoro M, Wilder-Smith P. Potential of optical coherence tomography for early diagnosis of oral malignancies. *Expert review of anticancer therapy*. 2010;10(3):321-9. Epub 2010/03/11. doi: 10.1586/era.09.191. PubMed PMID: 20214513; PMCID: 4038412.
  204. Lee KW. *Color atlas of oral pathology*. Philadelphia: Lea & Febiger; 1985. 148 p. p.
  205. Rivera DR, Brown CM, Ouzounov DG, Pavlova I, Kobat D, Webb WW, Xu C. Compact and flexible raster scanning multiphoton endoscope capable of imaging unstained tissue. *Proceedings of the National Academy of Sciences of the United States of America*. 2011;108(43):17598-603. Epub 2011/10/19. doi: 10.1073/pnas.1114746108. PubMed PMID: 22006303; PMCID: PMC3203813.
  206. Rivera DR, Brown CM, Ouzounov DG, Webb WW, Xu C. Use of a lensed fiber for a large-field-of-view, high-resolution, fiber-scanning microendoscope. *Optics letters*. 2012;37(5):881-3. Epub 2012/03/02. doi: 10.1364/ol.37.000881. PubMed PMID: 22378425.
  207. Pal R, Shilagard T, Yang J, Villarreal P, Brown T, Qiu S, McCammon S, Resto V, Vargas G. Remodeling of the Epithelial-Connective Tissue Interface in Oral Epithelial Dysplasia as Visualized by Noninvasive 3D Imaging. *Cancer Res*. 2016;76(16):4637-47. Epub 2016/06/16. doi: 10.1158/0008-5472.can-16-0252. PubMed PMID: 27302162; PMCID: PMC4987238.

## **Vita**

Rahul Pal was born in Kolkata, India on April 24<sup>th</sup>, 1986, the younger son of Dr. Himangshu Kumar Pal and Mrs. Kabita Pal. Rahul attended primary and secondary schools in Kolkata, India. He then attended Bidhannagar College in Kolkata, graduating in 2007 with a B.S. in Chemistry major. After college, he completed an M.S. degree in Biochemistry from University of Calcutta in 2009.

Rahul began his graduate career at The University of Texas Medical Branch at Galveston, Texas, in 2010 in the department of Biochemistry and Molecular Biology. He was advised by Gracie Vargas. During his graduate career, he published two first author journal articles in peer-reviewed scientific journals.

Permanent Address: 4A Rakhal Ghosh Lane, Alekhya Co-operative Society, Flat # 3C, Kolkata, India – 700085

This dissertation was typed by the author, Rahul Pal.